



5-2019

Surface Functionalization of Nanoparticles: from Lithium- Ion Battery Anode to High Refractive Index Optical Materials

Sisi Jiang

University of Tennessee, sjiang10@vols.utk.edu

Follow this and additional works at: https://trace.tennessee.edu/utk_graddiss

Recommended Citation

Jiang, Sisi, "Surface Functionalization of Nanoparticles: from Lithium- Ion Battery Anode to High Refractive Index Optical Materials. " PhD diss., University of Tennessee, 2019.
https://trace.tennessee.edu/utk_graddiss/5387

This Dissertation is brought to you for free and open access by the Graduate School at TRACE: Tennessee Research and Creative Exchange. It has been accepted for inclusion in Doctoral Dissertations by an authorized administrator of TRACE: Tennessee Research and Creative Exchange. For more information, please contact trace@utk.edu.

To the Graduate Council:

I am submitting herewith a dissertation written by Sisi Jiang entitled "Surface Functionalization of Nanoparticles: from Lithium- Ion Battery Anode to High Refractive Index Optical Materials." I have examined the final electronic copy of this dissertation for form and content and recommend that it be accepted in partial fulfillment of the requirements for the degree of Doctor of Philosophy, with a major in Chemistry.

Bin Zhao, Major Professor

We have read this dissertation and recommend its acceptance:

Brian Long, Sheng Dai, Tongye Shen

Accepted for the Council:

Dixie L. Thompson

Vice Provost and Dean of the Graduate School

(Original signatures are on file with official student records.)

**Surface Functionalization of Nanoparticles: from Lithium-
Ion Battery Anode to High Refractive Index Optical
Materials**

A Dissertation Presented for the

Doctor of Philosophy

Degree

The University of Tennessee, Knoxville

Sisi Jiang

May 2019

Acknowledgements

I would like to firstly thank my advisor at the University of Tennessee, Knoxville, Professor Bin Zhao. I learned knowledge in polymer and surface chemistry under your guideline. More importantly, you set the standard for logical and critical thinking, great attention to details and diligence and persistence in work as a scientist for me. The lessons I have learned from you will certainly be a company with me all through my entire career.

My gratitude also goes to Dr. Zhengcheng Zhang, the advisor of mine during my stay at Argonne National Laboratory (ANL) as a visiting graduate student. You led me into the electrochemical field with your rich knowledge as we work together in the Silicon Deep Dive project of Department of Energy (DOE). I also appreciate the opportunity you create for me to work with many other excellent experts in ANL. I have learned the importance of cooperation from you.

I would like to thank Professor Brian Long, Professor Sheng Dai, Professor Tongye Shen from UTK for serving on my committee and for graciously devoting your time and efforts in giving valuable suggestions on my research. I would also like to thank Dr. Lu Zhang and Dr. Chen Liao from ANL for giving me your guide and support in my research project.

I appreciate the funding provided by Department of Chemistry at the University of Tennessee, John Hopkins University Applied Physics Laboratory and DOE throughout my graduation study.

My special thanks go to Dr. Kewei Wang and Dr. Roger Wright, who shared their valuable experiences in the synthesis of hairy titanium dioxide and silica nanoparticles, as well as Dr. Wenxin Fu, who taught his rich knowledge in polymer chemistry to me patiently. I would also like to thank Bryan Seymour for your help to coordinate all the department and graduation affairs when

I was working at ANL. To all my other lab partners in Professor Zhao's research group and all my colleagues at ANL, I will always be grateful for your friendship and help, both in my career and my life.

My family has always been the strongest backing for me. To my parents, Judong and Yunnv, thank you for always loving me as who I am. I owe you huge debt that I can never repay. Also, to my in-laws, Weimin Hu and Zhilan Yang, and my aunts, uncles, cousins, thank you for your support and love.

Finally, to my husband, Bin, I would not be writing this without you. We earned all these together.

Abstract

Surface-functionalized nanoparticles (SF-NPs) have great potential to be used in many fields including biosensors, medicines, catalysis, environmental remediation and energy storage. This dissertation work demonstrate the development of solutions confronting specific problems in the application of nanoparticles with surface functionalization strategy. Chapter 1 presents an introduction.

The electrochemical performance of silicon anode in lithium-ion battery is closely related to the surface properties of silicon nanoparticles (SiNPs). In Chapter 2, an epoxy group is attached onto the surface of SiNPs through the formation of siloxane bond by surface silanization. Electrode based on epoxy-functionalized SiNPs shows a much improved cell performance due to the improved binding system by the chemical reaction between epoxy group and poly(acrylic acid) binder and the reduced parasitic reactions with electrolyte. In Chapter3, a series of specially designed functional groups featuring ethylene oxide of different chain length terminated with an epoxy group are covalently attached to SiNPs by surface hydrosilylation. When employed as active materials for Si-graphite electrode, the surface-functionalized SiNPs improve cell performance with enhanced Li^+ transport, stronger binding system and improved anode surface stability.

A feasible way to make processable high refractive index (RI) optical materials is to introduce high RI inorganic nanofillers into the processable polymer matrix. A strong interaction between the two components is desired to prevent aggregation of nanoparticles in polymer. In Chapter 4, sulfur-containing polymer brush-grafted titanium dioxide (TiO_2) nanoparticles (hairy TiO_2 NPs) are made by surface-initiated atom transfer radical polymerization (SI-ATRP). The incorporation of sulfur atom, which has high molar refraction, into side chain of vinyl monomers increases the intrinsic RI of the grafted polymer chains. The hairy TiO_2 NPs, featuring tunable

ratio between grafted polymers and inorganic core, good dispersion and processability, have great potential to be used alone or to be used as building block in processable high RI nanocomposites.

Chapter 5 presents surface functionalization of SiNPs by surface-initiated “living”/controlled radical polymerization (SI-LRP). Polymer-grafted SiNPs show good stability in common solvents and are expected to be applied in many practical fields including sustainable energy storage, semiconductors and optical industry.

A conclusion and future perspective are given in Chapter 6.

Table of Contents

Chapter 1. Introduction	1
1.1 Surface Functionalization of Nanoparticles	2
1.1.1 Nanoparticles Functionalized with Small Organic Ligands	3
1.1.1.1 Surface Functionalization of Silicon Nanoparticles	3
1.1.1.2 Surface Functionalization of Metal-Oxide Nanoparticles	5
1.1.2 Polymer Brush-Grafted Nanoparticles.....	8
1.2 Application-Specific Surface-Functionalized Silicon Nanoparticles Applied as Active Material in Lithium-Ion Battery	11
1.2.1 Introduction to Lithium-Ion Battery	11
1.2.2 Silicon-Based Lithium-Ion Battery.....	15
1.2.3 Surface-Functionalized Silicon Nanoparticles as Anode Materials in Lithium-Ion Battery.....	18
1.3 Application-Specific Surface-Functionalized TiO₂ Nanoparticles Applied as Processable High Refractive-Index Materials.....	20
1.3.1 High Refractive Index Polymers.....	20
1.3.2 High Refractive Index Organic-Inorganic Nanocomposites.....	23
1.4 Dissertation Overview	25
1.5 References	29
Chapter 2. Surface Functionalized Silicon Nanoparticles Applied as Anode Materials in Lithium-ion Battery	40
Abstract.....	41
2.1 Introduction.....	42

2.2 Experimental Section.....	44
2.2.1 Electrode and Electrolyte Materials.....	44
2.2.2 Synthesis of Surface-Functionalized SiNPs.....	45
2.2.3 Characterization of Functionalized SiNPs.....	45
2.2.4 Si Electrode Fabrication and Electrochemical Testing.....	46
2.2.6 Post-Test Analysis	46
2.3 Results and Discussion.....	47
2.3.1 Synthesis and Characterization of Functionalized SiNPs.....	47
2.3.2 Electrochemical Performance	50
2.4 Conclusions.....	61
2.5 Reference	62
Appendix A for Chapter 2. Surface Functionalized Silicon Nanoparticles applied as	
Anode Materials in Lithium-ion Battery.....	68
A.1 Supplemental Figures	69
A.2 X-Ray Photoelectron Spectroscopy: Working principle and application in	
interfacial analysis of LIB electrode	75
A.3 Reference.....	81
Chapter 3. Tailoring the Surface of Silicon Nanoparticles for Enhanced Chemical and	
Electrochemical Stabilities for Lithium-ion Batteries.....	82
Abstract.....	83
3.1 Introduction.....	84
3.2 Experimental Section.....	86
3.2.1 Materials	86

3.2.2 Synthesis of Oligo(ethylene oxide)-Epoxy-Terminated Allyloxy Precursors (Allyl-(EO) _n -Epoxy)	87
3.2.3 SiNPs Surface Functionalization by Hydrosilylation	88
3.2.4 Graphite/Silicon Anode Preparation and Electrochemical Performance Evaluation	89
3.2.5 Characterization of SF-SiNPs	89
3.3 Results and Discussion.....	90
3.3.1 Synthesis and Characterization of SF-SiNPs	90
3.3.2 Electrochemical stability at anode/electrolyte interface	96
3.3.3 Impact of Grating Density	100
3.4 Morphological Characterization	101
3.4 Conclusion	105
3.5 Reference	106
Appendix B for Chapter 3. Tailoring the Surface of Nano Silicon Nanoparticles	
Anode for Enhanced Chemical and Electrochemical Stabilities in for Lithium-ion	
Batteries	111
B.1 Calculation of Grafting Density of SF-SiNPs	112
B.2 Supplemental Figures	113
Chapter 4. Sulfur-Containing Polymer Brush-Grafted Titanium Dioxide	
Nanoparticles: Potential Processable High Refractive Index Hybrid Materials.....	
Abstract.....	126
4.1 Introduction.....	127
4.2 Experimental Section.....	130
4.2.1 Materials	130

4.2.2 General Characterization.	130
4.2.3 Synthesis of Sulfur-Containing Polymers.....	132
4.2.3.1 Synthesis of Sulfur-Containing Styrenic Monomer.....	132
4.2.3.2 Synthesis of Sulfur-Containing Methacrylate Monomer.....	133
4.2.4 Synthesis of sulfur-containing polymer by supplemental activator and reducing agent atom transfer radical polymerization (SARA-ATRP).....	133
4.2.4.1 Synthesis of Sulfur-Containing Styrenic Polymer PS1S	133
4.2.4.2 Synthesis of Sulfur-Containing Methacryloyl Polymer PM1S.....	134
4.2.5 Synthesis of Sulfur-Containing Polymer-Grafted TiO ₂ NPs	135
4.2.5.1 Synthesis of ATRP Initiator-Functionalized TiO ₂ NPs	135
4.2.5.2 Synthesis of PS1S Brush-Grafted TiO ₂ NPs (TiO ₂ Hairy NPs).....	136
4.2.6 Thin Film Preparation	137
4.2.6.1 Substrate Supported Thin Film of Polymers and Hairy Nanoparticles.....	137
4.2.6.2 Free-Standing Films of PS1S and PM1S	137
4.3 Results and Discussion.....	138
4.3.1 Synthesis and Characterization of Sulfur-Containing Polymer PS1S and PM1S.....	138
4.3.1.1 Synthesis and Characterization of PS1S	138
4.3.1.2 Synthesis and Characterization of PM1S.....	142
4.3.2 Synthesis and Characterization of Sulfur-Containing Polymer-Grafted TiO ₂ NPs.....	146
4.3.2.1 Synthesis of ATRP Initiator-Functionalized TiO ₂ NPs	146
4.3.2.2 Synthesis of Sulfur-Containing Polymer Brush-Grafted TiO ₂ NPs.....	146
4.3.3 Optical Properties of Thin Film Made from Sulfur-Containing Polymers and the Corresponding Hairy NPs	154

4.4 Conclusion	154
4.5 References	160
Appendix C for Chapter 4. Sulfur-containing Polymer Brush-grafted Titanium	
Dioxide Nanoparticles with Good Processability and High Refractive Index	164
Chapter 5. Polymer Brush-Grafted Silicon Nanoparticles by Surface-Initiated	
Controlled Radical Polymerization: Synthesis and Characterization	172
Abstract.....	173
5.1 Introduction.....	174
5.2 Experimental Section.....	177
5.2.1 Materials	177
5.2.2 General Characterization	177
5.2.3 Synthesis of Polymer Brush-Grafted SiNPs from the Surface of ATRP Initiator-	
Functionalized SiNPs Made by Surface Silanization	178
5.2.3.1 Preparation of ATRP Initiator-Functionalized SiNPs via Surface Silanization.	
.....	178
5.2.3.2 Synthesis of Polystyrene Brush-Grafted SiNPs from the Surface of INP-I-1	
by Surface-Initiated ATRP (SI-ATRP)	180
5.2.4 Synthesis of Polymer Brush-Grafted SiNPs from the Surface of ATRP Initiator-	
Functionalized SiNPs Made by Surface Hydrosilylation	181
5.2.4.1 Preparation of ATRP Initiator-Functionalized SiNPs via Surface	
Hydrosilylation.....	181
5.2.4.2 Synthesis of Polymer Brush-Grafted SiNPs from the surface of INP-II-1 by	
SI-ATRP.....	181

5.2.4.3 Synthesis of Poly(methyl acrylate) Brush-Grafted SiNPs by Surface-Initiated Single Electron transfer “Living”/Controlled Radical Polymerization (SET-LRP)	182
5.3 Results and Discussion.....	183
5.3.1 Solution Etching of SiNPs	183
5.3.2 Synthesis of Hairy SiNPs from Initiator-Functionalized SiNPs Made by Surface Silanization	183
5.3.3 Synthesis of Hairy SiNPs from Initiator-Functionalized SiNPs made by Surface Hydrosilylation	188
5.3.4 Comparison Between the Two Initiator Immobilization Methods	195
5.4 Conclusion	195
5.5 References	197
Appendix D for Chapter 5. Polymer Brush-Grafted Silicon Nanoparticles by Surface-Initiated Controlled Radical Polymerization: Synthesis and Characterization	203
D.1 Supplemental Figures	204
D.2 Calculation of Grafting Density of polymer Brushes on 92 nm Silicon Nanoparticles.....	209
Chapter 6. Conclusions and Future Work	211
6.1 Reference	216
Vita	217

List of Tables

1.1 Molar refractions of common atoms and groups.....	22
A.1 Loading densities, initial capacities, and capacity retentions of different Si electrodes.	71
3.1 Grafting densities; loading densities, initial capacities and Coulombic efficiencies, capacity retentions and charge-transfer resistances (R_{ct}) measured after 150 electrochemical cycles of the graphite/silicon composite electrodes beased on original SiNPs and SF-SiNPs.....	102
4.1 Molecular weight and polydispersity, monomer conversion and calculated DP of PS1Ss.....	143
4.2 Characterization data of sulfur-containing polymer brush-grafted TiO ₂ NPs.....	153
4.3 Thickness and RI value of sulfur-containing polymers. The thickness and refractive indices were measured on the films of the corresponding samples spin coated on the silicon wafer.....	155
5.1 Summary of hairy SiNPs using initiator NPs made by surface silanization.....	190
5.2 Summary of hairy SiNPs using initiator NPs made by surface hydrosilylation.....	194

List of Figures

1.1 Volumetric and gravimetric energy densities of different battery technologies.....	12
2.1 (a) FT-IR spectra and (b) TGA thermograms of pristine SiNPs, silanol-enriched SiNPs and epoxy SiNPs.....	49
2.2 (a) FT-IR spectra and (b) TGA thermograms of pristine SiNPs, silanol-enriched SiNPs and epoxy SiNPs.....	51
2.3 TGA profiles of (a) CH ₃ -SiNPs and CH ₃ -SiNPs treated with PAA binder, and (b) epoxy-SiNPs and epoxy-SiNPs treated with PAA binder.....	52
2.4 Electrochemical impedance spectroscopy of pristine SiNPs electrode and epoxy SiNPs electrode (a) after three formation cycles at C/20 and (b) after 100 cycle at C/3.....	54
2.5 SEM images of the freshly made Si/PAA electrodes with (a) pristine SiNPs, (b) Si-OH SiNPs, and (c) epoxy-SiNPs and cycled Si/PAA electrodes with (d) pristine SiNPs, (e) Si-OH SiNPs, and (f) epoxy-SiNPs as active materials.....	55
2.6 EDX elemental mapping (Si, C, O, F, P) for Si/PAA electrodes with (a) pristine SiNPs, (b) Si-OH SiNPs and (c) epoxy-SiNPs after 100 cycles.....	57
2.7 Si2p XPS spectra of the Si electrodes based on pristine SiNPs and epoxy-SiNPs before and after one formation cycle: (a) fresh Si electrode before cycling and (b) Si electrode after one formation cycle at delithiated state.....	58
2.8 (a) Adhesion strength of the Si anodes with pristine SiNPs, Si-OH SiNPs, epoxy-SiNPs, and CH ₃ -SiNPs as active materials, and (b) summarized data of average load per unit width (N/cm)	60

A1 TEM images of (A) pristine SiNPs, (B) silanol (Si-OH) enriched-SiNPs and (C) epoxy-SiNPs. The specimens were prepared by casting the particles on the carbon-coated copper grid from 1 mg/g dispersion of SiNPs in acetone.....69

A2 (a) FT-IR spectra of the pristine SiNPs and CH₃-SiNPs; (b) TGA profiles of pristine SiNPs and CH₃-SiNPs.....70

A3 EDX elemental mapping spectra showing the distribution of silicon, carbon and oxygen on the surface of Si/PAA electrodes based on (a) pristine SiNPs, (b) Si-OH SiNPs and (c) epoxy-SiNPs before cycling. (The elemental mapping results are shown in the right side; from top to bottom: Si, C and O)72

A4 Si_{2p} XPS spectra of (a) pristine SiNPs, Si-OH-SiNPs, epoxy-SiNPs and CH₃-SiNPs, and (b) the normalized Si_{2p} XPS spectra of pristine SiNPs, Si-OH-SiNPs, epoxy-SiNPs and CH₃-SiNPs.....73

A5 C_{1s} XPS spectra of Si electrodes based on (a) pristine SiNPs and (b) epoxy-SiNPs after one lithiation/delithiation cycle, (c) O_{1s} XPS and (d) F_{1s} XPS spectra of the pristine and epoxy-SiNPs electrode after one lithiation/delithiation cycle.74

A6 A schematic view of the interaction of an X-ray photon ($E = h\nu$) with an atomic orbital electron on 1s orbit.....76

A7 Illustration of XPS experiment. Reprint from <https://www.lanl.gov/orgs/nmt/nmtdo/AQarchive/04summer/XPS.html>.....78

A8 Schematic view of the interfacial phase transition the surface of the silicon anode during 1st lithitaiton/delithiation cycle. Reprint form ref. 5 with permission of American Chemistry Society.....80

3.1 (a) FTIR-ATR spectrum of original Si-H NPs, the inset is an enlarged figure of the Si-H bands, (b) Si 2p core-level spectrum of original Si-H NPs.....	93
3.2 (a) FTIR-ATR spectra and (b) TGA curve of the Si-C3-(EO) _n -Epoxy NPs The FTIR spectrum and TGA curve of original Si-H NPs are attached as reference.....	88
3.3 TEM images of Si-C3-(EO) ₁ -Epoxy NPs (a1) and Original Si-H NPs (b), a2 is a zoom-in image of a1. The specimens were prepared from 1 mg g ⁻¹ SiNPs aqueous suspension by casting the nanoparticles on the carbon-coated copper TEM grid. (c) are the optical images of aqueous dispersions (1 mg g ⁻¹) of original Si-H NPs and Si-C3-(EO) ₁ -Epoxy NPs, respectively. Left: freshly prepared dispersions which have been sonicated for 10 mins and Right: the same dispersion which has rested for 24h.....	95
3.4 Electrochemical Evaluation data: 1 st formation cycle (a) Voltage profiles and (b) Differential capacity profiles of electrodes based on original Si-H NPs (baseline) and Si-C3-(EO) _n -Epoxy NPs, respectively. The inset of (b) is a zoom-in of the differential capacity plot in the lithiation process; Electrochemical performance of graphite/Si composite electrodes (Li metal as counter electrode) over 150 cycles at C/3 rate: (c) specific charge capacity (lithiation: solid sphere; delithiation: empty sphere, shown to the left) and the corresponding coulombic efficiency (empty square, shown to the right); (d) EIS plots of baseline and SF-SiNPs electrodes, respectively (a) after 1st cycle at C/20 rate and (b) after 150 cycles at C/3 rate.....	97
3.5 Electrochemical performance of Si-C3-(EO) ₁ -Epoxy with different grafting density over 150 C/3 cycles: (a) specific capacity (lithiation: solid sphere; delithiation: empty sphere) and (b) the corresponding coulombic efficiency.....	103

3.6 EDX elemental mapping of pristine electrodes (C, Si and O) (a: baseline, and b: Si-C3-(EO) ₁ -Epoxy) and the cycled electrodes (C, Si, O, F and P) (c: baseline, d: Si-C3-(EO) ₁ -Epoxy)	104
B1 ¹ H NMR (a) and ¹³ C NMR (b) spectra of Allyl-(EO) ₁ -Epoxy in CDCl ₃	113
B2 ¹ H NMR (a) and ¹³ C NMR (b) spectra of Allyl-(EO) ₂ -OH in CDCl ₃	114
B3 ¹ H NMR (a) and ¹³ C NMR (b) spectra of Allyl-(EO) ₂ -Epoxy in CDCl ₃	115
B4 ¹ H NMR (a) and ¹³ C NMR (b) spectra of Allyl-(EO) ₄ -OH in CDCl ₃	116
B5 ¹ H NMR (a) and ¹³ C NMR (b) spectra of Allyl-(EO) ₄ -Epoxy in CDCl ₃	117
B6 DLS analysis results of (a) Si-H NPs and (b) Si-C3-(EO) ₁ -Epoxy NPs. The nanoparticles are dispersed in distilled water with a concentration of 1 mg/g.....	118
B7 (a) FTIR-ATR spectra and (b) TGA curves of the Si-C3-(EO) ₁ -Epoxy NPs obtained by surface hydrosilylation conducted in air (red curves) and in the argon-filled glovebox (blue curves). The FTIR spectrum and TGA curve of original Si-H NPs are attached as reference.....	119
B8 DQ/DV plots of the 2 nd and 3 rd C/20 formation cycle: (a) Si-C3-(EO) ₁ -Epoxy, (b) Si-C3-(EO) ₂ -Epoxy and (c) Si-C3-(EO) ₄ -Epoxy	120
B9 (a) FTIR spectrum and (b) TGA curve of the Si-C3-(EO) ₁ -OCH ₃ NPs.....	121
B10 Comparison study of electrochemical performance of graphite/Si composite electrodes based on Si-C3-(EO) ₁ -Epoxy and Si-C3-(EO) ₁ -OCH ₃ (Li metal as counter electrode) over 150 cycles at C/3 rate: (a) specific charge capacity (lithiation: solid sphere; delithiation: empty sphere) (b) the corresponding coulombic efficiency.....	122

B11 SEM images of the pristine electrodes (a: baseline, b: Si-C3-(EO) ₁ -Epoxy, c: Si-C3-(EO) ₂ -Epoxy and d: Si-C3-(EO) ₄ -Epoxy) and the cycled electrodes (e: baseline, f: Si-C3-(EO) ₁ -Epoxy, g: Si-C3-(EO) ₂ -Epoxy and h: Si-C3-(EO) ₄ -Epoxy).....	123
B12 EDX elemental mapping of pristine electrodes (C, Si and O) (a: Si-C3-(EO) ₂ -Epoxy, and b: Si-C3-(EO) ₄ -Epoxy) and the cycled electrodes (C, Si, O, F and P) (c: Si-C3-(EO) ₂ -Epoxy, d: Si-C3-(EO) ₄ -Epoxy).....	124
4.1 ¹ H NMR (a) and ¹³ C NMR (b) spectrum of S1S in CDCl ₃	140
4.2 Characterization data of PS1S-20.4k: SEC trace characterized by GPC (a), ¹ H NMR spectrum in CDCl ₃ (b), and TGA curve (c). The TGA analysis was performed in air at a heating rate of 20 °C/min from room temperature to 800 °C.....	141
4.3 ¹ H NMR (a) and ¹³ C NMR (b) spectrum of M1S in CDCl ₃	144
4.4 Characterization data of PM1S-23.2k: SEC trace characterized by GPC (a) ¹ H NMR spectrum in CDCl ₃ (b), and TGA curve (c). The TGA analysis was performed in air at a heating rate of 20 °C/min from room temperature to 800 °C.....	145
4.5 ¹ H NMR spectra of (a) PS1S-HNP-31.5k and (b) PM1S-HNP-25.5k in CDCl ₃	148
4.6 SEC trace of the dried free polymer PS1S formed from the free initiator ethyl 2-bromoisobutyrate in the synthesis of PS1S-HNP-31.5k (a) and TGA curves of (i) INP-1 and (ii) PS1S-HNP-31.5k (b).....	149
4.7 SEC trace of the dried free polymer PM1S formed from the free initiator ethyl 2-bromoisobutyrate in the synthesis of PM1S-HNP-25.5k (a) and TGA curves of (i) INP-1 and (ii) PM1S-HNP-25.5k (b).....	151
4.8 Bright-field TEM micrographs of polymer-grafted TiO ₂ NPs. (a) PS1S-HNP-11.8 k, (b) PS1S-HNP-22.6k, (c) PS1S-HNP-31.5k, (d) PS1S-HNP-43.3k and (e) PM1S-HNP-	

25.5k. The samples were cast onto carbon-coated, copper TEM grids from THF dispersion of the corresponding hairy NPs with a concentration of 1 mgmL ⁻¹	152
4.9 Optical pictures of free-standing films of (a) PS1S-20.4k and (b) PM1S-23.2k. highlighted in orange circles.....	156
4.10 Photos of sulfur-containing polymer brush-grafted TiO ₂ NPs (1 wt% dispersion in THF) at room temperature (a) from left to right are PS1S-HNP-11.8 k, PS1S-HNP-22.6k, PS1S-HNP-31.5 and PS1S-HNP-43.3k; (b) PM1S-HNP-25.5k PM1S brush-grafted TiO ₂ NPs.....	157
4.11 Bright-field TEM micrographs of polymer-grafted TiO ₂ NPs. (a) PS1S-HNP-11.8 k, (b) PS1S-HNP-22.6k, (c)PS1S-HNP-31.5k, (d) PS1S-HNP-43.3k and (e) PM1S-HNP-25.5k. The samples were cast onto carbon-coated, copper TEM grids from THF dispersion of the corresponding hairy NPs with a concentration of 1 mgmL ⁻¹	158
C1 HRMS (DART-TOF) of (A) S1S: m/z calc. 226.08; [M ⁺] 226.08; found 226.08073; mass error 3.23 ppm and (B) PM1S: m/z calc. 178.05; [MH ⁺] 179.05; found 179.04782; mass error -12.18 ppm.....	165
C2 SEC trace of PS1S-9.0k (a) and PS1S-31.8k (b).....	166
C3 ¹ H NMR (a) and ¹³ C NMR (b) spectra of the dopamine-terminated ATRP initiator in MeOH-d ₄ . Signals from methanol, water and ethyl acetate are marked with asterisks.....	167
C4 TGA curves (a) of iniator-functionalized TiO ₂ NPs. TGA curves of original TiO ₂ NPs is included as reference, and DLS profiles (b) of INP-1 and INP-2, The initiator NPs are dispersed in DMF with a concentration of 1 mgg ⁻¹	168

C5 SEC trace of the dried free polymer PS1S formed from the free initiator ethyl 2-bromoisobutyrate in the synthesis of PS1S-HNP-43.3k (a) and TGA curves of (i) INP-1 and (ii) PS1S-HNP-43.3k (b).....	169
C6 SEC trace of the dried free polymer PS1S formed from the free initiator ethyl 2-bromoisobutyrate in the synthesis of PS1S-HNP-22.6k (a) and TGA curves of (i) INP-1 and (ii) PS1S-HNP-22.6k (b).....	170
C7 SEC trace of the dried free polymer PS1S formed from the free initiator ethyl 2-bromoisobutyrate in the synthesis of PS1S-HNP-43.3k (a) and TGA curves of (i) INP-1 and (ii) PS1S-HNP-43.3k (b).....	171
5.1 Bright field TEM micrographs of original silicon nanopowder (a1 and a2) and (b) HF/HNO ₃ etched SiNPs after HF/HNO ₃ etching. The SiNPs were cast onto carbon-coated, copper TEM grids from the ethanol dispersions with a NP concentration of 1 mgmL ⁻¹	184
5.2 SEC trace of the dried free polymer polystyrene formed from the free initiator ethyl 2-bromoisobutyrate in the synthesis of PS-I-1-58.0k (a), TGA of (i) original SiNPs, (ii) INP-I-1 and (iii) PS-I-1-58.0k (b).....	187
5.3 Bright field TEM micrographs of hairy SiNPs PS-I-1-58.0k. The hairy NPs were cast onto carbon-coated, copper TEM grids from the THF dispersions with a hairy NPs concentration of 1 mgmL ⁻¹	189
5.4 SEC trace of the dried free polymer PMA formed from the free initiator ethyl 2-bromoisobutyrate in the synthesis of polymer brush-grafted silicon nanoparticles PMA-II-2-43.7k (a) and TGA curves of (i) INP-II-2 and (ii) PMA-II-2-43.7k (b)	192

5.5 Bright field TEM micrographs of hairy SiNPs PMA-II-2-43.7k. The hairy NPs were cast onto carbon-coated, copper TEM grids from the THF dispersions with a hairy NPs concentration of 1 mgmL⁻¹.....193

D1 SEC trace of the dried free polymer PnBA formed from the free initiator ethyl 2-bromoisobutyrate in the synthesis of polymer brush-grafted silicon nanoparticles PnBA-I-1-58.0k (a) and TGA curves of (i) INP-I-1 and (ii) PnBA-I-1-58.0k (b).....204

D2 SEC trace of the dried free polymer polystyrene formed from the free initiator ethyl 2-bromoisobutyrate in the synthesis of polymer brush-grafted silicon nanoparticles PS-I-2-31.7k (a) and TGA curves of (i) INP-I-2 and (ii) PS-I-2-31.7k (b)205

D3 SEC trace of the dried free polymer PnBA formed from the free initiator ethyl 2-bromoisobutyrate in the synthesis of polymer brush-grafted silicon nanoparticles PnBA-II-1-41.3k (a) and TGA curves of (i) INP-II-1 and (ii) PnBA-II-1-41.3k (b).....206

D4 SEC trace of the dried free polymer polystyrene formed from the free initiator ethyl 2-bromoisobutyrate in the synthesis of polymer brush-grafted silicon nanoparticles PS-II-1-41.1k (a) and TGA curves of (i) INP-II-1 and (ii) PS-II-1-41.1k (b)207

D5 SEC trace of the dried free polymer PnBA formed from the free initiator ethyl 2-bromoisobutyrate in the synthesis of polymer brush-grafted silicon nanoparticles PnBA-II-2-50.5k (a) and TGA curves of (i) INP-II-2 and (ii) PnBA-II-2-50.5k (b)208

List of Schemes

1.1 Surface functionalization of silicon nanoparticles through formation of (a) Si-O-Si-bond and (b) Si-R bond.....	4
1.2 The traditionally accepted mechanism for precious metal-catalyzed hydrosilation	6
1.3 Surface functionalization of a metal-oxide surface by (a) alkoxy silane, (b) phosphonate, (c) carboxylate and (d) catechol.....	7
1.4 Representative synthetic routes for polymer brush-grafted nanoparticles through (a) click chemistry, (b) silane chemistry and (c) surface-initiated controlled radical polymerization.....	9
1.5 Illustration of working principle of lithium-ion battery.....	14
1.6 Electrode reactions of different anode materials during charging: (a) graphite and (b) silicon.....	16
1.7 An overview of possible unfavorable consequences caused by rapid volume change of silicon anode and the representative strategies.....	19
2.1 Synthesis of surface-functionalized SiNPs with methyl and epoxy terminal groups..	48
3.1 (a) Synthesis of Allyl-(EO) _n -Epoxy and (b) Synthesis of SF-SiNPs by surface hydrosilylation.....	92
4.1 Synthesis of sulfur-containing monomer S1S and M1S and synthesis of the PS1S and PM1S by SARA-ATRP.....	139
4.2 (a) Synthesis of high sulfur-content polymer brush-grafted TiO ₂ NPs by surface-initiated atom transfer radical polymerization (SI-ATRP) and (b) synthesis of catechol-terminated ATRP initiator.....	147

5.1 Synthesis of polymer brush-grafted silicon nanoparticles from initiator-functionalized silicon nanoparticles made by (i) hydrolysis/condensation reaction of ATRP initiator-terminated triethoxysilane and (ii) surface hydrosilylation.....186

List of Abbreviations

AIBN: 2,2'-Azobis(2-methylpropionitrile)

ATRP: Atom transfer radical polymerization

BPO: benzoyl peroxide

C: graphite

CE: Coulombic efficiency

CMC: Carboxymethyl cellulose

¹³C NMR: Carbon nuclear magnetic resonance spectroscopy

DLS: Dynamic light scattering

DMC: Dimethyl carbonate

DMF: *N,N*-dimethylformamide

DMSO: Dimethyl sulfoxide

DP: Degree of polymerization

dQ/dV: Differential voltage

EBiB: Ethyl 2-bromoisobutyrate

EC: Ethyl carbonate

EDX: Energy-dispersive X-ray spectroscopy

EIS: Electrochemical impedance spectroscopy

EMC: Ethyl methyl carbonate

FEC: Fluoroethylene carbonate

FTIR: Fourier-transform infrared spectroscopy

GaN: Gallium nitride

Gen 2 electrolyte: 1.2 M LiPF₆ in a liquid mixture of ethylene carbonate and ethyl methyl carbonate in 3:7 by weight

GPTEs: Glycidylpropyltriethoxysilane

GPC: Gel permeation chromatography

¹H NMR: Proton nuclear magnetic resonance spectroscopy

HNP: Hairy nanoparticles

HRMS: High resolution mass spectrometry

HRIP: High refractive index polymer

H-terminated: Hydride-terminated

INP: Initiator nanoparticles

LCD: Liquid crystal display

LED: Light emitting diode

LIB: Lithium-ion battery

Me₆-TREN: Hexamethylated tris(2-aminoethyl)amine

MA: Methyl acrylate

Mefp: *Mytilus edulis foot protein*

M-O NPs: Metal-oxide nanoparticles

MTES: Methyltriethoxysilane

nBA: n-butyl acrylate

NCA: nickel cobalt Aluminum oxide

NMC: Nickel manganese cobalt oxide

NMR: Nuclear magnetic resonance

NMRP: Nitroxide-mediated radical polymerization

NP: Nanoparticle

NPs: Nanoparticle

NREL: National Renewable Energy Laboratory

OH-terminated: Hydroxide-terminated

PMDETA: *N, N, N', N', N''*- Pentamethyldiethylenetriamine

PAA: Poly(acrylic acid)

PC: Personal computer

PDI: Polydispersity

PDMS: Poly(dimethyl siloxane)

PGMA: Poly(Glycidyl methyl acrylate)

PMA: Poly(methyl acrylate)

PnBA: Poly(n-butyl acrylate)

PVDF: Poly(vinylidene fluoride)

RAFT: Reversible addition–fragmentation chain-transfer polymerization

RI: Refractive index

R_{ct} : Charge-transfer resistance

R_e : ohmic resistance of the electrode

R_{int} : Interfacial resistance

S: Sulfur

SAM: Self-assembled monolayer

SEC: Size exclusion chromatography

SEI: Solid-electrolyte interphase

SEM: Scanning electron microscopy

SET-LRP: Single electron transfer living radical polymerization

SF-SiNPs: Surface-functionalized silicon nanoparticles

SI: Surface-initiated

SI-ATRP: Surface-initiated atom transfer radical polymerization

SI-CRP: Surface-initiated controlled radical polymerization

SiNPs: Silicon nanoparticles

TEM: Transmission electron microscopy

TG-DSC: Thermogravimetry-differential scanning calorimetry

TGA: Thermogravimetric analysis THF: Tetrahydrofuran

TLC: Thin-layer chromatography

VC: Vinylene carbonate

XPS: X-ray photoelectron spectroscopy

Chapter 1. Introduction

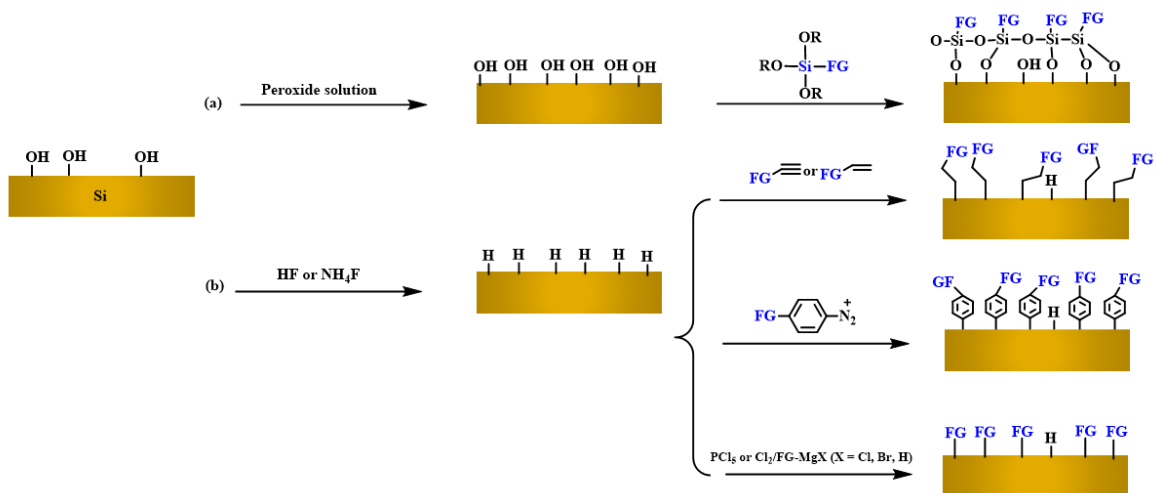
1.1 Surface Functionalization of Nanoparticles

A nanoparticle (NP), by definition, is a microscopic particle of which the typical size is between 1-100 nm on at least one dimension. As the size of the material approaches nanoscale, the percentage of surface area becomes significant in relative to that of total volume. As a result, many interesting properties that differ nanoparticles (NPs) from their bulk counterparts emerge. For instance, semiconductor NPs can confine their own electrons and exhibit quantum effects.¹ Sufficiently small ferromagnetic NPs may randomly flip direction of magnetization upon thermal treatment.² These unique properties of NPs draw emerging scientific attentions due to their great potential to open new avenues in many fields such as biology and medicine,³ semiconductors,¹ optics and energy. However, just like the two sides of a coin, while large surface area of the NPs brings many desirable properties, it also makes the NPs highly chemically reactive and physically aggregative. Therefore, NPs are usually surface functionalized with small organic ligands or polymers for passivation or stabilization purpose.⁴ As a matter of fact, surface functionalization, when at first glance serves as an inevitable pretreatment to passivate or stabilize NPs, is now one of the hottest research trends as many application-specific functionalities can be achieved by it. The possibility of surface-functionalized NPs to be used as biosensors,⁵ control release systems,⁶ catalysts,⁷ quantum dots,⁸ and so on have been extensively explored. NPs can be categorized into different types including semiconductor NPs, metal or metal-oxide NPs, carbon-based NPs, ceramic NPs and organic-based NPs. Likewise, the organic surface ligands can be small organic groups or polymer chains. Functionalization methods vary accordingly.

1.1.1 Nanoparticles Functionalized with Small Organic Ligands

1.1.1.1 Surface Functionalization of Silicon Nanoparticles

Silicon NPs (SiNPs), with many characteristic features like high energy capacity, high refractive index, semiconductivity, have been extensively used as the anodes of lithium-ion batteries,⁹ biosensors,¹⁰ microelectronics,¹¹ etc. For most of the applications, the surface of the SiNPs need to be functionalized with organic moieties to unlock application-related properties. In general, anchoring of surface organic groups on SiNPs can be classified into two types, one is through the formation of siloxane (Si-O-Si-R) bond while the other is through the formation of Si-C-R bond (Scheme 1.1). Surface Si-O-Si-R bond can be achieved by surface condensation reaction between hydroxyl-terminated SiNPs (OH-terminated SiNPs), and hydrolyzed organosilane compounds, which is also named as surface silanization reaction.¹² Most SiNPs possess a native layer of oxides upon exposed to ambient air, which contains sub-oxides and defects. Therefore, before surface silanization, SiNPs are usually chemically oxidized by being boiled in peroxide solutions. Siloxane functionality offers an effective passivation of particle surface plus varying functionality. Yet, siloxane bond is not kinetically stable and is inclined to hydrolysis. Besides, the imbedded insulant oxide-layer on particle surface may be a potential issue for certain applications. A more direct alternative is to functionalize the surface *via* formation of covalent Si-C bond, which is realized through coupling of activated precursors with hydride-terminated surface of SiNPs (H-terminated SiNPs). H-terminated silicon surface is created by removing native oxide layer *via* treatment with aqueous solution of hydrofluoric acid (HF) or ammonium fluoride (NH₄F). A variety of routes have been developed towards formation of surface Si-C bond, including but not limited to hydrosilylation, halogenation/alkylation, reduction of diazonium salts¹³ among which hydrosilylation, where Si-H bond is inserted across unsaturated precursors (olefin, acetylene,

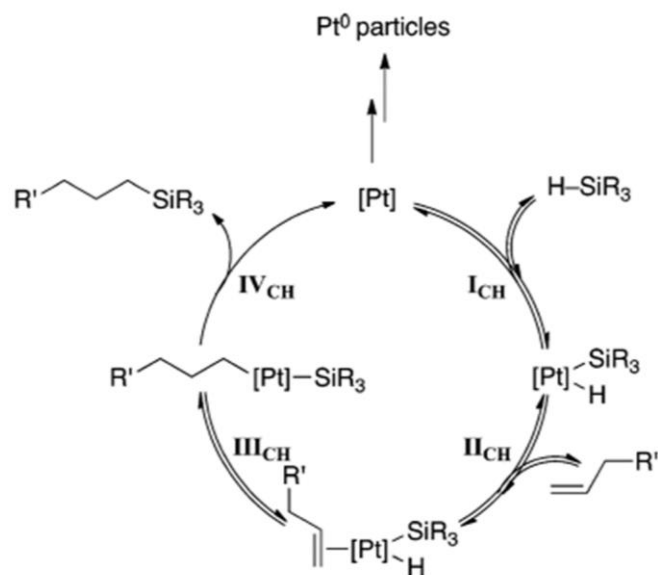


Scheme 1.1. Surface functionalization of silicon nanoparticles through formation of (a) Si-O-Si-R bond¹² and (b) Si-R bond.¹³

aldehyde, etc), is the most useful method. The pioneering work of surface hydrosilylation is conducted by Linford and Chidsey, in which they covalently bound an alkyl monolayer to silicon surface through a free-radical mechanism.¹⁴ In their work, the silyl radicals were generated by thermal decomposition of peroxide precursors. Later, many other radical excitation medias were explored including light,¹⁵ bias potential^{16, 17} and catalysts^{18, 19}. Precious metal-based catalysts, which is represented by Karstedt's catalyst, a platinum (0) complex containing vinyl siloxane ligand, are used most frequently to promote the selectivity and efficiency of surface hydrosilylation. To date, the reaction mechanism brought up by Chalk and Harrod²⁰ are the most recognized one, where unsaturated precursors and hydride of R_3SiH is inserted onto platinum by oxidization addition, followed by rearrangement of hydride. Then an irreversible reduction elimination step leads to the formation of Si-C bond (Scheme 1.2).²¹

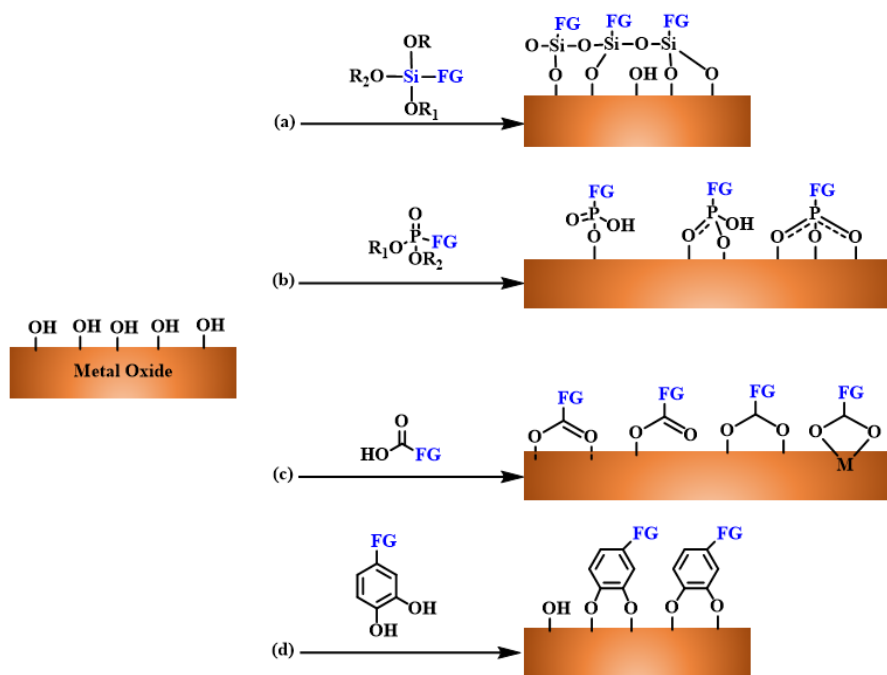
1.1.1.2 Surface Functionalization of Metal-Oxide Nanoparticles

Metal-oxide nanoparticles (M-O NPs) are of great scientific interests with their optical and magnetic properties. Thiols, carboxylate, silanes and phosphonates are frequently used modifiers for metal oxide NP surface. They can react with NP surface atom *via* coordination, electrostatic or hydrogen bonding interaction²² (Scheme 1.3). Among them, silane chemistry is the most popular method for surface functionalization of metal-oxide nanoparticles in that there are rich sources of commercial silane compounds that bear different functionalities and that functionalization efficiency is high. The reaction mechanism is quite similar to that of the surface silanization in 1.1.2.1, where a condensation reaction occurs between silane and M-OH groups on the metal oxide surface to form M-O-Si bond. On the other hand, the past decade has also witnessed an increasing trend in exploiting biomimetic surface modifiers like marine mussel-inspired adhesives. Marine mussel is known for its ability to anchor onto a variety of inorganic or organic substrates such as



Scheme 1.2. The traditionally accepted mechanism for precious metal-catalyzed hydrosilylation.

Reprint from ref.21 with permission of American Chemical Society.

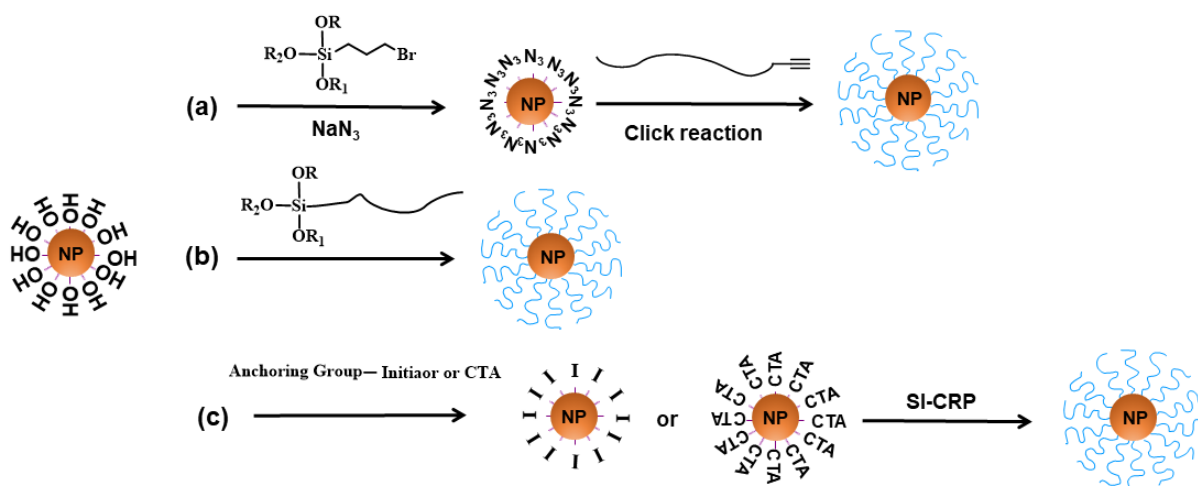


Scheme 1.3. Surface functionalization of a metal-oxide surface by (a) silane, (b) phosphonate, (c) carboxylate²² and (d) catechol.²³

metal, metal-oxide, silica, mica, polymers and so on even under water. Though the adhesion mechanism is still under debate, it is well-accepted that it is the catecholic units, which are rich in the *Mytilus edulis foot protein* (Mefp), that contribute to the adhesion ability of marine mussel.²³⁻
²⁵ As a matter of fact, catechol group-containing modifiers have already been widely used in surface modification of different metal-oxide surfaces. For example, a catechol-terminated biofunctional groups have been anchored onto ferromagnetic (Fe₂O₃) NPs for protein separation²⁶, and a catechol-end DNA has been tethered onto titanium dioxide (TiO₂) NPs for drug delivery.²⁷ Throughout years, a series of studies have been conducted to dig into the mechanism behind catechol's adhesive ability and different theories have been proposed like coordination,²⁸ bidentate or monodentate chelation,²³ bridged bidentate chelation²⁹ and so on.

1.1.2 Polymer Brush-Grafted Nanoparticles

Apart from small organic groups, polymers are another intriguing type of surface ligand. NPs with polymer chains tethered on the surface are often named as polymer brush-grafted NPs. The NPs vary from inorganic to metallic ones of all kinds of shapes including sphere, rod, wire or other irregular shapes and of different sizes ranging from tens to hundreds of nanometers. In terms of polymer, different brush architectures such as homopolymer, copolymer, mixed can be achieved.³⁰ This versatile class of materials can exhibit desired properties from both sides. Polymer brush-grafted NPs are generally fabricated through either “grafting to” or “grafting from” method (Scheme 1.4). For “grafting to”, very often, both or one of the two parties, premade polymer chains are functionalized with suitable ligands and the polymers are attached to the core NPs *via* reactions. Common examples for “grafting to” methods are thiol-end polymers grafting to gold nanoparticles³¹, azide- or thiol-terminated polymers attached to alkene- or alkyne- functionalized NPs^{32, 33} and trialkoxysilane terminated polymers attached to metal oxide or semiconductor



Scheme 1.4. Representative synthetic routes for polymer brush-grafted nanoparticles through (a) click chemistry,³² (b) silane chemistry,³⁴ and (c) surface-initiated controlled radical polymerization.³⁰

NPs.³⁴ Straightforward and controllable as “grafting to” method is, the grafting density of the grafted polymers is usually low due to the steric hinderance between the grafted and incoming polymer chains. In addition, the longer the polymer chains, the harder for the chain to diffuse to the grating site. “Grafting from”, also referred to surface-initiated (SI) polymerization, where the polymer brush is grown *in-situ* from the surface initiator grafted on NPs surface, is an alternative method to make polymer brush-grafted NPs with much higher grafting density, as monomer is easier to diffuse to the bound-propagating sites than pre-formed polymer chain. Furthermore, the adoption of controlled radical polymerization techniques such as nitroxide-mediated radical polymerization (NMRP),³⁵ atom transfer radical polymerization (ATRP) and its variations,³⁶⁻³⁸ single electron transfer living radical polymerization (SET-LRP),^{39, 40} and reversible addition-fragmentation chain transfer (RAFT) polymerization^{41, 42} in SI-polymerization gives polymer brush with well-defined architecture and low polydispersity. Immobilization of initiators can be achieved by silane chemistry, coordination or catechol chemistry. In addition to bound initiators, “free” or “sacrificial” initiators are also added to monitor the polymerization progress. It has been well-established that the molecular weight and polydispersity of the surface bound polymer brushes are essentially identical to the polymer initiated from these “free” initiators.^{43, 44} Our group has accumulated extensive research experience in making polymer brush-grafted NPs for fundamental research purpose. Silica (SiO₂) NPs grafted with thermosensitive polymer brushes were synthesized by surface-initiated ATRP (SI-ATRP) and the phase transition behavior of the hybrid particles was well studied.⁴⁴ Later, hybrid micellar network hydrogels composed of thermosensitive block polymer and polymer brush-grafted SiO₂ NPs were made and the effects of particle location and phase transition behavior on the gel properties of the hydrogel were investigated.^{45, 46} It was also found that SiO₂ NPs grafted with copolymer brushes composed of

two immiscible blocks exhibited reversible sol-gel transition in aqueous solution.⁴⁷ Polymer brush-grafted NPs also find way in many practical applications. For example, polymer brush-grafted SiO₂ and TiO₂ NPs synthesized either by SI-ATRP or surface-RAFT polymerization showed great potential as lubricant additive for wear and friction reduction.^{48, 49}

1.2 Application-Specific Surface-Functionalized Silicon Nanoparticles Applied as Active Material in Lithium-Ion Battery

1.2.1 Introduction to Lithium-Ion Battery

A battery, consisting of one or more cells that are connected in series and/or in parallel, is a device that converts electrochemical energy into electricity and thus is used as a source of power. It is with no exaggeration to say that the modern society runs on batteries, especially those secondary electrochemical accumulators, which is evidenced by increasing reliance on smart phones, mobile personal computers (PCs) and other portable devices as well as rocketing expansion of electrical vehicle market. Invention and commercialization of lithium-ion battery (LIB) based on carbonaceous materials and transition metal-oxide in early 1990s by Sony signified the biggest revolution so far in the development of rechargeable batteries.⁵⁰ Compared with other rechargeable energy storage systems like nickel / cadmium, nickel / metal hydride and lead-acid batteries, LIB has the advantages of higher energy density (both gravimetric and volumetric) as shown in Figure 1.1, operating voltage (lithium is one of the most electropositive elements, -3.04 V versus standard hydrogen electrode), longer life span, wider range of operating temperature and lighter weight.⁵¹ LIB is, fundamentally, based on reversible redox reactions and intercalation-deintercalation process of lithium. A lithium-ion battery is composed of a cell containing one positive (cathode) and one negative electrode (anode) supported by their current collectors and

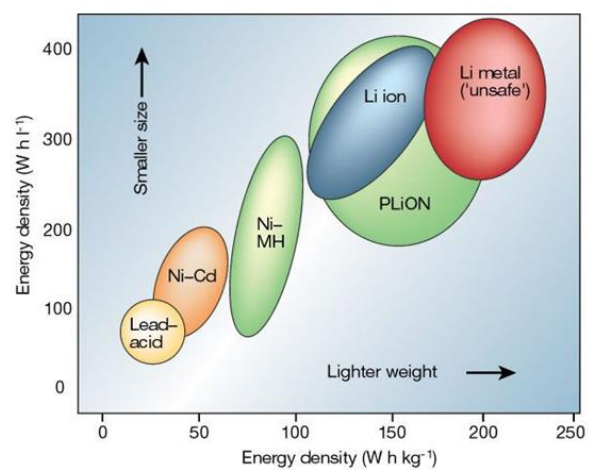
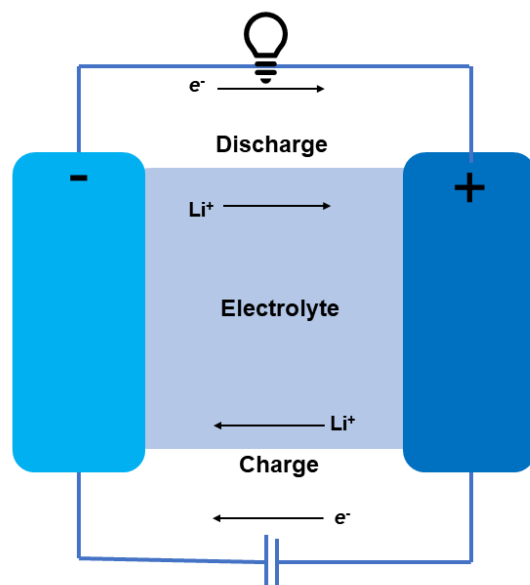


Figure 1.1. Volumetric and gravimetric energy densities of different battery technologies. Reprint from ref.52 with permission of Nature Publishing Group.

separated by an ionic conductor, which is often an electrolyte solution containing dissolved lithium salts. One key to make workable cell is to avoid direct contact between electrodes and electrode/electrolyte while at the same time to enable the ion transport between the two electrodes. Therefore, the electrolyte is imbibed in a porous separator which act not only as a physical barrier but also a membrane for ion transportation. Once the two electrodes are connected externally, chemical reactions occur on both ends, liberating electrons and thus providing energy. To be more specific, during discharge, Li^+ is deintercalated and released from the anode and flow spontaneously from negative electrode to positive electrode *via* electrolyte. At the same time, electrons are generated and conducted to the current collector through an internal conductive network and then transported to the cathode *via* the external circuit. Finally, on the cathode end, Li^+ are intercalated to the host material.⁵¹ The charging process will be a reverse of discharging process (Scheme 1.5). In terms of electrode materials, cathode materials are typically transitional metal oxide and anode materials have evolved from the lithium metal, which is considered not safe due to lithium dendrite issue, to carbonaceous materials like graphite, which is used in most of today's commercial LIB. The quantity of electrical energy, which is expressed either gravimetric (Whkg^{-1}) or volumetric (WhL^{-1}), that a battery is able to deliver is expressed as the product of the voltage (V) and capacity (mAhg^{-1}), which depends on the intrinsic properties of the active materials of the cell electrodes.⁵² The state-of-the-art LIB system based on graphite paired with lithium metal oxide such as lithium nickel manganese cobalt oxide (NMC), lithium nickel cobalt aluminum oxide (NCA) has a specific energy of between 150 – 250 Whkg^{-1} .⁵³ Driven by increasing demand, LIB market is expected to witness the highest growth rate in the next five years with an estimated revenue of \$ 69 billion by 2022 and is forecasted to take over lead-acid battery to have the NO.1 market share by 2024.⁵⁴ However, in contrast to the fast-growing market share, the pace



Scheme 1.5. Illustration of working principle of lithium-ion battery

in improving energy storage capability of LIB falls far behind with the energy density of LIB increased by only twofold.⁵²

1.2.2 Silicon-Based Lithium-Ion Battery

Apart from difference in packing technology and electrode formula, the energy density of LIB is mostly determined by the active materials of both cathode and anode. Regarding the anode materials, current commercial LIB anode depends almost solely on graphite (C). During charging, each Li^+ takes six carbon atoms for full intercalation (Scheme 1.6). Upon full intercalation, graphite can provide a specific capacity of around 370 mAh/g, which sets a ceiling for current LIB technology. Therefore, there is growing desire to find substituent materials to graphite and to build the next-generation high-energy-density LIB. Group IV (silicon, germanium, tin, *etc*) elements, which can form alloy with lithium, has been proposed to be strong candidates to fulfill this goal. Among them, silicon (Si), with its more than 10 times higher specific capacity (~ 4200 mAh/g when fully alloyed to $\text{Li}_{22}\text{Si}_5$), low discharge potential plateau (~ 0.1 V vs Li^+/Li), earth richness, and advanced technologies that are already set up in semiconductor industry, stands out to be the most promising alternative to graphite.^{9, 55} The biggest hurdle that prevents the massive commercialization of silicon anode is the dramatic capacity fade (~ 90 % capacity loss) within first 5 electrochemical cycles, which is believed to be highly related to the almost 400 % volume expansion/contraction of Si during lithiation/delithiation process.⁵⁶ To begin with, the alloying of Li^+ with Si is not isotropic, which will result in two phases, namely, Li_xSi and Si. Volume expansion was found to mainly occur at the phase boundary between these two phases, leading to anisotropic swelling and stress magnification and eventually to mechanical fracture and pulverization over extended electrochemical cycle. As a result, a considerable amount of active materials will be lost.⁵⁷ The initial effort to mitigate this issue is to use nanostructured silicon



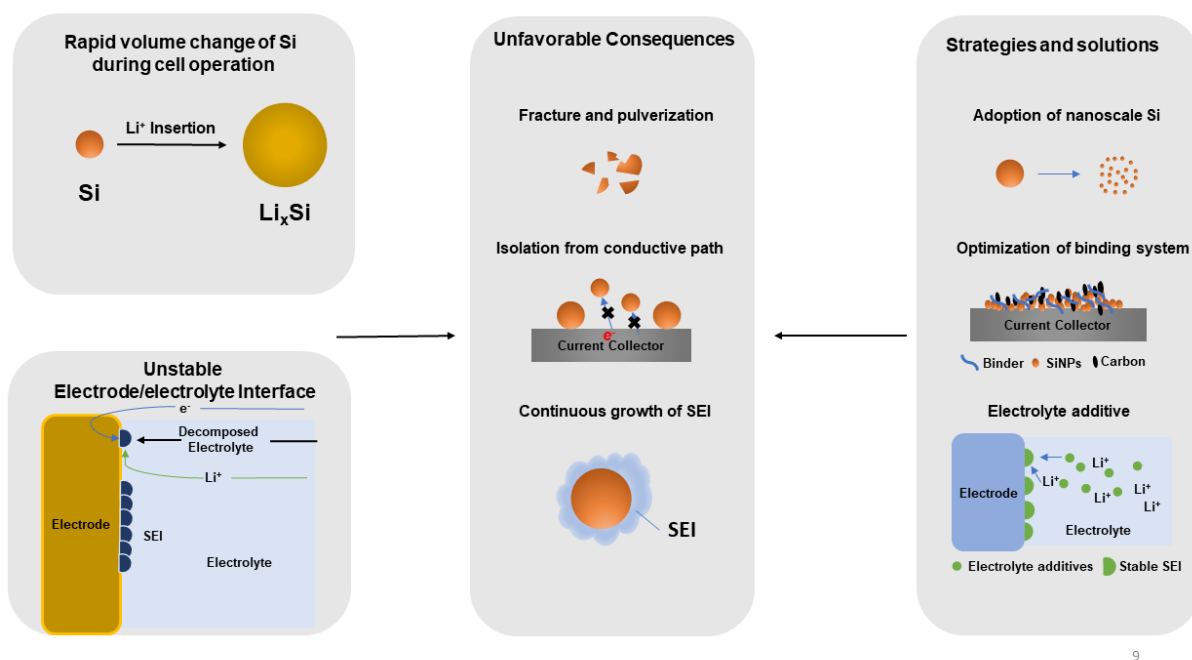
Scheme 1.6. Electrode reactions of different anode materials during charging: (a) graphite and (b) silicon

materials instead of bulk silicon because it has been reported that cracking in silicon may propagate by dislocation emission from cracking tip and that this propagation may not proceed when the crack size is below 150 nm⁵⁸; however, while nanostructured silicon did a better job alleviating the cracking problems, the capacity retention ability of Si-NP still did not improve much, indicating there are some other underlying factors determining the capacity stability.⁵⁹ The unstable solid electrolyte interphase (SEI) layer at electrode/electrolyte interface might be one of them. The working voltage of LIB is beyond the electrochemical stability of most of the carbonate solvents like ethylene carbonate (EC), dimethyl carbonate (DMC) and ethyl methyl carbonate (EMC) in the electrolyte. As a result, decomposition of solvent will occur during cell operation at electrode/electrolyte interface, along with some other side reactions related to the lithium salts and impurities in the electrolyte, the consequence is that Li⁺ and electrolyte solvents are consumed parasitically and that interfacial resistance increases as non-conductive byproducts adds up. The huge volume change of Si worsens this process by continuously exposing fresh Si to electrolyte and forming new SEI.⁶⁰ It is therefore of high significance to stabilize electrode/electrolyte interface. Some electrolyte additives have been adopted to address this issue. For instance, some sacrificial additives like vinylene carbonate (VC) that are electrochemically reduced prior to electrolyte carbonate are added to form insoluble solid layer on the electrode surface to prevent further decomposition of electrolyte solvent.⁶¹ Another type of additives represented by fluoroethylene carbonate (FEC) can couple with product of the decomposition and form stable SEI on the anode surface.⁶² Last but not least, rearrangement of electrode structure might cause detachment of active materials from current collector, leading to loss of conductive pathway.⁶³ To promote the integrity of electrode structure, new polymer binders were designed. Carboxylic acid (-COOH) or hydroxyl (-OH) functional group containing polymer binders such as carboxymethyl

cellulose (CMC)⁶⁴ and poly(acrylic acid) (PAA)⁶⁵ binder have been shown to improve capacity retention of Si electrode than the conventional binders such as polyvinylidene fluoride (PVDF) that works for graphite anode. It is believed that the formation of covalent bond or hydrogen bond between these binders and Si NP helps to provide cohesion between SiNPs and the conductive additives such as carbon particles, and improve electrical contact between SiNPs and the current collector (copper foil), thus facilitating the integrity of the electrode over electrochemical cycles.

1.2.3 Surface-Functionalized Silicon Nanoparticles as Anode Materials in Lithium-Ion Battery

As have been mentioned in 1.1, when the size of the materials reduces to nanoscale, the surface properties dominate bulk, and so as the case with Si NP-based anode. Recently, there is an increasing number of studies on direct surface modification of Si NP to promote the capacity retention of Si NP in LIB. For instance, Kang, *et al* modified the surface of SiNPs with amine (-NH₂) groups by silane chemistry and claimed that the surface -NH₂ can form ionic bond with PAA binder, which promotes the stability of the electrode for better capacity retention.⁶⁶ Biomimetic strategies were also employed. Bie and coworkers modified the surface of SiNPs by forming a thin layer of polydopamine *via in-situ* polymerization of dopamine around particle surface. When the modified SiNPs were mixed with PAA binder, the imino groups of surface-polydopamine can further react with the carboxyl groups of PAA binder and promote binding properties.⁶⁷ Apart from promoting binding system within electrode, it was also found functional group can affect SEI formation. Li's work presented that different functional groups (silanol, carboxyl group and siloxane) on Si NP surface can affect the SEI composition at the electrode interface after extended formation, which is also corresponding to the electrochemical performance.⁶⁸ More recently, Wang modified the surface of Si NP with analogues of several common electrolyte additives like



9

Scheme 1.7. An overview of possible unfavorable consequences caused by rapid volume change of silicon anode and the representative strategies.⁵⁵

VC and FEC by click chemistry and the modification improved the capacity retention of the Si NP-based electrode by better surface passivation.⁶⁹ While existing works on surface functionalization of silicon anode materials are still mainly limited to the two aspects, i.e., promote better electrode structure and optimize SEI formation, they have demonstrated that particle-level functionalization has great potential and feasibility to enhance electrochemical performance of SiNP-based LIB.

1.3 Application-Specific Surface-Functionalized TiO₂ Nanoparticles Applied as Processable High Refractive-Index Materials

1.3.1 High Refractive Index Polymers

Refractive index (RI, n) is a parameter describing how light propagates through a certain medium, compared with a vacuum, as expressed in Equation 1.1,

$$n = \frac{c}{v} \quad (\text{Equation 1.1})$$

where c is the speed of light in vacuum and v is the phase velocity of light in that medium. High RI materials are of increasing demand in modern optical applications. For example, high RI encapsulants for light emitting diode (LED) are in need to reduce the RI contrast at the LED die gallium nitride (GaN) ($n = 2.5$) – air interface to make LEDs brighter and more power-efficient.⁷⁰ ⁷¹ Also, high RI photodetectors are desirable for image sensors to increase the signal sensitivity.⁷² Other applications include antireflective coatings for liquid crystal displays (LCDs),^{73, 74} optical data communication and storage, polarizers and so on. While RI values of the materials are the primary concerns for these applications, other optical properties should also be considered such as absorption coefficient and optical dispersion.⁷⁵ The latter is a parameter describing the variation of n with wavelength. Polymers, with their high processability, lightness and mechanical strength,

are considered promising candidate for high RI materials, however, the narrow range of RI (between 1.3 -1.7 in UV visible range) limited their use in this field. Lots of effort have been put throughout years to break the high RI limit of polymers. According to Lorentz-Lorenz equation (Equation 1.2), refractive index of a substance correlates with its molecular properties:⁷⁶:



$$\frac{n^2-1}{n^2+1} = \frac{4\pi}{3} \frac{\rho N_A}{M_w} \alpha = \frac{[R]}{V_M} \quad (\text{Equation 1.2})$$

where n is refractive index, ρ is density, N_A is Avogadro's number, M_w is molecular weight and α is polarizability, $[R]$ is the molar refraction ($[R] = \frac{4\pi}{3} N_A \alpha$), and V_M is the molar volume of a certain substance. n can be further exacted and expressed as

$$n = \sqrt{\frac{1+[R]/V_M}{1-[R]/V_M}} \quad (\text{Equation 1.3})$$

Accordingly, n of a substance increases with molar refraction, which is determined by polarizability as well as molar density. Table 1.1 shows the molar refractions $[R]$ of common atoms and groups. It will be a feasible strategy to introduce high $[R]$ moieties, such as π -conjugated groups, organometallic groups, higher halogen and sulfur atoms, *etc.*, into the side chains or backbones of polymers to increase the intrinsic n . Halogen-containing (meth)acrylates have been reported to be polymerized by free radical polymerization. The n values of the resultant polymers are in the range of 1.67 – 1.77, adjustable by varying the type and number of halogen atoms introduced.⁷⁷ Polymer structures including length of linker groups also affect n as well as other properties such as glass transition temperature (T_g), which in turn affect processability. Paquet *et al.* prepared high RI polyferrocenes (RI ~ 1.72) with a relatively high Abbe number. Sulfur atom is also extensively used as RI enhancer for polymers with its relatively high atomic polarizability, good chemical stability and adaptability to be incorporated into polymers.⁷⁹ Ueda and coworkers

Table 1.1. Molar refractions of common atoms and groups^{77, 78}

Substituents	[R]/cm ³ mol ⁻¹	Substituents	[R]/cm ³ mol ⁻¹
H	1.100		1.733
C	2.418		2.398
O (hydroxyl)	1.525	4-member ring	0.400
O (carbonyl)	2.211	Phenyl (C₆H₅)	25.463
O (ether, ester)	1.643	Naphthyl (C₁₀H₇)	43.000
F	0.95	S (thiol) SH	7.691
Cl	5.967	S (dithia)	8.112
Br	8.865	S (thiolcarbonyl)	7.970
I	13.900	PH₃	9.104

synthesized polyimides featuring phenyl thioethers varying in sulfur contents. The RIs of polymers increase with increasing sulfur contents of repeating unit.⁸⁰ Other reported sulfur rich HRIPs including thioether and pyridine-bridged aromatic polyimides,⁸¹ sulfone and thioether containing polyamides,⁸² sulfur-containing poly(methyl acrylate),⁸³ etc. Despite these efforts, most of the reported high RI polymers still only have a small adjustable RI range ($n \sim 1.65 - 1.75$), while any further efforts to increase the intrinsic RI of polymer will be at the cost of sacrificing other desired properties of the materials such as transparency and processability. Therefore, it remains a big challenge to develop HRIPs with excellent both optical properties and good processability.

1.3.2 High Refractive Index Organic-Inorganic Nanocomposites

Inorganic materials such as TiO₂ (anatase $n = 2.45$, rutile $n = 2.71$ at 500 nm), zirconium dioxide (ZrO₂, $n = 2.10$ at 500 nm), zinc sulfide (ZnS, $n = 2.36$ at 632.8 nm), lead sulfide (PbS, $n = 4.33$ at 632.8 nm) and Si ($n = 3.88$ at 632.8 nm) have high refractive indexes. However, they usually have poor processability. Marriage of high RI inorganic nanoparticles with polymers opens a new avenue for developing processable high RI materials that combine merits from both sides. A linear dependency of nanocomposites' RI on the volume fraction of inorganic and organic components have been found in many systems:

$$\frac{n_c^2-1}{n_c^2+1} = \varphi_p \frac{n_p^2-1}{n_p^2+1} + (1 - \varphi_p) \frac{n_m^2-1}{n_m^2+1} \quad (\text{Equation 1.4})$$

where n_c , n_p and n_m are RIs of the nanocomposites, inorganic nanoparticles and polymer matrix, respectively, and φ_p is volume fraction of the nanoparticles.⁸⁴⁻⁸⁶ In other words, the RIs of the nanocomposites are adjustable by varying n value of each components and their volume ratio. On the other hand, the transparency loss of the nanocomposites is mainly caused by light scattering of the dispersed particles in the polymer matrix, as can be described by Rayleigh scattering equation:

$$\frac{I}{I_0} = \exp \left\{ -\frac{32\pi^4 \varphi_p x r^3 n m^4 \left[\frac{(n_p/n_m)^2 - 1}{(n_p/n_m)^2 + 2} \right]}{\lambda^4} \right\} \quad (\text{Equation 1.5})$$

In the equation, transparency loss, as expressed by the ratio between the intensities of the transmittance light (I) and incident light (I_0), depends on both the size and volume fraction (φ_p) of the nanoparticles as well as the mismatch between RI values of NP (n_p) and polymers (n_m).⁷⁷ Since large RI mismatch between NP and polymer matrix and a relative high loading of NP are prerequisites for such nanocomposites, it is crucial to reduce the particle size and prevent agglomeration of NP in the polymer matrix. Preparation methods for organic-inorganic nanocomposites can be divided into two categories, i.e., *in-situ* route and *ex-situ* route. The most common *in-situ* method is sol-gel technique, where functionalized polymers are present during the sol-gel synthesis of NP from the precursors and the inorganic and organic components are bonded together by condensation or other reaction between functionalized polymers and the precursors. Problems with sol-gel method lie in that a variety of byproducts will be produced during reaction, which leads to shrinkage during drying and compromise the mechanical properties. Besides, the linkage between the organic and inorganic domains are usually too weak to prevent the aggregation of NPs. Furthermore, it is hard to control the final properties of NP in the system with *in-situ* method. *Ex-situ* methods varying from the simplest blending method to polymer brush approach are more frequently used. Papadimitrakopoulos, *et al* blended colloidal suspensions of silicon nanoparticles that are prepared by ball milling followed by sonication and centrifugation with poly(ethylene oxide) to fabricate high RI nanocomposites. The highest RI of the obtained nanocomposites reached 3.2 at 500 nm.⁸⁶ However, these silicon nanocomposites exhibit increased scattering in the red and the near IR region of the visible spectrum probably due to the aggregation of the silicon NPs in the gelation polymer. To achieve better dispersion of NP, a polymer brush approach is usually adopted, which is generally carried out by either a “grafting

to” or a “grafting from” method. The “grafting to” method is a straightforward and controllable route to prepare polymer brush-grafted nanoparticles, where polymers a functional group can be attached onto NP surface by click chemistry or coupling reactions like silane chemistry. Tao prepared transparent polymer nanocomposites by grafting poly(glycidyl methacrylate) (PGMA) chains onto anatase TiO₂ nanoparticles *via* alkyne azide “click” chemistry. The highest RI of the nanocomposites reached 1.80 at 500 nm.⁸⁷ Li *et al.* grafted a poly(dimethyl siloxance) (PDMS) onto the surface of ZrO₂ nanoparticles to disperse the nanofillers into the polymer. With RI ranging from 1.50 – 1.65 at 500 nm and good optical transparency, the polymer nanocomposites are used as LED encapsulants.⁸⁸ However, the “grafting to” techniques usually cannot achieve high grafting density, especially with long polymer chains. This problem can be addressed by “grafting from” or surface-initiated polymerization, in which polymer brushes are grown directly from the surface of initiator-functionalized nanoparticles as monomer molecules can diffuse to the propagating sites on the core surface more easily. Therefore, the “grafting from” technique has the advantage of producing a denser polymer layer on the surface of NPs. Besides, the grafting density of the polymer brush-grafted NPs is tunable by adjusting the number of surface initiators on particle surfaces. Furthermore, desired architectures and chain length of the brush can be obtained with the application of SI-LRP. All these advantages make “grafting from” a suitable method to make high RI polymer brush-grafted NPs with adjustable RI values and good processability.

1.4 Dissertation Overview

This dissertation research is devoted to developing specific solutions to address problems in practical application of nanoparticles with surface functionalization strategy. In particular, we demonstrated that functionalization on particle level can improve the electrochemical performance

of silicon anode in lithium-ion battery and that polymer brush-grafted TiO₂ nanoparticles are promising processable high refractive index (RI) materials with good processability and tunable RI value.

Chapter 2 presents surface functionalization of silicon nanoparticles (SiNPs) with epoxy group by surface silanization reaction between surface silanol group and trialkoxysilane-terminated functional precursors. Successful surface functionalization was confirmed by Fourier-transform infrared spectroscopy (FTIR) and thermogravimetric analysis (TGA) analysis. When the surface-functionalized SiNPs (SF-SiNPs) are applied as anode in lithium-ion battery, the epoxy group on the particle surface can react with PAA binder to promote integrity of electrode structure and can stabilize the electrode/electrolyte interface to mitigate parasitic reaction of electrolyte solvents with electrode, thus improving the electrochemical performance of the anode. Post-test analysis including electrochemical impedance spectroscopy (EIS), scanning electron microscopy (SEM)/energy-dispersive X-ray spectroscopy (EDX) and X-ray photoelectron spectroscopy (XPS) analysis confirmed the proposed mechanism behind the performance improvement.

Chapter 3 demonstrates surface functionalization of SiNPs with a series of specially designed functional groups featuring ethylene oxide of different chain lengths that are terminated with an epoxy group *via* formation of covalent Si-C bond by surface hydrosilylation reaction between surface Si-H groups and allyloxy-terminated functional precursors. When applied as active material in silicon-graphite composite electrode, SF-SiNPs show enhanced stability in electrode in lamination. Furthermore, during cell operation, surface ethylene oxide group facilitates transport of Li⁺, mitigating irreversible capacity loss and increasing capacity retention, while surface epoxy group improves binder-particle interaction, promoting efficient utility of the capacity of active materials. EIS and SEM/EDX analysis shed lights on the mechanism of performance

improvement. Finally, it was found that grafting density of surface functional groups was closely related to the electrochemical performance of SiNPs.

Chapter 4 describes the synthesis of sulfur-containing polymer brush-grafted titanium dioxide (TiO_2) nanoparticles (hairy TiO_2 NPs) towards processable high refractive index (RI) materials. Sulfur (S) atom has high molar refraction and good compatibility with polymer. The incorporation of S into the side chain of styrenic- and methacrylatetype polymer increases the RIs of the polymers by around 0.1. Catechol chemistry is adopted to immobilize ATRP initiator onto the surface of TiO_2 NPs. Then polymer brushes were grown from the surface of initiator-grafted TiO_2 NPs by SI-ATRP. The grafting of polymer brushes was confirmed by characterization techniques including nuclear magnetic resonance spectroscopy (NMR), TGA, and transmission electron microscopy (TEM). The molecular weight and polydispersity of the polymer brushes can be estimated from gel permeation chromatography (GPC) analysis of the free polymer initiated from “free initiator” present in the SI-ATRP system. The hairy TiO_2 NPs can be made into thin films. It is expected that the hairy TiO_2 NPs can exhibit tunable RI by varying the ratio between polymer chains and the inorganic core.

Chapter 5 provides an effective method to stabilize SiNPs. SI-ATRP and SI-(SET-LRP) is employed to functionalize the surface of SiNPs with polymer brushes. The LRP initiators are anchored onto the particle surface with two different methods: surface silanization and surface hydrosilylation. While surface silanization approach gives hairy SiNPs with higher grafting density, the surface hydrosilylation provides us with a non-oxide option to synthesize hairy SiNPs. TEM analysis reveals good stability of the hairy SiNPs in common solvents. The hairy SiNPs are expected to exhibit better compatibility and processability than bare SiNPs and to be applied in many practical fields such as semiconductors, optics and sustainable energy storage.

A summary of this dissertation research and future work are provided in Chapter 6.

1.5 References

1. Smith, A. M.; Nie, S., Semiconductor nanocrystals: structure, properties, and band gap engineering. *Acc. Chem. Res.* **2010**, *43*, 190-200.
2. Gubin, S. P., *Magnetic Nanoparticles*. Wiley-VCH: 2009.
3. Salata, O. V., Applications of nanoparticles in biology and medicine. *J Nanobiotechnology* **2004**, *2*, 3.
4. Nagarajan, R., Nanoparticles: Building Blocks for Nanotechnology. In *Nanoparticles: Synthesis, Stabilization, Passivation, and Functionalization*, American Chemical Society: 2008; Vol. 996, pp 2-14.
5. Jiang, S.; Win, K. Y.; Liu, S.; Teng, C. P.; Zheng, Y.; Han, M. Y., Surface-functionalized nanoparticles for biosensing and imaging-guided therapeutics. *Nanoscale* **2013**, *5*, 3127-3148.
6. Slowing, I. I.; Vivero Escoto, J. L.; Wu, C. W.; Lin, V. S. Y., Mesoporous silica nanoparticles as controlled release drug delivery and gene transfection carriers. *Adv. Drug Del. Rev.* **2008**, *60*, 1278-1288.
7. Lu, A. H.; Salabas, E. E.; Schüth, F., Magnetic nanoparticles: synthesis, protection, functionalization, and application. *Angew. Chem. Int. Ed.* **2007**, *46*, 1222-1244.
8. Zhu, S.; Song, Y.; Zhao, X.; Shao, J.; Zhang, J.; Yang, B., The photoluminescence mechanism in carbon dots (graphene quantum dots, carbon nanodots, and polymer dots): current state and future perspective. *Nano Res.* **2015**, *8*, 355-381.
9. Wu, H.; Cui, Y., Designing nanostructured Si anodes for high energy lithium ion batteries. *Nano Today* **2012**, *7*, 414-429.

10. Vigneshvar, S.; Sudhakumari, C.; Senthilkumaran, B.; Prakash, H., Recent advances in biosensor technology for potential applications—an overview. *Front Bioeng Biotechnol.* **2016**, *4*, 11.
11. Pavesi, L.; Turan, R., *Silicon nanocrystals: fundamentals, synthesis and applications*. John Wiley & Sons: 2010.
12. Koelling, J.; Kolb, K., Infrared study of reaction between alkoxy silanes and silica. *ChemComm* **1965**, 6-7.
13. Veerbeek, J.; Huskens, J., Applications of Monolayer - Functionalized H - Terminated Silicon Surfaces: A Review. *Small Methods* **2017**, *1*, 1700072.
14. Linford, M. R.; Chidsey, C. E. D., Alkyl monolayers covalently bonded to silicon surfaces. *J. Am. Chem. Soc.* **1993**, *115*, 12631-12632.
15. Faucheux, A.; Gouget Laemmel, A. C.; Henry de Villeneuve, C.; Boukherroub, R.; Ozanam, F.; Allongue, P.; Chazalviel, J. N., Well-Defined Carboxyl-Terminated Alkyl Monolayers Grafted onto H-Si(111): Packing Density from a Combined AFM and Quantitative IR Study. *Langmuir* **2006**, *22*, 153-162.
16. Robins, E.; Stewart, M.; Buriak, J., Anodic and cathodic electrografting of alkynes on porous silicon. *Chem. Commun.* **1999**, 2479-2480.
17. Koiry, S.; Aswal, D.; Saxena, V.; Padma, N.; Chauhan, A.; Joshi, N.; Gupta, S.; Yakhmi, J.; Guerin, D.; Vuillaume, D., Electrochemical grafting of octyltrichlorosilane monolayer on Si. *Appl. Phys. Lett.* **2007**, *90*, 113118.
18. Buriak, J. M.; Stewart, M. P.; Geders, T. W.; Allen, M. J.; Choi, H. C.; Smith, J.; Raftery, D.; Canham, L. T., Lewis Acid Mediated Hydrosilylation on Porous Silicon Surfaces. *J. Am. Chem. Soc.* **1999**, *121*, 11491-11502.

19. Buriak, J. M., Organometallic Chemistry on Silicon and Germanium Surfaces. *Chem. Rev.* **2002**, *102*, 1271-1308.
20. Chalk, A.; Harrod, J., Reactions between dicobalt octacarbonyl and silicon hydrides. *J. Am. Chem. Soc.* **1965**, *87*, 1133-1135.
21. Meister, T. K.; Riener, K.; Gigler, P.; Stohrer, J. r.; Herrmann, W. A.; Kühn, F. E., Platinum Catalysis Revisited • Unraveling Principles of Catalytic Olefin Hydrosilylation. *ACS Catalysis* **2016**, *6*, 1274-1284.
22. Neouze, M.-A.; Schubert, U., Surface Modification and Functionalization of Metal and Metal Oxide Nanoparticles by Organic Ligands. *J Monatshefte für Chemie - Chemical Monthly* **2008**, *139*, 183-195.
23. Ye, Q.; Zhou, F.; Liu, W., Bioinspired catecholic chemistry for surface modification. *Chem. Soc. Rev.* **2011**, *40*, 4244-4258.
24. Ruiz-Molina, D.; Saiz Poseu, j.; Busque, F.; Nador, F.; Mancebo, J., The Chemistry behind Catechol-Based Adhesion. *Angew. Chem. Int. Ed.* **2019**, *58*, 696-714.
25. Lee, H.; Dellatore, S. M.; Miller, W. M.; Messersmith, P. B., Mussel-inspired surface chemistry for multifunctional coatings. *Science* **2007**, *318*, 426-430.
26. Xu, C.; Xu, K.; Gu, H.; Zheng, R.; Liu, H.; Zhang, X.; Guo, Z.; Xu, B., Dopamine as a robust anchor to immobilize functional molecules on the iron oxide shell of magnetic nanoparticles. *J. Am. Chem. Soc.* **2004**, *126*, 9938-9939.
27. Rajh, T.; Saponjic, Z.; Liu, J.; Dimitrijevic, N. M.; Scherer, N. F.; Vega-Arroyo, M.; Zapol, P.; Curtiss, L. A.; Thurnauer, M. C., Charge transfer across the nanocrystalline-DNA interface: Probing DNA recognition. *Nano Lett.* **2004**, *4*, 1017-1023.

28. Moser, J.; Punchihewa, S.; Infelta, P. P.; Graetzel, M., Surface complexation of colloidal semiconductors strongly enhances interfacial electron-transfer rates. *Langmuir* **1991**, *7*, 3012-3018.
29. Dalsin, J. L.; Lin, L.; Tosatti, S.; Vörös, J.; Textor, M.; Messersmith, P. B., Protein resistance of titanium oxide surfaces modified by biologically inspired mPEG–DOPA. *Langmuir* **2005**, *21*, 640-646.
30. Zoppe, J. O.; Ataman, N. C.; Mocny, P.; Wang, J.; Moraes, J.; Klok, H.-A., Surface-initiated controlled radical polymerization: state-of-the-art, opportunities, and challenges in surface and interface engineering with polymer brushes. *Chem. Rev.* **2017**, *117*, 1105-1318.
31. Lowe, A. B.; Sumerlin, B. S.; Donovan, M. S.; McCormick, C. L., Facile preparation of transition metal nanoparticles stabilized by well-defined (co) polymers synthesized via aqueous reversible addition-fragmentation chain transfer polymerization. *J. Am. Chem. Soc.* **2002**, *124*, 11562-11563.
32. Ranjan, R.; Brittain, W. J., Combination of living radical polymerization and click chemistry for surface modification. *Macromolecules* **2007**, *40*, 6217-6223.
33. Asmussen, S. V.; Vallo, C. I., Facile preparation of silver-based nanocomposites via thiol-methacrylate ‘click’ photopolymerization. *Eur. Polym. J.* **2016**, *79*, 163-175.
34. Tsyalkovsky, V.; Klep, V.; Ramaratnam, K.; Lupitsky, R.; Minko, S.; Luzinov, I., Fluorescent reactive core–shell composite nanoparticles with a high surface concentration of epoxy functionalities. *Chem. Mater.* **2007**, *20*, 317-325.
35. Ladmiral, V.; Morinaga, T.; Ohno, K.; Fukuda, T.; Tsujii, Y., Synthesis of monodisperse zinc sulfide particles grafted with concentrated polystyrene brush by surface-initiated nitroxide-mediated polymerization. *Eur. Polym. J.* **2009**, *45*, 2788-2796.

36. Hui, C. M.; Pietrasik, J.; Schmitt, M.; Mahoney, C.; Choi, J.; Bockstaller, M. R.; Matyjaszewski, K., Surface-initiated polymerization as an enabling tool for multifunctional nanoengineered hybrid materials. *Chem. Mater.* **2013**, *26*, 745-762.
37. Fristrup, C. J.; Jankova, K.; Hvilsted, S., Surface-initiated atom transfer radical polymerization—A technique to develop biofunctional coatings. *Soft matter* **2009**, *5*, 4623-4634.
38. Banerjee, S.; Paira, T. K.; Mandal, T. K., Surface confined atom transfer radical polymerization: access to custom library of polymer-based hybrid materials for speciality applications. *Polym. Chem.* **2014**, *5*, 4153-4167.
39. Turan, E.; Caykara, T., A facile route to end-functionalized poly (N-isopropylacrylamide) brushes synthesized by surface-initiated SET-LRP. *React. Funct. Polym.* **2011**, *71*, 1089-1095.
40. Tian, J.; Xu, D.; Liu, M.; Deng, F.; Wan, Q.; Li, Z.; Wang, K.; He, X.; Zhang, X.; Wei, Y., Marrying mussel inspired chemistry with SET - LRP: A novel strategy for surface functionalization of carbon nanotubes. *J. Polym. Sci., Part A: Polym. Chem.* **2015**, *53*, 1872-1879.
41. Stenzel, M. H.; Zhang, L.; Huck, W. T. S., Temperature - Responsive Glycopolymer Brushes Synthesized via RAFT Polymerization Using the Z - group Approach. *Macromol. Rapid Commun.* **2006**, *27*, 1121-1126.
42. Moraes, J.; Ohno, K.; Maschmeyer, T.; Perrier, S. b., Monodisperse, charge-stabilized, core-shell particles via silica-supported reversible addition-fragmentation chain transfer polymerization for cell imaging. *Chem. Mater.* **2013**, *25*, 3522-3527.

43. Husseman, M.; Malmström, E. E.; McNamara, M.; Mate, M.; Mecerreyes, D.; Benoit, D. G.; Hedrick, J. L.; Mansky, P.; Huang, E.; Russell, T. P., Controlled synthesis of polymer brushes by “living” free radical polymerization techniques. *Macromolecules* **1999**, *32*, 1424-1431.
44. Li, D.; Sheng, X.; Zhao, B., Environmentally responsive “hairy” nanoparticles: Mixed homopolymer brushes on silica nanoparticles synthesized by living radical polymerization techniques. *J. Am. Chem. Soc.* **2005**, *127*, 6248-6256.
45. Hu, B.; Henn, D. M.; Wright, R. A. E.; Zhao, B., Hybrid Micellar Hydrogels of a Thermosensitive ABA Triblock Copolymer and Hairy Nanoparticles: Effect of Spatial Location of Hairy Nanoparticles on Gel Properties. *Langmuir* **2014**, *30*, 11212-11224.
46. Hu, B.; Wright, R. A. E.; Jiang, S.; Henn, D. M.; Zhao, B., Hybrid micellar network hydrogels of thermosensitive ABA triblock copolymer and polymer brush-grafted nanoparticles: Effect of LCST transition of polymer brushes on gel property. *Polymer* **2016**, *82*, 206-216.
47. Wright, R. A. E.; Hu, B.; Henn, D. M.; Zhao, B., Reversible sol–gel transitions of aqueous dispersions of silica nanoparticles grafted with diblock copolymer brushes composed of a thermosensitive inner block and a charged outer block. *Soft matter* **2015**, *11*, 6808-6820.
48. Wright, R. A. E.; Wang, K.; Qu, J.; Zhao, B., Oil - Soluble Polymer Brush Grafted Nanoparticles as Effective Lubricant Additives for Friction and Wear Reduction. *Angew.Chem.Int.Ed* **2016**, *55*, 8656-8660.
49. Seymour, B. T.; Wright, R. A. E.; Parrott, A. C.; Gao, H.; Martini, A.; Qu, J.; Dai, S.; Zhao, B., Poly(alkyl methacrylate) Brush-Grafted Silica Nanoparticles as Oil Lubricant

- Additives: Effects of Alkyl Pendant Groups on Oil Dispersibility, Stability, and Lubrication Property. *ACS Appl. Mater. Interfaces* **2017**, *9*, 25038-25048.
50. Minami, T., *Solid state ionics for batteries*. Springer Science & Business Media: 2006.
 51. Tarascon, J. M.; Armand, M., Issues and challenges facing rechargeable lithium batteries. *Nature* **2001**, *414*, 359.
 52. Armand, M.; Tarascon, J. M., Building better batteries. *Nature* **2008**, *451*, 652.
 53. Zubi, G.; Dufo-López, R.; Carvalho, M.; Pasaoglu, G., The lithium-ion battery: State of the art and future perspectives. *Renew Sust Energ Rev* **2018**, *89*, 292-308.
 54. Ankit Gupta, A. S. B. *Lithium Ion Battery Market Size* Globler market insights: 2017.
 55. Chae, S.; Ko, M.; Kim, K.; Ahn, K.; Cho, J., Confronting issues of the practical implementation of Si anode in high-energy lithium-ion batteries. *Joule* **2017**, *1*, 47-60.
 56. Li, H.; Huang, X.; Chen, L.; Zhou, G.; Zhang, Z.; Yu, D.; Mo, Y. J.; Pei, N., The crystal structural evolution of nano-Si anode caused by lithium insertion and extraction at room temperature. *Solid State Ion.* **2000**, *135*, 181-191.
 57. McDowell, M. T.; Lee, S. W.; Harris, J. T.; Korgel, B. A.; Wang, C.; Nix, W. D.; Cui, Y., In situ TEM of two-phase lithiation of amorphous silicon nanospheres. *Nano Lett.* **2013**, *13*, 758-764.
 58. Liu, X. H.; Zhong, L.; Huang, S.; Mao, S. X.; Zhu, T.; Huang, J. Y., Size-dependent fracture of silicon nanoparticles during lithiation. *ACS Nano* **2012**, *6*, 1522-1531.
 59. Graetz, J.; Ahn, C. C.; Yazami, R.; Fultz, B., Highly reversible lithium storage in nanostructured silicon. *Electrochem. Solid-State Lett.* **2003**, *6*, A194-A197.

60. Kumar, R.; Tokranov, A.; Sheldon, B. W.; Xiao, X.; Huang, Z.; Li, C.; Mueller, T., In situ and operando investigations of failure mechanisms of the solid electrolyte interphase on silicon electrodes. *ACS Energy Lett* **2016**, *1*, 689-697.
61. Chen, L.; Wang, K.; Xie, X.; Xie, J., Effect of vinylene carbonate (VC) as electrolyte additive on electrochemical performance of Si film anode for lithium ion batteries. *J. Power Sources* **2007**, *174*, 538-543.
62. Choi, N.-S.; Yew, K. H.; Lee, K. Y.; Sung, M.; Kim, H.; Kim, S.-S., Effect of fluoroethylene carbonate additive on interfacial properties of silicon thin-film electrode. *J. Power Sources* **2006**, *161*, 1254-1259.
63. Ryu, J. H.; Kim, J. W.; Sung, Y.-E.; Oh, S. M., Failure modes of silicon powder negative electrode in lithium secondary batteries. *Electrochem. Solid-State Lett.* **2004**, *7*, A306-A309.
64. Li, J.; Lewis, R. B.; Dahn, J. R., Sodium carboxymethyl cellulose a potential binder for Si negative electrodes for Li-ion batteries. *Electrochem. Solid-State Lett.* **2007**, *10*, A17-A20.
65. Magasinski, A.; Zdyrko, B.; Kovalenko, I.; Hertzberg, B.; Burtovyy, R.; Huebner, C. F.; Fuller, T. F.; Luzinov, I.; Yushin, G., Toward Efficient Binders for Li-Ion Battery Si-Based Anodes: Polyacrylic Acid. *ACS Appl. Mater. Interfaces* **2010**, *2*, 3004-3010.
66. Kang, S.; Yang, K.; White, S. R.; Sottos, N. R., Silicon Composite Electrodes with Dynamic Ionic Bonding. *Adv. Energy Mater.* **2017**, *7*, 1700045.
67. Bie, Y.; Yang, J.; Liu, X.; Wang, J.; Nuli, Y.; Lu, W., Polydopamine Wrapping Silicon Cross-linked with Polyacrylic Acid as High-Performance Anode for Lithium-Ion Batteries. *ACS Appl. Mater. Interfaces* **2016**, *8*, 2899-2904.
68. Higgins, T. M.; Park, S.-H.; King, P. J.; Zhang, C.; McEvoy, N.; Berner, N. C.; Daly, D.; Shmeliov, A.; Khan, U.; Duesberg, G.; Nicolosi, V.; Coleman, J. N., A Commercial

- Conducting Polymer as Both Binder and Conductive Additive for Silicon Nanoparticle-Based Lithium-Ion Battery Negative Electrodes. *ACS Nano* **2016**, *10*, 3702-3713.
69. Gao, Y.; Yi, R.; Li, Y. C.; Song, J.; Chen, S.; Huang, Q.; Mallouk, T. E.; Wang, D., General Method of Manipulating Formation, Composition, and Morphology of Solid-Electrolyte Interphases for Stable Li-Alloy Anodes. *J. Am. Chem. Soc.* **2017**, *139*, 17359-17367.
70. Kim, J. S.; Yang, S. C.; Bae, B. S., Thermally stable transparent sol-gel based siloxane hybrid material with high refractive index for light emitting diode (LED) encapsulation. *Chem. Mater.* **2010**, *22*, 3549-3555.
71. Kim, Y. H.; Bae, J. Y.; Jin, J.; Bae, B. S., Sol-gel derived transparent zirconium-phenyl siloxane hybrid for robust high refractive index LED encapsulant. *ACS Appl. Mater. Interfaces* **2014**, *6*, 3115-3121.
72. Lott, J.; Xia, C.; Kosnosky, L.; Weder, C.; Shan, J., Terahertz photonic crystals based on barium titanate/polymer nanocomposites. *Adv. Mater.* **2008**, *20*, 3649-3653.
73. Liou, G. S.; Lin, P. H.; Yen, H. J.; Yu, Y. Y.; Tsai, T. W.; Chen, W. C., Highly flexible and optical transparent 6F-PI/TiO₂ optical hybrid films with tunable refractive index and excellent thermal stability. *J. Mater. Chem.* **2010**, *20*, 531-536.
74. Su, H. W.; Chen, W. C., High refractive index polyimide-nanocrystalline-titania hybrid optical materials. *J. Mater. Chem.* **2008**, *18*, 1139-1145.
75. Liu, J. G.; Ueda, M., High refractive index polymers: fundamental research and practical applications. *J. Mater. Chem.* **2009**, *19*, 8907-8919.
76. Lorentz, H. A., Ueber die Beziehung zwischen der Fortpflanzungsgeschwindigkeit des Lichtes und der Körperdichte. *Annalen der Physik* **1880**, *245*, 641-665.

77. Lü, C.; Yang, B., High refractive index organic–inorganic nanocomposites: design, synthesis and application. *Journal of Materials Chemistry* **2009**, *19*, 2884-2901.
78. Macdonald, E. K.; Shaver, M. P., Intrinsic high refractive index polymers. *Polym. Int.* **2015**, *64*, 6-14.
79. Paquet, C.; Cyr, P. W.; Kumacheva, E.; Manners, I., Polyferrocenes: metallopolymers with tunable and high refractive indices. *Chem. Commun.* **2004**, 234-235.
80. Liu, J.-g.; Nakamura, Y.; Shibasaki, Y.; Ando, S.; Ueda, M., High refractive index polyimides derived from 2, 7-bis (4-aminophenylenesulfanyl) thianthrene and aromatic dianhydrides. *Macromolecules* **2007**, *40*, 4614-4620.
81. Terraza, C. A.; Liu, J. G.; Nakamura, Y.; Shibasaki, Y.; Ando, S.; Ueda, M., Synthesis and properties of highly refractive polyimides derived from fluorene - bridged sulfur - containing dianhydrides and diamines. *J. Polym. Sci., Part A: Polym. Chem.* **2008**, *46*, 1510-1520.
82. Kausar, A.; Zulfiqar, S.; Sarwar, M. I., Recent developments in sulfur-containing polymers. *Polym Rev* **2014**, *54*, 185-267.
83. Okutsu, R.; Ando, S.; Ueda, M., Sulfur-containing poly(methyl acrylate) with high refractive indices and high Abbe's numbers. *Chem. Mater.* **2008**, *20*, 4017-4023.
84. Zimmennann, L.; Weibel, M.; Caseri, W.; Suter, U. W., High refractive index films of polymer nanocomposites. *J. Mater. Res.* **1993**, *8*, 1742-1748.
85. Kyprianidou-Leodidou, T.; Caseri, W.; Suter, U. W., Size variation of PbS particles in high-refractive-index nanocomposites. *J. Phys. Chem.* **1994**, *98*, 8992-8997.
86. Papadimitrakopoulos, F.; Wisniecki, P.; Bhagwagar, D. E., Mechanically Attrited Silicon for High Refractive Index Nanocomposites. *Chem. Mater.* **1997**, *9*, 2928-2933.

87. Tao, P.; Li, Y.; Rungta, A.; Viswanath, A.; Gao, J.; Benicewicz, B. C.; Siegel, R. W.; Schadler, L. S., TiO₂ nanocomposites with high refractive index and transparency. *J. Mater. Chem.* **2011**, *21*, 18623-18629.
88. Li, Y.; Wang, L.; Natarajan, B.; Tao, P.; Benicewicz, B. C.; Ullal, C.; Schadler, L. S., Bimodal “matrix-free” polymer nanocomposites. *RSC Adv.* **2015**, *5*, 14788-14795.

**Chapter 2. Surface Functionalized Silicon Nanoparticles Applied as Anode
Materials in Lithium-ion Battery**

A version of this chapter was originally published by Sisi Jiang, Bin Hu, Ritu Sahore, Linghong Zhang, Haihua Liu, Lu Zhang, Wenquan Lu, Bin Zhao, and Zhengcheng Zhang : Jiang, S.; Hu, B.; Sahore, R.; Zhang, L.; Liu, H.; Zhang, L.; Lu, W.; Zhao, B.; Zhang, Z., Surface-Functionalized Silicon Nanoparticles as Anode Material for Lithium-Ion Battery. *ACS Applied Materials & Interfaces* **2018**, *10* (51), 44924-44931. Sisi Jiang is the only first author of this article

Abstract

This chapter presents a proof of concept that electrochemical performance of lithium-ion battery can be optimized by functionalization of silicon anode on the particle level. An epoxy group was successfully attached to the surface of silicon nanoparticles (SiNPs) *via* a silanization reaction between silanol-enriched SiNPs and functional silanes. The epoxy-functionalized SiNPs showed much improved cell performance compared with the pristine SiNPs due to the increased stability with electrolyte and the formation of a covalent bond between the epoxy group and the polyacrylic acid binder. Furthermore, the anode laminate made from epoxy-SiNPs showed much enhanced adhesion strength. Post-test analysis shed light on how the epoxy-functional group affects the physical and electrochemical properties of the SiNPs anode.

2.1 Introduction

The lithium-ion battery (LIB) has become the most extensively used battery chemistry for consumer electronics and transportation.¹ Over the past three decades, tremendous efforts have been exerted to improve the energy density of LIBs to meet the requirement of emerging new devices such as long-lasting tablets, drones and electric vehicles. However, the energy density of conventional LIBs, where graphite is used as an anode material is compromised due to its low theoretical capacity (372 mAh/g).² Silicon, with its extremely high theoretical specific capacity upon full lithiation (~ 4200 mAh/g), low discharge potential plateau (~ 0.1 V vs Li^+/Li), natural abundance, and low toxicity, has been considered as one of the most promising anode materials for the next generation LIBs.³ Nevertheless, the biggest hurdle for the Si anode is the large volume expansion/contraction (~ 300 %) during the lithiation/delithiation process, resulting in rapid capacity fade over extended cycles. Several performance decay mechanisms have been proposed, including pulverization of large particles during the rapid Li^+ insertion/extraction, loss of electrical contact caused by the rearrangement of electrode structure, and/or instability of the electrode/electrolyte interface.⁴ To mitigate these issues, nanostructured material like silicon nanoparticles (SiNPs) has been investigated.⁵ Different from the micro-sized particles, the SiNPs have much higher surface area, which efficiently releases the stress caused by the drastic volume change during the lithiation/delithiation process and thus prevents the particle pulverization. It is also believed that SiNPs possess higher average binding energy per atom to the surface.⁶ However, the large volume change still occurs even for the Si nanoparticles, and the repeated expansion/contraction leads to the frequent exposure of the lithiated silicon to the electrolyte and ultimate disintegration of the active particles due to the weak interaction of the SiNPs with other components of the anode. To solve the issue, the majority of the research has been focused on

tailoring the structure of the polymer binders to increase the binding strength with the SiNPs. Hu and coworkers recently reported the effect of the molecular weight of the polyacrylic acid (PAA) binder on the cycling performance of the Si-graphite composite anode.⁷ Other properties including the degree of crosslinking,^{8, 9} macromolecule architecture,¹⁰ lithiation degree,¹¹ and electronic/ionic conductivity¹²⁻¹⁵ of the polymer binder, have also been extensively explored. Surface functionality of Si particles, on the other hand, is equally crucial when it comes to maintaining the integrity of the electrode during cycling, especially for the nano-scaled Si particles. However, the research on this topic is scarce and mainly focused on how the surface SiO_x layers¹⁶⁻¹⁹ or the electrolyte additives^{20, 21} would affect the electrochemical properties of the SiNPs. For example, Li and coworkers reported how the silanol, carboxyl, and siloxane groups on the surface of the SiNPs affect solid-electrolyte-interphase (SEI) formation and the SEI chemical composition.¹³ The first research on the binder and SiNPs interaction was carried out by Bie *et al.*, in which the surface of the SiNPs was modified by a thin layer of polydopamine *via* hydrogen bonding between hydroxyl groups of the polymer and the surface silanol groups. Although the amino groups further react with the carboxyl groups of the PAA binder, forming a more integrated electrode, the reaction is simultaneous, and the shelf-life of the electrode slurry is not sufficient to complete the electrode coating.²²

The best-performing polymer binder for the Si anode usually contains carboxyl groups in the structure such as alginate, carboxymethyl cellulose (CMC), PAA, and partially lithiated PAA.²³⁻²⁸ It is our idea to design and synthesize SiNPs with a layer of reactive epoxy groups attached to the particle surface. The self-assembled monolayers (SAM) act as a protective frontier from the electrolyte solution mitigating the active lithium trapping during the lithiation process. The chemical reaction between the carboxyl groups from the PAA binder and the epoxy groups from

the SiNPs forms covalent bonding between the SiNPs and the binder. Furthermore, the epoxy group helps provide strong adhesion of the SiNPs and binder to the surface of the copper current collector affording an integrated Si electrode with superior electrochemical performance.

In this chapter a two-step approach was employed to introduce the epoxy group to the surface of commercial silicon nanoparticles. The SiNPs were first treated by hydrogen peroxide (H_2O_2) to enrich the surface silanol (Si-OH) group followed by a surface hydrolysis/condensation reaction with the epoxy-containing silane precursor. For comparison, methylsilane surface-modified SiNPs were also synthesized by the same procedure, and the impact on the cycling performance was directly compared in coin cell tests. Post-test analysis included Fourier-transform infrared spectroscopy (FT-IR), X-ray photoelectron spectroscopy (XPS), thermogravimetric analysis (TGA), and scanning electron microscopy/energy-dispersion X-ray spectroscopy (SEM/EDX). The results shed light on the source of the improved electrochemical performance of the epoxy-functionalized SiNPs anode materials.

2.2 Experimental Section

2.2.1 Electrode and Electrolyte Materials

Silicon nanoparticles with an average particle size of 80 nm were purchased from Hydro Quebec. Absolute ethanol (200 proof), hydrogen peroxide (H_2O_2 , 30 wt% aqueous solution), and triethylamine (99.0%) were purchased from Acros and were used as received. Tetrahydrofuran (THF, HPLC grade) was purchased from Acros and was dried over 4Å molecular sieves prior to use. Glycidylpropyltriethoxysilane (GPTES) and methyltriethoxysilane (MTES) were purchased from Gelest, Inc., and were used as received. Conductive carbon (Timcal C45, 50-60 nm) was purchased from Timcal. Gen II electrolyte (1.2 M LiPF_6 in a liquid mixture of ethylene carbonate

and ethyl methyl carbonate in 3:7 by weight) was provided by Tomiyama Pure Chemical Industries. Fluoroethylene carbonate (FEC, Solvay) was dried and vacuum distilled before use.

2.2.2 Synthesis of Surface-Functionalized SiNPs

Synthesis of Si-OH enriched SiNPs: To a 100 mL round-flask equipped with a magnetic stirring bar and N₂ inlet, pristine SiNPs (0.998 g) were mixed with absolute ethanol (20 mL). The mixture was ultrasonicated for 15 min until a homogeneous dispersion was formed. Then, H₂O₂ (30 wt% aqueous solution, 40 mL) was added to the flask and the mixture was stirred at 75°C for 48 h under N₂. The Si-OH SiNPs were isolated by centrifugation (14,000 rpm, 30 min) with a yield of 86.7%.

Synthesis of epoxy-SiNPs: Si-OH enriched SiNPs (0.500 g) were dispersed in dry tetrahydrofuran (10 mL) in a 100 mL flask equipped with a magnetic stirring bar and N₂ inlet. After 15 min ultrasonication, GPTES (1.000 g) and triethylamine (0.500 g) were added dropwise to the dispersion. The reaction mixture was stirred and refluxed at 75°C for 48 h under N₂. After centrifugation (14,000 rpm, 30 min), the particles were further dispersed in dry tetrahydrofuran for a 2nd centrifugation. The final product was obtained after vacuum drying at 50°C overnight (0.437 g, 87.4% yield). By the same method, methyl functionalized SiNPs (CH₃-SiNPs) were prepared by reacting Si-OH SiNPs with MTES precursor.

2.2.3 Characterization of Functionalized SiNPs

Fourier-transform infrared spectra were acquired on a Thermo Scientific Nicolet iS5 spectrometer using attenuated total reflection model. Thermogravimetric analysis was conducted in an argon atmosphere with a heating rate of 20°C/min from room temperature to 800°C using the NETZSCH STA 449 F3 Jupiter for simultaneous thermogravimetry-differential scanning calorimetry (STA/TG-DSC). The morphologies of SiNPs were analyzed by an FEI Tecnai F20ST scanning/transmission electron microscopy (TEM). The TEM specimens were prepared from 1

mg/g SiNPs suspension in acetone solvent by casting the Si particles on the carbon-coated copper TEM grid.

2.2.4 Si Electrode Fabrication and Electrochemical Testing

Surface-functionalized SiNPs (70%), Timcal C45 carbon black (10%), and PAA binder ($M_n = 175$ KDa) (20%) were thoroughly mixed in deionized water and stirred at room temperature. The resulting uniform slurry was then cast onto Cu foil with a 50 μm -gap doctor blade. The dried and calendared electrode was punched into 1.6 cm^2 circular disks with a loading of 1.0 mg/cm^2 . 2032 coin cells were assembled with the SiNPs anode and cycled using a Maccor cycler with a C/3 rate and a cutoff voltage of 1.5-0.01 V after three C/20 formation cycles. Electrochemical impedance spectroscopy (EIS) was performed with a Solartron Analytical 1400 Cell Test System in the frequency range of 1 MHz to 0.1 Hz.

2.2.5 Adhesion Strength of the Si Electrodes

An adhesion test of the Si/PAA electrode was performed on an Instron 3343 universal test machine. The preparation of the laminate is the same as described in section 2.4. The electrodes were cut into squares with fixed dimension (50 mm x 20 mm). The current collector side of the electrode was fixed by a clamp while the active coating side of the electrode was taped with Scotch magic tape (3M). The electrode was gradually peeled by pulling the tape at an angle of 180° with a constant rate of 10 mm/s. The applied force was measured, recorded, and plotted.^{10, 29, 30}

2.2.6 Post-Test Analysis

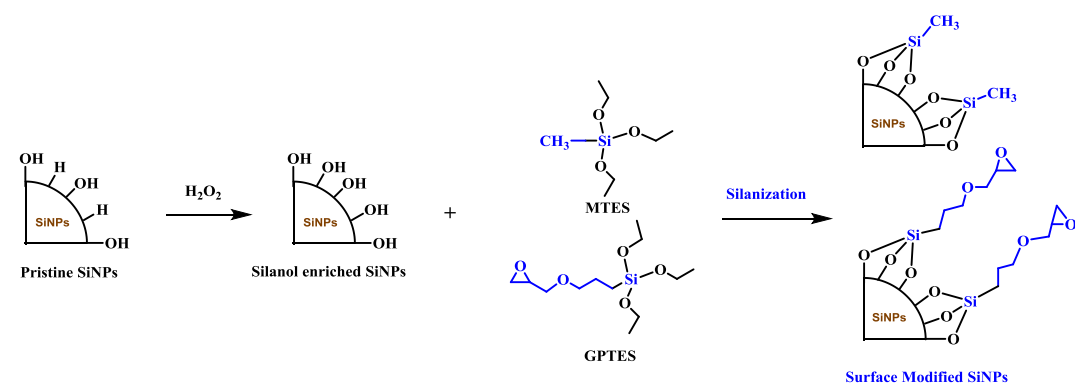
The cycled coin cells were disassembled in the argon-filled glovebox, and the electrodes were thoroughly rinsed with anhydrous dimethyl carbonate and dried in a vacuum oven. The morphologies and the elemental mapping of the cycled electrodes were examined with SEM (Hitachi S-4700-II) and EDX (the Bruker XFlash® 6 | 60), respectively. Surface analysis of the

SiNPs was performed by XPS (PHI 5000 VersaProbe II System from Physical Electronics) with a base pressure of $\sim 2 \times 10^{-9}$ torr. The spectra were obtained with an Al K α radiation ($h\nu = 1486.6$ eV) beam (100 μm , 25 W) and electron beam sample neutralization, in fixed analyzer transmission mode. Peak fitting was performed using Shirley background correction and the Gaussian-Lorentzian curve synthesis available in CasaXPS software.

2.3 Results and Discussion

2.3.1 Synthesis and Characterization of Functionalized SiNPs

Commercial SiNPs were first treated by hydrogen peroxide solution to convert Si-H and Si-O-Si groups to silanol (-Si-OH) group. The Si-OH SiNPs are subject to surface hydrolysis/condensation reaction with GPTES (Scheme 2.1). The pristine SiNPs showed a broad peak at 1100 cm^{-1} (expands from 1000 cm^{-1} to 1250 cm^{-1}) in the FT-IR spectrum (Figure 2.1a), which is a typical stretching vibration peak for the Si-O-Si bond and indicates the existence of a native SiO_x layer on the pristine SiNPs¹⁹. After the hydrogen peroxide treatment, the increase in Si-OH peak intensity ($\sim 3300\text{ cm}^{-1}$) indicates that more silanol group was generated on the surface of the pristine SiNPs³¹ and confirms the successful enrichment of surface silanol group. During the synthesis of epoxy-terminated SiNPs, a hydrolysis and condensation reaction formed a new Si-O-Si bond on the surface of the particle. The FT-IR spectrum of epoxy-SiNPs is also shown in Figure 2.1a. The band at $1250\text{-}1500\text{ cm}^{-1}$ originated from the ring expansion or breathing of the epoxy ring,³² and typical C-H vibration bands of the alkyl group appear at 2923 cm^{-1} and 2880 cm^{-1} . The TGA data further confirmed the successful attachment of the epoxy group. As shown in Figure 2.1b, negligible weight loss (0.3%) was observed for the pristine SiNPs. However, this value increased to 3.2% for the epoxy-SiNPs. The TEM images of the synthesized SiNPs are



Scheme 2.1. Synthesis of surface-functionalized SiNPs with methyl and epoxy terminal groups

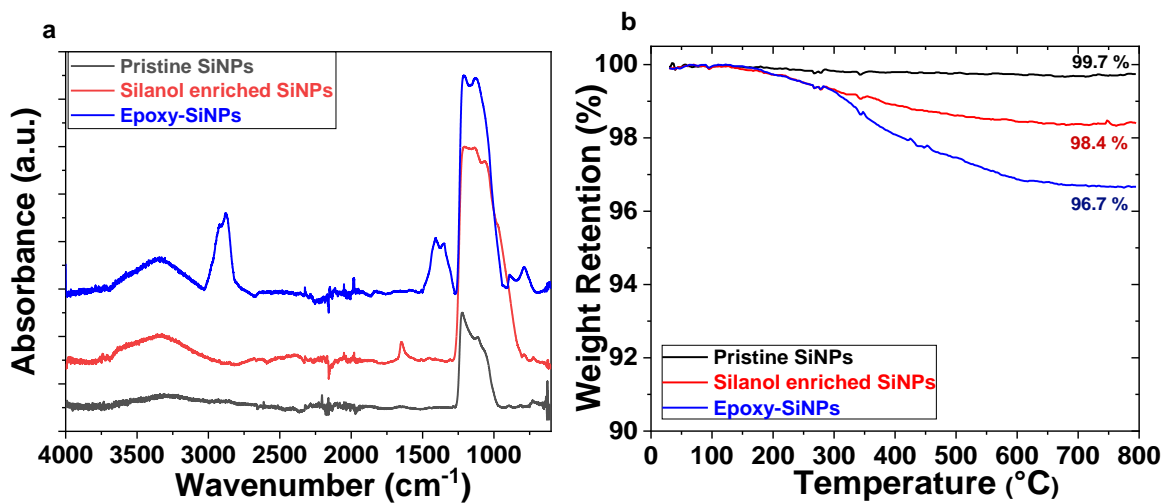


Figure 2.1. (a) FT-IR spectra and (b) TGA thermograms of pristine SiNPs, silanol-enriched SiNPs, and epoxy-SiNPs.

provided in Figure A1 in the Appendix. Methyl-terminated SiNPs ($\text{CH}_3\text{-SiNPs}$) were also synthesized by reacting Si-OH SiNPs with MTES, and the FT-IR and TGA data are provided in Figure A2.

2.3.2 Electrochemical Performance

To determine the electrochemical performance, Si electrodes were coated with pristine SiNPs, $\text{CH}_3\text{-SiNPs}$, and epoxy-SiNPs as active anode materials. After three C/20 formation cycles, the Si/Li cells were operated for 100 cycles at a C/3 rate. Cell capacity and Coulombic efficiency for three formation cycles at C/20 rate are shown in Figure 2.2a, and the cycling performance for one 100 cycles at the C/3 rate is shown in Figure 2.2b. The pristine SiNPs electrode shows an initial delithiation capacity of 1989 mAh/g and an average capacity 1890 mAh/g for 100 cycles. Both values for the epoxy-SiNPs electrode are much higher (initial capacity of 2294 mAh/g and average capacity of 2169 mAh/g) than those for the pristine anode. Surprisingly, the $\text{CH}_3\text{-SiNPs}$ electrode exhibited rapid fade in capacity with increasing cycle number (initial capacity of 1976 mAh/g and average capacity of 1212 mAh/g) (Figure 2.2b). These data clearly indicate that the functional group on the surface of the SiNPs dictates the electrochemical performance of the Si electrode. The cell performance agrees well with our initial approach of introducing epoxy group on the surface of SiNPs to promote the integration of active particles with the binder, current collector, and other cell components. To further verify this positive impact, the chemical reaction between the epoxy-SiNPs and PAA binder was examined by mixing the SiNPs and PAA binder with the same composition used in the anode slurry and stirring at room temperature overnight. The reacted SiNPs were isolated by high-speed centrifugation and subjected to TGA analysis. For the $\text{CH}_3\text{-SiNP}$ particles, the TGA profiles are almost identical before and after the reaction with PAA binder (Figure 2.3a); nevertheless, an additional weight loss was observed for the PAA

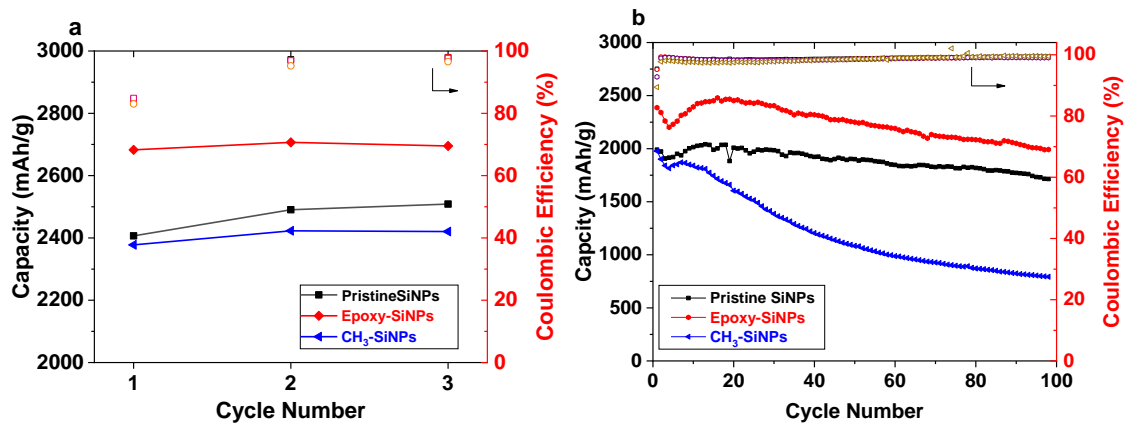


Figure 2.2. Initial capacity and Coulombic efficiency of Si/Li cells: (a) three C/20 formation cycles and (b) one-hundred C/3 cycles.

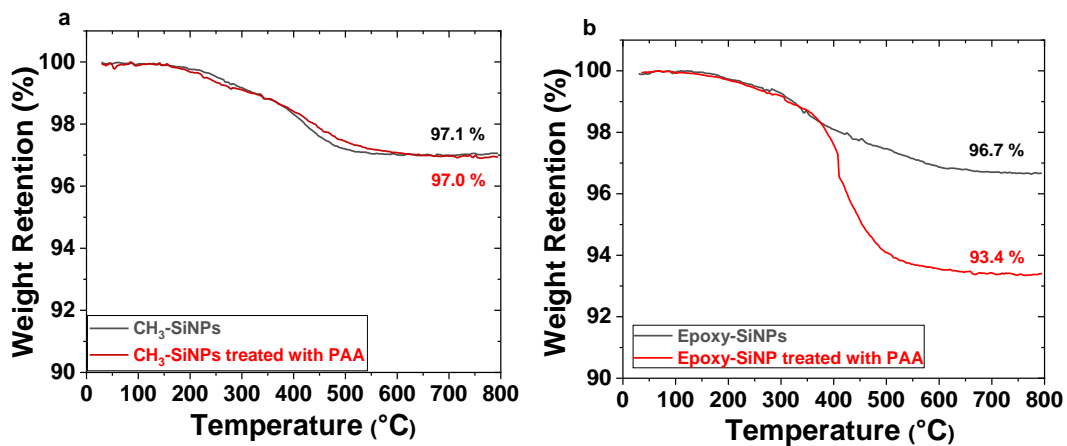


Figure 2.3. TGA profiles of (a) CH₃-SiNPs and CH₃-SiNPs treated with PAA binder, and (b) epoxy-SiNPs and epoxy-SiNPs treated with PAA binder.

treated epoxy-SiNPs as shown in Figure 2.3b. This indicates that PAA segments were attached to the surface of the epoxy-SiNPs particles *via* the ring-opening addition reaction of the epoxy group with the hydroxyl group from the PAA binder.

The surface functional group on the SiNPs does change the interfacial property of the Si electrode. Figure 2.4 show the Nyquist plots for the Si electrode after three formation cycles at C/20 and 100 cycles at C/3. The plot for the epoxy-SiNP electrode shows two semicircles in the high and medium frequency regions representing the interfacial impedance (R_{int}) and charge-transfer impedance (R_{ct}) (Figure 2.4a).³³⁻³⁶ However, both R_{int} and R_{ct} were decreased compared with the values for pristine SiNPs. It is known that R_{int} is closely related to the nature of the SEI layer. The smaller R_{int} indicates that the SEI is stable and prevents further chemical and/or electrochemical reactions with the electrolyte. The decrease in R_{ct} also proves that surface modification could facilitate the charge transfer at the interface. The same trend is also evident for the cycled electrodes (Figure 2.4b) with threefold increase for the epoxy-SiNPs compared with the pristine SiNPs electrode, indicating that a more robust and less resistive SEI was formed on the surface of the epoxy Si particles. Interestingly, the ohmic resistance of the electrode (R_e) (intercept with the Z' axis at the high frequency region) remains the same as that for the pristine electrode.

The formation of the covalent bond of epoxy-SiNPs and PAA binder benefits the electrode integrity especially during extended cycling. Figures 2.5a-c are SEM images of the freshly made electrode with pristine SiNPs, Si-OH SiNPs and epoxy-SiNPs as active materials. The electrode morphology is similar, and active material, carbon black and binder were distributed uniformly. The molar ratio of Si, C and O was close to the feeding ratio of the slurry as determined by the EDX element mapping (Figure A3). However, after 100 cycles, large cracks appeared in the cycled pristine SiNPs (Figure 2.5d). In contrast, no such cracking was observed in the Si-OH and epoxy-

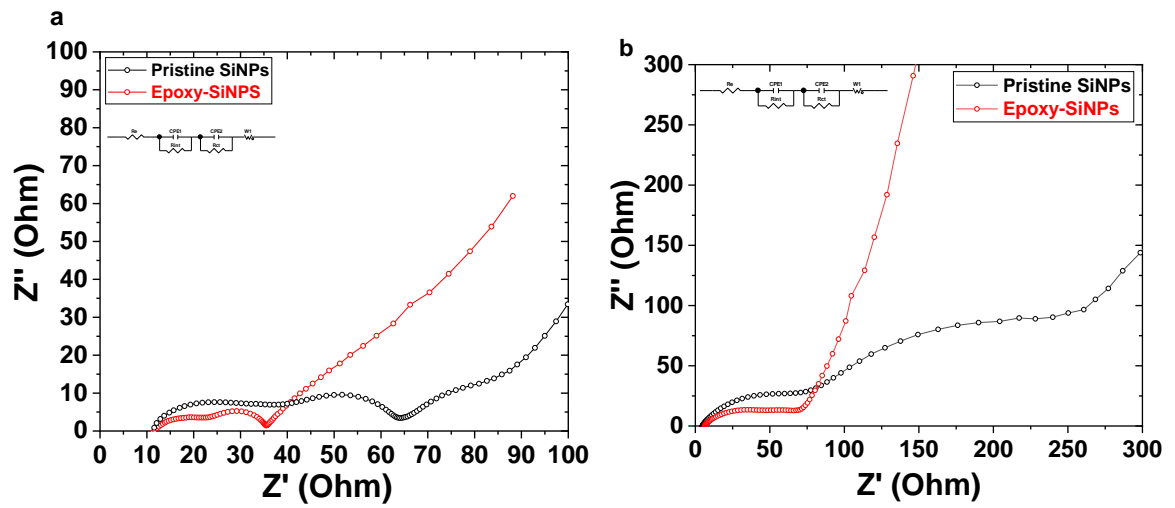


Figure 2.4. Electrochemical impedance spectroscopy of pristine SiNPs electrode and epoxy SiNPs electrode (a) after three formation cycles at C/20 and (b) after 100 cycle at C/3.

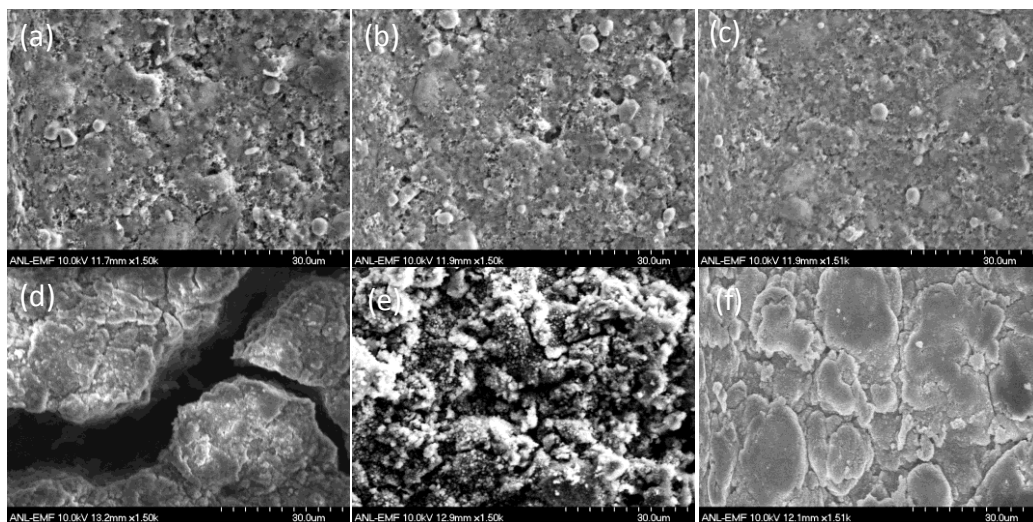


Figure 2.5. SEM images of the freshly made Si/PAA electrodes with (a) pristine SiNPs, (b) Si-OH SiNPs, and (c) epoxy-SiNPs and cycled Si/PAA electrodes with (d) pristine SiNPs, (e) Si-OH SiNPs, and (f) epoxy-SiNPs as active materials.

SiNPs anodes (Figures 2.5e-f), suggesting the functional groups help preserve the electrode integrity even at the deep cycling stage. Figure 2.6 shows the surface chemical composition of the cycled electrodes: pristine SiNPs, Si-OH SiNPs, and epoxy-SiNPs. For all three electrodes, the detectable surface Si amount decreased, indicating the formation of a thick SEI layer. Fluorine and phosphate were detected from the surface of all three cycled electrodes due to the decomposition of the electrolyte. The surface of the electrode made from epoxy-SiNPs has much less fluorine and phosphate content than that of the other two electrodes, as shown in Figure 2.6c. This finding suggests that the surface modification of SiNPs mitigated the continuous reduction/decomposition of the electrolyte. It is worth mentioning that the fluorine content on the surface of the electrode made from Si-OH SiNPs is much higher than that on the surfaces of the other two electrodes (Figure 2.6b). We speculate that the surface silanol group tends to eliminate water *via* a condensation reaction during repeated cycling, leading to severe hydrolysis of the LiPF₆ electrolyte salt at the electrode surface.¹³

The surface of the cycled electrodes was examined by XPS. Figure 2.7a show the Si_{2p} spectra of the pristine SiNPs and epoxy-SiNPs electrode before cycling. The peaks related to elemental silicon (99.4 eV) and oxidized silicon SiO_x (103.5 eV) resemble the spectra of their corresponding nanoparticles (Figure A4), indicating that the epoxy-SiNPs nanoparticles remain inert after exposure to the aqueous slurry. After one formation cycle, new peaks appeared in both spectra at 102 eV (Figure 2.7b), a characteristic peak of Li_xSiO_y formed by irreversible reduction of SiO_x at the electrode surface.^{37, 38} However, a lower intensity Li_xSiO_y peak was observed for the epoxy-SiNPs electrode. In addition, the presence of a new peak at a binding energy of 98 eV (Li_xSi) from the pristine SiNPs electrode implies that not all the lithium was extracted from the pristine SiNPs electrode. Figure A5 in the SI shows the XPS spectra of C_{1s}, O_{1s} and F_{1s}. Without the surface

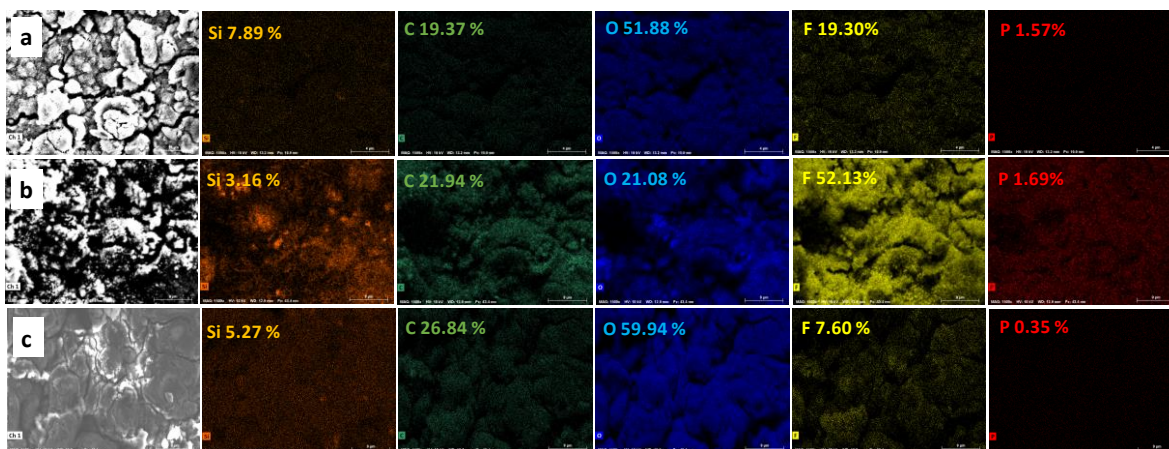


Figure 2.6. EDX elemental mapping (Si, C, O, F, P) for Si/PAA electrodes with (a) pristine SiNPs, (b) Si-OH SiNPs and (c) epoxy-SiNPs after 100 cycles.

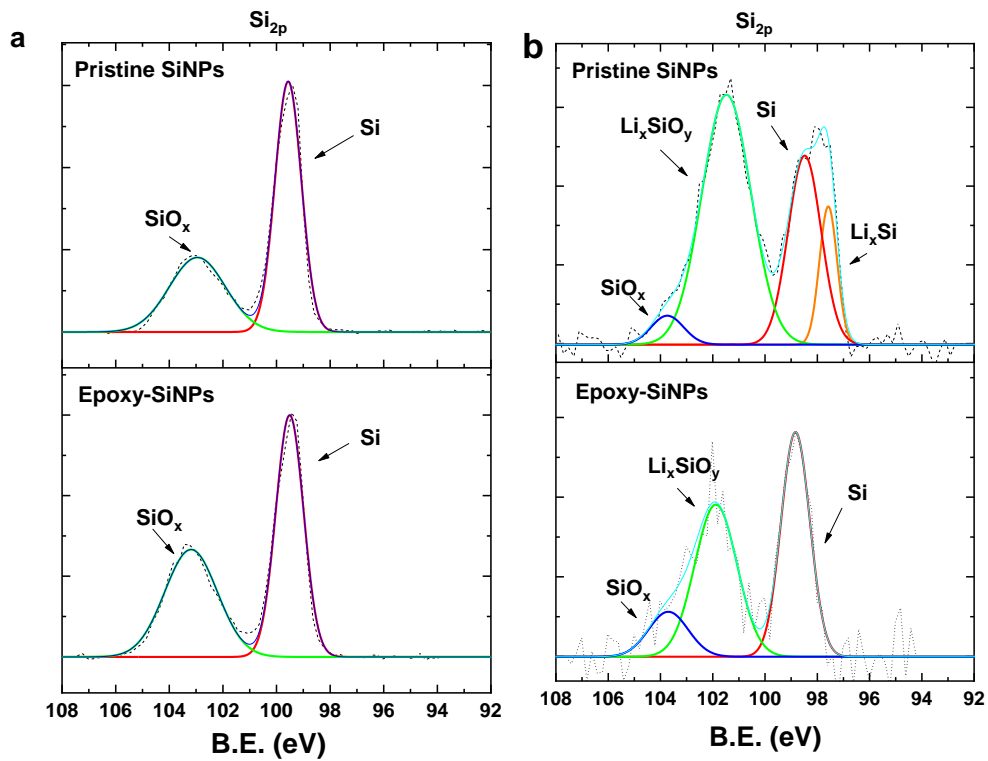


Figure 2.7. Si_{2p} XPS spectra of the Si electrodes based on pristine SiNPs and epoxy-SiNPs before and after one formation cycle: (a) fresh Si electrode before cycling and (b) Si electrode after one formation cycle at delithiated state.

group, the pristine SiNPs tends to react with the lithiated silicon causing impedance buildup and the polarization of the electrode. In contrast, the epoxy-functionalized SiNPs reduced the parasitic reactions with Li_xSi and enabled the reversible lithium insertion and extraction. As a matter of fact, the Li_xSi peak was not observed on the XPS spectrum of the epoxy-SiNPs electrode at the fully delithiation state. Surface modification of silicon nanoparticles could mitigate the irreversible reduction of SiO_x during lithiation and facilitate the extraction of lithium during delithiation. Since both Li_xSiO_y and Li_xSi species contribute to the irreversible capacity in the first lithiation/delithiation cycle, the XPS results are in good agreement with the higher initial capacity and Coulombic efficiency of the epoxy-SiNPs electrode.

The binding strength is critical to the electrochemical performance of the Si-based electrode since strong bonding between the active particles and the particle/current collector help maintain the electrical contacts and the integrity of the Si anode.³⁹ A peel test was employed to evaluate the adhesive strength of the Si/PAA anode. A continuous force was applied to the surface of the electrode and when the Si/PAA anode was peeled off of the current collector (copper foil in this case), the resulting load/width (N/cm) reflects the adhesive strength of the whole electrode. Figure 2.8 summarizes the test results. The epoxy-SiNPs showed the strongest adhesion among the tested three electrodes, which is attributed to the high reactivity and strong interaction of the epoxy group with hydroxyl groups from the PAA binder and the Cu current collector. This result confirms one of our initial material design ideas, i.e., introducing an epoxy group onto the surface of nanosilicon particles will maintain the electrode integrity and thus exert a positive impact on the electrochemical performance.

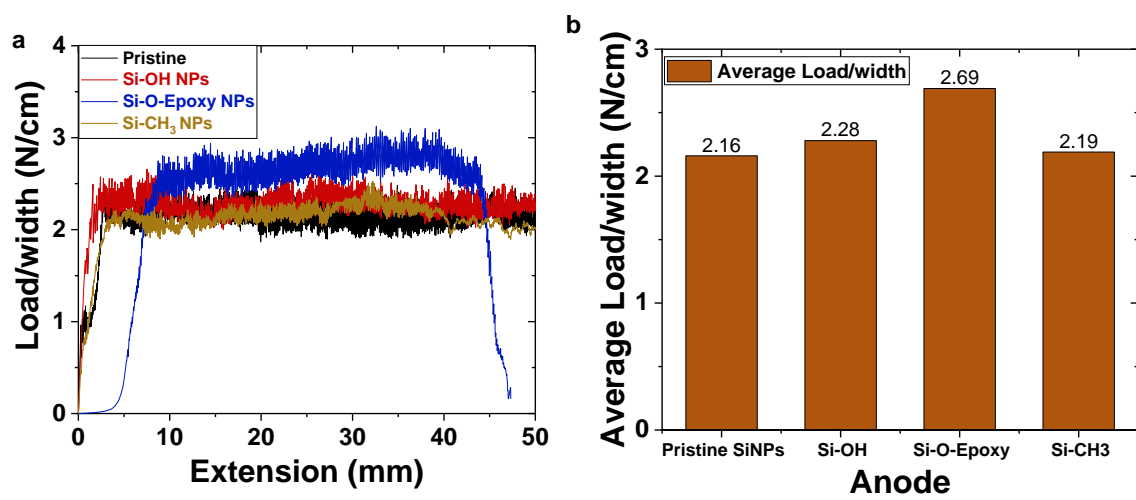


Figure 2.8. (a) Adhesion strength of the Si anodes with pristine SiNPs, Si-OH SiNPs, epoxy-SiNPs, and CH₃-SiNPs as active materials, and (b) summarized data of average load per unit width (N/cm).

2.4 Conclusions

Surface functionalized SiNPs were designed and synthesized *via* a silanization reaction between functional trialkoxysilane and Si-OH-enriched SiNPs. The epoxy-functionalized SiNPs showed much improved performance compared with the pristine and methyl-substituted Si particles due to the formation of covalent bonding between the epoxy group and the hydroxyl group from the polyacrylic acid binder. Furthermore, the surface functionalization protected the parasitic reactions of the Li_xSi with electrolyte and enabled the reversible insertion and extraction of lithium with much improved initial capacity and capacity retention compared with the anode prepared with pristine Si particles. Additionally, the enhanced chemical stability of the functionalized silicon particles enabled a successful aqueous slurry making/electrode coating process with no observed gassing or foaming issues. This research provided insight that the surface functionalization on the particle level of the silicon anode is a feasible approach to mitigate the parasitic reactions of the pristine Si powder and Li_xSi with the electrolyte, tailor the formation and chemical composition of SEI, and manipulate the interaction of active material with other electrode components to enable Si anode materials in next generation lithium-ion batteries with improved electrochemical performance.

2.5 Reference

1. Nitta, N.; Wu, F.; Lee, J. T.; Yushin, G., Li-ion battery materials: present and future. *Mater. Today* **2015**, *18*, 252-264.
2. Goriparti, S.; Miele, E.; De Angelis, F.; Di Fabrizio, E.; Proietti Zaccaria, R.; Capiglia, C., Review on recent progress of nanostructured anode materials for Li-ion batteries. *J. Power Sources* **2014**, *257*, 421-443.
3. Feng, K.; Li, M.; Liu, W.; Kashkooli, A. G.; Xiao, X.; Cai, M.; Chen, Z., Silicon-Based Anodes for Lithium-Ion Batteries: From Fundamentals to Practical Applications. *Small* **2018**, *14*, 1702737.
4. Wu, H.; Cui, Y., Designing nanostructured Si anodes for high energy lithium ion batteries. *Nano Today* **2012**, *7*, 414-429.
5. Szczech, J. R.; Jin, S., Nanostructured silicon for high capacity lithium battery anodes. *Energy Environ. Sci.* **2011**, *4*, 56-72.
6. Roduner, E., Size matters: why nanomaterials are different. *Chem. Soc. Rev.* **2006**, *35*, 583-592.
7. Hu, B.; Shkrob, I. A.; Zhang, S.; Zhang, L.; Zhang, J.; Li, Y.; Liao, C.; Zhang, Z.; Lu, W.; Zhang, L., The existence of optimal molecular weight for poly(acrylic acid) binders in silicon/graphite composite anode for lithium-ion batteries. *J. Power Sources* **2018**, *378*, 671-676.
8. Lim, S.; Chu, H.; Lee, K.; Yim, T.; Kim, Y.-J.; Mun, J.; Kim, T.-H., Physically cross-linked polymer binder induced by reversible acid–base interaction for high-performance silicon composite anodes. *ACS Appl. Mater. Interfaces* **2015**, *7*, 23545-23553.

9. Wei, L.; Hou, Z., High performance polymer binders inspired by chemical finishing of textiles for silicon anodes in lithium ion batteries. *J. Mater. Chem. A* **2017**, *5*, 22156-22162.
10. Cao, P. F.; Naguib, M.; Du, Z.; Stacy, E.; Li, B.; Hong, T.; Xing, K.; Voylov, D. N.; Li, J.; Wood, D. L.; Sokolov, A. P.; Nanda, J.; Saito, T., Effect of Binder Architecture on the Performance of Silicon/Graphite Composite Anodes for Lithium Ion Batteries. *ACS Appl. Mater. Interfaces* **2018**, *10*, 3470-3478.
11. Hays, K. A.; Ruther, R. E.; Kukay, A. J.; Cao, P.; Saito, T.; Wood, D. L.; Li, J., What makes lithium substituted polyacrylic acid a better binder than polyacrylic acid for silicon-graphite composite anodes? *J. Power Sources* **2018**, *384*, 136-144.
12. Park, S.-J.; Zhao, H.; Ai, G.; Wang, C.; Song, X.; Yuca, N.; Battaglia, V. S.; Yang, W.; Liu, G., Side-Chain Conducting and Phase-Separated Polymeric Binders for High-Performance Silicon Anodes in Lithium-Ion Batteries. *J. Am. Chem. Soc.* **2015**, *137*, 2565-2571.
13. Higgins, T. M.; Park, S.-H.; King, P. J.; Zhang, C.; McEvoy, N.; Berner, N. C.; Daly, D.; Shmeliov, A.; Khan, U.; Duesberg, G.; Nicolosi, V.; Coleman, J. N., A Commercial Conducting Polymer as Both Binder and Conductive Additive for Silicon Nanoparticle-Based Lithium-Ion Battery Negative Electrodes. *ACS Nano* **2016**, *10*, 3702-3713.
14. Ling, M.; Liu, M.; Zheng, T.; Zhang, T.; Liu, G., Investigating the Doping Mechanism of Pyrene Based Methacrylate Functional Conductive Binder in Silicon Anodes for Lithium-Ion Batteries. *J. Electrochem. Soc.* **2017**, *164*, A545-A548.
15. Song, M.-S.; Chang, G.; Jung, D.-W.; Kwon, M.-S.; Li, P.; Ku, J.-H.; Choi, J.-M.; Zhang, K.; Yi, G.-R.; Cui, Y.; Park, J. H., Strategy for Boosting Li-Ion Current in Silicon Nanoparticles. *ACS Energy Lett* **2018**, *3*, 2252-2258.

16. Xun, S.; Song, X.; Grass, M. E.; Roseguo, D. K.; Liu, Z.; Battaglia, V. S.; Liu, G., Improved Initial Performance of Si Nanoparticles by Surface Oxide Reduction for Lithium-Ion Battery Application. *Electrochem. Solid-State Lett.* **2011**, *14*, A61-A63.
17. Xun, S.; Song, X.; Wang, L.; Grass, M. E.; Liu, Z.; Battaglia, V. S.; Liu, G., The Effects of Native Oxide Surface Layer on the Electrochemical Performance of Si Nanoparticle-Based Electrodes. *J. Electrochem. Soc.* **2011**, *158*, A1260-A1266.
18. Toudjine, A.; Morcrette, M.; Courty, M.; Davoisne, C.; Lejeune, M.; Mariage, N.; Porcher, W.; Larcher, D., Partially Oxidized Silicon Particles for Stable Aqueous Slurries and Practical Large-Scale Making of Si-Based Electrodes. *J. Electrochem. Soc.* **2015**, *162*, A1466-A1475.
19. Zhang, L.; Liu, Y.; Key, B.; Trask, S. E.; Yang, Z.; Lu, W., Silicon Nanoparticles: Stability in Aqueous Slurries and the Optimization of the Oxide Layer Thickness for Optimal Electrochemical Performance. *ACS Appl. Mater. Interfaces* **2017**, *9*, 32727-32736.
20. Zhang, S.; He, M.; Su, C.-C.; Zhang, Z., Advanced electrolyte/additive for lithium-ion batteries with silicon anode. *Curr Opin Chem Eng* **2016**, *13*, 24-35.
21. Rezqita, A.; Sauer, M.; Foelske, A.; Kronberger, H.; Trifonova, A., The effect of electrolyte additives on electrochemical performance of silicon/mesoporous carbon (Si/MC) for anode materials for lithium-ion batteries. *Electrochim. Acta* **2017**, *247*, 600-609.
22. Bie, Y.; Yang, J.; Liu, X.; Wang, J.; Nuli, Y.; Lu, W., Polydopamine Wrapping Silicon Cross-linked with Polyacrylic Acid as High-Performance Anode for Lithium-Ion Batteries. *ACS Appl. Mater. Interfaces* **2016**, *8*, 2899-2904.
23. Li, J.; B. Lewis, R.; R. Dahn, J., Sodium carboxymethyl cellulose - A potential binder for Si negative electrodes for Li-ion batteries. *Electrochem. Solid-State Lett* **2007**, *10*, A17-A20.

24. Magasinski, A.; Zdyrko, B.; Kovalenko, I.; Hertzberg, B.; Burtovyy, R.; Huebner, C. F.; Fuller, T. F.; Luzinov, I.; Yushin, G., Toward Efficient Binders for Li-Ion Battery Si-Based Anodes: Polyacrylic Acid. *ACS Appl. Mater. Interfaces* **2010**, *2*, 3004-3010.
25. Erk, C.; Brezesinski, T.; Sommer, H.; Schneider, R.; Janek, J., Toward Silicon Anodes for Next-Generation Lithium Ion Batteries: A Comparative Performance Study of Various Polymer Binders and Silicon Nanopowders. *ACS Appl. Mater. Interfaces* **2013**, *5*, 7299-7307.
26. Nguyen, C. C.; Yoon, T.; Seo, D. M.; Guduru, P.; Lucht, B. L., Systematic Investigation of Binders for Silicon Anodes: Interactions of Binder with Silicon Particles and Electrolytes and Effects of Binders on Solid Electrolyte Interphase Formation. *ACS Appl. Mater. Interfaces* **2016**, *8*, 12211-12220.
27. Karkar, Z.; Guyomard, D.; Roué, L.; Lestriez, B., A comparative study of polyacrylic acid (PAA) and carboxymethyl cellulose (CMC) binders for Si-based electrodes. *Electrochim. Acta* **2017**, *258*, 453-466.
28. Kovalenko, I.; Zdyrko, B.; Magasinski, A.; Hertzberg, B.; Milicev, Z.; Burtovyy, R.; Luzinov, I.; Yushin, G., A Major Constituent of Brown Algae for Use in High-Capacity Li-Ion Batteries. *Science* **2011**, *334*, 75-79.
29. Drdácký, M.; Lesák, J.; Rescic, S.; Slížková, Z.; Tiano, P.; Valach, J., Standardization of peeling tests for assessing the cohesion and consolidation characteristics of historic stone surfaces. *Mater. Struct.* **2012**, *45*, 505-520.
30. Munaoka, T.; Yan, X.; Lopez, J.; To, J. W. F.; Park, J.; Tok, J. B.-H.; Cui, Y.; Bao, Z., Ionically Conductive Self-Healing Binder for Low Cost Si Microparticles Anodes in Li-Ion Batteries. *Adv. Energy Mater.* **2018**, *8*, 1703138.

31. Aguiar, H.; Serra, J.; González, P.; León, B., Structural study of sol–gel silicate glasses by IR and Raman spectroscopies. *J. Non-Cryst. Solids* **2009**, *355*, 475-480.
32. Vreugdenhil, A. J.; Balbyshev, V. N.; Donley, M. S., Nanostructured silicon sol-gel surface treatments for Al 2024-T3 protection. *J. Coat. Technol. Res.* **2001**, *73*, 35-43.
33. Tang, K.; Fu, L.; White, R. J.; Yu, L.; Titirici, M.-M.; Antonietti, M.; Maier, J., Hollow Carbon Nanospheres with Superior Rate Capability for Sodium-Based Batteries. *Adv. Energy Mater.* **2012**, *2*, 873-877.
34. Su, M.; Wang, Z.; Guo, H.; Li, X.; Huang, S.; Xiao, W.; Gan, L., Enhancement of the Cyclability of a Si/Graphite@Graphene composite as anode for Lithium-ion batteries. *Electrochim. Acta* **2014**, *116*, 230-236.
35. Kwon, Y. H.; Minnici, K.; Huie, M. M.; Takeuchi, K. J.; Takeuchi, E. S.; Marschilok, A. C.; Reichmanis, E., Electron/Ion Transport Enhancer in High Capacity Li-Ion Battery Anodes. *Chem. Mater.* **2016**, *28*, 6689-6697.
36. Shobukawa, H.; Alvarado, J.; Yang, Y.; Meng, Y. S., Electrochemical performance and interfacial investigation on Si composite anode for lithium ion batteries in full cell. *J. Power Sources* **2017**, *359*, 173-181.
37. Philippe, B.; Dedryvère, R.; Allouche, J.; Lindgren, F.; Gorgoi, M.; Rensmo, H.; Gonbeau, D.; Edström, K., Nanosilicon Electrodes for Lithium-Ion Batteries: Interfacial Mechanisms Studied by Hard and Soft X-ray Photoelectron Spectroscopy. *Chem. Mater.* **2012**, *24*, 1107-1115.
38. Philippe, B.; Dedryvère, R.; Gorgoi, M.; Rensmo, H.; Gonbeau, D.; Edström, K., Role of the LiPF₆ Salt for the Long-Term Stability of Silicon Electrodes in Li-Ion Batteries – A Photoelectron Spectroscopy Study. *Chem. Mater.* **2013**, *25*, 394-404.

39. Wu, M.; Xiao, X.; Vukmirovic, N.; Xun, S.; Das, P. K.; Song, X.; Olalde-Velasco, P.; Wang, D.; Weber, A. Z.; Wang, L.-W.; Battaglia, V. S.; Yang, W.; Liu, G., Toward an Ideal Polymer Binder Design for High-Capacity Battery Anodes. *J. Am. Chem. Soc.* **2013**, *135*, 12048-12056.

**Appendix A for Chapter 2. Surface Functionalized Silicon Nanoparticles
applied as Anode Materials in Lithium-ion Battery**

A.1 Supplemental Figures

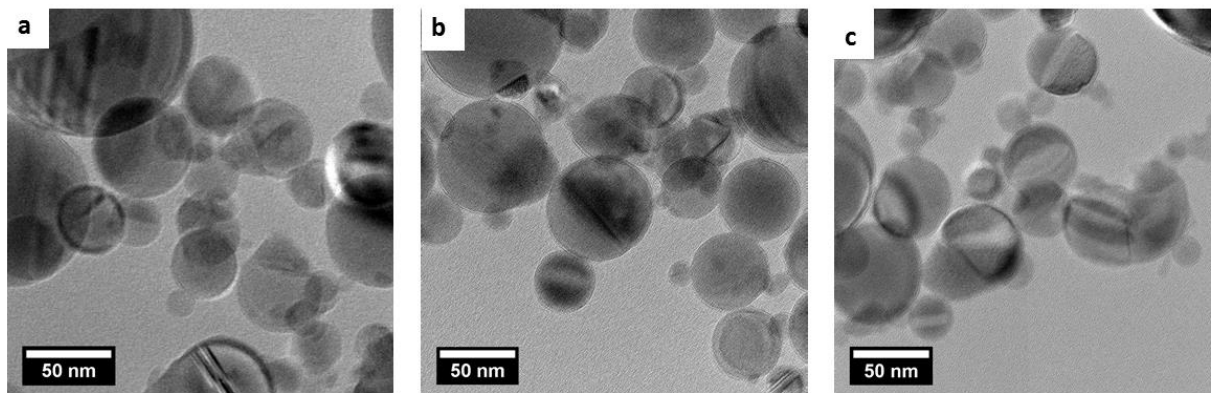


Figure A1. TEM images of (A) pristine SiNPs, (B) silanol (Si-OH) enriched-SiNPs and (C) epoxy-SiNPs. The specimens were prepared by casting the particles on the carbon-coated copper grid from 1 mg/g dispersion of SiNPs in acetone.

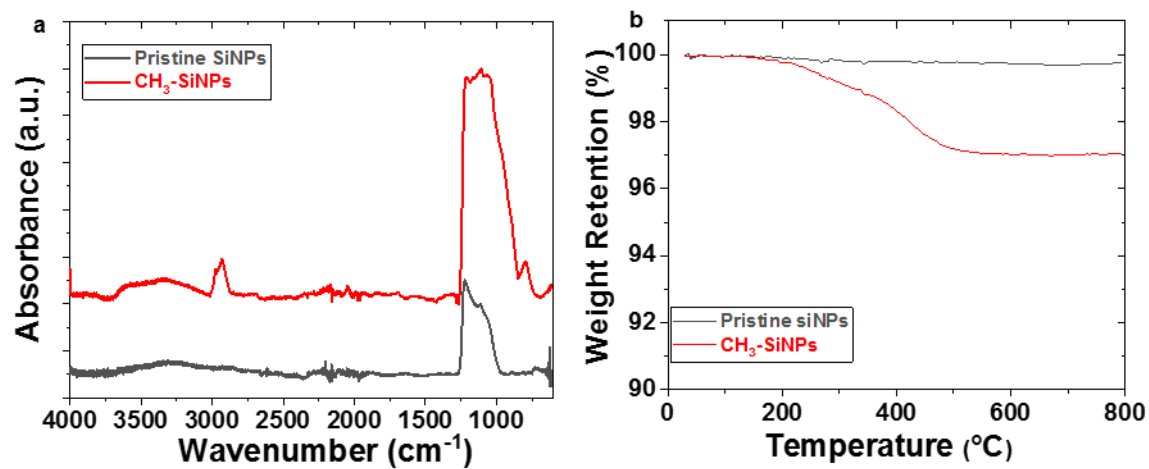


Figure A2. (a) FT-IR spectra of the pristine SiNPs and CH₃-SiNPs; (b) TGA profiles of pristine SiNPs and CH₃-SiNPs.

Table A.1. Loading densities, initial capacities, and capacity retentions of different Si electrodes.

Sample	Loading density, mg/cm²	Initial capacity, mAh/g	Capacity retention, %	Average Capacity, mAh/g
Pristine SiNPs	0.9	1989	86.2	1890
Silanol-SiNPs	0.8	2066	88.1	1968
Epoxy-SiNPs	0.8	2294	86.2	2169
CH₃-SiNPs	0.7	1976	39.7	1212

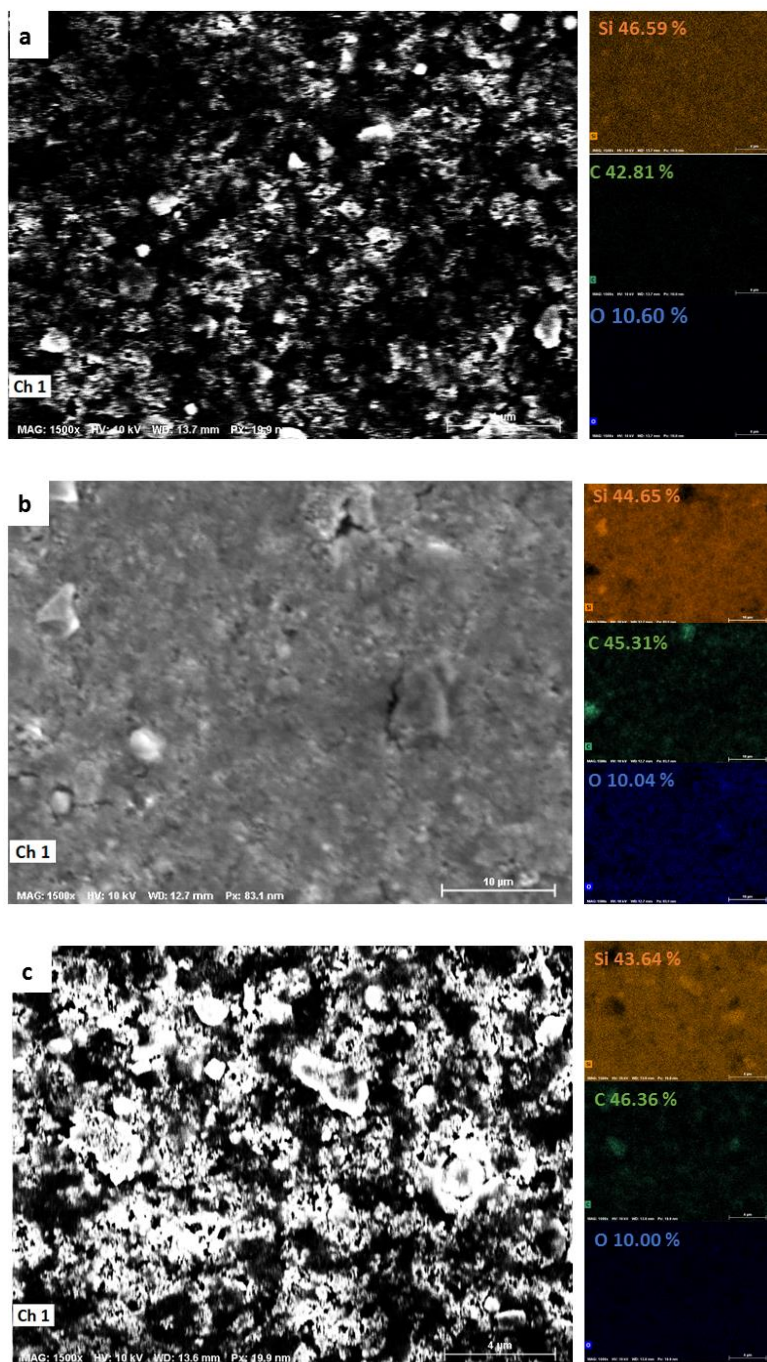


Figure A3. EDX elemental mapping spectra showing the distribution of silicon, carbon and oxygen on the surface of Si/PAA electrodes based on (a) pristine SiNPs, (b) Si-OH SiNPs and (c) epoxy-SiNPs before cycling. (The elemental mapping results are shown in the right side; from top to bottom: Si, C and O).

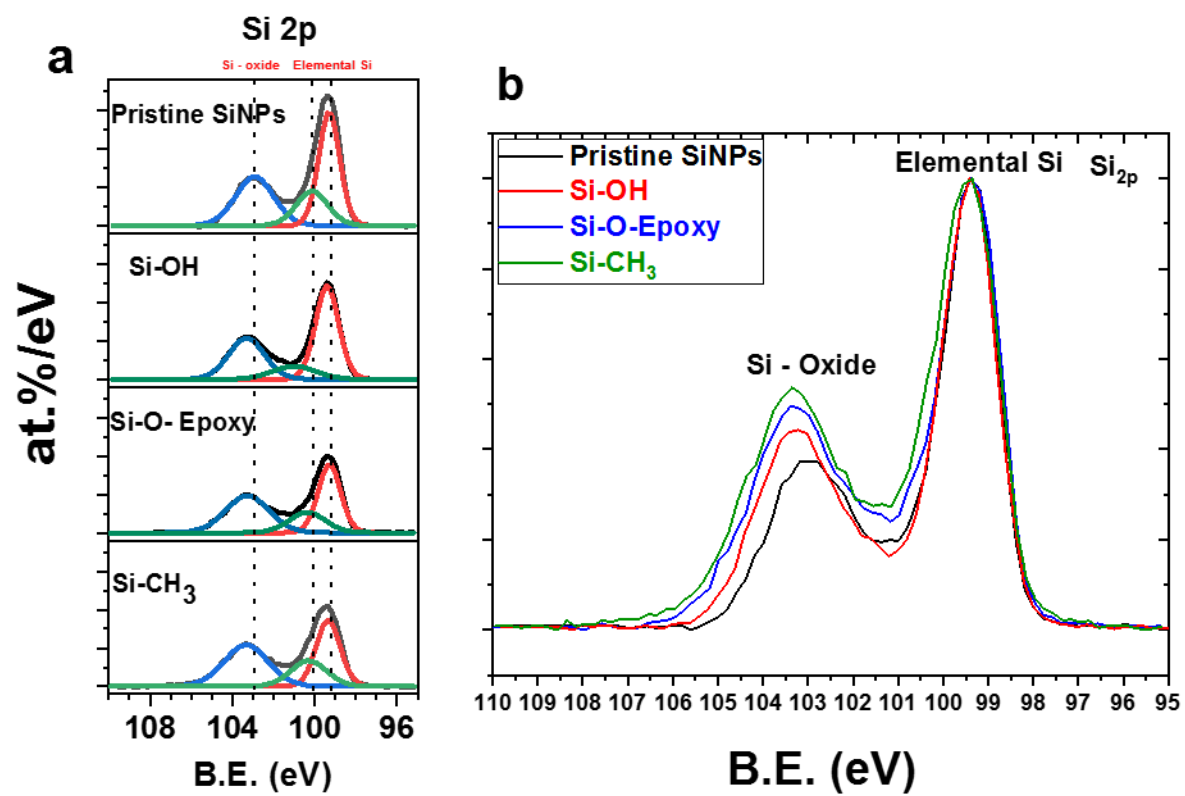


Figure A4. Si_{2p} XPS spectra of (a) pristine SiNPs, Si-OH-SiNPs, epoxy-SiNPs and CH₃-SiNPs, and (b) the normalized Si_{2p} XPS spectra of pristine SiNPs, Si-OH-SiNPs, epoxy-SiNPs and CH₃-SiNPs.

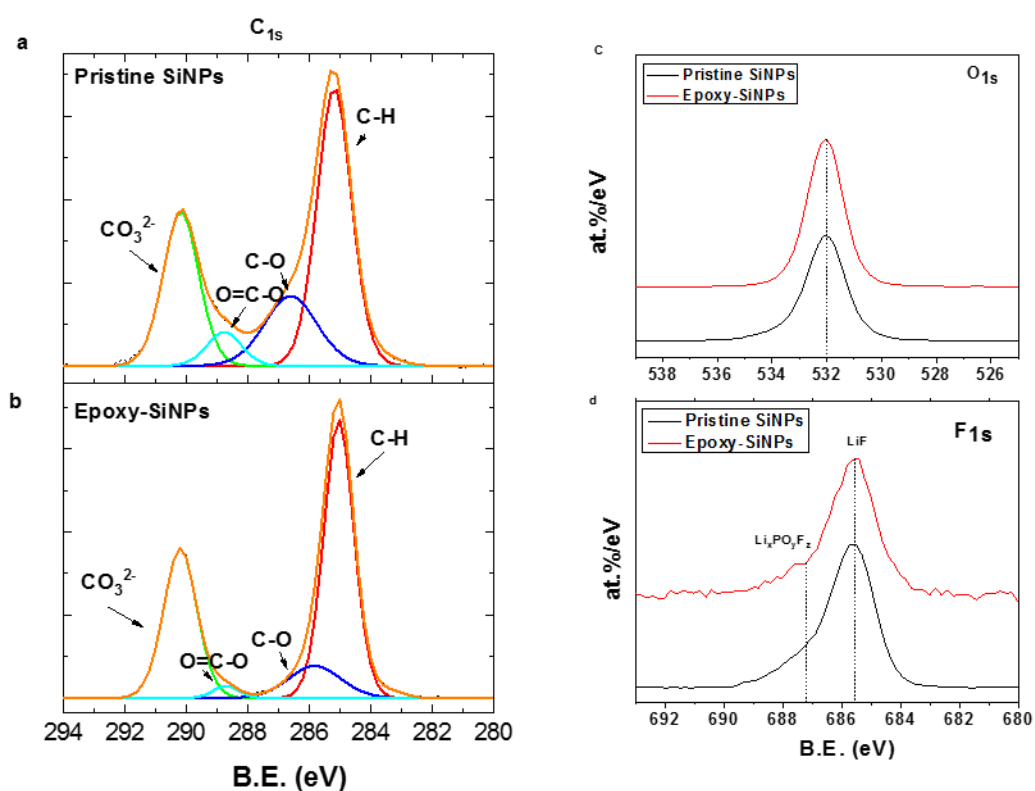


Figure A5. C_{1s} XPS spectra of Si electrodes based on (a) pristine SiNPs and (b) epoxy-SiNPs after one lithiation/delithiation cycle, (c) O_{1s} XPS and (d) F_{1s} XPS spectra of the pristine and epoxy-SiNPs electrode after one lithiation/delithiation cycle.

The characteristic peaks of C-C (284eV, from carbon black and PAA binder) were observed on C_{1s} core level spectra of the fresh electrodes (data not shown). After one cycle, those peaks were no longer detected, indicating the formation of SEI layer on electrode surface. In addition, new peaks at 290.5 eV appeared, which corresponds to the carbonate group (CO₃²⁻) (Figure A5a-b). The O_{1s} and F_{1s} XPS spectra of the two electrodes at delithiation state showed high concentration of C-O species and less inorganic LiF species in the SEI formed on the surface of the epoxy-SiNPs particles (Figure A5c-d).

A.2 X-Ray Photoelectron Spectroscopy: Working principle and application in interfacial analysis of LIB electrode

XPS is a surface characterization technique. It reveals the chemical elements present at the surface of the sample and chemical bonding information between these elements. The working principle of XPS is based on photoelectric effect, which states that there is a threshold in frequency ($E = h\nu$), below which light, regardless of its intensity, fails to eject electron from a certain metallic surface, where h is Planck constant (6.62×10^{-34} J s) and ν is frequency (Hz) of the radiation. When the frequency of the incident light surpass that threshold value, the photon may interact with atomic orbital electron such that there is complete transfer of the photon's energy to the electron (Figure A6). The kinetic energy (E_k) varies linearly with the frequency of the incident photon but is independently of its intensity: $E_k = h\nu - E_b$, where E_k is the electron kinetic energy, $h\nu$ is the photon energy and E_b is the electron binding energy. XPS is surface sensitive because only electrons from top atomic layer can be emitted without loss of energy.¹ The depth of analysis for an XPS depends on several factors including the morphology of the sample and the energy of the

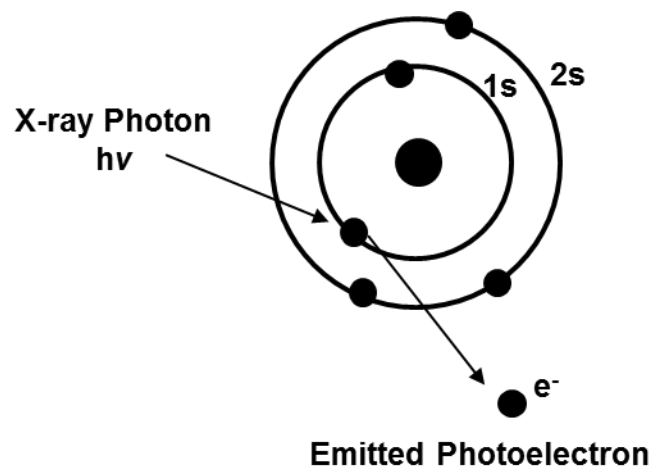


Figure A6. A schematic view of the interaction of an X-ray photon ($E = h\nu$) with an atomic orbital electron on 1s orbit.

X-ray photons.² The analysis depth of the XPS used in this work (Al K α radiation ($h\nu = 1486.6$ eV)) is around 3-10 nm.

Figure A7 shows a typical XPS experiment. An X-ray source provides photons of energy $h\nu$ hit the sample. Electrons are then emitted, of which the kinetic energy is measured by an electron analyzer. The result will be output as a spectrum featuring photoelectron intensity as a function of the binding energy. Each binding energy peak on the spectrum corresponds to a specific element. Thus the elements present on the sample surface can be identified. Furthermore, the chemical bond between the elements can be obtained based on chemical shift effect. When an atom is bonded to an electronegative species, its electrons will be attracted to that species due to the difference in electronegativity. As a result, the 1s electrons of that atom will be bond more strongly to the nucleus due to less electrostatic shielding of the nucleus from all other electrons, and thus leads to a higher binding energy. Conversely, if the atom is bonded to an electron-donating species, the electron density of the atom will increase, resulting in increased shielding for the nuclear and therefore decreased 1s electron binding energy. By interpreting different peaks on the spectrum of a certain element, the chemical bonding information can be derived.³

XPS has been used to study the electrode/electrolyte interface of lithium-ion battery (LIB). Chan and coworkers utilize XPS to analyze the surface chemistry of solid electrolyte interphase (SEI) on the silicon nanowire LIB anodes in traditional electrolyte (1M LiPF₆ EC: DEC electrolyte). They found out that the formation of SEI on silicon anode surface is a dynamic process due to the drastic volume change of silicon anode during cell operation. Reduction products of electrolyte solvents including inorganic salt LiCO₃, organic hydrocarbon and PEO-oligomers as well as decomposition product of lithium salt such as LiF constitutes the major composition of SEI on silicon anode.⁴ Philippe studied the interfacial phase transition on silicon anode surface with

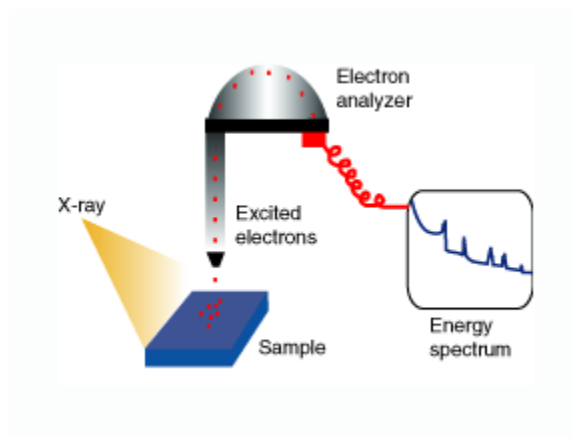


Figure A7. Illustration of XPS experiment. Reprint from <https://www.lanl.gov/orgs/nmt/nmtdo/AQarchive/04summer/XPS.html>

traditional electrolyte (1M LiPF₆ EC: DEC electrolyte) during lithiation/delithiation process by XPS (Figure A8). In general, silicon anode has a native layer of silicon oxide at the surface. During discharge, the formation of SEI due to reduction of electrolyte solvent is observed first at initial discharge stage (0.5 V vs Li⁺/Li) before lithium insertion. Upon further discharge to 0.1 V vs Li⁺/Li, Li insertion begins, the inserted Li reacts with both silica and silicon, resulting in the production of Li₂O, Li_xSiO_y interfacial phases and Li-Si alloy. After complete discharge (0.01 V vs Li⁺/Li), the alloy process is almost completed with some remaining Si. In addition, silica is almost reduced, leading to more Li₂O and Li_xSiO_y. Charge process is a partial reversible process of discharge. After fully charge (0.9 V vs Li⁺/Li), lithium is almost fully extracted from the core of the particle and Li₂O disappears from the interfacial phases.⁵ We used XPS to study the difference in chemical composition on the surface of silicon anode made from pristine and surface-functionalized SiNPs.⁶

In summary, the formation of SEI and the electrochemical/chemical reactions occurs at electrode/electrolyte interface are very complex and are closely related to the electrochemical performance of the electrode in LIB. As a powerful surface characterization technique, XPS proves to be a useful tool in the analysis of the interfacial phase transition and chemical composition of SEI at LIB electrode surface.

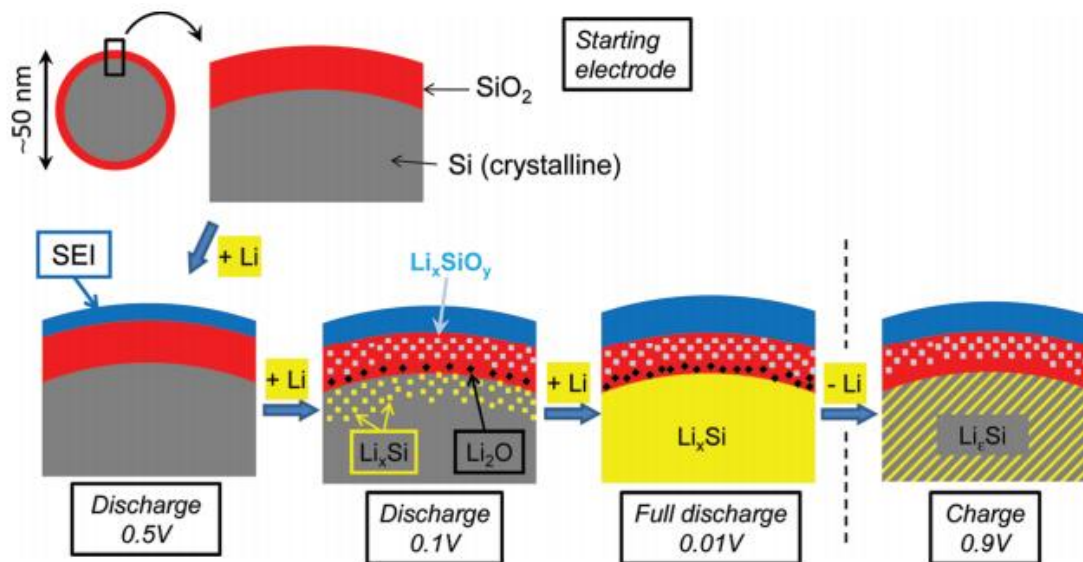


Figure A8. Schematic view of the interfacial phase transition the surface of the silicon anode during 1st lithitaiton/delithiation cycle. Reprint form ref. 5 with permission of American Chemistry Society.

A.3 Reference

1. Vickerman, J. C.; Gilmore, I. S., *Surface analysis: the principal techniques*. John Wiley & Sons: 2011.
2. Eshkenazi, V.; Peled, E.; Burstein, L.; Golodnitsky, D., XPS analysis of the SEI formed on carbonaceous materials. *Solid State Ion.* **2004**, *170*, 83-91.
3. McIntyre, N. S.; Sunder, S.; Shoesmith, D. W.; Stanchell, F. W., Chemical information from XPS—applications to the analysis of electrode surfaces. *J. Vac. Sci. Technol.* **1981**, *18*, 714-721.
4. Chan, C. K.; Ruffo, R.; Hong, S. S.; Cui, Y., Surface chemistry and morphology of the solid electrolyte interphase on silicon nanowire lithium-ion battery anodes. *J. Power Sources* **2009**, *189*, 1132-1140.
5. Philippe, B.; Dedryvère, R.; Allouche, J.; Lindgren, F.; Gorgoi, M.; Rensmo, H.; Gonbeau, D.; Edström, K., Nanosilicon Electrodes for Lithium-Ion Batteries: Interfacial Mechanisms Studied by Hard and Soft X-ray Photoelectron Spectroscopy. *Chem. Mater.* **2012**, *24*, 1107-1115.
6. Jiang, S.; Hu, B.; Sahore, R.; Zhang, L.; Liu, H.; Zhang, L.; Lu, W.; Zhao, B.; Zhang, Z., Surface-Functionalized Silicon Nanoparticles as Anode Material for Lithium-Ion Battery. *ACS Appl. Mater. Interfaces* **2018**, *10*, 44924-44931.

**Chapter 3. Tailoring the Surface of Silicon Nanoparticles for Enhanced
Chemical and Electrochemical Stabilities for Lithium-ion Batteries**

Abstract

Organic monolayers of epoxy-containing oligo(ethylene oxide)s with different repeating ethylene oxide units were grafted to the surface of Si-H terminated silicon nanoparticles (SiNPs) via a Pt-catalyzed hydrosilylation reaction. When employed as a high-capacity anode, the organic layer suppressed the chemical and electrochemical reactivity of the as-grown and lithiated silicon (Li_xSi) particles with high material utilization. A more robust Si/electrolyte interphase was formed with the participation of the grafted organic groups with facilitated Li^+ transfer and was further enforced by electrode integrity via the epoxy/poly(acrylic acid) (PAA) binder reaction. The improved cycling performance, post-test analysis, and electrochemical impedance spectroscopy indicate that surface functionalization on the Si particle level to tailor the Si/electrolyte interphase is a feasible approach to enabling high-capacity Si material in high energy-density lithium-ion batteries

3.1 Introduction

Pursuit of wireless and “green” lifestyle calls for advances in portable electronic devices and electric vehicles running on lithium-ion batteries (LIBs). The majority of today’s commercial LIBs still employ graphite as the anode material and its low energy capacity (about 372 mAh/g) limits the maximum energy density of the cell. Therefore, many efforts have been paid in searching anode substituents for the next-generation high-energy high-voltage LIBs. Silicon (Si) is the most promising anode among all Li-alloy-based materials due to its high theoretical capacity (~ 4200 mAh/g for $\text{Li}_{4.4}\text{Si}$), abundance in earth crust and low toxicity.¹ As a matter of fact, silicon has already been used in commercial LIBs, such as the one in Tesla Model S and was claimed to promote the electronic car’s one-charging range by 6 %.² However, Si undergoes a huge volume change and particle pulverization, which leads to rapid rearrangement of electrode structure after each cycling and isolate active materials from conductive pathway, both ionically and electronically.^{3,4} Furthermore, the reductive decomposition of electrolyte and loss of active lithium on the surface of Si anode during repeated lithiation and delithiation causes rapid capacity fade of the cell. The accumulated SEI layer will also add to the resistance of the electrode.⁵⁻⁷ Another challenge is associated with the gas generation observed during the electrode fabrication process especially when an aqueous binder solution is used and during the cycling.⁸ Overall, the above issues are closely related to the high surface reactivity of the commercial Si particles and the instability of the lithiated silicon (Li_xSi) with the surrounding environment. Although a variety of strategies such as new designs of electrolyte and electrolyte additives,⁹⁻¹¹ particle size optimization,¹² polymeric engineering,¹³⁻¹⁶ and nanocomposite design¹⁷ have been extensively employed, the poor stability of the SEI is still the major obstacle for the sustainable electrochemical performance. The formation of the traditional SEI during the initial cycles is a complex process

and the chemical composition and the structure of the SEI could not be precisely controlled or identified. Inspired by the semiconductor industry^{18, 19}, a new strategy was proposed to address the SEI stability issue by introducing the organic functional groups onto the surface of the silicon particles as an artificial SEI component. Li *et al.* and Jiang *et al.* from our group reported how the functional groups such as $-\text{SiOH}$, $\text{Si}(\text{CH}_2)_3\text{COOH}$, $-\text{Si-O-Si}$ and epoxy impact the electrochemical performance of Si anode.^{20, 21} The surface modification utilizes a silanization reaction between the silanol groups ($-\text{SiOH}$) around the surface of the native silicon oxide layer of SiNPs and the trialkoxysilane $\text{RSi}(\text{OR}')_3$. To eliminate the impact of the native SiO_x layer and to enhance chemical stability of the functionalized SiNPs, functional group directly attached to the surface of bulk Si is desired. Gao *et al.* anchored a hybrid organic group for SEI reinforcement on the surface of SiNPs by azide-alkyne click chemistry.²² However, this functionalization process includes multiple steps and the nature of click chemistry inevitably introduces undesirable organic moieties like azide groups on the surface.

In this chapter, a straightforward approach was developed by a Pt-catalyzed hydrosilylation reaction between the allyl-(ethylene oxide)_n-epoxy precursor and the as-prepared silicon hydride ($^*\text{-SiH}_x$, where $^*\text{Si}$ denotes a surface Si atom) groups on the surface of SiNPs prepared by the nonthermal plasma method.²³⁻²⁷ The specially designed artificial SEI is speculated to have the following advantages: (1) organic-rich chemical composition with high flexibility to accommodate the volume change of Si particle, (2) reinforcement in SEI resilience by formation of new SEI component via epoxy reduction reaction,²⁸ (3) enhanced electrode integrity due to the 3-D network formation of the epoxy with the polymer binder, and (4) facilitated Li^+ transfer at the Si and electrolyte interface due to the chelating effect of the oligo(ethylene oxide) moiety.²⁹ Silicon composite electrode using surface functionalized SiNPs (SF-SiNPs) as active anode material was

evaluated. Compared with the baseline anode, the SF-SiNPs exhibit significantly improved electrochemical performance, including first cycle coulombic efficiency (CE), capacity retention and low impedance increase. Furthermore, capacity retention ability of the SF-SiNPs was found to be closely related to the grafting density of the functional groups. We hypothesize that these improved electrochemical properties result from the homogeneity of the electrode structure provided by the oligo(ethylene oxide) epoxide surface functionalities and their ability to interact and chemically bind to the polymer binder.

3.2 Experimental Section

3.2.1 Materials

The Si-H terminated nanoparticles (Si-H NPs) with an average size of 5-20 nm, was synthesized by Nathan Neale and his coworkers at National Renewable Energy Laboratory (NREL) by plasma synthesis and was stored in glove box in the original container prior to use.²³ ²⁴ Ethylene glycol allyl methyl ether was purchased from Gelest, Inc., and was vacuum distilled from CaH₂ before use. Epichlorohydrin (99 %) was purchased from Sigma-Aldrich. Poly(acrylic acid) (PAA) binder with a claimed weight average molecular weight of 450KDa was purchased from Sigma-Aldrich and was dissolved in deionized water with a concentration of 10 wt%. Toluene (ACS reagents, $\geq 99.5\%$) was purchased from Sigma-Aldrich and was dried over 4Å molecular sieves prior to use. Graphite flakes (MagE) were obtained from Hitachi. Conductive carbon (C45, 50-60 nm) was purchased from Timcal. Gen 2 electrolyte (1.2 M LiPF₆ in a liquid mixture of ethylene carbonate and ethyl methyl carbonate in 3:7 by weight) was provided by Tomiyama Pure Chemical Industries. Fluoroethylene carbonate (FEC, Solvay) was dried and vacuum distilled before use.

3.2.2 Synthesis of Oligo(ethylene oxide)-Epoxy-Terminated Allyloxy Precursors (Allyl-(EO)_n-Epoxy)

Oligo(ethylene oxide)-epoxy-terminated allyloxy precursors varying in chain length of ethylene oxide unit were synthesized as shown in Scheme 3.1 and were named as Allyl-(EO)_n-Epoxy. Below is a description of synthetic procedure of Allyl-(EO)₂-Epoxy.

Synthesis of 2-(2-Allyloxy-ethoxy) ethanol (Allyl-(EO)₂-OH): To a 250mL three-necked round bottom flask equipped with a magnetic stir bar, a mixture of diethylene glycol (10.61 g, 0.10 mol) and 50% aqueous solution of NaOH (4.00 g, corresponding to 0.05 mol NaOH) was added and was stirred at 50 °C for 1 h. Allyl bromide (6.05 g, 0.05 mol) was added dropwise through a dropping funnel. The mixture was stirred at 60 °C for 2 h and then at 80 °C for 20 h. The mixture was cooled to room temperature, diluted with dichloromethane (30 mL) and poured into a separatory funnel. Distilled water (DI H₂O, 50 mL) was added to the mixture and the organic layer was extracted. The aqueous layer was washed with dichloromethane (30mL, 2 times) and the combined organic extraction was dried over anhydrous MgSO₄ overnight. The solid was filtered and the residue was concentrated by rotovapor to give the product (5.91g, 0.04 mol, Yield: 80.0 %). ¹H NMR (CDCl₃) δ (ppm): 5.81 – 5.93 (m, 1 H, CH₂=CH–), 5.12 – 5.27 (m, 2 H, OH CH₂=CH–), 3.97 – 4.00 (t, 2 H, CH–CH₂–O), 3.55 – 3.70 (m, 8 H, (CH₂–CH₂–O)₂), 2.96 (s, 1 H, –CH₂–OH). ¹³C NMR (CDCl₃) δ (ppm): 134.41 (CH₂CHCH₂), 117.46 (CH₂CHCH₂), 72.55, 72.24, 70.34, 69.41, 61.66 (Ethylene Oxide). Using the similar method, Allyl-(EO)₄-OH was synthesized with reaction between tetraethylene oxide and allyl bromide

*Synthesis of 2-[2-(2-allyloxyethoxy)ethoxymethyl]oxirane (Allyl-(EO)₂-Epoxy)*³⁰: In a 150mL two-necked round bottom flask equipped with a mechanical stirrer, a 50% aqueous NaOH solution

(4.80 g, corresponding to 0.06 mol NaOH), tetrabutylammonium hydrogen sulfate (2.04 g, 0.006 mol), and Allyl-(EO)₂-OH (4.42 g, 0.03 mol) were added. The mixed solution was cooled in an ice bath and epichlorohydrin (5.66 g, 0.06 mol) was added dropwise within 30 min. The temperature of the mixture was then allowed to be raised to the room temperature. After stirring for 17 h, the reaction mixture was poured into iced DI H₂O and transferred to a separatory funnel. The organic layer was collected, and the aqueous layer was extracted with dichloromethane (30mL) for 2 times, The combined organic portion was dried with anhydrous MgSO₄ overnight. The mixture was concentrated by rotorvapor and the residue was distilled from CaH₂ and the fraction at 120 °C/0.7 Torr was collected (3.34 g, Yield: 55.0 %). ¹H NMR (CDCl₃) δ (ppm): 5.82 – 5.96 (m, 1 H, CH₂=CH–), 5.12 – 5.28 (m, 2 H, OH CH₂=CH–), 3.98 – 4.01 (m, 2 H, CH–CH₂–O), 3.74 – 3.79 (dd, O–CHH–Epoxy), 3.56 – 3.71(m, 8 H, (CH₂–CH₂–O)₂), 3.37 – 3.43 (dd, 1 H, O–CHH–Epoxy), 3.11 – 3.16 (m, 1 H, CH of Epoxy), 2.75 – 2.78 (dd, 1 H. CHH of Epoxy), 2.57 – 2.59 (dd, 1 H, CHH of Epoxy). ¹³C NMR (CDCl₃) δ (ppm): 134.73(CH₂CHCH₂), 117.11(CH₂CHCH₂), 72.23, 71.98, 70.74, 70.67, 70.63, 69.41(Ethylene Oxide), 50.82, 44.20 (Epoxy). Allyl-(EO)₁-Epoxy and Allyl-(EO)₄-Epoxy were synthesized by a reaction between epichlorohydrin and the corresponding Allyl-(EO)_n-OH following the similar procedure.

3.2.3 SiNPs Surface Functionalization by Hydrosilylation

Hydrosilylation reaction was performed in an argon-purged glove box. Si-H NPs (0.050 g) were dispersed in toluene (5 mL) in a 20-mL vial equipped with a rubber septum and a stir bar. The resulting mixture was mechanically stirred until a homogeneous dispersion was formed. After that, excessive amount of allyl-(EO)_n-Epoxy (0.250 g) was added into the dispersion, followed by the injection of Karstedt's catalyst (10 μL) with a microsyringe. The temperature of the reaction mixture was raised to 45 °C and kept for 5 h. The resultant SF-SiNPs were isolated by high-speed

centrifugation (14,000 rpm, 30 min) and rinsed twice by toluene to remove the trace amount of catalyst and unreacted precursors. The obtained surface functionalized SiNPs (SF-SiNPs) were then dried in a vial in a high-vacuumed oven at 50 °C overnight. The SF-SiNPs were named as Si-C3-(EO)_n-Epoxy.

3.2.4 Graphite/Silicon Anode Preparation and Electrochemical Performance Evaluation

The composite electrode slurry composed of 15 wt% SF-SiNPs, 73 wt% MagE, 10 wt% PAA and 2 wt% Timcal C45 was mixed thoroughly and was casted onto a copper current collector. The electrode was punched into round disks with a loading of around 1.6 mg/cm² and evaluated by Si/Li 2032 coin cell. The electrode disks were dried at 130 °C under vacuum for 5 h. Celgard 2325 was used as separator and Gen 2 with 10% FEC was used as electrolyte. The cutoff voltage is 0.01-1.5 V and the cycling rate is C/3 following three C/20 formation cycles at room temperature.

3.2.5 Characterization of SF-SiNPs

Surface analysis of the original Si-H NPs was performed by X-ray photoelectron spectroscopy (XPS, PHI 5000 VersaProbe II System from Physical Electronics) with a base pressure of $\sim 2 \times 10^{-9}$ torr. The spectra were obtained with an Al K α radiation ($h\nu = 1486.6$ eV) beam (100 μ m, 25 W) and electron beam sample neutralization in fixed analyzer transmission mode. Peak fitting was performed using Shirley background correction and the Gaussian-Lorentzian curve synthesis available in CasaXPS software. Fourier-transform infrared (FTIR) spectra were acquired on a Thermo Scientific Nicolet iS5 spectrometer using attenuated total reflection model placed in an Argon-filled glove box. Thermogravimetric analysis (TGA) was conducted at a heating rate of 20°C/min from 30 °C to 800°C with Argon purge using the NETZSCH STA 449 F3 Jupiter for simultaneous thermogravimetry-differential scanning calorimetry (STA/TG-DSC). The morphology of SiNPs was analyzed with an FEI Tecnai F20ST

scanning/transmission electron microscopy ((S)TEM). Dynamic light scattering (DLS) measurements of aqueous dispersions of the SiNPs (1 mg g^{-1}) were conducted using a Brookhaven Instruments Zetaplus S/N 21308 zeta potential analyzer equipped a solid-state laser ($\lambda = 661.0\text{ nm}$) at a scattering angle of 90° . The dispersions were added into cuvettes and the cuvettes were sealed with PE stoppers. The cuvette was placed in the cell holder of the light scattering instrument.

Electrochemical impedance spectra of the coin cells after 150th cycle at C/3, respectively, were recorded versus an open-circuit voltage in the frequency range between 1MHz to 0.1 Hz on a Solartron analytical 1400 CellTest System. The cycled coin cells were disassembled in the argon-filled glovebox, and the composite electrodes were rinsed thoroughly with anhydrous dimethyl carbonate (DMC) and were dried in a vacuum oven. The morphologies and the elemental mapping of the cycled electrodes were examined with JEOL JCM-6000Plus scanning electron microscopy (SEM) equipped with MP-05030EDK energy-dispersive X-ray spectroscopy (EDX).

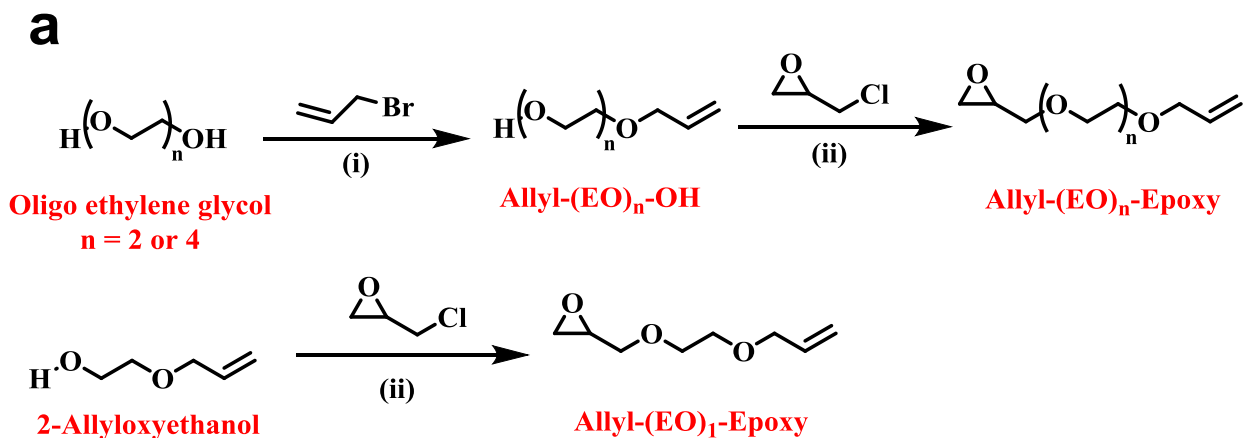
3.3 Results and Discussion

3.3.1 Synthesis and Characterization of SF-SiNPs

Three functional precursors allyl-(EO)_n-Epoxy ($n = 1, 2$ or 4) were synthesized via the reaction between allyloxy ethylene glycol with different number of ethylene oxide units and epichlorohydrin (Scheme 3.1a). The structures of the precursors were confirmed by NMR analysis (Figure B1- B5). The precursors were then successfully anchored onto the surface of the Si-H SiNPs by a Pt-catalyzed hydrosilylation reaction (Scheme 3.1b) in an argon-filled glovebox. To maximize the loading of the functional group on the particle surface, excessive stoichiometric feed ratios of precursor/Si-H SiNPs were used and the unreacted precursor was separated from the

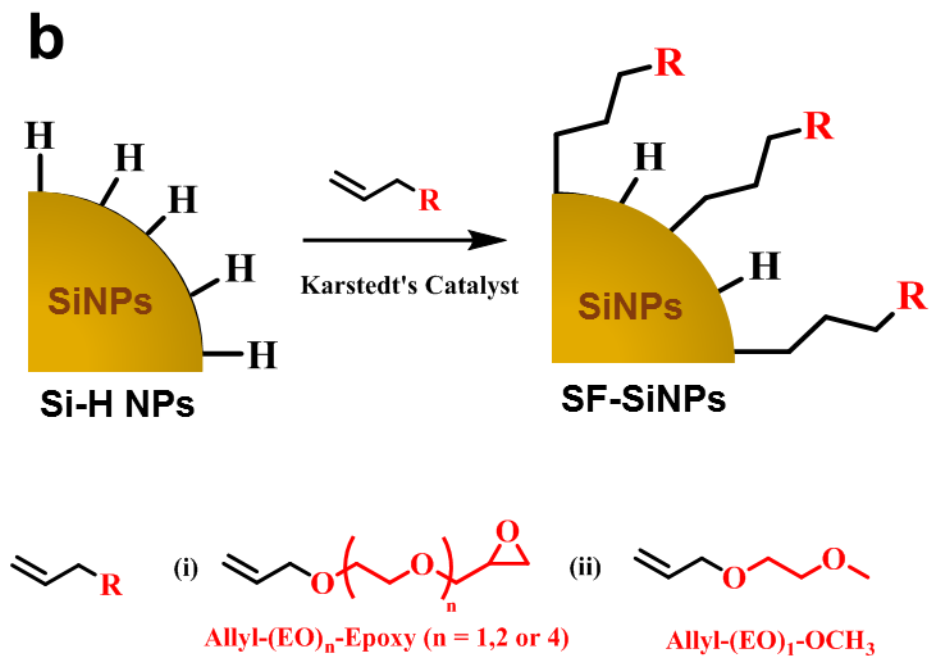
particles using high-speed centrifugation. The obtained three new SF-SiNPs, i.e. Si-C3-(EO)₁-Epoxy, Si-C3-(EO)₂-Epoxy, Si-C3-(EO)₄-Epoxy NPs were vacuum dried at elevated temperature prior to use. For simplification, the three SF-SiNPs are named as (EO)₁, (EO)₂ and (EO)₄ NPs in the following context.

Original Si-H NPs are subjected to both FTIR and XPS analysis. The strong and broad peak around 2100 cm⁻¹ originates from the Si-H stretching vibrations (2087 cm⁻¹ for SiH, 2108 cm⁻¹ for SiH₂ and 2138 cm⁻¹ for SiH₃, inset in Figure 3.1a). No obvious peak at 1100 cm⁻¹ was observed indicating the Si-H SiNPs is SiO_x free on the surface.²⁶ Si_{2p} XPS analysis (main peak at 99.4 eV) is consistent with the IR data²⁶ (Figure 3.1b). After hydrosilylation, new IR peaks show up for the SF-SiNPs (Figure 3.2a). Strong vibrational peak of alkyl (C-H bond) at 2880 and 2930 cm⁻¹, ether (C-O) bond at around 1050 cm⁻¹, Si-C bond stretching mode at 1040 cm⁻¹ (overlapped with the C-O bands) and bending mode 850 cm⁻¹, and epoxy ring breath mode at 1250-1500 cm⁻¹ confirm the successful attachment of the precursor to the SiNPs.³¹ Not all the Si-H groups were reacted, which might result from the steric hindrance, especially for the long and bulky precursor Allyl-(EO)₄-Epoxy.³² Figure 3.3a and 3.3b show TEM images of (EO)₁ NPs and the original Si-H NPs, respectively. The average diameter of the Si NP was around 10 nm. The SF-SiNPs distribute evenly without significant agglomeration compared with the pristine particles. This phenomenon can be further verified by a dispersion experiment illustrated in Figure 3.3c. The SF-SiNPs dispersion remain unchanged after 24 h, whereas the pristine particle dispersion was translucent initially and precipitated after 24 h. DLS analysis draws the same conclusion and the data are provided in Figure B6.³³



(i): NaOH (50 wt % aq)

(ii): NaOH (50 wt % aq), tetrabutylammonium hydrogen sulfate



Scheme 3.1 (a) Synthesis of Allyl-(EO)_n-Epoxy and (b) Synthesis of SF-SiNPs by surface hydrosilylation

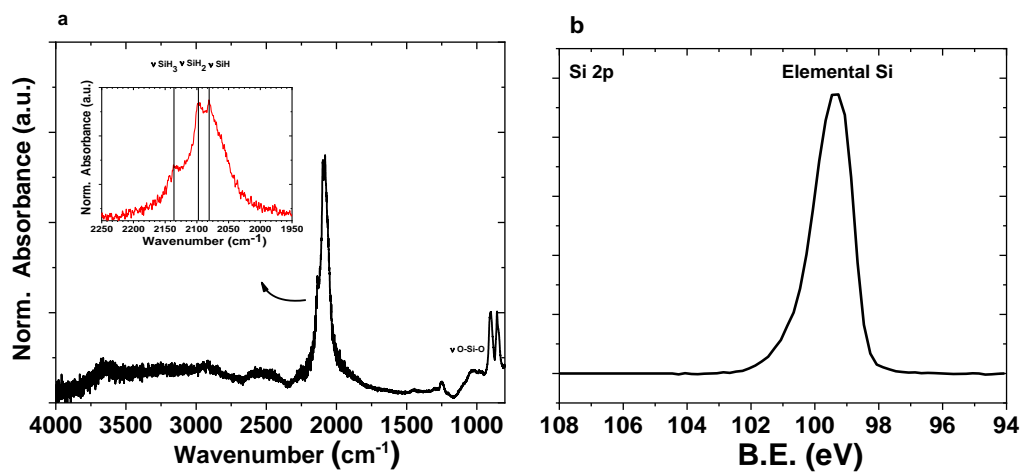


Figure 3.1. (a) FTIR-ATR spectrum of original Si-H NPs (the inset is an enlarged figure of the Si-H bands) and (b) Si 2p core-level spectrum of original Si-H NPs.

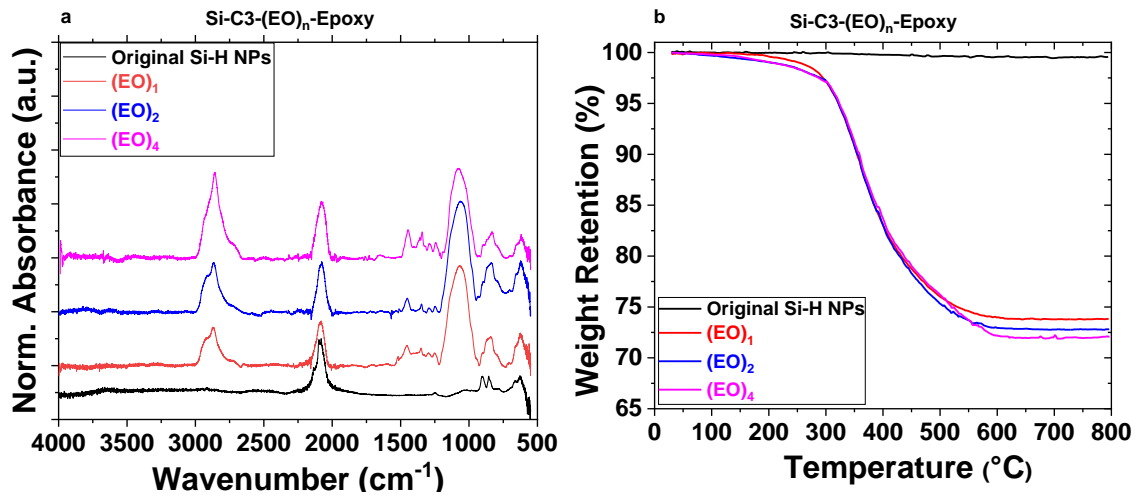


Figure 3.2. (a) FTIR-ATR spectra and (b) TGA curve of the Si-C3-(EO)_n-Epoxy NPs. The FTIR spectrum and TGA curve of original Si-H NPs are included as reference.

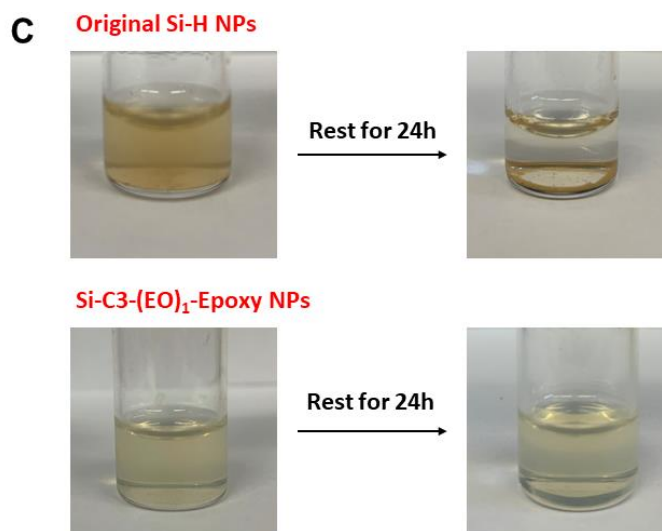
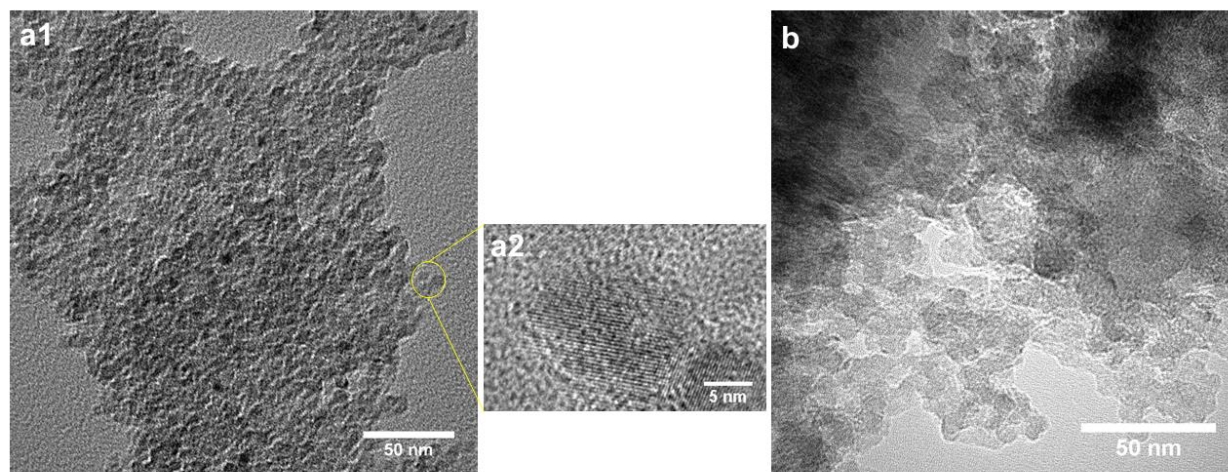


Figure 3.3. TEM images of Si-C3-(EO)₁-Epoxy NPs (a1) and Original Si-H NPs (b). a2 is a zoom-in image of a1. The specimens were prepared from 1 mg g⁻¹ SiNPs aqueous suspensions by casting the nanoparticles on the carbon-coated copper TEM grid. (c) are the optical images of aqueous dispersions (1 mg g⁻¹) of original Si-H NPs and Si-C3-(EO)₁-Epoxy NPs, respectively. Left: freshly prepared dispersions which have been sonicated for 10 mins, and Right: the same dispersions have rested for 24 h.

3.3.2 Electrochemical stability at anode/electrolyte interface

Si/graphite composite electrodes were prepared by using SF-SiNPs, as also the original SiNPs. Electrochemical performances of the prepared electrodes were evaluated in coin cells using lithium metal as the counter electrode and specific capacities were calculated based on actual loading of active materials. The cells were first subjected to three slow-rate cycles with rate of 0.15 mAh/g in the potential range of 0.01 – 1.5 V. The voltage profile for the first cycle is shown in Figure 3.4a; the first-cycle discharge (lithiation) and charge (delithiation) capacities of electrodes containing the original Si-H NPs (baseline), (EO)₁, (EO)₂ and (EO)₄ NPs are 1013/695, 1074/834, 1102/855 and 1172/903 mAh/g, respectively, with the corresponding initial Coulombic efficiencies (CE) calculated as 68.6, 77.6, 77.6 and 77.0 %, respectively. Both the initial capacities and CEs of the SF-SiNPs electrode show improvement compared with those of the baseline. One possible reason is that surface functionalization helps to passivate the highly reactive Si-H surface, resulting in less irreversible capacity loss. Study of the differential capacity (dQ/dV) plot (Figure 3.4b) further confirmed this hypothesis. The baseline electrode has two significant reduction peaks at around 1.3 V and 1.2 V, respectively, while each of the SF-SiNPs electrode has only one reduction peak near 1.0 V that is also low in intensity. Another noticeable difference is that while the typical reduction peak of Gen II electrolyte at 0.8 V, which is due to the decomposition of organic solvent,¹¹ is still visible in the dQ/dV plot of baseline electrode, the peak becomes negligible for SF-SiNPs. The result suggests that adoption of SF-SiNPs in the electrode helps to stabilize electrode/electrolyte interface. The dQ/dV plots of the 2nd and 3rd formation cycles (Figure B8) are almost overlapped with each other for SF-SiNPs, indicating good cycling reversibility.

Cycling stability of the three electrodes at C/3 rate was studied, where the C rate is

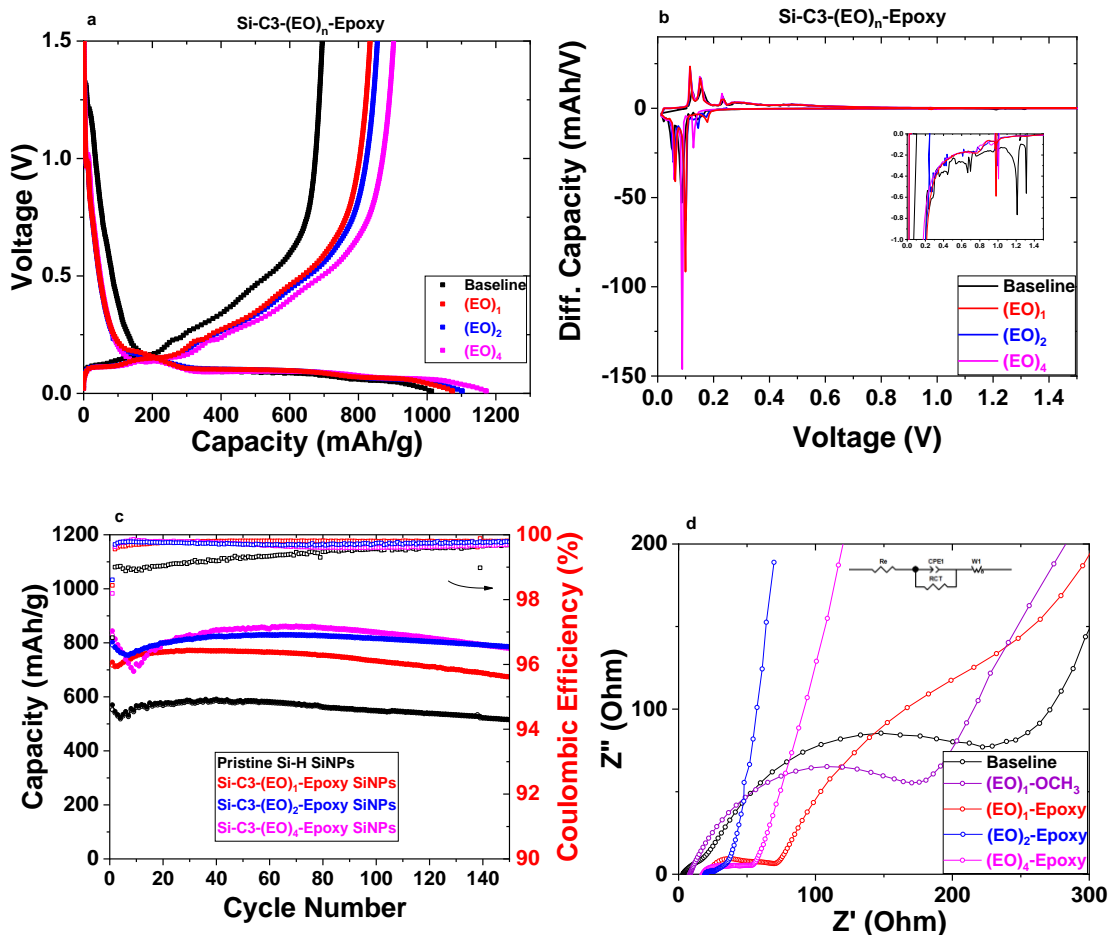


Figure 3.4. Electrochemical evaluation data: 1st formation cycle (a) voltage profiles and (b) differential capacity profiles of electrodes based on original Si-H NPs (baseline) and Si-C3-(EO)_n-Epoxy NPs, respectively. The inset in (b) is a zoom-in of the differential capacity plot in the lithiation process. Electrochemical performance of graphite/Si composite electrodes (Li metal as counter electrode) over 150 cycles at C/3 rate: (c) specific charge capacity (lithiation: solid sphere; delithiation: empty sphere, shown to the left) and the corresponding coulombic efficiency (empty square) and (d) EIS plots of baseline and SF-SiNPs electrodes, respectively, after 150 cycles at C/3 rate

determined by the lithiation capacity of the 3rd formation cycle. As shown in Figure 3.4c, baseline electrode has an initial delithiation capacity of 552 mAh/g and then the capacity went through a slight drop during the first several cycles before it bounced back. A very similar performance trend was found in our previous study on silicon-based anode. The capacity decay during the initial few cycles might be attributed to electrolyte wetting process or formation of SEI. Then the capacity gradually increased and reached the highest 586 mAh/g at 40th cycle. After that, the capacity gradually dropped to 514 mAh/g after 150 cycles. The capacity retention (capacity at 150th cycle/initial capacity) of the baseline electrode is 93.5 %. In general, the initial capacity of the baseline is lower than the theoretical value of the composite electrode, but it keeps a rather stable performance throughout extended cycles. The particle size might play a role in such behavior of the composite electrode. Original SiNPs feature a large contact area with the electrolyte due to its ultrasmall particle size (diameter ~ 10 nm), which gives rise to more side reactions and the consequently higher irreversible capacity loss. However, after a stable SEI layer is formed at the particle surface, the large surface area endows the particle with a better ability to alleviate the stress brought about by volume change, thus preventing rapid capacity decay. After functionalizing the surface with an (ethylene-oxide)-epoxy group, an apparent increase in the initial capacity was observed. The initial capacities of the Si-C3-(EO)₁-Epoxy electrode is 717 mAh/g, a 36.5 % increase compared with that of the baseline. Then the capacity profile of the (EO)₁-electrode follows similar pattern with the baseline electrode within the first 50 cycles with the highest capacities reaching 770mAh/g neat 40th cycle. The capacity retention after 150 cycles is 94.1 %. (EO)₁-electrode also outstands in CE stability with CEs stabilize at 99.7% after initial cycle. In contrast, the initial CE of the baseline is below 97 %, and it takes about 100 alloying/dealloying cycles before the CE finally stabilizes near 99.7 %.

To understand the distinct role of the two functional groups, i.e., ethylene oxide and epoxy group in the improvement of electrochemical performance, SF-SiNPs functionalized with only ethylene oxide were synthesized using ethylene glycol allyl methyl ether (allyl-(EO)₁-OCH₃) as the precursor (Scheme 3.1b) and the resultant Si-C3-(EO)₁-OCH₃ NPs have a comparable grafting density to that of the Si-C3-(EO)₁-Epoxy NPs. The initial capacity of the composite electrode based on Si-C3-(EO)₁-OCH₃ is in between those of the baseline and the Si-C3-(EO)₁-Epoxy electrode. Interestingly, the capacity after 150th cycle is higher than the initial capacity, resulting in a capacity retention of more than 100 % (Figure B10). This comparison study gives us a clearer picture of the different roles of the two functional groups in the improvement of capacity and capacity retention. It is likely that surface ethylene oxide group helps to maintain capacity retention with its ability to facilitate lithium ion transfer while the epoxy group improves efficient utility of the capacity of active material by promoting electrode structure integrity with stronger binder-active material interaction and mitigating parasitic reactions at electrode/electrolyte interface.²⁰ Interestingly, the improvement in capacity retention did not increase linearly with the number of surface ethylene oxide unit. Despite that (EO)₄ electrode has the highest grafting density of ethylene oxide units on the surface, (EO)₂ electrode has the highest capacity retention among the three dual-functional SiNPs electrodes.

EIS studies were performed on SF-SiNPs after 150 electrochemical cycles at C/3. The Nyquist plots (Figure 3.4d) of both the baseline and SF-SiNPs electrodes showed a depressed semicircle in the high-frequency range, which is in accordance with charge-transfer resistance at the electrode/electrolyte interface and a sloped line in the high-frequency range, which represents diffusion-controlled Warburg impedance. For a quantitative comparison, the experimental EIS data were fitted using the equivalent circuit shown at the right top of the EIS spectra, where R_e is

the ohmic resistance of the electrode and electrolyte, R_{ct} is the charge-transfer resistance at electrode/electrolyte interface, CPE1 is the double-layer capacitance and W_1 is the Warburg impedance.²⁹ Surface functionalization improves the R_{ct} as the charge-transfer resistances of both Si-C3-(EO)₁-OCH₃ and Si-C3-(EO)_n-Epoxy are smaller than that of the baseline. The improvement is more significant for the Si-C3-(EO)_n-Epoxy with Si-C3-(EO)₂-Epoxy electrode having the lowest R_{ct} , which is only 1/10 that of the baseline. The non-linear dependence of R_{ct} on the number of ethylene oxide unit on the particle surface is in accordance with the trend of capacity retention. It is believed that both ionic and electronic resistance influence the behavior of R_{ct} as charge transfer reaction is required to bring Li⁺ and electron to the interface reaction sites.³⁴ Though (EO)₄ electrode has the theoretically highest Li⁺ conductivity with its highest surface ethylene oxide density, (EO)₂ electrode has a denser epoxy group coverage, which helps to maintain the Si electrode structure after extended cycles and thus contributes to building good electronic networks between Si particles and preventing the portions of Si particles from being isolated from electrical pathway. Table 3.1 summarizes the general characterization data of the silicon-graphite composite electrodes based on pristine and surface-functionalized SiNPs.

3.3.3 Impact of Grafting Density

It is manifested that surface functionalization could stabilize the interface. Next question is how the grafting density (GD) of the functional groups on the surface of SiNPs will impact the electrochemical performance. The following equation was used to calculate the grafting density using the following equation.^{33, 35}

$$\frac{\left(\frac{wt_{FG}\%}{wt_{NP}\%}\right) \times \left(\rho_{NP} \frac{4}{3} \pi r_{NP}^3\right)}{M_w} \times N_A \times \frac{1}{4\pi r_{NP}^2} \quad (\text{Equation 3.1})$$

where wt_{FG}% is the weight percentage of the functional group and wt_{NP}% is the weight percentage of the SiNPs. Both values were obtained from the TGA thermograms of the SF-SiNPs shown in

Figure 1d. ρ_{NP} and r_{NP} are the density and the radius of the SiNPs, M_w is the molecular weight of the functional group and N_A is the Avogadro's number (6.02×10^{23}). The grafting densities of the SF-SiNPs were summarized in Table 1. The maximized grafting density of different groups are different depending on its molecular structure. The allyl-(EO)4-Epoxy has the longest chain length, but the grafting density is the lowest, 3.6 chain/nm². This is probably due to the steric hindrance of the longer chain preventing the hydrosilylation reaction. Despite its low GD, the cell performance is the best among all the materials. It is speculated that the five oxygen atoms in the functional group has an optimal chelating geometry, which is feasible for Li⁺ solvation with facilitated transfer at the anode/electrolyte interphase. For the shorter functional group, it has the highest GD of 5.1 due to the small size of the precursor. By lowering the feed ratio of allyl-(EO)2-Epoxy to Si-H SiNPs, a lower GD SiNPs sample (GD=2.2) was prepared and its performance was compared with the higher one. Figure 3.5 shows the capacity retention and the Coulombic efficiency of these two samples. Overall, both electrodes showed higher initial capacities and Coulombic efficiencies than the pristine anode. This improvement clearly indicated that the more surface coverage of the SiNPs, the less surface reactivity, with improved affinity with the binder and electrode integrity.

3.4 Morphological Characterization

Surface functionalization could promote the particle distribution in pure Si electrode and the Si/graphite composite electrode. Figure 3.6 is the SEM/EDX spectra of the Si/graphite composite anode before and after cycling. SF-SiNPs tend to be well distributed within the matrix of the graphite active material (Figure 3.6b and Figure B12a-b), whereas the pristine SiNPs caused huge particle agglomeration (Figure 3.6a). This morphological difference could explain the high

Table 3.1. Grafting densities, loading densities, initial capacities and Coulombic efficiencies, capacity retentions and charge-transfer resistances (R_{ct}) measured after 150 electrochemical cycles of the graphite/silicon composite electrodes based on original SiNPs and SF-SiNPs

Sample	Grafting density, chains/nm ²	Loading density, mg/cm ²	Initial capacity ^a , mAh/g	Initial Coulombic efficiency ^a , %	Capacity retention ^b , %	R_{ct} ^c , Ω
Si-H	N/A	1.6	552	96.8	93.5	170.6 \pm 11.6
(EO) ₁ -OCH ₃ ^d	4.4	1.6	572	98.2	101.9	135.3 \pm 3.4
(EO) ₁ -Epoxy ^e	5.1	1.6	717	98.4	94.1	50.8 \pm 0.8
(EO) ₂ -Epoxy ^e	4.2	1.6	803	98.2	97.9	12.2 \pm 0.6
(EO) ₄ -Epoxy ^e	3.6	1.6	828	98.6	94.3	39.9 \pm 0.6

^a specific delithiation capacity and Coulombic efficiency after first C/3 cycle, ^b capacity at 150th cycles/initial capacity, ^c R_{ct} after 150 cycles, ^d Si-C3-(EO)₁-OCH₃ electrode, ^e Si-C3-(EO)_n-Epoxy electrode.

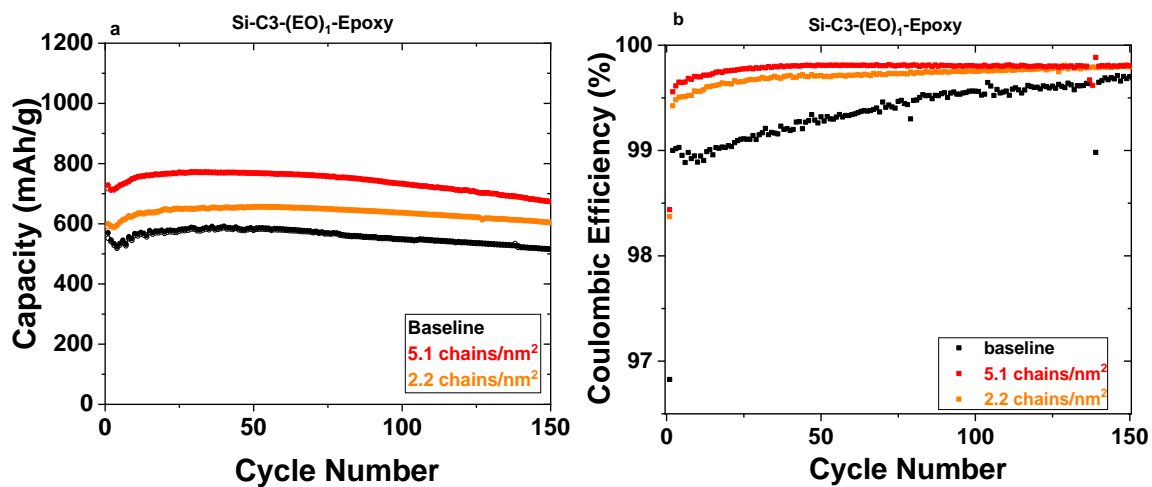


Figure 3.5. Electrochemical performance of Si-C3-(EO)₁-Epoxy with different grafting density over 150 C/3 cycles: (a) specific capacity (lithiation: solid sphere; delithiation: empty sphere) and (b) the corresponding coulombic efficiency.

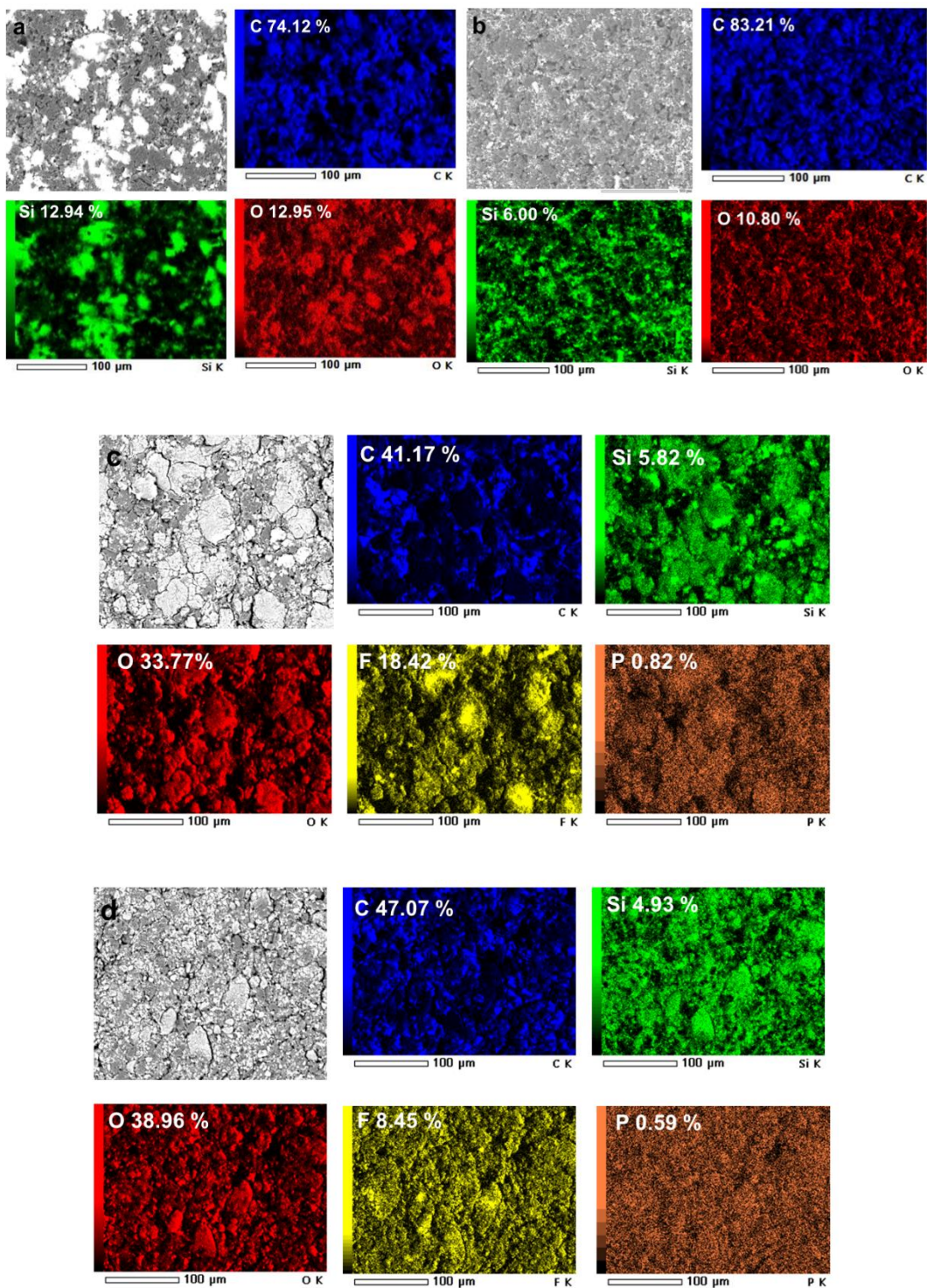


Figure 3.6. EDX elemental mapping of pristine electrodes (C, Si and O) (a: baseline, and b: Si-C₃-(EO)₂-Epoxy) and the cycled electrodes (C, Si, O, F and P) (c: baseline, d: Si-C₃-(EO)₂-Epoxy)

utilization of the Si material in the composite anode reflected by the higher initial capacity of SF-SiNPs. Interestingly, the same morphology was retained even after 150 cycles as observed in Figure 3.6c and 3.6d. Furthermore, the pristine SiNPs showed much more F-rich decomposition products on the surface of the electrode, compared with the SF-SiNPs anode, indicating that the surface functionalization could mitigate the parasitic reactions with electrolyte during repeated cycling. This result is also consistent with the results of the electrochemical analysis.

3.4 Conclusion

In summary, surface functionalization is demonstrated to be a sufficient way to stabilize the surface of the high capacity silicon anode. A Pt-catalyzed hydrosilylation reaction was performed on the Si-H terminated SiNPs forming a Si-C covalent bond between the particle and the functional group. Physical, electrochemical and post-test analysis indicated that the SF-SiNPs are chemically stabilized when in contact with air and water during the slurry making and electrode coating process. It also prevents the agglomeration of the nano-sized silicon particles and thus improves the utilization of the active silicon material in the composite anode. Anode electrodes based on SF-SiNPs showed much improved cycling performance compared with the baseline. To be more specific, ethylene oxide group helps to improve cycling stability probably by facilitating lithium ion transport within the electrode while epoxy group triggers more efficient utility of electrode's capacity by promoting homogeneity of the electrode. Additionally, it has also been demonstrated that higher functionality coverage leads to better cell performance. Future research will be focused on the identification of the optimal surface groups. Under this platform, functional groups can be designed and developed to tailor the surface of the silicon materials for high-energy density lithium ion batteries.

3.5 Reference

1. Feng, K.; Li, M.; Liu, W.; Kashkooli, A. G.; Xiao, X.; Cai, M.; Chen, Z., Silicon - Based Anodes for Lithium - Ion Batteries: From Fundamentals to Practical Applications. *Small* **2018**, *14*, 1702737.
2. Mims, C., "The Battery Boost We've Been Waiting for Is Only a Few Years Out". *Wall Street Journal* 03-18, 2018.
3. Park, C. M.; Kim, J. H.; Kim, H.; Sohn, H. J., Li-alloy based anode materials for Li secondary batteries. *Chem. Soc. Rev.* **2010**, *39*, 3115-3141.
4. Yoon, T.; Nguyen, C. C.; Seo, D. M.; Lucht, B. L., Capacity fading mechanisms of silicon nanoparticle negative electrodes for lithium ion batteries. *J. Electrochem. Soc.* **2015**, *162*, A2325-A2330.
5. Kalnaus, S.; Rhodes, K.; Daniel, C., A study of lithium ion intercalation induced fracture of silicon particles used as anode material in Li-ion battery. *J. Power Sources* **2011**, *196*, 8116-8124.
6. Kumar, R.; Tokranov, A.; Sheldon, B. W.; Xiao, X.; Huang, Z.; Li, C.; Mueller, T., In situ and operando investigations of failure mechanisms of the solid electrolyte interphase on silicon electrodes. *ACS Energy Lett* **2016**, *1*, 689-697.
7. Chae, S.; Ko, M.; Kim, K.; Ahn, K.; Cho, J., Confronting issues of the practical implementation of Si anode in high-energy lithium-ion batteries. *Joule* **2017**, *1*, 47-60.
8. Rodrigues, M.; Trask, S.; Shkrob, I. A.; Abraham, D., Quantifying gas generation from slurries used in fabrication of Si-containing electrodes for lithium-ion cells. *J. Power Sources* **2018**, *395*, 289-294.

9. Choi, N.-S.; Yew, K. H.; Lee, K. Y.; Sung, M.; Kim, H.; Kim, S. S., Effect of fluoroethylene carbonate additive on interfacial properties of silicon thin-film electrode. *J. Power Sources* **2006**, *161*, 1254-1259.
10. Chen, L.; Wang, K.; Xie, X.; Xie, J., Effect of vinylene carbonate (VC) as electrolyte additive on electrochemical performance of Si film anode for lithium ion batteries. *J. Power Sources* **2007**, *174*, 538-543.
11. Xu, C.; Lindgren, F.; Philippe, B.; Gorgoi, M.; Björefors, F.; Edström, K.; Gustafsson, T., Improved Performance of the Silicon Anode for Li-Ion Batteries: Understanding the Surface Modification Mechanism of Fluoroethylene Carbonate as an Effective Electrolyte Additive. *Chem. Mater.* **2015**, *27*, 2591-2599.
12. Szczech, J. R.; Jin, S., Nanostructured silicon for high capacity lithium battery anodes. *Energy Environ. Sci.* **2011**, *4*, 56-72.
13. Bie, Y.; Yang, J.; Liu, X.; Wang, J.; Nuli, Y.; Lu, W., Polydopamine wrapping silicon cross-linked with polyacrylic acid as high-performance anode for lithium-ion batteries. *ACS Appl. Mater. Interfaces* **2016**, *8*, 2899-2904.
14. Higgins, T. M.; Park, S. H.; King, P. J.; Zhang, C.; McEvoy, N.; Berner, N. C.; Daly, D.; Shmeliov, A.; Khan, U.; Duesberg, G., A commercial conducting polymer as both binder and conductive additive for silicon nanoparticle-based lithium-ion battery negative Electrodes. *ACS Nano* **2016**, *10*, 3702-3713.
15. Hu, B.; Shkrob, I. A.; Zhang, S.; Zhang, L.; Zhang, J.; Li, Y.; Liao, C.; Zhang, Z.; Lu, W.; Zhang, L. J. J. o. P. S., The existence of optimal molecular weight for poly (acrylic acid) binders in silicon/graphite composite anode for lithium-ion batteries. **2018**, *378*, 671-676.

16. Cao, P. F.; Naguib, M.; Du, Z.; Stacy, E.; Li, B.; Hong, T.; Xing, K.; Voylov, D. N.; Li, J.; Wood III, D. L., Effect of Binder Architecture on the Performance of Silicon/Graphite Composite Anodes for Lithium Ion Batteries. *ACS Appl. Mater. Interfaces* **2018**, *10*, 3470-3478.
17. Tang, K.; Fu, L.; White, R. J.; Yu, L.; Titirici, M. M.; Antonietti, M.; Maier, J., Hollow carbon nanospheres with superior rate capability for sodium - based batteries. *Adv. Energy Mater.* **2012**, *2*, 873-877.
18. Buriak, J. M., Organometallic Chemistry on Silicon and Germanium Surfaces. *Chem. Rev.* **2002**, *102*, 1271-1308.
19. Buriak, J. M., Illuminating Silicon Surface Hydrosilylation: An Unexpected Plurality of Mechanisms. *Chem. Mater.* **2014**, *26*, 763-772.
20. Jiang, S.; Hu, B.; Sahore, R.; Zhang, L.; Liu, H.; Zhang, L.; Lu, W.; Zhao, B.; Zhang, Z., Surface-Functionalized Silicon Nanoparticles as Anode Material for Lithium-Ion Battery. *ACS Appl. Mater. Interfaces* **2018**, *10*, 44924-44931.
21. Higgins, T. M.; Park, S.-H.; King, P. J.; Zhang, C.; McEvoy, N.; Berner, N. C.; Daly, D.; Shmeliov, A.; Khan, U.; Duesberg, G.; Nicolosi, V.; Coleman, J. N., A Commercial Conducting Polymer as Both Binder and Conductive Additive for Silicon Nanoparticle-Based Lithium-Ion Battery Negative Electrodes. *ACS Nano* **2016**, *10*, 3702-3713.
22. Gao, Y.; Yi, R.; Li, Y. C.; Song, J.; Chen, S.; Huang, Q.; Mallouk, T. E.; Wang, D., General Method of Manipulating Formation, Composition, and Morphology of Solid-Electrolyte Interphases for Stable Li-Alloy Anodes. *J. Am. Chem. Soc.* **2017**, *139*, 17359-17367.

23. Hanrahan, M. P.; Fought, E. L.; Windus, T. L.; Wheeler, L. M.; Anderson, N. C.; Neale, N. R.; Rossini, A. J., Characterization of Silicon Nanocrystal Surfaces by Multidimensional Solid-State NMR Spectroscopy. *Chem. Mater.* **2017**, *29*, 10339-10351.
24. Carroll, G. M.; Limpens, R.; Neale, N. R., Tuning Confinement in Colloidal Silicon Nanocrystals with Saturated Surface Ligands. *Nano Lett.* **2018**, *18*, 3118-3124.
25. Mangolini, L.; Thimsen, E.; Kortshagen, U., High-yield plasma synthesis of luminescent silicon nanocrystals. *Nano Lett.* **2005**, *5*, 655-659.
26. Wheeler, L. M.; Anderson, N. C.; Palomaki, P. K. B.; Blackburn, J. L.; Johnson, J. C.; Neale, N. R., Silyl radical abstraction in the functionalization of plasma-synthesized silicon nanocrystals. *Chem. Mater.* **2015**, *27*, 6869-6878.
27. Kortshagen, U. R.; Sankaran, R. M.; Pereira, R. N.; Girshick, S. L.; Wu, J. J.; Aydil, E. S., Nonthermal plasma synthesis of nanocrystals: fundamental principles, materials, and applications. *Chem. Rev.* **2016**, *116*, 11061-11127.
28. Jiang, S.; Hu, B.; Sahore, R.; Zhang, L.; Liu, H.; Zhang, L.; Lu, W.; Zhao, B.; Zhang, Z., Surface-Functionalized Silicon Nanoparticles as Anode Material for Lithium-Ion Battery. *ACS Appl. Mater. Interfaces* **2018**.
29. Munaoka, T.; Yan, X.; Lopez, J.; To, J. W. F.; Park, J.; Tok, J. B.-H.; Cui, Y.; Bao, Z., Ionically Conductive Self-Healing Binder for Low Cost Si Microparticles Anodes in Li-Ion Batteries. *Adv. Energy Mater.* **2018**, *8*, 1703138.
30. Sun, X.-G.; Kerr, J. B., Synthesis and characterization of network single ion conductors based on comb-branched polyepoxide ethers and lithium bis (allylmalonato) borate. *Macromolecules* **2006**, *39*, 362-372.

31. Clark, R. J.; Aghajamali, M.; Gonzalez, C. M.; Hadidi, L.; Islam, M. A.; Javadi, M.; Mobarok, M. H.; Purkait, T. K.; Robidillo, C. J. T.; Sinenikov, R., From Hydrogen Silsesquioxane to Functionalized Silicon Nanocrystals. *Chem. Mater.* **2016**, *29*, 80-89.
32. Li, X.; He, Y.; Swihart, M. T., Surface Functionalization of Silicon Nanoparticles Produced by Laser-Driven Pyrolysis of Silane followed by HF–HNO₃ Etching. *Langmuir* **2004**, *20*, 4720-4727.
33. Hu, B.; Henn, D. M.; Wright, R. A. E.; Zhao, B., Hybrid Micellar Hydrogels of a Thermosensitive ABA Triblock Copolymer and Hairy Nanoparticles: Effect of Spatial Location of Hairy Nanoparticles on Gel Properties. *Langmuir* **2014**, *30*, 11212-11224.
34. Kwon, Y. H.; Minnici, K.; Huie, M. M.; Takeuchi, K. J.; Takeuchi, E. S.; Marschilok, A. C.; Reichmanis, E., Electron/Ion Transport Enhancer in High Capacity Li-Ion Battery Anodes. *Chem. Mater.* **2016**, *28*, 6689-6697.
35. Benoit, D. N.; Zhu, H.; Lillierose, M. H.; Verm, R. A.; Ali, N.; Morrison, A. N.; Fortner, J. D.; Avendano, C.; Colvin, V. L., Measuring the Grafting Density of Nanoparticles in Solution by Analytical Ultracentrifugation and Total Organic Carbon Analysis. *Anal. Chem.* **2012**, *84*, 9238-9245.

**Appendix B for Chapter 3. Tailoring the Surface of Nano Silicon
Nanoparticles Anode for Enhanced Chemical and Electrochemical Stabilities
in for Lithium-ion Batteries**

B.1 Calculation of Grafting Density of SF-SiNPs

The Si-C3-(EO)₁-Epoxy with a weight retention of 73.8 % when heating to 800 °C was used as an example here. The weight retention of the original Si-H NPs at 800 °C is 99.6 %. Assuming the original SiNPs did not have any weight loss after heating, then the weight retention of Si-C3-(EO)₁-Epoxy was adjusted to 74.1 %. Therefore, the ratio of the silicon residue to the volatile portion at 800 °C was calculated to be 100:34.9. The molecular weight of the (CH₂)₃-O-(CH₂-CH₂-O)₁-Epoxy chains is 159 g/mol. Assuming the SiNPs are with an average diameter of 10 nm and using the density of silicon, which is 2.33 g/cm³, the mass of a single silicon NP is 1.22×10^{-18} g. The mass of the functional group on one single silicon NP is then calculated to be 4.26×10^{-19} g. Therefore the number of functional groups grafted on one silicon NP is $4.26 \times 10^{-19} \text{ g} / 159 \text{ g/mol} \times 6.022 \times 10^{23} = 1613$ chains. Therefore, Hence, the functionality density on SiNPs is 1613 chains / $(\pi \times 10^2) = 5.1$ chains/nm². The calculation of functionality density is based on the assumption that the weight loss of SF-SiNPs at 800 °C solely comes from the grafted functional groups.

B.2 Supplemental Figures

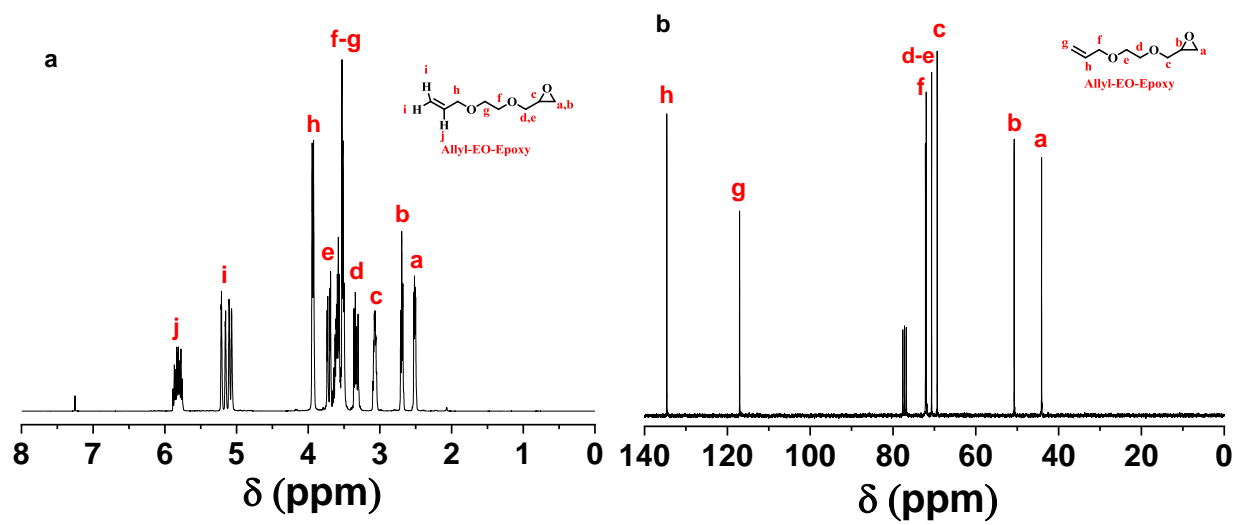


Figure B1. ^1H NMR (a) and ^{13}C NMR (b) spectra of Allyl-(EO)₁-Epoxy in CDCl_3 .

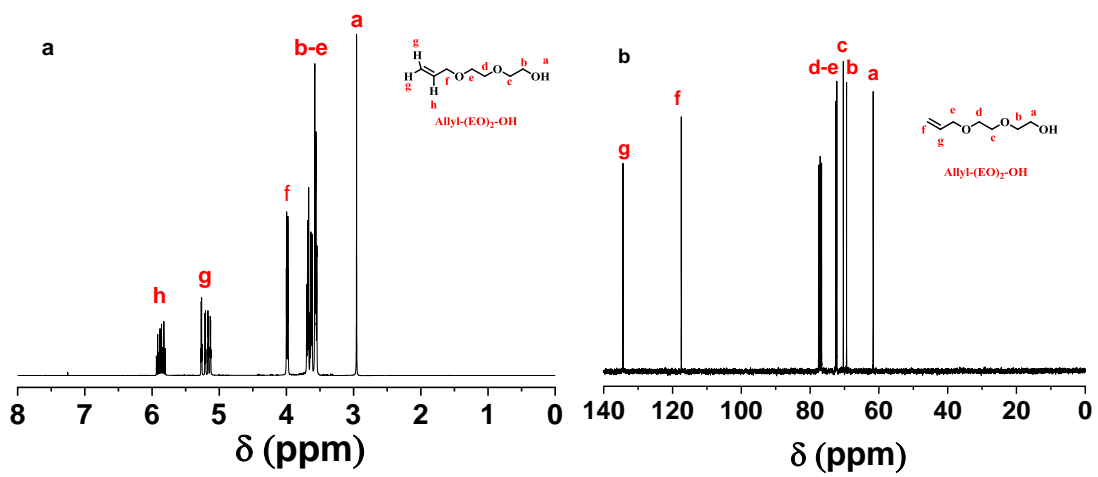


Figure B2. ^1H NMR (a) and ^{13}C NMR (b) spectrums of Allyl-(EO) $_2$ -OH in CDCl_3 .

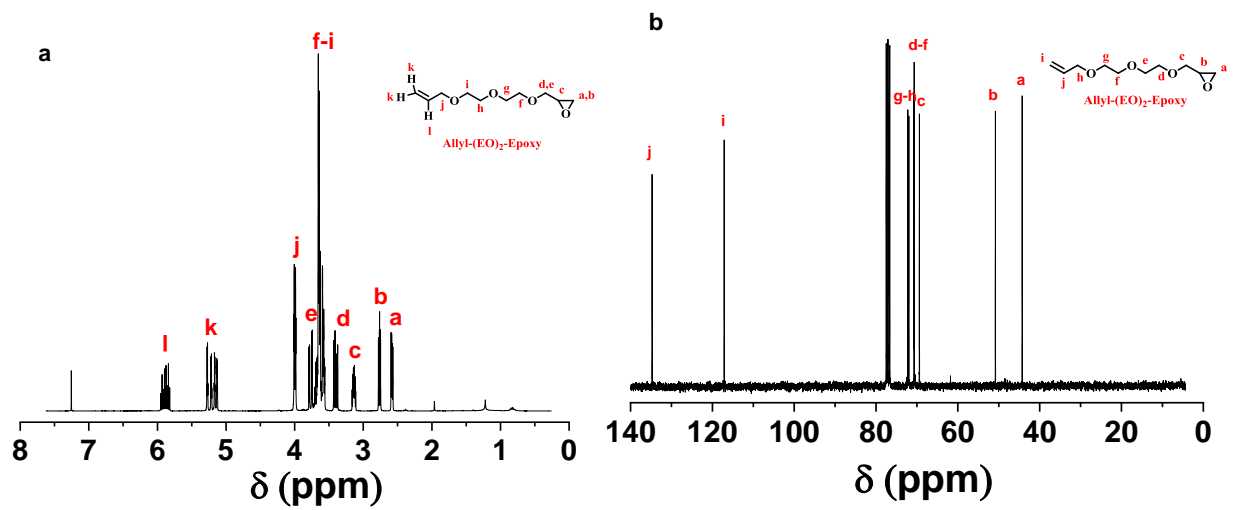


Figure B3. ^1H NMR (a) and ^{13}C NMR (b) spectra of Allyl-(EO)₂-Epoxy in CDCl_3 .

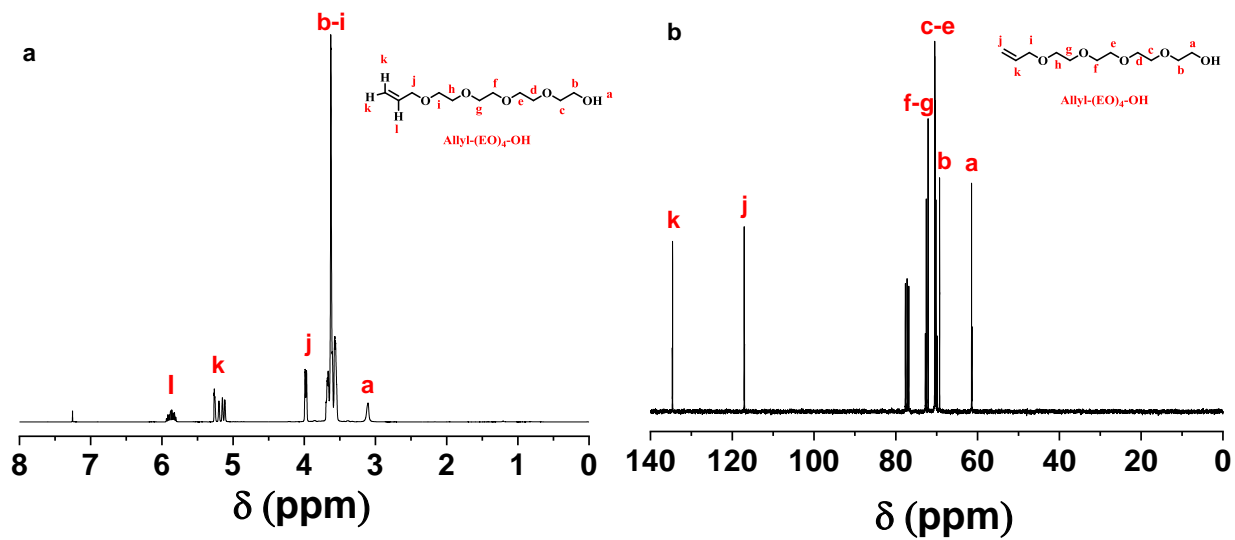


Figure B4. ^1H NMR (a) and ^{13}C NMR (b) spectra of Allyl-(EO) $_4$ -OH in CDCl_3 .

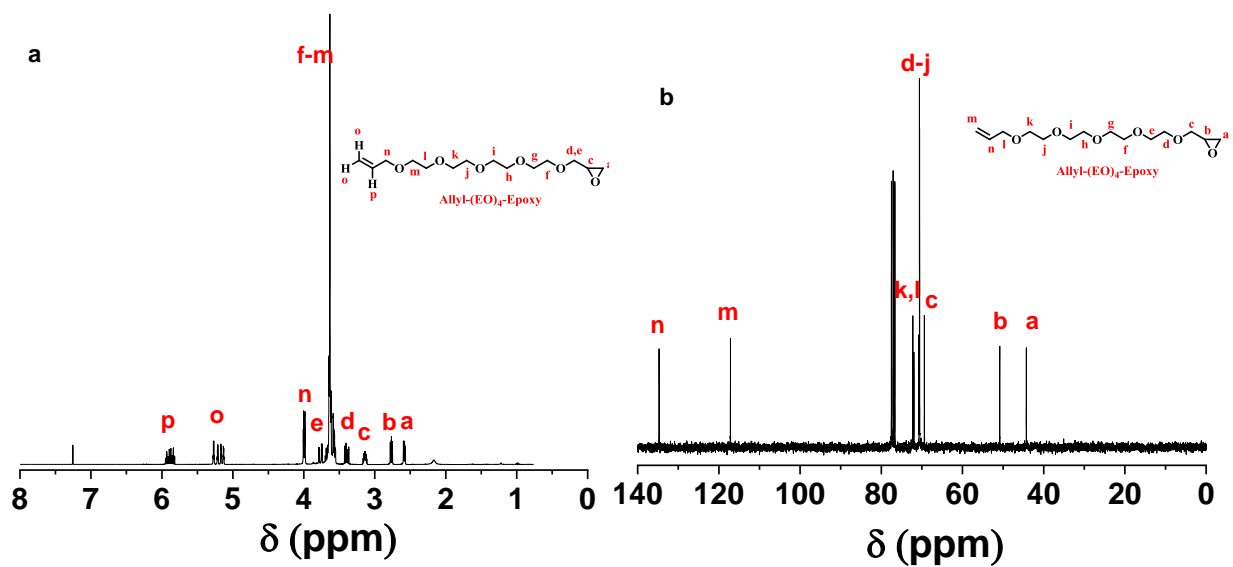


Figure B5. ^1H NMR (a) and ^{13}C NMR (b) spectra of Allyl-(EO) $_4$ -Epoxy in CDCl_3 .

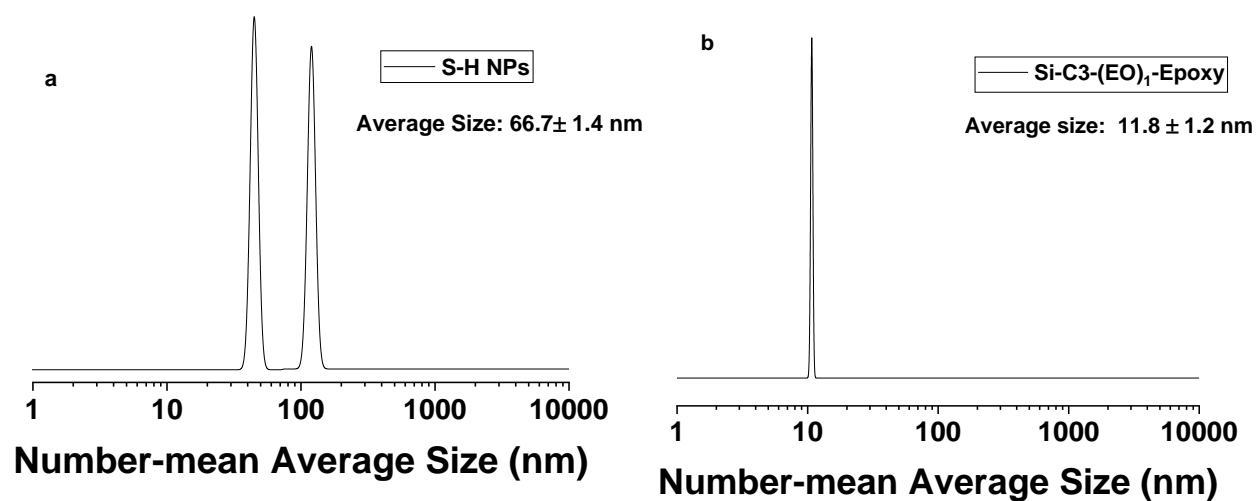


Figure B6. DLS analysis results of (a) Si-H NPs and (b) Si-C3-(EO)₁-Epoxy NPs. The nanoparticles are dispersed in distilled water with a concentration of 1 mg/g.

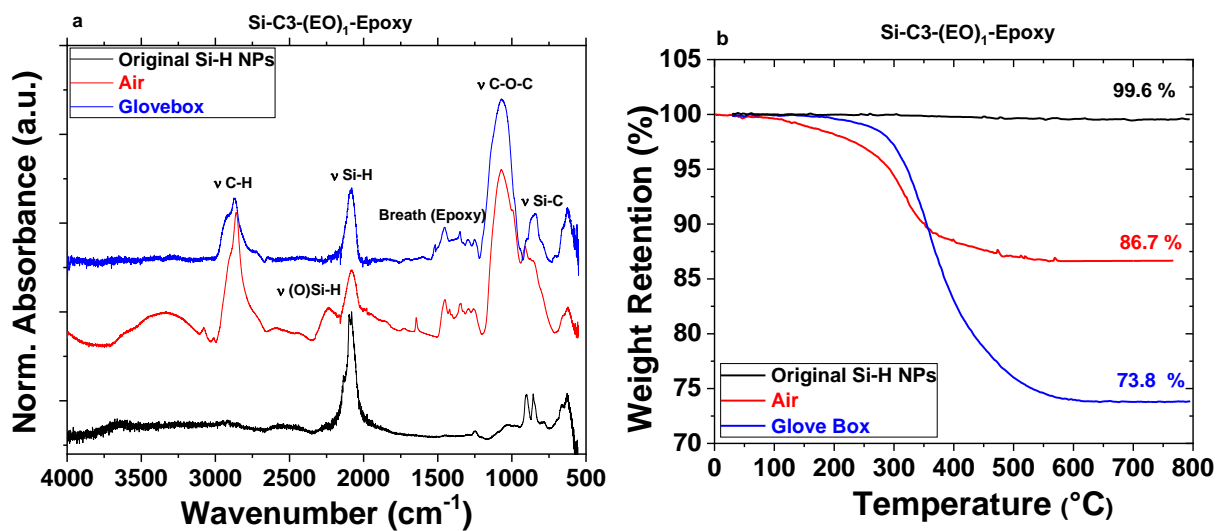


Figure B7. (a) FTIR-ATR spectra and (b) TGA curves of the Si-C3-(EO)₁-Epoxy NPs obtained by surface hydrosilylation conducted in air (red curves) and in the argon-filled glovebox (blue curves). The FTIR spectrum and TGA curve of original Si-H NPs are included as reference.

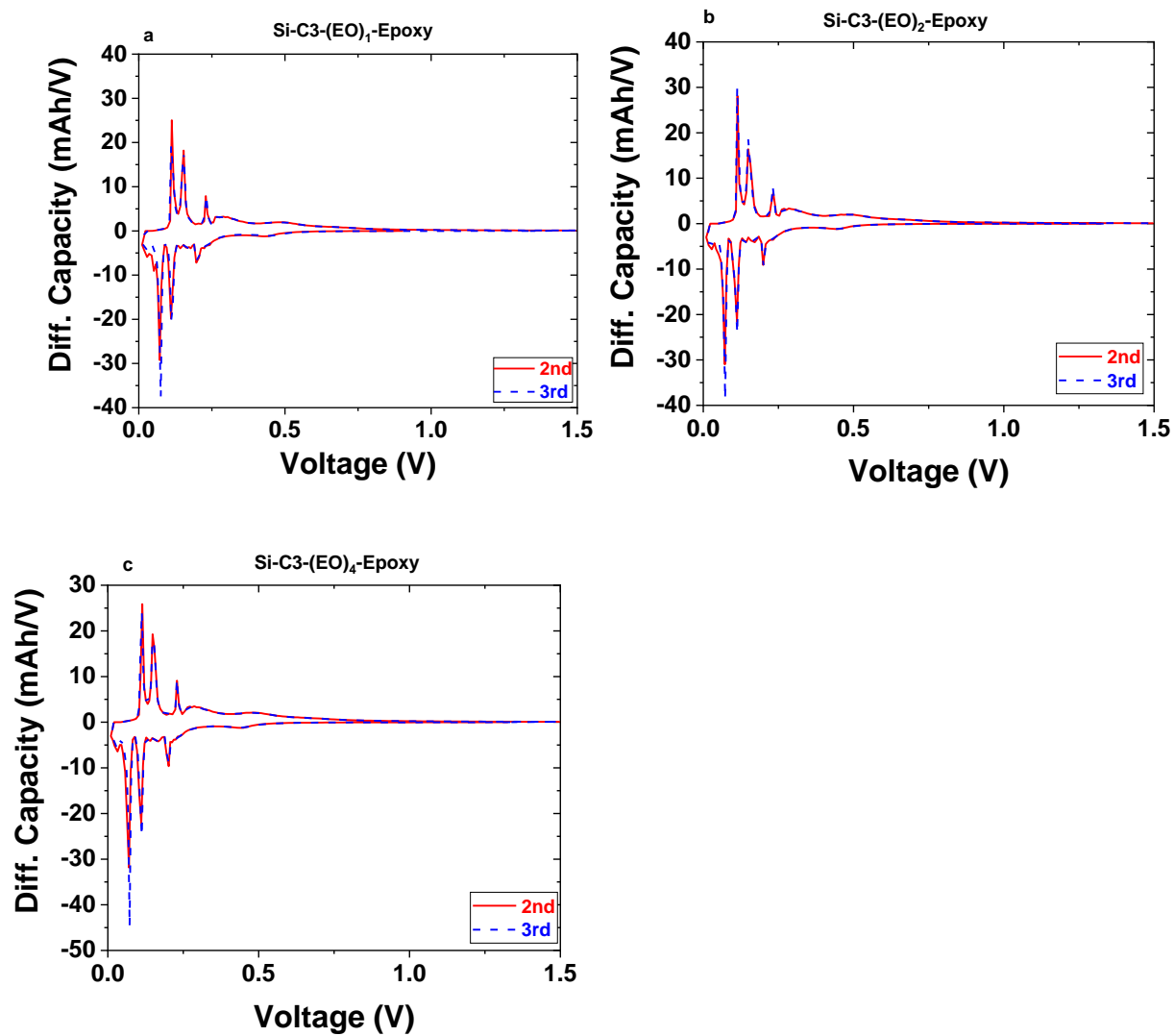


Figure B8. DQ/DV plots of the 2nd and 3rd C/20 formation cycle: (a) Si-C3-(EO)₁-Epoxy, (b) Si-C3-(EO)₂-Epoxy and (c) Si-C3-(EO)₄-Epoxy.

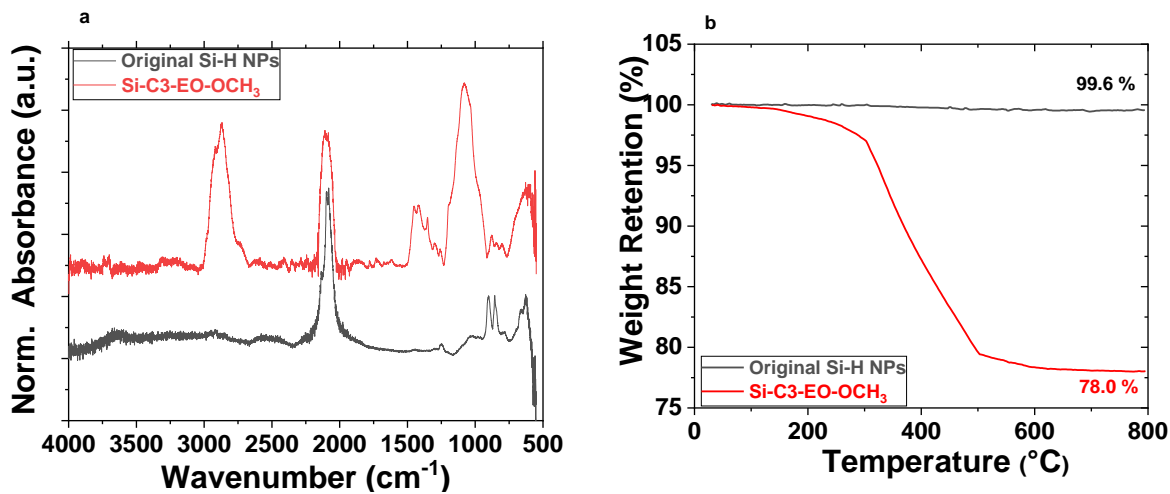


Figure B9. (a) FTIR spectrum and (b) TGA curve of the Si-C3-(EO)₁-OCH₃ NPs.

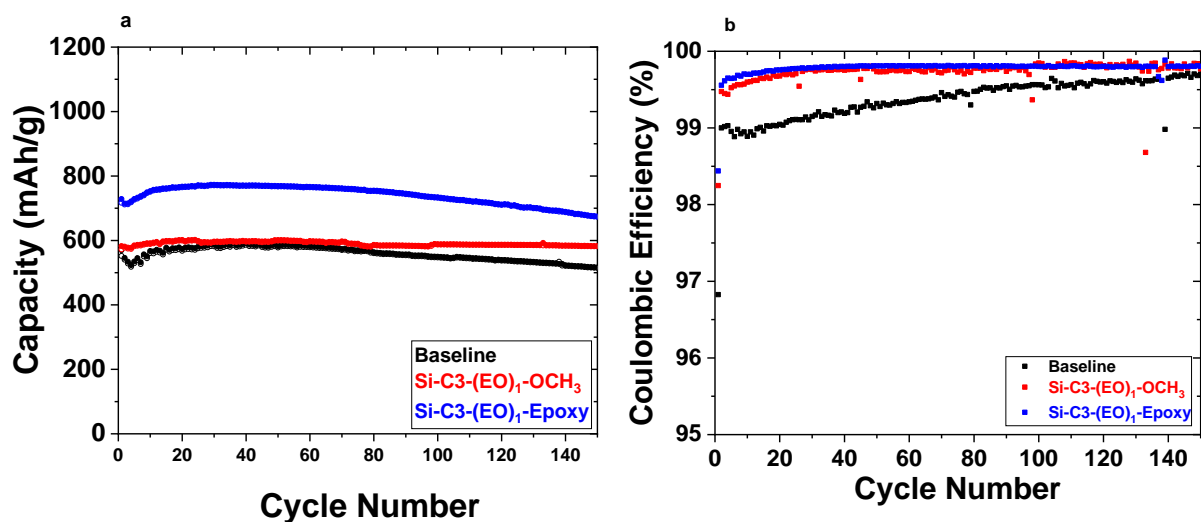


Figure B10. Comparison study of electrochemical performance of graphite/Si composite electrodes based on Si-C3-(EO)₁-Epoxy and Si-C3-(EO)₁-OCH₃ (Li metal as counter electrode) over 150 cycles at C/3 rate: (a) specific charge capacity (lithiation: solid sphere; delithiation: empty sphere) (b) the corresponding coulombic efficiency.

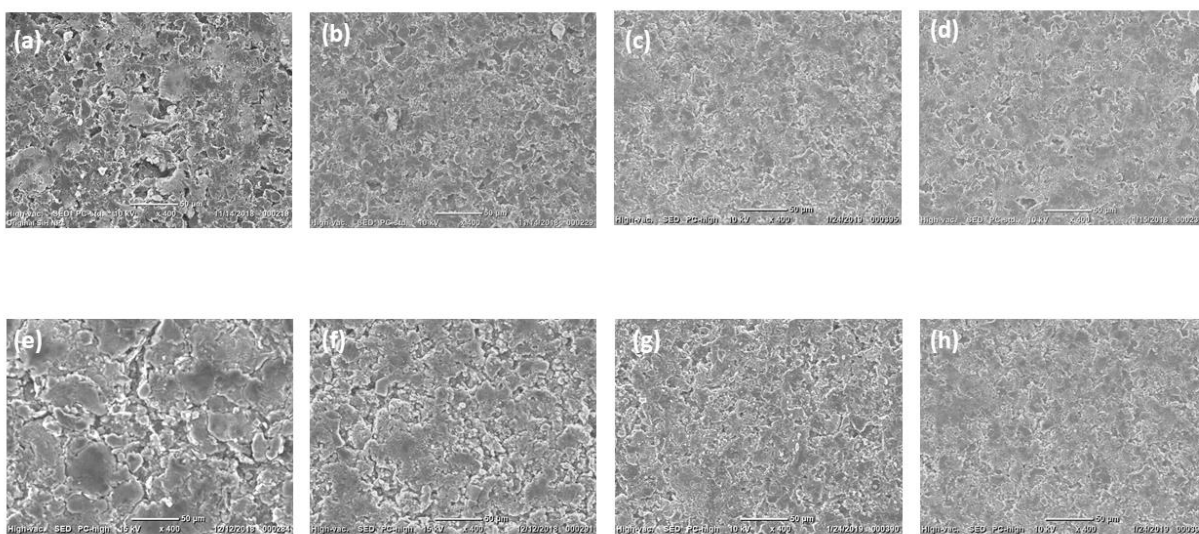


Figure B11. SEM images of the pristine electrodes (a: baseline, b: Si-C3-(EO)₁-Epoxy, c: Si-C3-(EO)₂-Epoxy and d: Si-C3-(EO)₄-Epoxy) and the cycled electrodes (e: baseline, f: Si-C3-(EO)₁-Epoxy, g: Si-C3-(EO)₂-Epoxy and h: Si-C3-(EO)₄-Epoxy).

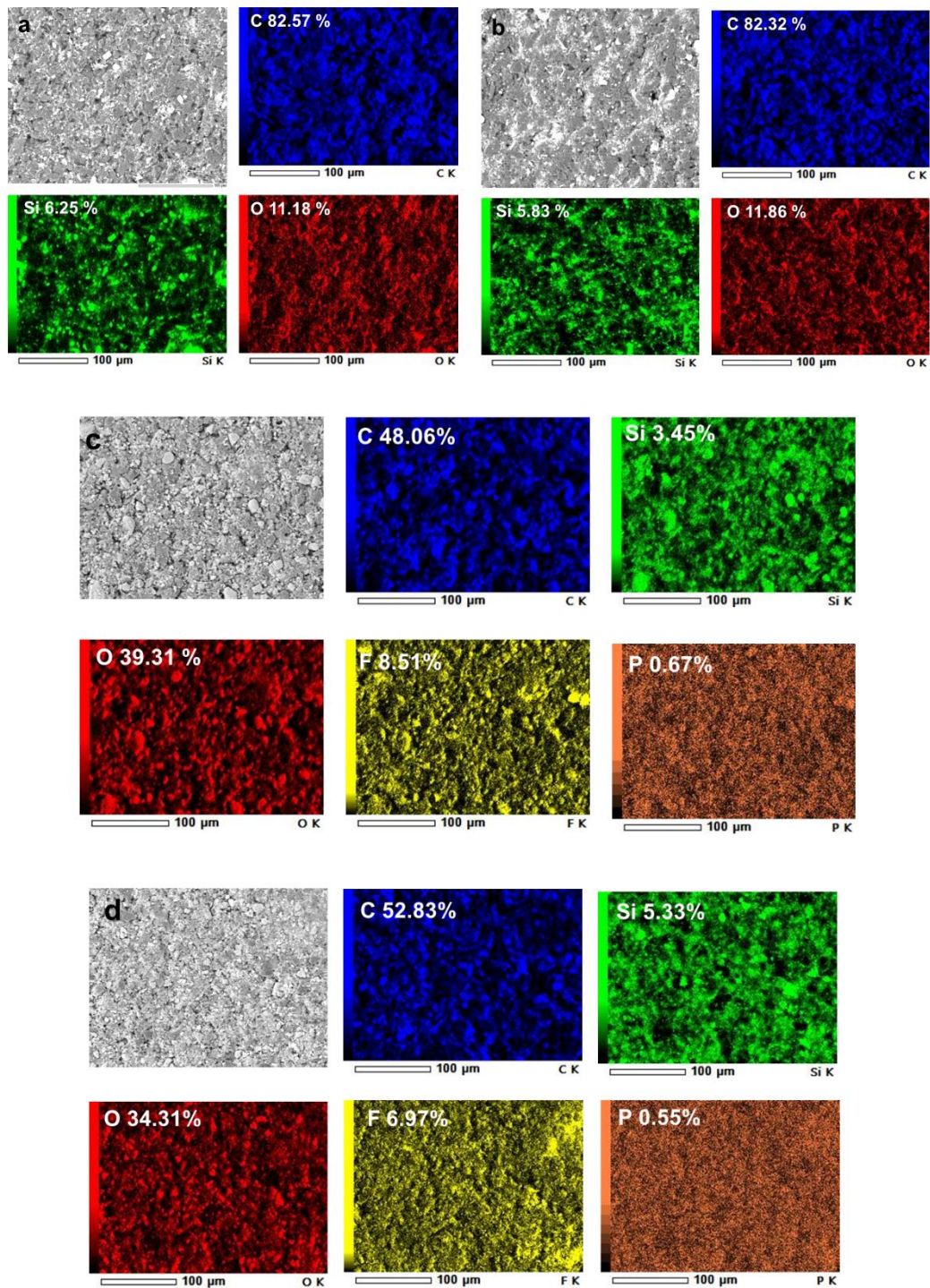


Figure B12. EDX elemental mapping of pristine electrodes (C, Si and O) (a: Si-C3-(EO)₁-Epoxy, and b: Si-C3-(EO)₄-Epoxy) and the cycled electrodes (C, Si, O, F and P) (c: Si-C3-(EO)₁-Epoxy, d: Si-C3-(EO)₄-Epoxy).

**Chapter 4. Sulfur-Containing Polymer Brush-Grafted Titanium Dioxide
Nanoparticles: Potential Processable High Refractive Index Hybrid Materials**

Abstract

This chapter presents a potential approach towards processable high refractive index (RI, n) materials. Polymers have advantages over other high-RI materials as they are light in weight and easy to process. However, the narrow RI range (1.3 – 1.7) of polymers limited their application in high RI industry. Two extensively used strategies to increase RI of polymers are (1) to increase intrinsic n by incorporating high molar refraction atoms or groups into the backbone or side chain of polymers and (2) to fabricate high RI nanocomposites by introducing high RI inorganic nanoparticles into polymer matrix. This work presents a combination of the two methods towards processable high RI materials. With high molar refraction and good compatibility with polymers, sulfur atom is incorporated into the side chain of styrenic and methacrylate-type polymers. The sulfur-containing polymers have higher refractive index than their sulfur-free counterparts. Then sulfur-containing polymer brush-grafted TiO₂ nanoparticles (Hairy NPs) were synthesized by surface-initiated atom transfer radical polymerization (SI-ATRP). The hairy NPs can form homogeneous dispersion in common organic solvents and can be processed into thin films. It is expected that the hairy NPs can exhibit tunable RI values by varying the ratio between the grafted polymer chains and inorganic core.

4.1 Introduction

Refractive index (RI, n) is a parameter describing how light propagates through a medium, compared with its travel in vacuum and is calculated as the quotient of light speed in vacuum and the phase velocity of light in a certain medium.¹ Processable materials with high refractive index are required for many applications in optical industry, including anti-reflective coating and photonic devices such as image sensors² and light-emitting diodes (LEDs).^{3,4} High RI polymers (HRIPs) are good candidates for these applications in that they are light in weight and are easy to process.⁵ Furthermore, most of the polymers have high mechanical strength. What limits the use of polymers in high RI industry is their narrow range of RIs, which is between 1.3-1.7 in UV-visible region. Great efforts have been made to increase intrinsic RIs of polymers. Lorentz-Lorenz equation qualitatively describes the correlation between RI and polarizability of a substance², as is shown in Equation 4.1:

$$\frac{n^2-1}{n^2+1} = \frac{4\pi}{3} \frac{\rho N_A}{M_w} \alpha \quad (\text{Equation 4.1})$$

where n is refractive index, ρ is density, N_A is Avogadro's number, M_w is molecular weight and α is polarizability. To better quantify such correlation, molar refraction $[R]$, where $[R] = \frac{4\pi}{3} N_A \alpha$ and molar volume V_M are introduced and equation (1) can be simplified into

$$\frac{n^2-1}{n^2+1} = \frac{[R]}{V_M} \quad (\text{Equation 4.2})$$

Then, the relation between RI and molecular property of the substance can be deduced by solving Equation 4.2 for n , yielding Equation 4.3, which indicates that n increases with increasing $[R]$ while decreases with increasing V_M .

$$n = \sqrt{\frac{1+[R]/V_M}{1-[R]/V_M}} \quad (\text{Equation 4.3})$$

Based on Lorentz-Lorenz equation, one feasible way to increase the RI value of a polymer is to introduce substituents with high $[R]$ and low V_M (high density). Sulfur atom, with its relatively high atomic polarizability, good chemical stability and adaptability to be incorporated into polymers, has been extensively used as RI enhancer in developing intrinsic high RI polymers.⁶ Ueda and coworkers conducted a series of researches on sulfur-rich polyimides.⁷⁻¹² They synthesized polyimides featuring phenyl thioether groups varying in sulfur content and confirmed that RIs of polymers increased with increasing sulfur content of repeating unit.⁷ They also incorporated sulfone and other sulfur-containing groups into the backbone of the polymer to increase RI.^{8, 11} Other sulfur-rich HRIPs, including thioether and pyridine-bridged aromatic polyimides,¹² sulfone and thioether containing polyamides,¹³ are also reported. Nevertheless, the intrinsic RIs of most of HRIPs are still in the range of 1.65-1.75 while any further efforts to increase the intrinsic RI of polymer will be at the cost of sacrificing other desired properties of the materials such as transparency and processability. Inorganic materials such as TiO₂ (anatase, $n = 2.45$, rutile, $n = 2.71$ at 500 nm)¹⁴, ZrO₂ ($n = 2.10$ at 500 nm)¹⁵, ZnS ($n = 2.36$ at 620 nm)¹⁶, silicon ($n = 4.3$ at 500 nm)¹⁷ usually have RIs (in the range of 2.0-5.0 in UV-visible region). However, they are usually rigid, fragile and have poor processability. The introduction of high RI inorganic nanoparticles into organic polymers to form nanocomposites stands out to be an alternative strategy to produce processable high RI materials by combining the advantages from both sides.¹⁸ ¹⁹ The nanocomposites are generally fabricated either by physically blending nanoparticles into the polymer matrix or chemically tethering the polymer chains onto the nanoparticles (“grafting to” method), whereas the latter method produces a more homogenous system due to the stronger interaction between the two components. Tao *et al.* prepared transparent polymer nanocomposites by grafting poly(glycidyl methacrylate) (PGMA) chains onto anatase TiO₂ nanoparticles via

alkyne-azide “click” chemistry. The highest RI of the nanocomposites reached 1.80 at 500 nm.²⁰ Xu and coworkers synthesized ZnS-polymer nanocomposites with the highest RI reaching 1.82 by copolymerization of different acrylic monomers in the presence of polymerizable-group-functionalized ZnS nanoparticles.¹⁶ It has been found that there is a linear dependency of nanocomposite’s RI on the volume fraction of inorganic and organic components. The RIs of the nanostructured organic-inorganic materials can be predicted by Equation 4.4:

$$\frac{n_c^2-1}{n_c^2+1} = \varphi_p \frac{n_p^2-1}{n_p^2+1} + (1 - \varphi_p) \frac{n_m^2-1}{n_m^2+1} \quad (\text{Equation 4.4})$$

where n_c , n_p and n_m are RIs of the nanocomposites, inorganic nanoparticles and polymer matrix, respectively and φ_p is the volume fraction of the nanoparticles.²¹ Tunable RIs can be achieved by adjusting the volume ratio between inorganic nanoparticles and polymer matrix.

In this work, we proposed a strategy towards processable high RI material by combining high RI sulfur-containing polymers with inorganic titanium dioxide (TiO₂) nanoparticles. Traditional sulfur-containing HRIPs are usually synthesized by Michael polyaddition or polycondensation reactions, where the molecular weight and polydispersity are not controllable. Herein, sulfur-containing styrenic and methacrylate-type monomers were designed, synthesized and polymerized by atom transfer radical polymerization (ATRP). The RI of the sulfur-containing styrenic polymer is around 1.68 while the RI of the methacrylate polymer is around 1.60, higher than the corresponding polystyrene ($n = 1.59$) and poly(methyl methacrylate) ($n = 1.49$), respectively. A “grafting from” method, where polymer brushes were grown from the surface of initiator-functionalized nanoparticles through surface-initiated ATRP (SI-ATRP), was employed to fabricate the sulfur-containing polymer brush-grafted TiO₂ NPs (hairy TiO₂ NPs). Compared with “grafting to” method, where polymers are made in advance, “grafting from” method has the advantage of making hairy NPs with higher grafting density as monomer molecules can diffuse

more easily to the propagating sites. Furthermore, the ratio between the inorganic nanoparticles and the grafted polymer chains can be adjusted by controlling the monomer conversion during polymerization to achieve tunable RI value. Nuclear magnetic resonance (NMR) spectroscopy, thermogravimetric analysis (TGA) and transition electron microscopy (TEM) were employed to characterize the hairy TiO₂ NPs. The hairy NPs show good dispersity in common organic solvents and have good film formation ability, exhibiting high potential to be used as processable high RI materials.

4.2 Experimental Section

4.2.1 Materials

15 wt % aqueous dispersion of anatase titanium dioxide (TiO₂) nanoparticles with a vendor-claimed diameter between 5-15 nm was purchased from US Research Nanomaterials, Inc. CuBr (98%, Aldrich) was stirred in glacial acetic acid overnight, filtered, and washed with absolute ethanol and diethyl ether. The purified CuBr was dried under vacuum. Ethyl 2-bromoisobutyrate (EBiB, 98%, Aldrich) was dried with CaH₂ and distilled under reduced pressure. Hexamethylated tris(2-aminoethyl)amine (Me₆-TREN) was synthesized as described in the literature.²² Dry tetrahydrofuran (THF) was obtained by adding sodium and benzophenone to THF and heating solvent at reflux under N₂ flow for several hours until it turns deep blue in color. All other chemical reagents were purchased from either Sigma Aldrich or Fisher/Acros and used without further purification.

4.2.2 General Characterization.

¹H NMR spectra were recorded on a Varian Mercury 500 NMR spectrometer. Size exclusion chromatography (SEC) of the sulfur-containing polymers and free polymers formed in the

synthesis of hairy NPs was carried out at ambient temperature using PL-GPC 20 (an integrated SEC system from Polymer Laboratories, Inc.) with a refractive index detector, one PLgel 5 μm guard column (50×7.5 mm), and two PLgel 5 μm mixed-C columns (each 300×7.5 mm, linear range of molecular weight from 200 to 2 000 000 Da). THF was used as the solvent, and the flow rate was 1.0 mL/min. Narrow-disperse polystyrene standards were used to calibrate the system. The data were processed using Cirrus GPC/SEC software (Polymer Laboratories, Inc.). Thermogravimetric analysis (TGA) was performed at a heating rate of 20 $^{\circ}\text{C}/\text{min}$ from room temperature to 800 $^{\circ}\text{C}$ using the NETZSCH STA 449 F3 Jupiter for simultaneous thermogravimetry-differential scanning calorimetry (STA/TG-DSC). The polymers and nanoparticles were dried at 45 $^{\circ}\text{C}$ in vacuum for > 5 h prior to analysis. Transmission electron microscopy (TEM) was performed on a FEI Tecnai F20ST scanning/transmission electron microscopy ((S)TEM). Samples of hairy NPs were drop-cast from dispersions in tetrahydrofuran (THF) with a concentration of ~ 1 mg/mL onto a carbon-coated, copper TEM grid using a glass pipette and the solvent was evaporate at ambient conditions. Dynamic light scattering (DLS) measurements of dispersions of the initiator-functionalized TiO_2 NPs in *N,N*-dimethylformamide (DMF) (1mg/g) were conducted using a Brookhaven Instruments BI-200SM goniometer equipped with a PCI BI-9000AT digital correlator and a solid-state laser (model 25-LHP-928-249, $\lambda = 633$ nm) at a scattering angle of 90° . The dispersions were added into borosilicate glass cuvettes and the cuvettes were sealed with PE stoppers. The cuvette was placed in the holder of the light scattering instrument. The refractive indices of sulfur-containing polymers were measured on a Gaertner Scientific Corporation 18910AK laser ellipsometer ($\lambda = 623.8$ nm, incidental angle = 60°). For each sample, the thicknesses and RI values of 10 random spots on the thin film were measured. The samples were made by spinning coating 1 wt % of polymer chloroform solutions

on silicon wafers at a spin coating rate of 11,000 rpm for 60 s using a Specialty Coating System, INC P-600 spin coater.

4.2.3 Synthesis of Sulfur-Containing Polymers

4.2.3.1 Synthesis of Sulfur-Containing Styrenic Monomer

Synthesis of (phenyl(4-vinylbenzyl)sulfane) (S1S) To a solution of NaH (1.440 g, 60% in oil, 0.036 mol) in THF (20 mL), benzenethiol (3.250 g, 0.029 mol) was added dropwise by a disposable syringe. The resulting white mixture was stirred under room temperature for 30 min. Vinylbenzyl chloride (VBC, 5.069 g, 90%, 0.033 mol) in THF (25 mL) was then added dropwise to the reaction mixture. The color of the resulting mixture immediately turned from white to orange after VBC was added. The reaction mixture was then stirred overnight under room temperature. Thin-layer chromatography (TLC) and ^1H NMR spectroscopy were employed to monitor the reaction. Upon completion, the reaction mixture was filtered and THF was removed on a rotary evaporator. Distilled water (DI H_2O) (20 mL) was added into the reaction mixture and the mixture was poured into a separatory funnel and was extracted with CH_2Cl_2 (20 mL). The extraction was repeated for 3 times. The combined organic fractions were washed two times with DI H_2O (30 mL) and were dried with anhydrous Na_2SO_4 overnight. The solvents were removed on a rotary evaporator, and column chromatography (1:1 CH_2Cl_2 /hexane) was employed for purification. 5.080 g pure product as white powder was obtained after purification (76.0 % yield). ^1H NMR (CDCl_3) δ (ppm): 7.31 – 7.36 (m, 4H, aromatic), 7.24 – 7.29 (m, 4H, aromatic), 7.17 – 7.22 (m, 1H, aromatic), 6.70 (dd, 1H, $\text{CH}_2=\text{CH}-$), 5.74 (dd, 1H, $\text{CHH}=\text{CH}-$), 5.24 (dd, 1H, $\text{CHH}=\text{CH}-$), 4.12 (s, 2H, $(\text{CH})_2\text{C}-\text{CH}_2$). ^{13}C NMR (CDCl_3) δ (ppm): 137.09, 136.53, 136.43 (aromatic), 136.26 (CH_2CHCH), 129.92, 128.99, 126.35 (aromatic), 113.75 (CH_2CH), 38.87

(CHCS). HRMS (DART-TOF): m/z calc. 226.08; $[M^+]$: 226.08; found 226.08073; mass error: 3.94 ppm.

4.2.3.2 Synthesis of Sulfur-Containing Methacrylate Monomer

Synthesis of (S-phenyl 2-methylprop-2-enethioate) (M1S) To a solution of benzenethiol (1.109 g, 0.010 mol) in dry THF (40 mL), triethylamine (1.248 g, 0.012 mol) was added under nitrogen. Then, the solution was cooled at 0 °C, and a solution of methacryloyl chloride (1.113 g, 0.011 mol) in dry THF (20 mL) was added dropwise. After the solution was stirred for 23 h at room temperature, 1 M HCl aqueous solution (5 mL) was added into the reactor to quench the reaction. THF was removed on the rotary evaporator and the mixture was then diluted with DI H₂O (50 mL) and was extracted three times with CH₂Cl₂ (30 mL per portion). The organic phase was dried over anhydrous Na₂SO₄, filtered, and concentrated. The crude product was purified by vacuum distillation with hydroquinone as inhibitor to yield a colorless and transparent liquid with a yield of 10.9%. ¹H NMR (CDCl₃) δ (ppm): 7.40 – 7.47 (m, 5H, aromatic), 6.22 (dd, 1H, CHH=C), 5.70 (dd, 1H, CHH=C), 2.02 (dd, 3H, CH₃-C). ¹³C NMR (CDCl₃) δ (ppm): 191.46 (C=O), 143.57 (C=CH₂), 134.89 (aromatic), 129.13 (C=CH₂), 127.65, 123.79 (aromatic), 18.36 (CCH₃).

4.2.4 Synthesis of sulfur-containing polymer by supplemental activator and reducing agent atom transfer radical polymerization (SARA-ATRP)

4.2.4.1 Synthesis of Sulfur-Containing Styrenic Polymer PS1S

S1S (2.011 g, 8.885 mmol) was dissolved in anisole (3.133 g) and the resulting mixture was sonicated for 10 min until a homogeneous solution was made. Then initiator EBiB stock solution in anisole (0.067 g, 82.38 mg/g, 0.028 mmol), CuBr powder (3.0 mg, 0.021 mmol), Cu(0) powder (4.0 mg, 0.019 mmol), Me₆-TREN (8.294 mg, 0.036 mmol) and ¹H NMR inner standard trioxane (20.3 mg, 0.225 mmol) were added into the resulting mixture. After degassed by three

freeze–pump–thaw cycles, the flask was placed in an oil bath with a preset temperature of 105 °C. ¹H NMR spectroscopy was employed to monitor the progress of polymerization. After 22 h, the flask was removed from the oil bath and opened to air. The reaction mixture was diluted with THF and was passed through a short column of silica gel (bottom)/activated basic aluminum oxide (Al₂O₃) (top) (2/1, v/v). The polymer was then precipitated by adding the reaction mixture dropwise in 100 mL methanol. This process was repeated for another two times. Degree of polymerization (DP) was 83, calculated from the ¹H NMR spectrum of the sample taken from the reaction mixture at the beginning and at the end of the polymerization using the integrals of the peaks at 5.24 ppm (CHH=CH– from S1S) and 5.18 – 5.19 ppm (-O-CH₂ from trioxane) and the feed ratio between the monomer and initiator. *M*_{n,SEC} of the polymer was 20.4 KDa with a PDI of 1.24. This batch of polymer was designated as PS1S-20.4k. Using similar method, PS1S-9.0k and PS1S-31.8k were also synthesized.

4.2.4.2 Synthesis of Sulfur-Containing Methacryoyl Polymer PM1S

To a two-necked 25 mL round-bottom flask equipped with a stir bar, M1S (1.785 g, 10.014 mmol), initiator EBiB stock solution in anisole (0.128 g, 82.38 mg/g , 0.054 mmol), CuBr powder (4.0 mg, 0.028 mmol), Cu(0) powder (2.0 mg, 0.031 mmol), Me₆-TREN (13.2 mg, 0.057 mmol), ¹H NMR inner standard trioxane (20.4 mg, 0.226 mmol) and anisole (2.000 g) were mixed. The resulting mixture was then subject to three cycles of freeze–pump–thaw. After that, the flask was placed in an oil bath with a preset temperature of 95 °C. Polymerization was monitored by ¹H NMR spectroscopy. After 25 h, the polymerization was quenched by transferring the flask into ice bath and bubbling the reaction mixture with air. Then the mixture was diluted with THF (5 mL) and was passed through a short column of silica gel (bottom)/activated basic Al₂O₃ (top) (2/1, v/v). Unreacted monomer and other compounds were removed by precipitation method as described in

synthesis of PS1S. DP was 139, determined from the ^1H NMR spectra of the samples taken from the reaction mixture at the beginning and at the end of the polymerization using the integrals of the peaks at 5.70 ppm ($\text{CHH}=\text{CH}-$ from M1S) and 5.18 – 5.19 ppm ($-\text{O}-\text{CH}_2$ from trioxane) and the feed ratio between the monomer and initiator. $M_{n,\text{SEC}}$ of the polymer was 23.2 KDa with a PDI of 1.29. The polymer was named as PM1S-23.2k.

4.2.5 Synthesis of Sulfur-Containing Polymer-Grafted TiO_2 NPs

4.2.5.1 Synthesis of ATRP Initiator-Functionalized TiO_2 NPs

Synthesis of 2-bromo-N-(3,4-dihydroxyphenethyl)-2-methylpropanamide (catechol-terminated ATRP initiator) $\text{Na}_2\text{B}_4\text{O}_7 \cdot 10\text{H}_2\text{O}$ (3.852 g, 0.010 mol) was added into a 250 mL three-necked round bottom flask, followed by the addition of 100 mL DI H_2O . Then the solution was bubbled with N_2 for 30 min. After that, dopamine hydrochloride (1.924 g, 0.010 mol) was added into the solution. The flask was then immersed into an ice bath, and 2-bromo-2 methylpropionyl bromide (2.604 g, 0.011 mol) was injected dropwise using a disposable syringe. The pH of the reaction mixture was then adjusted to 9-10 using Na_2CO_3 . The mixture was stirred in dark at room temperature. After 23 h of reaction, the pH of the reaction mixture was adjusted to 2 using 6 M HCl solution (20 mL). Then the mixture was extracted with ethyl acetate (100 ml) for 3 times. After that, the combined ethyl acetate extracts were dried over anhydrous Na_2SO_4 overnight. After filtration and concentration, a brown viscous oil was obtained. Yield: 1.802 g, 59.6 %.

Original $\text{TiO}_2/\text{DI H}_2\text{O}$ dispersion (2.133 g, 15 wt%, containing 0.320 g TiO_2 NPs) was weighed in a 25 mL two-necked round bottom flask equipped with a stir bar and was diluted with DMF (3 mL). The flask was then bubbled with N_2 for 10 min. Catechol-terminated ATRP initiator (0.501 g, 1.66 mmol) was weighed in a vial, followed by the addition of DMF (2 mL) to form a solution. This initiator solution was added into the flask containing TiO_2 NPs dispersion dropwise.

The reaction mixture was stirred in dark at room temperature overnight. After 48 h of reaction, the initiator NPs were isolated by ultracentrifugation (Beckman Optima L-90k Ultracentrifuge with type 60 Ti rotor, 35,000 rpm, 4 °C, 1 h). The collected NPs were redispersed in DMF and isolated again by ultracentrifugation (35,000 rpm, 4 °C, 1 h). This washing process was repeated a total of four times. Then the purified initiator NPs (designated as INP-1) were redispersed in anisole. An aliquot of the NP dispersion (0.100 g) was taken out and dried in a small vial under high vacuum over 5 h. The mass of the initiator NPs was 1.83 mg; thus, the concentration of the initiator NPs in the dispersion was 18.3 mg/g solution. Number-averaged dimeters in DMF measured by DLS: 19.2 ± 0.6 nm. Using the similar approach, INP-2 were also obtained with a concentration of 27.0 mg/g solution (Number-averaged dimeters in DMF: 20.6 ± 0.8 nm)

4.2.5.2 Synthesis of PS1S Brush-Grafted TiO₂ NPs (TiO₂ Hairy NPs)

Described here is the synthesis of PS1S brush-grafted TiO₂ Nanoparticles with free PS1S $M_{n,SEC}$ of 31.5 kDa (PS1S-HNP-31.5k) using INP-1 via SI-ATRP. S1S monomer (2.510 g, 11.090 mmol) was mixed with INP-1 dispersion in anisole (2.747 g, 18.2 mg/g dispersion, an equivalence of 50 mg initiator NPs) in a vial. Then this mixture was sonicated for 15 min (Fisher Scientific Model B200 Ultrasonic Cleaner) until a translucent dispersion was formed (dispersion 1). After that, to a 25 mL two-necked round bottom flask equipped with a stir bar, CuBr powder (4.8 mg, 0.033 mmol), Cu(0) powder (2.3 mg, 0.036 mmol), free initiator EBiB (4.4 mg, 0.023 mmol) and ¹H NMR inner standard trioxane (11.6 mg, 0.129 mmol) were added, followed by the addition of the dispersion 1. After degassed by two freeze–pump–thaw cycles, Me₆-TREN (15.0 mg, 0.065 mmol) was added into the mixture through a degassed microsyringe. Then one more round of freeze-pump-thaw was performed before the flask was placed in an oil bath with a preset temperature of 105 °C. ¹H NMR was employed to monitor the progress of polymerization. After

the reaction proceeded for 19 h, the flask was removed from the oil bath and opened to air. The reaction mixture was diluted with THF. The particles were isolated by centrifugation (35,000 rpm, 1h). This washing process was repeated for another three times. A portion of the supernatant liquid from the first cycle was passed through a short column of silica gel (bottom)/activated basic aluminum oxide (top) (2/1, v/v). The molecular weight of the free polymer was 31.5 kDa, with PDI of 1.23, calculated from the ^1H NMR spectra of the samples taken from the reaction mixture at the beginning and at the end of the polymerization using the integrals of the peaks at 5.18–5.22 ppm ($-\text{CH}=\text{CH}_2$ from S1S) and 5.18 – 5.19 ppm ($-\text{O}-\text{CH}_2$ from trioxane), the conversion was 29.7 %. Using the same method, PS1S-HNP-11.8k, PS1S-HNP-22.6k and PS1S-HNP-43.3k were synthesized from INP-1. PM1S-HNP-25.5k was synthesized using similar procedure with a polymerization temperature of 95 °C from INP-2.

4.2.6 Thin Film Preparation

4.2.6.1 Substrate Supported Thin Film of Polymers and Hairy Nanoparticles

Spin coating was used to make thin films of both polymers and hairy nanoparticles on glass substrates. The substrates were first immersed into a fresh made piranha solution, which is a mixture of concentrated sulfuric acid (H_2SO_4 , 98 %) and hydrogen peroxide (H_2O_2 , 30 % aqueous solution) with a volume ratio of 3:1, to get rid of all the organic residue and were rinsed with DI H_2O prior to use. The thin films were obtained by spin coating 1 wt % sample solution (for free polymers, chloroform was used as the solvent; for hairy NPs, THF was used as the solvent) onto the substrate at a spin coating rate of 11,000 rpm for 60 s.

4.2.6.2 Free-Standing Films of PS1S and PM1S

Thin films of PS1S and PM1S were spin coated on glass substrates from 1 wt % chloroform solutions of the corresponding polymers. Then the substrate-supported thin films were put into a

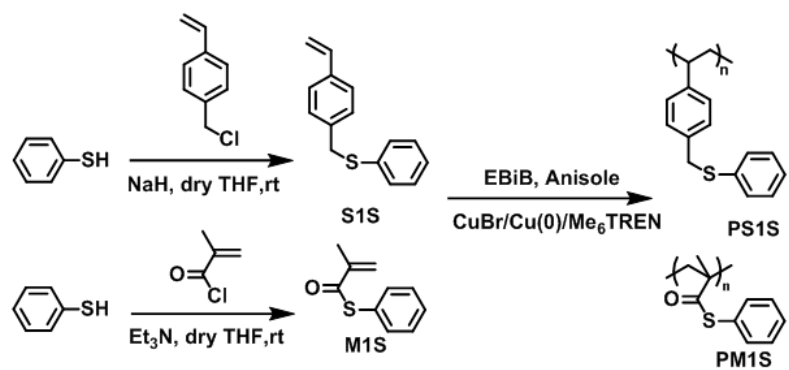
PTFE centrifuge tube with a stir bar and etching solution (11 mL 10 wt % HF water solution) in it. The PTFE centrifuge tube was preset in an ice bath. Once the glass was etched by HF, the reaction was quenched by adding $\text{Ca}(\text{OH})_2$ saturated solution into the tube until the pH of the reaction mixture was above 6. The freestanding film was taken out of the tube by a tweezer.

4.3 Results and Discussion

4.3.1 Synthesis and Characterization of Sulfur-Containing Polymer PS1S and PM1S

4.3.1.1 Synthesis and Characterization of PS1S

Sulfur-containing styrenic monomer phenyl(4-vinylbenzyl)sulfane (S1S) was synthesized via the reaction between 4-vinylbenzylchloride and thiophenol with the presence of NaH (Scheme 4.1). The function of NaH is to deprotonate thiophenol so that it can react with 4-vinylbenzyl chloride via nucleophilic substitution. The ^1H NMR and ^{13}C NMR (Figure 4.1) confirmed the structure of S1S. Supplemental activator and reducing agent-atom transfer radical polymerization (SARA-ATRP) was employed to polymerize the S1S. ATRP is based on the mechanism of transition metal-mediated atom transfer radical addition. Cu (0) and CuBr powder of equal molar ratio were added into the polymerization system. Copper powder acted as a supplemental activator (SA) other than CuBr and the reducing agent (RA) of Cu (II) generated during ATRP to reproduce Cu (I).²³ The polymerization was quenched after a desired monomer conversion was reached. Then the reaction mixture was passed through a short silica gel (bottom) /basic Al_2O_3 (top) column to get rid of copper salt. Unreacted monomer and other compounds were removed by repetitive precipitation/redissolution method. ^1H NMR spectrum of the polymer is shown in Figure 4.2b; the disappearance of the peaks of vinyl groups near 5.00 – 6.00 ppm indicated that the monomer



Scheme 4.1. Synthesis of sulfur-containing monomer S1S and M1S and synthesis of PS1S and PM1S by SARA-ATRP.

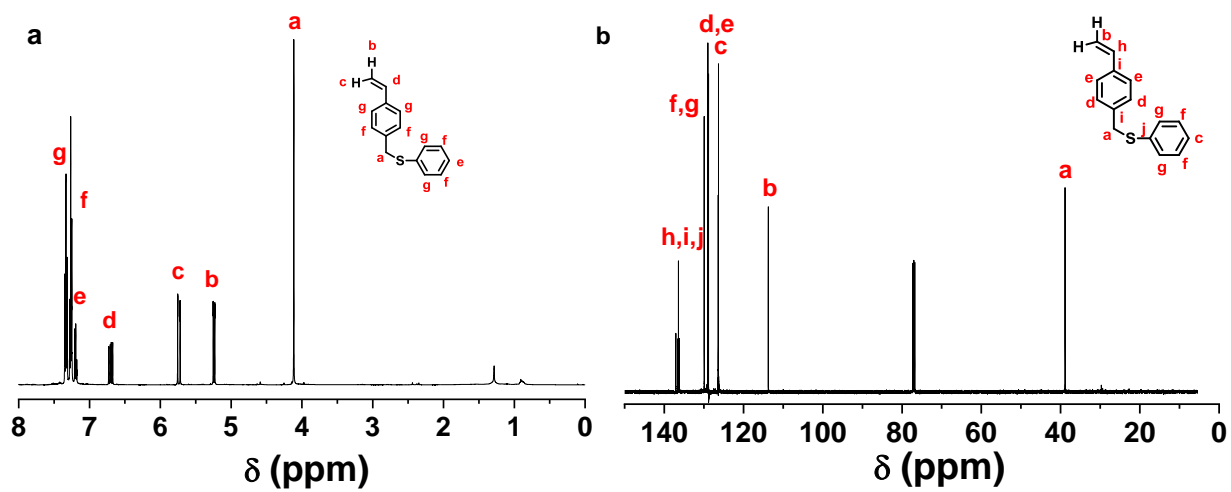


Figure 4.1. ^1H NMR (a) and ^{13}C NMR (b) spectrum of S1S in CDCl_3 .

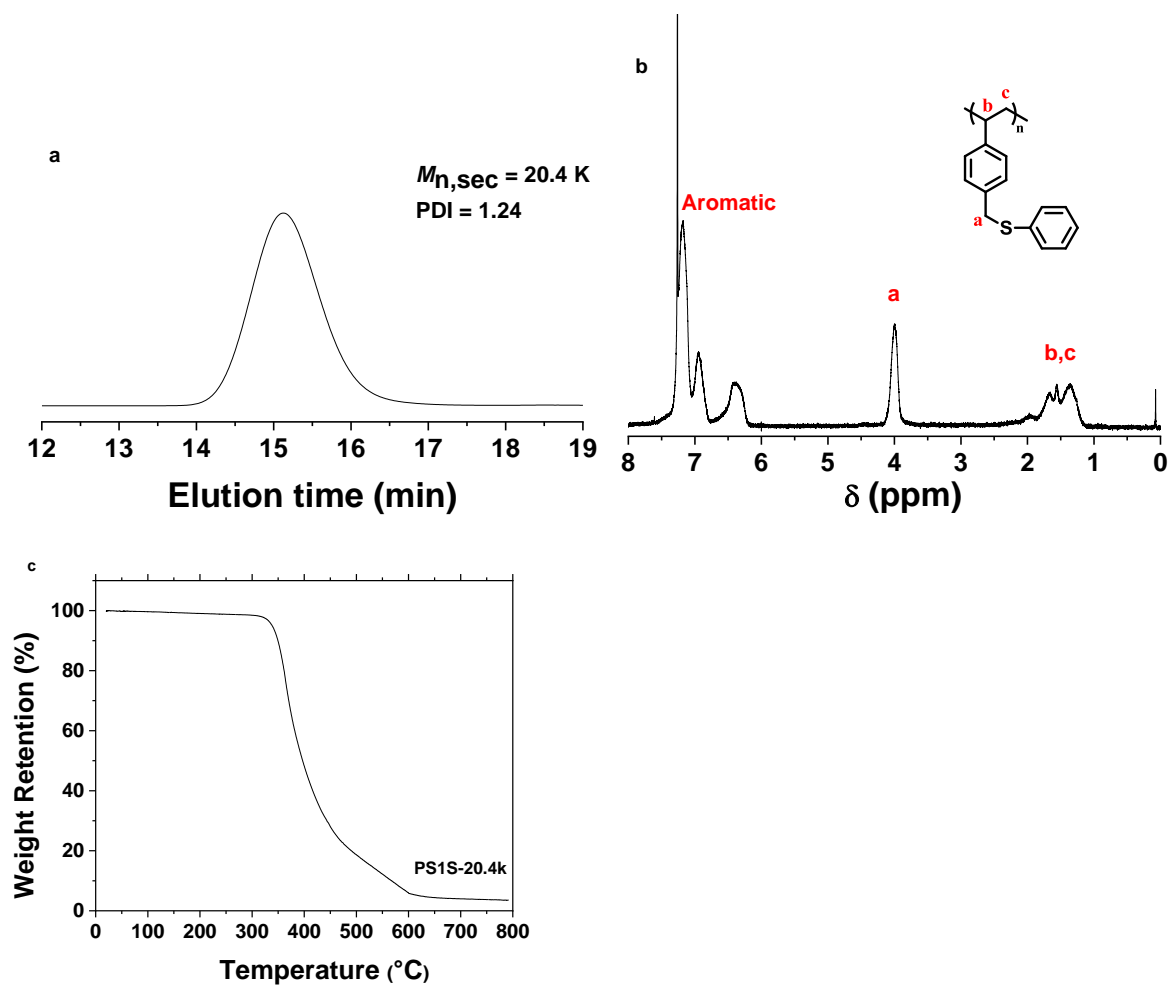


Figure 4.2. Characterization data of PS1S-20.4k: SEC trace (a), ^1H NMR spectrum in CDCl_3 (b), and TGA curve (c). The TGA analysis was performed in air at a heating rate of $20 \text{ }^{\circ}\text{C}/\text{min}$ from room temperature to $800 \text{ }^{\circ}\text{C}$.

was completely removed. Degree of polymerization (DP) was calculated as a product of the monomer conversion, determined by ^1H NMR, and the ratio [monomer]:[initiator]. Molecular weight and PDI were characterized by size exclusion chromatography (SEC). Thermal properties of PS1S was studied by TGA. Thermal decomposition of PS1S starts at near 310 °C. A slight slope change in the decomposition plot around 450 °C signifies a second phase of decomposition, which is probably the break-down of S-C bond.²⁴ The polymer is completely decomposed by 600 °C (Figure 4.2c). A total of three PS1S samples were synthesized, as summarized in table 4.1.

4.3.1.2 Synthesis and Characterization of PM1S

Monomer M1S was synthesized via the substitution reaction between benzenethiol and methacryloyl chloride under basic condition. ^1H NMR and ^{13}C NMR (Figure 4.3) spectra of the product in CDCl_3 confirmed the structure. PM1S was successfully made by SARA-ATRP. The polymer was isolated from the monomer by precipitation in methanol. ^1H NMR spectrum of PM1S is shown in Figure 4.4 b. Peaks between 1.2 ppm and 2.5 ppm signify the protons in backbone and the peaks between 7.3 ppm and 7.5 ppm refer to the protons in aromatic ring. The conversion of the monomer is 78.1%, determined by NMR analysis and DP was 139. The M_n of PM1S-1 is 23.2 KDa with a PDI of 1.29, characterized by GPC (Figure 4.4a). TGA analysis of the polymer shows that the onset temperature of thermal decomposition of PM1S is near 250 °C and then the decomposition is divided into two stages, a fast stage in the temperature between 250 °C and 400 °C and a slow stage above 400 °C. The decomposition trend is similar to that of PS1S, where the slow stage above 400 °C might be attributed to the decomposition of S-C bonds. The decomposition finally stabilizes at above 500 °C with 2.3 % residue (Figure 4.4c).

Table 4.1. Molecular weight and polydispersity, monomer conversion and calculated DP of PS1Ss

Sample	$M_{n,SEC}$(KDa), PDI^a	Conversion (%), DP^b
PS1S-9.0k	9.0, 1.21	18.8, 38
PS1S-20.4k	20.4, 1.24	28.2, 83
PS1S-31.8k	31.8, 1.28	41.3, 142

a: determined by GPC; b: conversion determined by NMR spectroscopy; b: DP = conversion × feed ratio ([monomer]:[initiator])

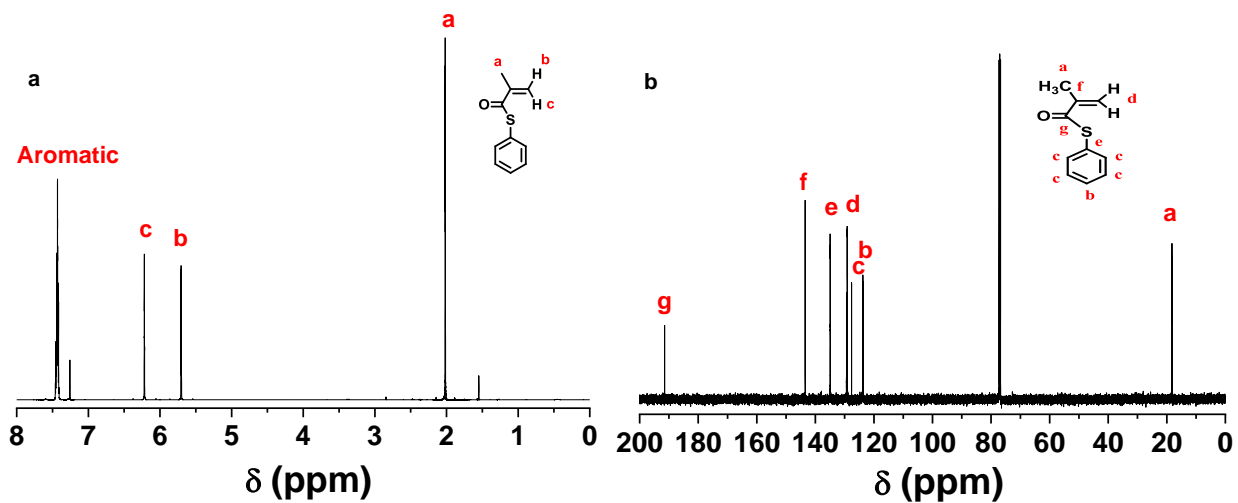


Figure 4.3. ^1H NMR (a) and ^{13}C NMR (b) spectrum of MIS in CDCl_3 .

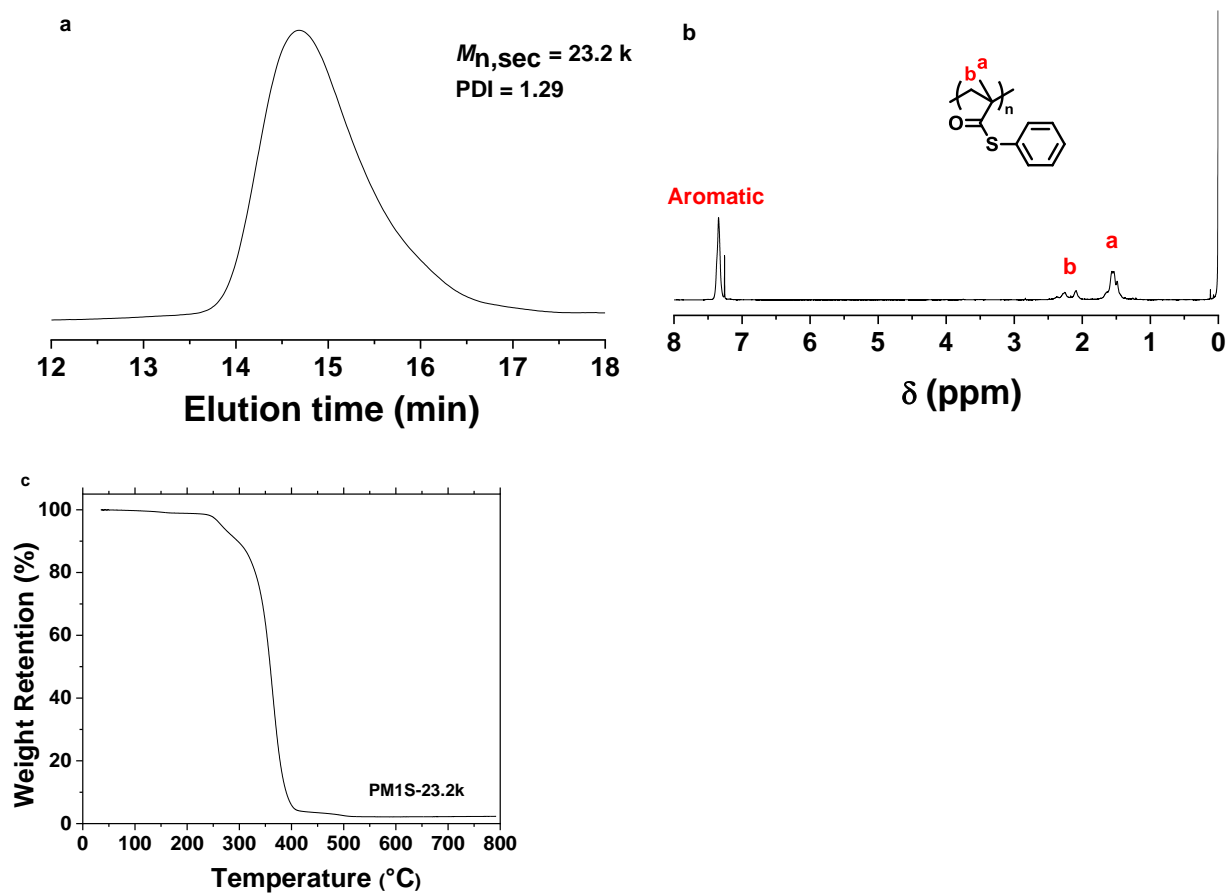


Figure 4.4. Characterization data of PM1S-23.2k: SEC trace (a), ^1H NMR spectrum in CDCl_3 (b), and TGA curve (c). The TGA analysis was performed in air at a heating rate of $20 \text{ }^\circ\text{C}/\text{min}$ from room temperature to $800 \text{ }^\circ\text{C}$.

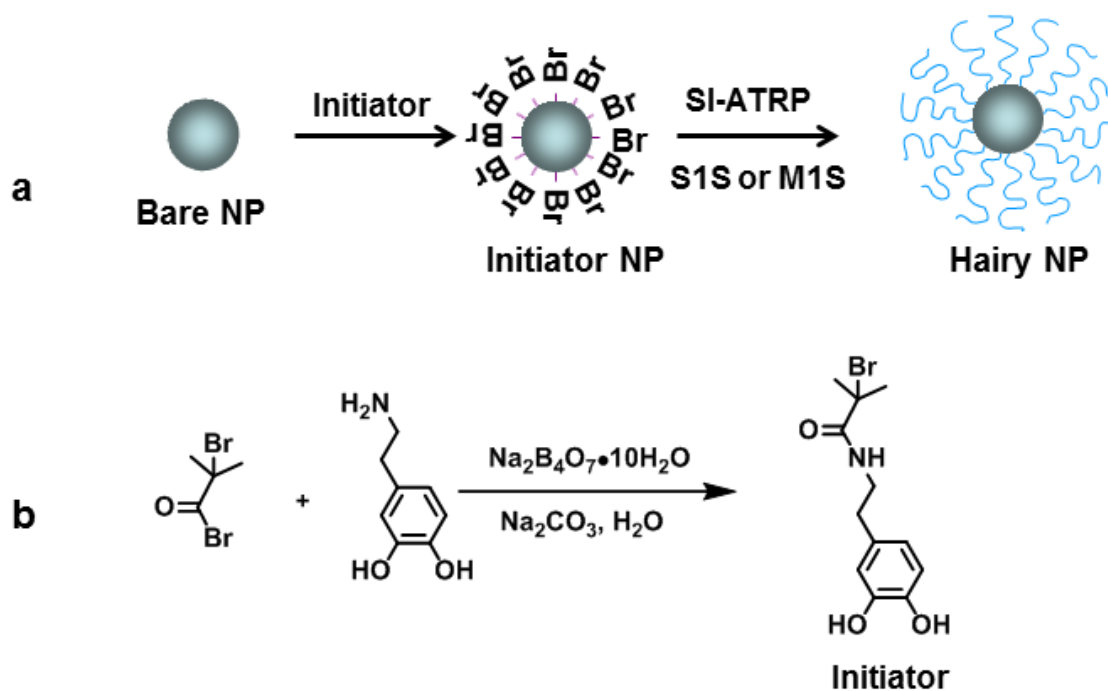
4.3.2 Synthesis and Characterization of Sulfur-Containing Polymer-Grafted TiO₂ NPs

4.3.2.1 Synthesis of ATRP Initiator-Functionalized TiO₂ NPs

Catechol chemistry, inspired by marine mussel's excellent ability to anchor onto a variety of surfaces, was employed to synthesize ATRP initiator-functionalized TiO₂ NPs. ATRP initiator was functionalized with catechol group via the reaction between dopamine and 2-bromo-2-methylpropionyl bromide (Scheme 4.2b). The chemical structure of catechol-terminated ATRP initiator was confirmed by NMR (Figure C3). Then the initiator was added into TiO₂/DI H₂O dispersion. Through chemical interaction between catechol group and the native layer of hydroxide group around the TiO₂ NPs, ATRP initiator was adsorbed on the particle surface. After immobilization reaction, the initiator NPs were collected by ultracentrifugation. Two batches of ATRP initiator-functionalized TiO₂ NPs were synthesized and were designated as INP-1 and INP-2, respectively. TGA analysis reveals that compared with the original TiO₂ NPs, of which there is only neglectable weight loss when heated to 800 °C, the weight loss of the initiator NPs at the same temperature was around 15 %, indicating successful immobilization. The size distributions of INPs were studied by DLS. The average size of INP-1 is 19.2 nm and that of INP-2 is 20.6 nm (Figure C4).

4.3.2.2 Synthesis of Sulfur-Containing Polymer Brush-Grafted TiO₂ NPs

PS1S-HNP-31.5k was grown by ATRP from the surface of INP-1. The obtained hairy NPs were purified by repetitive dispersion in THF and ultracentrifugation. ¹H NMR spectrum (Figure 4.5a) of the hairy NPs obtained after centrifugation indicated the successful growth of polymer from the surface of nanoparticles. SEC analysis (Figure 4.6a) shows that the $M_{n,SEC}$ and PDI of the free copolymer formed from EBiB were 31.5 KDa and 1.23, respectively. It is well established that the molecular weight and polydispersity of the free polymer initiated from free initiator are



Scheme 4.2. (a) Synthesis of sulfur-containing polymer brush-grafted TiO₂ NPs by surface-initiated atom transfer radical polymerization (SI-ATRP) and (b) synthesis of catechol-terminated ATRP initiator

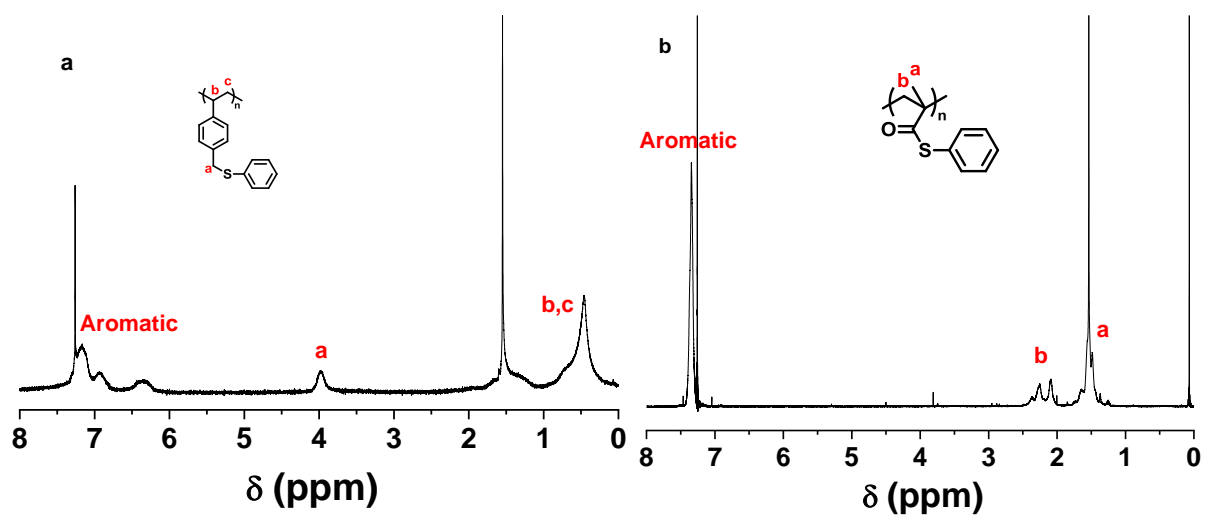


Figure 4.5. ^1H NMR spectra of (a) PS1S-HNP-31.5k and (b) PM1S-HNP-25.5k in CDCl_3

essentially the same as the polymer brush grown from the surface of the initiator particles.²⁶⁻²⁸ The degree of polymerization (DP) of the free polymer was 132, calculated from the final conversion of the monomers determined from the ¹H NMR spectrum and the molar ratio of the monomer to the sum of free initiator and surface initiator. Figure 4.6b shows the TGA curves of the initiator NPs and hairy particles. The weight retention of the PS1S-HNP-31.5k was 33.2 % and that of the initiator NPs was 85.5 % at 800 °C. Using the average size of TiO₂ NPs (19.2 nm), TGA data and the DP of the free polymer, the density of TiO₂ NPs (4.23 g/cm³) and assuming the TiO₂ NPs is spherical, the grafting density of PS1S brushes was found to be 0.49 chains/nm². Calculation of grafting density was described in detail elsewhere.²⁹ Another three PS1S brush-grafted TiO₂ NPs samples differing in the molecular weight of the grafted PS1S were synthesized using the INP-1 as the initiator NPs. The grafting densities of the hairy NPs are in the range of 0.46-0.52 chains/nm². TGA analysis reveals that the weight loss of the hairy NPs increases with increasing molecular weight. Also synthesized was the PM1S polymer brush-grafted TiO₂ NPs, PM1S-HNP-25.5k, initiated from INP-2. Successful functionalization was confirmed by NMR (Figure 4.5b) and TGA analysis (Figure 4.7b). The grafting density is 0.52 chains/nm². The morphologies of polymer brush-grafted TiO₂ NPs were investigated by transition electron microscopy (TEM) (Figure 4.8). The samples were casted onto the TEM grid from THF dispersion of the corresponding nanoparticles. Hairy TiO₂ NPs are irregular in shapes and are self-assembled into packed patterns due to repulsion between grafted polymer brushes with lower molecular weight polymer brushes resulting in denser pattern. Characterization data of the sulfur-containing polymer brush-grafted TiO₂ NPs are summarized in Table 4.2.

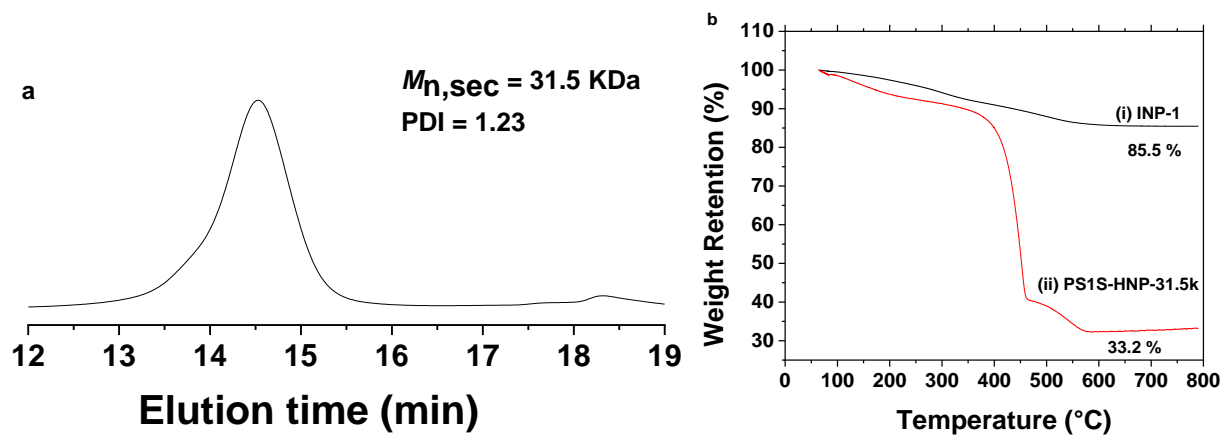


Figure 4.6. SEC trace of the dried free polymer PS1S formed from the free initiator ethyl 2-bromoisobutyrate in the synthesis of PS1S-HNP-31.5k (a) and TGA curves of (i) INP-1 and (ii) PS1S-HNP-31.5k (b)

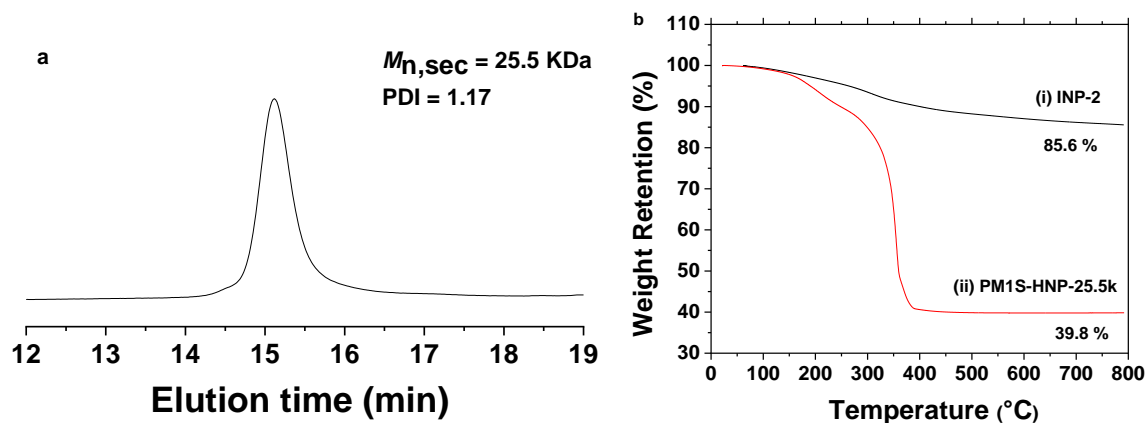


Figure 4.7. SEC trace of the dried free polymer PM1S formed from the free initiator ethyl 2-bromoisobutyrate in the synthesis of PM1S-HNP-25.5k (a) and TGA curves of (i) INP-1 and (ii) PM1S-HNP-25.5k (b)

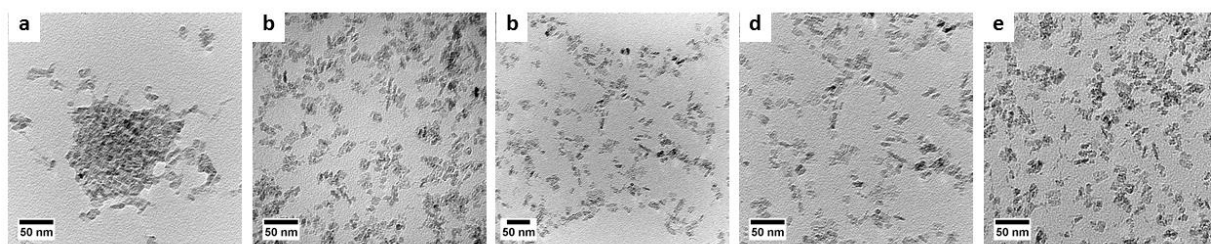


Figure 4.8. Bright-field TEM micrographs of polymer-grafted TiO₂ NPs. (a) PS1S-HNP-11.8 k, (b) PS1S-HNP-22.6k, (c) PS1S-HNP-31.5k, (d) PS1S-HNP-43.3k and (e) PM1S-HNP-25.5k. The samples were cast onto carbon-coated copper TEM grids from THF dispersion of the corresponding hairy NPs with a concentration of 1 mgmL⁻¹.

Table 4.2. Characterization data of sulfur-containing polymer brush-grafted TiO₂ NPs

Initiator NPs	Hairy NPs	Ratio ^a(M:I), Monomer Conversion (%)	<i>M</i>_{n,SEC} (KDa), PDI ^b	DP ^c	σ (Chains/nm²) ^d
INP-1	PS1S-HNP-11.8k	160:1 31.22	11.8, 1.21	46	0.49
	PS1S-HNP-22.6k	157:1, 58.93	22.6, 1.20	86	0.46
	PS1S-HNP-31.5k	478:1, 29.7	31.5, 1.23	132	0.49
	PS1S-HNP-43.3k	467:1, 47.81	43.3 1.24	207	0.52
INP-2	PM1S-HNP-25.5k	154:1, 77.73	25.5, 1.17	119	0.52

^a Monomer/free initiator ^b The values of *M*_{n,SEC} and polydispersity indices (PDI) were obtained by size exclusion chromatography (SEC) calibrated with polystyrene standards. ^c The degree of polymerization (DP) was calculated using the monomer conversion and the molar feed ratio of monomer to the sum of free initiator and surface initiator. ^d Grafting density was calculated by using TGA data, DPs of polymers, and the diameter of TiO₂ nanoparticle size of 19.16 nm from DLS data.

4.3.3 Optical Properties of Thin Film Made from Sulfur-Containing Polymers and the Corresponding Hairy NPs

RI values of thin films made from sulfur-containing polymers are summarized in table 4.3. The polymer films were casted on silicon wafer and then subjected to RI measurement on a laser ellipsometer. The average thickness of the films was between 80 – 90 nm. The RI value of the thin film made from PS1S is in the range of 1.6717 to 1.6839 at 623.8 nm. Compared with the RI value of polystyrene, which is 1.590, the RI values of PS1S is about 0.1 higher, indicating that the incorporation of sulfur atoms into the side chain of polystyrene can increase the RI value of the polymer. The RI of PM1S at 623.8 nm is 1.6047. Considering the RI of PMMA is around 1.49, the RI of PM1S is reasonable. Transparent and free-standing thin films of PS1S and PM1S (Figure 4.9) were made by casting polymer onto a substrate, followed by an etching process. sulfur-containing polymer brush-grafted TiO₂ NPs can form homogenous dispersion (1 wt %) in THF (Figure 4.10). Substrate-supported thin films of hairy NPs were made by spin coating the dispersions on the glass substrates (Figure 4.11). It is worth mentioning that PS1S-HNP-11.8k is not able to form very homogeneous film due to the relatively low polymer content, which indicates that there might be a trade-off between high RI and processability for polymer nanocomposites.

4.4 Conclusion

Sulfur-containing polymer brush-grafted TiO₂ NPs were synthesized to be applied as processable high RI hybrid materials. The polymer chains tethered onto the particles contain sulfur as the intrinsic RI enhancer. An increase of 0.1 in RI was observed after the incorporation of sulfur atom into styrenic or methacrylate type polymers compared with their sulfur-free counterparts.

Table 4.3. Thickness and RI value of sulfur-containing polymers. The thickness and refractive indices were measured on the films of the corresponding samples spin coated on the silicon wafer.

Sample (Polymer)	Thickness (nm)	<i>n</i> (623.8 nm)
PS1S-9.0k	97.29±7.66	1.6822±0.0470
PS1S-20.4k	93.53±2.30	1.6837±0.0071
PS1S-31.8k	95.47±1.60	1.6839±0.0055
PM1S-23.2k	85.30±2.93	1.6047±0.0167

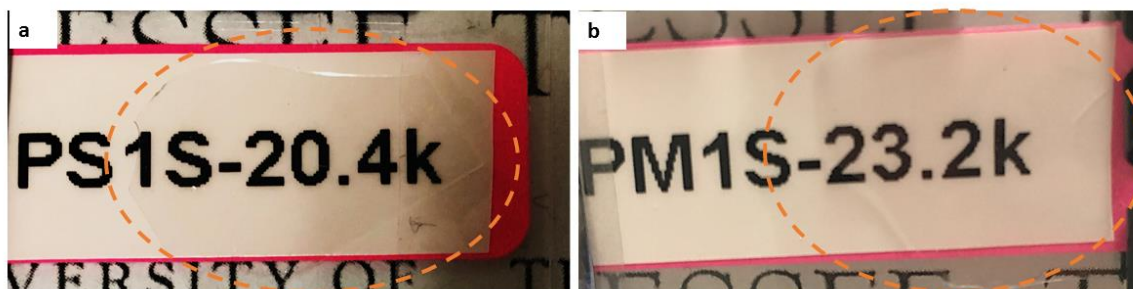


Figure 4.9. Optical pictures of free-standing films of (a) PS1S-20.4k and (b) PM1S-23.2k.

Highlighted in orange circles

Polymer Brush-Grafted TiO₂ NPs (1% Dispersion in THF)

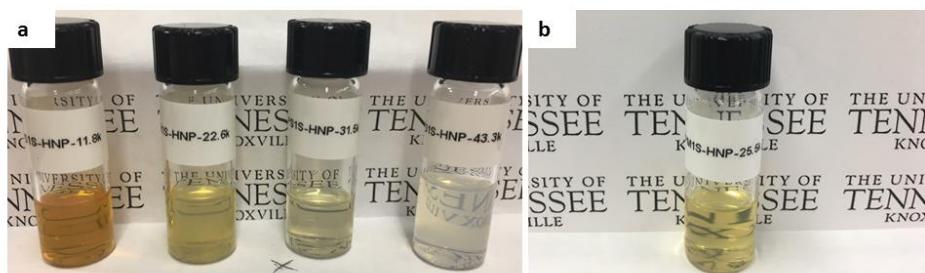


Figure 4.10. Photos of sulfur-containing polymer brush-grafted TiO₂ NPs (1 wt% dispersion in THF) at room temperature (a) from left to right are PS1S-HNP-11.8 k, PS1S-HNP-22.6k, PS1S-HNP-31.5 and PS1S-HNP-43.3k and (b) PM1S-HNP-25.5k

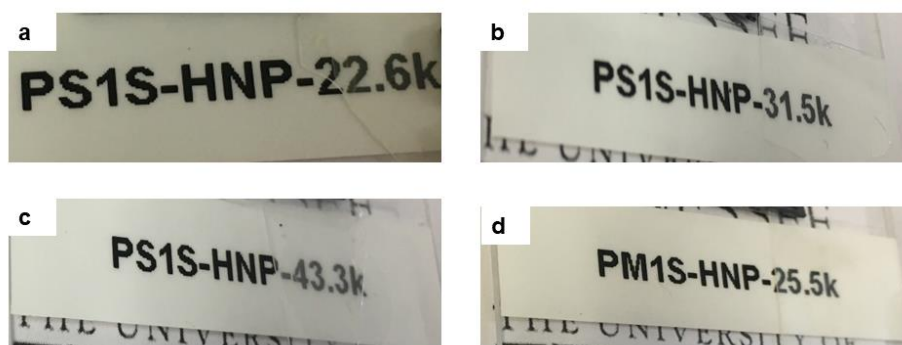


Figure 4.11. Photographs of films made from 1wt% of sulfur-containing brush-grafted TiO₂ NPs in THF. The film was made by spin coating on glass substrates. (a) PS1S-HNP-22.6k, (b) PS1S-HNP-31.5k, (c) PS1S-HNP-43.3k, (d) PM1S-HNP-25.5k.

Polymer chains were grown from ATRP-initiator-grafted TiO₂ NPs by SI-ATRP. Successful polymer grafting was confirmed by NMR, TGA and TEM study. The hairy NPs can form homogeneous dispersion in common organic solvents. Thin films of the hairy NPs were made by spinning coating the dispersion on substrates. The relative content between tethered polymer chains and inorganic high RI core of the polymer-brush-grafted TiO₂ NPs can be adjusted by controlling feeding ratio [initiator NPs]:[monomer] and monomer conversion. Hairy NPs with lower polymer content tends to have higher theoretical value but compromised film formation ability, indicating a trade-off between RI value and processability. The hairy NPs show good potential to be used alone as high RI materials or to be used as building blocks in high RI nanocomposites.

4.5 References

1. Hecht, E., *Optics*. Addison-Wesley: 2002.
2. Higashihara, T.; Ueda, M., Recent Progress in High Refractive Index Polymers. *Macromolecules* **2015**, *48*, 1915-1929.
3. Kim, J. S.; Yang, S. C.; Bae, B. S., Thermally stable transparent sol-gel based siloxane hybrid material with high refractive index for light emitting diode (LED) encapsulation. *Chem. Mater.* **2010**, *22*, 3549-3555.
4. Chung, P. T.; Chiou, S. H.; Tseng, C. Y.; Chiang, A. S. T., Preparation and Evaluation of a Zirconia/Oligosiloxane Nanocomposite for LED Encapsulation. *ACS Appl. Mater. Interfaces* **2016**, *8*, 9986-9993.
5. Macdonald, E. K.; Shaver, M. P., Intrinsic high refractive index polymers. *Polym. Int.* **2015**, *64*, 6-14.
6. Kausar, A.; Zulfiqar, S.; Sarwar, M. I., Recent Developments in Sulfur-Containing Polymers. *Polym Rev* **2014**, *54*, 185-267.
7. Liu, J. G.; Nakamura, Y.; Suzuki, Y.; Shibasaki, Y.; Ando, S.; Ueda, M., Highly refractive and transparent polyimides derived from 4, 4'-[m-Sulfonylbis (phenylenesulfanyl)] diphthalic anhydride and various sulfur-containing aromatic diamines. *Macromolecules* **2007**, *40*, 7902-7909.
8. Liu, J. G.; Nakamura, Y.; Shibasaki, Y.; Ando, S.; Ueda, M., High refractive index polyimides derived from 2, 7-bis (4-aminophenylenesulfanyl) thianthrene and aromatic dianhydrides. *Macromolecules* **2007**, *40*, 4614-4620.

9. You, N. H.; Suzuki, Y.; Yorifuji, D.; Ando, S.; Ueda, M., Synthesis of high refractive index polyimides derived from 1, 6-bis (p-aminophenylsulfanyl)-3, 4, 8, 9-tetrahydro-2, 5, 7, 10-tetrathiaanthracene and aromatic dianhydrides. *Macromolecules* **2008**, *41*, 6361-6366.
10. You, N. H.; Nakamura, Y.; Suzuki, Y.; Higashihara, T.; Ando, S.; Ueda, M., Synthesis of highly refractive polyimides derived from 3, 6-bis (4-aminophenylenesulfanyl) pyridazine and 4, 6 - bis (4 - aminophenylenesulfanyl) pyrimidine. *J. Polym. Sci., Part A: Polym. Chem.* **2009**, *47*, 4886-4894.
11. Okutsu, R.; Ando, S.; Ueda, M., Sulfur-Containing Poly(meth)acrylates with High Refractive Indices and High Abbe's Numbers. *Chem. Mater.* **2008**, *20*, 4017-4023.
12. Terraza, C. A.; Liu, J. G.; Nakamura, Y.; Shibasaki, Y.; Ando, S.; Ueda, M., Synthesis and properties of highly refractive polyimides derived from fluorene - bridged sulfur - containing dianhydrides and diamines. *J. Polym. Sci., Part A: Polym. Chem.* **2008**, *46*, 1510-1520.
13. Zhang, G.; Li, D. S.; Huang, G. S.; Wang, X. J.; Long, S. R.; Yang, J., Synthesis and properties of polyamides containing high contents of thioether units. *React. Funct. Polym.* **2011**, *71*, 775-781.
14. Lynch, D. W.; Hunter, W. R., Comments on the Optical Constants of Metals and an Introduction to the Data for Several Metals. In *Handbook of Optical Constants of Solids*, Palik, E. D., Ed. Academic Press: Boston, 1985; pp 275-367.
15. Li, Y.; Wang, L.; Natarajan, B.; Tao, P.; Benicewicz, B. C.; Ullal, C.; Schadler, L. S., Bimodal "matrix-free" polymer nanocomposites. *RSC Advances* **2015**, *5*, 14788-14795.

16. Xu, J.; Zhang, Y.; Zhu, W.; Cui, Y., Synthesis of Polymeric Nanocomposite Hydrogels Containing the Pendant ZnS Nanoparticles: Approach to Higher Refractive Index Optical Polymeric Nanocomposites. *Macromolecules* **2018**, *51*, 2672-2681.
17. Papadimitrakopoulos, F.; Wisniecki, P.; Bhagwagar, D. E., Mechanically Attrited Silicon for High Refractive Index Nanocomposites. *Chem. Mater.* **1997**, *9*, 2928-2933.
18. Lü, C.; Yang, B., High refractive index organic–inorganic nanocomposites: design, synthesis and application. *J. Mater. Chem.* **2009**, *19*, 2884-2901.
19. Liu, J. G.; Ueda, M., High refractive index polymers: fundamental research and practical applications. *J. Mater. Chem.* **2009**, *19*, 8907-8919.
20. Tao, P.; Li, Y.; Rungta, A.; Viswanath, A.; Gao, J.; Benicewicz, B. C.; Siegel, R. W.; Schadler, L. S., TiO₂ nanocomposites with high refractive index and transparency. *J. Mater. Chem.* **2011**, *21*, 18623-18629.
21. Zimmennann, L.; Weibel, M.; Caseri, W.; Suter, U. W., High refractive index films of polymer nanocomposites. *J. Mater. Res.* **1993**, *8*, 1742-1748.
22. Ciampolini, M.; Nardi, N., Five-Coordinated High-Spin Complexes of Bivalent Cobalt, Nickel, and Copper with Tris (2-dimethylaminoethyl) amine. *Inorg. Chem.* **1966**, *5*, 41-44.
23. Matyjaszewski, K.; Tsarevsky, N. V.; Braunecker, W. A.; Dong, H.; Huang, J.; Jakubowski, W.; Kwak, Y.; Nicolay, R.; Tang, W.; Yoon, J. A., Role of Cu⁰ in controlled/“living” radical polymerization. *Macromolecules* **2007**, *40*, 7795-7806.
24. Zhang, S., Understanding of sulfurized polyacrylonitrile for superior performance lithium/sulfur battery. *Energies* **2014**, *7*, 4588-4600.
25. Saiz Poseu, J.; Mancebo Aracil, J.; Nador, F.; Busqué, F.; Ruiz Molina, D., The Chemistry behind Catechol - Based Adhesion. *Angew. Chem. Int. Ed.* **2019**, *58*, 696-714.

26. Wright, R. A. E.; Hu, B.; Henn, D. M.; Zhao, B., Reversible sol–gel transitions of aqueous dispersions of silica nanoparticles grafted with diblock copolymer brushes composed of a thermosensitive inner block and a charged outer block. *Soft matt* **2015**, *11*, 6808-6820.
27. Wright, R. A. E.; Wang, K.; Qu, J.; Zhao, B., Oil - Soluble Polymer Brush Grafted Nanoparticles as Effective Lubricant Additives for Friction and Wear Reduction. *Angew.Chem.Int.Ed* **2016**, *55*, 8656-8660.
28. Seymour, B. T.; Wright, R. A. E.; Parrott, A. C.; Gao, H.; Martini, A.; Qu, J.; Dai, S.; Zhao, B., Poly(alkyl methacrylate) Brush-Grafted Silica Nanoparticles as Oil Lubricant Additives: Effects of Alkyl Pendant Groups on Oil Dispersibility, Stability, and Lubrication Property. *ACS Appl. Mater. Interfaces* **2017**, *9*, 25038-25048.
29. Hu, B.; Henn, D. M.; Wright, R. A. E.; Zhao, B., Hybrid Micellar Hydrogels of a Thermosensitive ABA Triblock Copolymer and Hairy Nanoparticles: Effect of Spatial Location of Hairy Nanoparticles on Gel Properties. *Langmuir* **2014**, *30*, 11212-11224.

**Appendix C for Chapter 4. Sulfur-containing Polymer Brush-grafted
Titanium Dioxide Nanoparticles with Good Processability and High
Refractive Index**

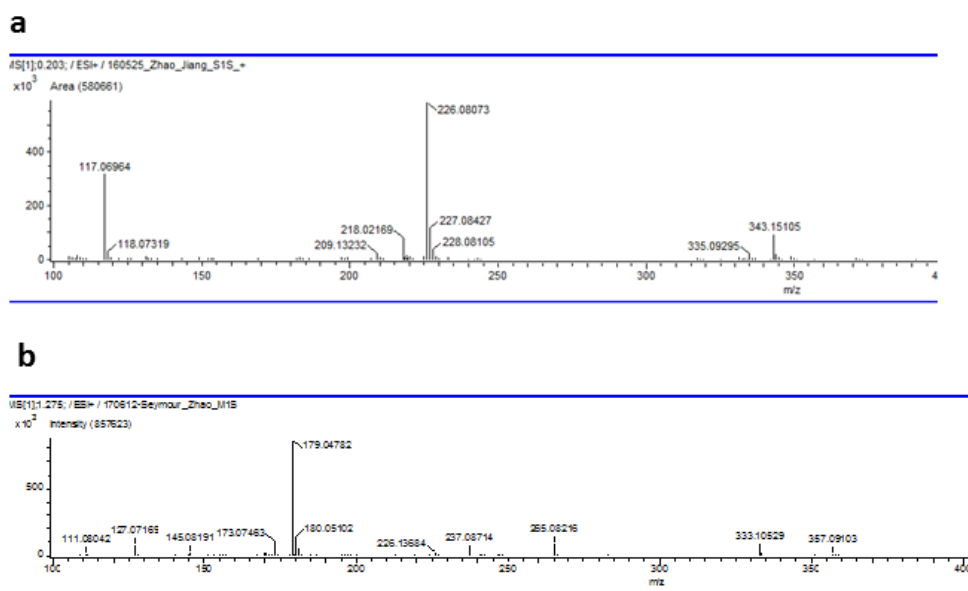


Figure C1. High resolution mass spectrometry (DART-TOF) of (A) S1S: m/z calc. 226.08; [M^+] 226.08; found 226.08073; mass error 3.23 ppm and (B) PM1S: m/z calc. 178.05; [MH^+] 179.05; found 179.04782; mass error -12.18 ppm

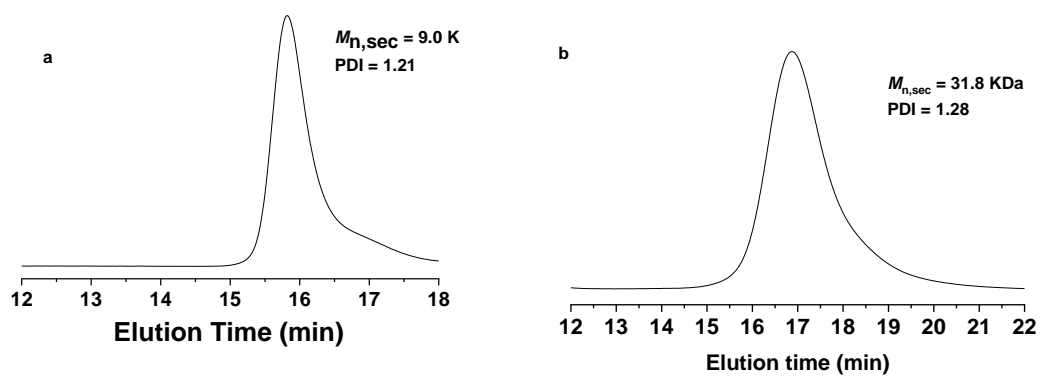


Figure C2. SEC trace of PS1S-9.0k (a) and PS1S-31.8k (b)

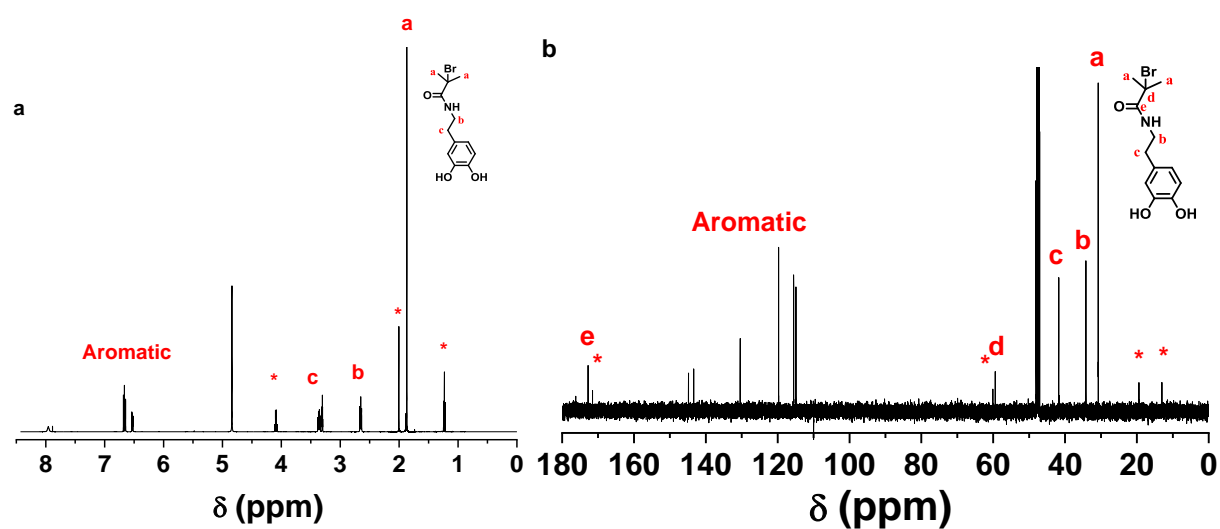


Figure C3. ^1H NMR (a) and ^{13}C NMR (b) spectra of the dopamine-terminated ATRP initiator in MeOH-d_4 . Signals from water and ethyl acetate are marked with asterisks.

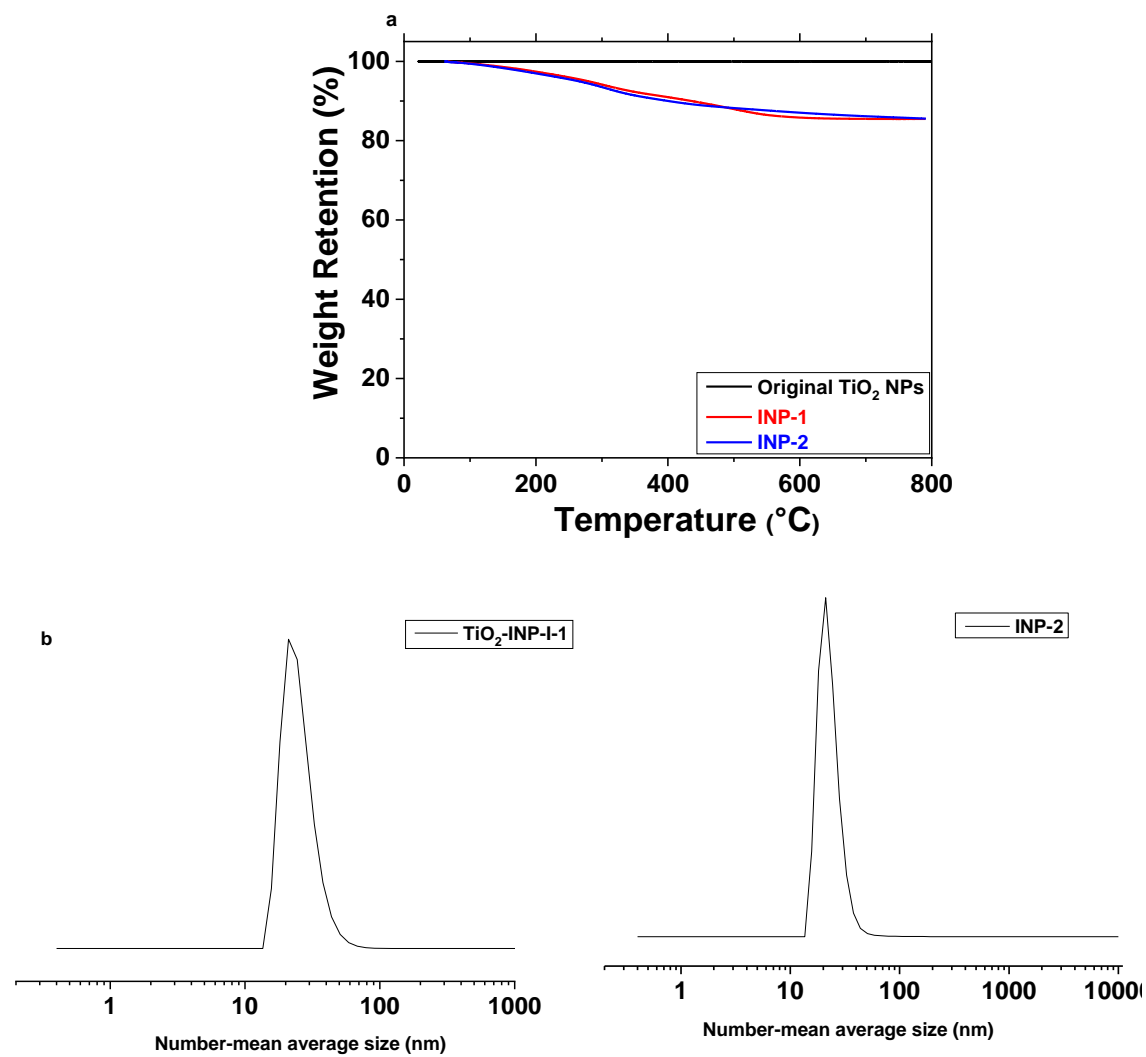


Figure C4. TGA curves (a) of initiator-functionalized TiO₂ NPs. TGA curve of original TiO₂ NPs is included as reference, and DLS profiles (b) of INP-1 and INP-2. The initiator NPs are dispersed in DMF with a concentration of 1 mgg⁻¹.

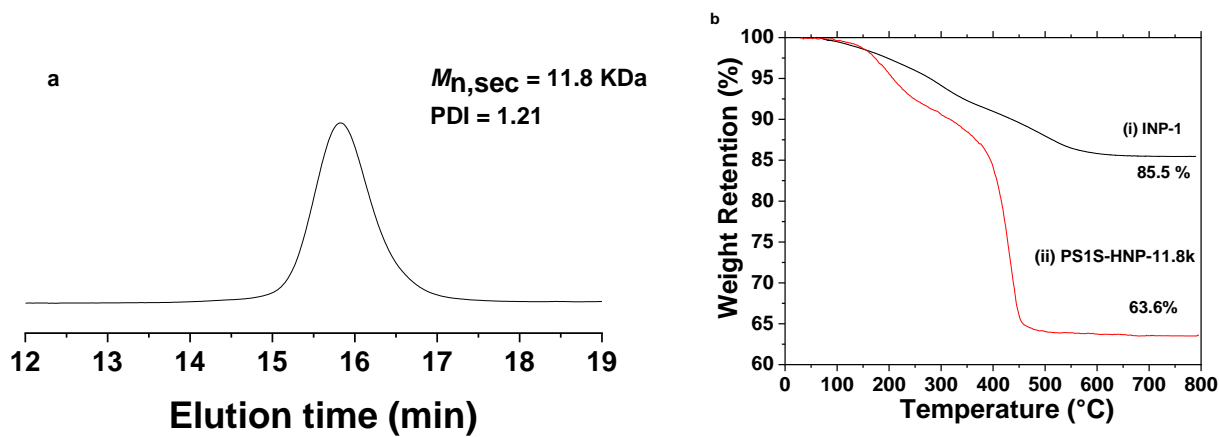


Figure C5. SEC trace of the dried free polymer PS1S formed from the free initiator ethyl 2-bromoisobutyrate in the synthesis of PS1S-HNP-11.8k (a) and TGA curves of (i) INP-1 and (ii) PS1S-HNP-11.8k (b).

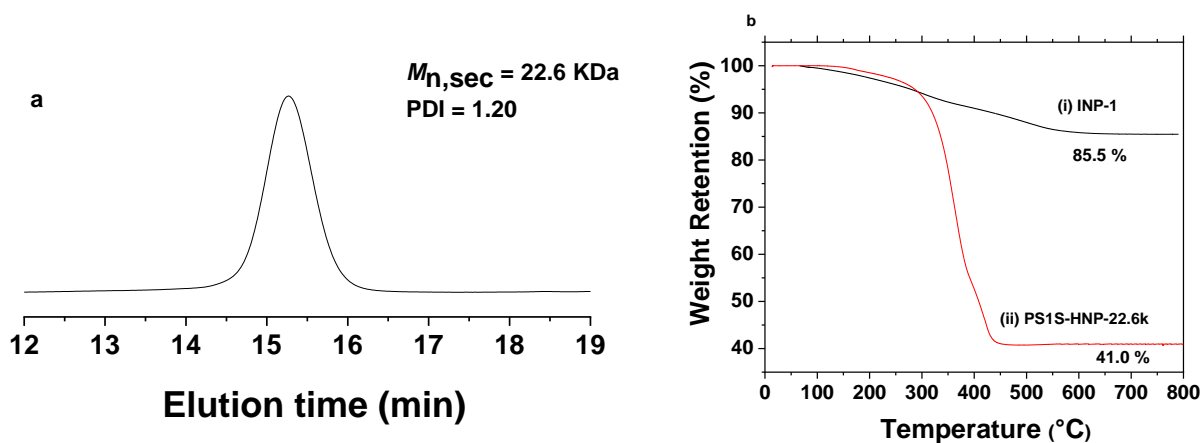


Figure C6. SEC trace of the dried free polymer PS1S formed from the free initiator ethyl 2-bromoisobutyrate in the synthesis of PS1S-HNP-22.6k (a) and TGA of (i) INP-1 and (ii) PS1S-HNP-22.6k (b).

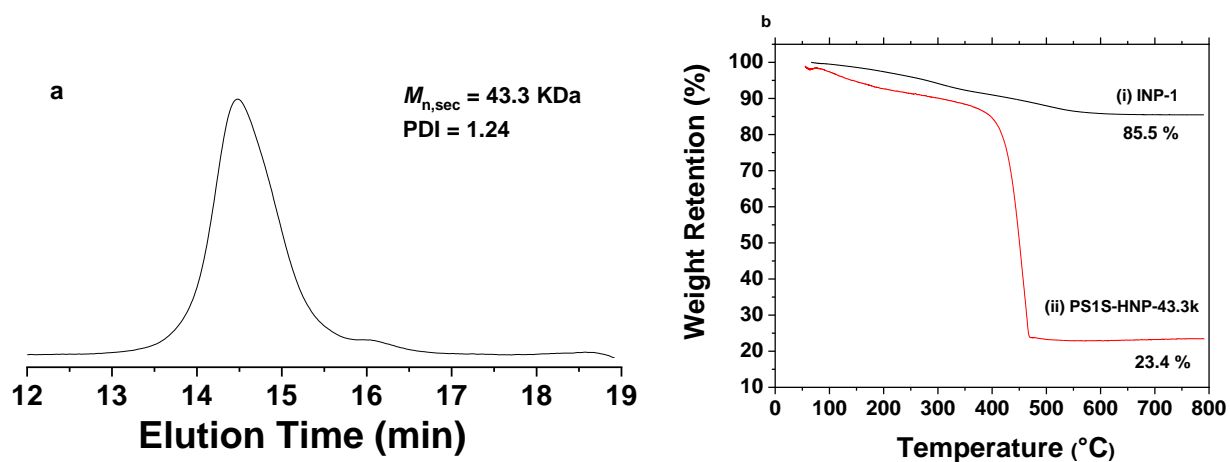


Figure C7. SEC trace of the dried free polymer PS1S formed from the free initiator ethyl 2-bromoisobutyrate in the synthesis of PS1S-HNP-43.3k (a) and TGA of (i) INP-1 and (ii) PS1S-HNP-43.3k (b).

**Chapter 5. Polymer Brush-Grafted Silicon Nanoparticles by Surface-Initiated
Controlled Radical Polymerization: Synthesis and Characterization**

Abstract

This chapter presents an effective method to functionalize silicon nanoparticles (SiNPs) with polymers. Two surface immobilization methods: (i) surface silanization and (ii) surface hydrosilylation were employed to functionalize SiNPs with an ATRP initiator. Then polymer brushes were grafted from the surface of SiNPs via surface-initiated controlled radical polymerization from the surface of initiator-functionalized SiNPs. The amount of the polymer brushes on SiNPs was determined by thermogravimetric analysis and the morphology of hairy NPs was studied by transmission electron microscopy. Grafting densities of the polymer brush-grafted SiNPs (hairy SiNPs) made through surface silanization method are in the range of 0.77 – 0.84 chains/nm² while those of the hairy SiNPs made through surface hydrosilylation are in between 0.30 – 0.56 chains/nm², indicating that surface silanization method gives a denser initiator coverage than surface hydrosilylation method.

5.1 Introduction

Silicon nanoparticles (SiNPs), with such properties as high refractive index (~ 4.3) at infrared regions, high energy capacity and tunable photoluminescence,¹⁻⁴ have attracted much attention due to the potential use in the fields of high RI materials,⁵ sustainable energy technologies^{6,7} and bioimaging^{8,9}. Problem exists that the weak forces (mainly Van der Waals interactions) between bare SiNPs usually cannot sustain the thermal or mechanical stresses occurring during the processing of the particles.¹⁰ For example, while many applications require the SiNPs to be made into thin films, crack and many other defects will form in the films made of bare particles directly.^{11,12} It is therefore of great significance to develop surface pretreatment method to enhance compatibility and processability of SiNPs. As is the case for many inorganic nanoparticles, the surface pretreatment of SiNPs can be achieved by combining the nanoparticles with organic molecules so that the obtained nanocomposites can retain the desired properties from both sides. The simplest way to achieve this is to blend the nanoparticles with organic matrix such as low molecular weight surfactants or high molecular weight polymers. For instance, to fabricate processable high RI nanocomposites, Papadimitrakopoulos and coworkers combined an ethanolic suspension of SiNPs with an aqueous solution of gelatin. The obtained mixture was spin coated on silicon wafers and annealed to give thin films of which the RI values are directly proportional to the volume fraction of SiNPs in the nanocomposites.⁵ Simple as it is, blending method has a big drawback as the dispersion of the particles in the organic matrix is usually not homogeneous due to phase separation. On the other hand, surface modification of SiNPs based on chemical method, where small molecules or polymers are covalently attached onto the surface of SiNPs can usually result in better dispersion even at higher particle loading. Surface hydrosilylation, first introduced by Linford and Chidsey,^{13,14} is so far the most commonly used method for modifying the surface

of SiNPs by the formation of Si-C bond through insertion of an unsaturated C-C bond (usually an alkyne or alkene) into surface Si-H bond. Throughout years, surface hydrosilylation of all derivatives (activated thermally,¹⁵⁻¹⁷ photochemically,^{18,19} catalyzed by transition metals^{20,21} or by other mechanism) have been reported. For instance, radical-initiated surface hydrosilylation using 2,2'-azobis(2-methylpropionitrile) (AIBN) or benzoyl peroxide (BPO) as initiator have been employed to modify silicon nanocrystals.²⁴ Polymers are advantageous over small molecules with their excellent processability and great mechanic strength. Polymer brush-grafted SiO₂, TiO₂ and ZrO₂ NPs have been reported.^{25-30, 34} The modification methods can be categorized into either “grafting to” or “grafting from”. In “grafting to” method, end-functionalized polymers are grafted onto the surface of functionalized NPs, while in “grafting from” method polymer brushes are grown from the surface of initiator-functionalized inorganic NPs. In general, “grafting from” method gives hairy NPs with higher grafting density in that monomers can diffuse to the propagating site on the particles more easily than polymers.^{29,31-33} The hairy NPs made by “grafting from” method have been shown to exhibit excellent dispersability and processability. For instance, poly(lauryl methacrylate) brush-grafted silica and titania NPs synthesized by surface-initiated atom transfer radical polymerization have been used as lubricant additives for friction and wear reduction.³⁴ Both “grafting to” and “grafting from” methods have been used to modify bulk silicon surface.³⁵⁻⁴² However, from my best knowledge, there is so far no report on the surface modification of SiNPs with polymers.

In this chapter, we presented the synthesis of hairy SiNPs by surface-initiated controlled radical polymerization (SI-CRP) from the surface of initiator-functionalized SiNPs. Two approaches were developed for the immobilization of ATRP initiator onto the surface of SiNPs, namely, (i) surface silanization (surface hydrolysis/condensation of ATRP initiator-terminated

triethoxysilane) method and (ii) surface hydrosilylation method. In method (i), commercial silicon nanopowder was first etched by a mixture of nitric acid (HNO_3) and hydrofluoric acid (HF) to reduce the aggregation of the particles, and then the etched SiNPs were treated with hydrogen peroxide (H_2O_2) to enrich silanol groups onto the particle surface.⁴³ An ATRP initiator was then immobilized onto the particle surface by hydrolysis/condensation reaction of triethoxysilane-terminated ATRP initiator. Surface-initiated atom transfer radical polymerization (SI-ATRP) of styrene or n-butyl acrylate from the surface of the initiator functionalized NPs gives hairy NPs with the grafting density around 0.8 chains/ nm^2 . Although the well-known silane chemistry proves to be a robust approach to functionalize the surface of inorganic NPs, the inevitable introduction of a silicon oxide layer on SiNPs could cause some issues, especially in the cases where non-oxide SiNPs are needed.^{44,45} Surface hydrosilylation is an oxide-free alternative to directly introduce the initiator onto the surface of SiNPs. HNO_3/HF etching was used as the first step to introduce Si-H bond onto the surface of SiNPs, and then an ATRP initiator functionalized with an alkene group was linked to the surface of Si-H NPs by surface hydrosilylation. Different polymers including polystyrene (PS), poly(n-butyl acrylate) (PnBA) and poly(methyl acrylate) (PMA), were grown from the initiator-functionalized silicon particles with a grafting density varying from 0.30 to 0.56 chains/ nm^2 using SI-CRP. Successful growth of the polymer chains from the surface of initiator-functionalized SiNPs made by the two protocols were confirmed by thermogravimetric (TGA) analysis, and the morphology of the hairy SiNPs were studied by transition electron microscopy (TEM). This work presents an effective method for functionalizing the surface of SiNPs with polymer chains.

5.2 Experimental Section

5.2.1 Materials

Silicon nanopowder (Si, 98+%, < 80 nm according to U.S. Research Nanomaterials, Inc) and triethoxysilane (95%, Acros) was used as received. A platinum–divinyltetramethyldisiloxane complex in xylene (2.1–2.4% Pt concentration in xylene) was purchased from Gelest, Inc. CuBr (98%, Aldrich) was stirred in glacial acetic acid overnight, filtered, and washed with absolute ethanol and diethyl ether. The purified CuBr was dried under vacuum. *N, N, N', N', N''*-Pentamethyldiethylenetriamine (PMDETA, 99%, Aldrich) and ethyl 2-bromoisobutyrate (EBiB, 98%, Aldrich) were dried with CaH₂ and distilled under reduced pressure. Hexamethylated tris(2-aminoethyl)amine (Me₆-TREN) was synthesized as described in the literature⁴⁶. Methyl acrylate (MA, 99%, contains ≤100 ppm monomethyl ether hydroquinone (MEHQ) as inhibitor, Aldrich) and n-butyl acrylate (nBA, 99%, stabilized by 10-200 ppm MEHQ, Acros) were passed through a column of silica gel (bottom)/activated basic aluminum oxide (top) (2/1, v/v), respectively to remove the inhibitor and were stored in a refrigerator prior to use. Styrene (> 99%, contains 4-tert-butylcatechol as stabilizer, Aldrich) was distilled to remove the stabilizer and was stored in a refrigerator prior to use. All other chemical reagents were purchased from either Sigma Aldrich or Fisher/Acros and used without further purification.

5.2.2 General Characterization

¹H NMR spectra were recorded on a Varian Mercury 300 NMR spectrometer. Size exclusion chromatography (SEC) of the free polymers formed in the synthesis of hairy NPs was carried out at ambient temperature using PL-GPC 20 (an integrated SEC system from Polymer Laboratories, Inc.) with a refractive index detector, one PLgel 5 μm guard column (50 × 7.5 mm), and two PLgel 5 μm mixed-C columns (each 300 × 7.5 mm, linear range of molecular weight from 200 to 2 000

000 Da). THF was used as the solvent, and the flow rate was 1.0 mL/min. Narrow-disperse polystyrene standards were used to calibrate the system. The data were processed using Cirrus GPC/SEC software (Polymer Laboratories, Inc.). Thermogravimetric analysis (TGA) was performed under Argon purge at a heating rate of 20 °C/min from room temperature to 800 °C using TA Q-series Q50. The NPs were dried at 45 °C in vacuum for > 5 h prior to analysis. Transmission electron microscopy (TEM) was performed using a Zeiss Libra 200 HT FE MC microscope, and bright field images were taken with a bottom mounted Gatan UltraScan US1000XP CCD camera. Samples were drop-cast from dispersions in ethanol (for original silicon particles and silicon particles after etching) or tetrahydrofuran (THF) (for hairy silicon particles) with a concentration of 1 mg/mL onto a carbon-coated, copper TEM grid using a glass pipette and were dried at ambient conditions.

5.2.3 Synthesis of Polymer Brush-Grafted SiNPs from the Surface of ATRP Initiator-Functionalized SiNPs Made by Surface Silanization

5.2.3.1 Preparation of ATRP Initiator-Functionalized SiNPs via Surface Silanization.

What is described here is the synthesis of ATRP initiator functionalized SiNPs (INP-I-1) by surface silanization. 10-Undecenyl 2-bromoisobutyrate (long-chain ATRP, 0.206 g, 0.64 mmol), triethoxysilane (2 mL, 10.84 mmol), and the platinum–divinyltetramethyldisiloxane complex in xylenes (2.1–2.4% platinum concentration, 20 µL) were added into a 25-mL two-necked round-bottom flask. The mixture was stirred at 45 °C under N₂. ¹H NMR spectroscopy was used to monitor the reaction. Once the reaction was complete, excess triethoxysilane was removed under vacuum at 45 °C. The product was used directly in the next step for the preparation of INP-I-1. Yield: 0.196 g, 95.2 %. The original silicon nanopowder (0.540 g) were dispersed in pure methanol (10 mL) in a PTFE centrifuge tube with a stir bar inside it. The tube was then put into an ultrasonic

bath while being stirred. A mixture of HF (48 wt %, 10 mL) and HNO₃ (69 wt %, 1 mL) was added to the resulting dispersion. The etching reaction was carried out for 30 min before the reaction mixture was diluted with pure methanol (20 mL). The NPs were then isolated with centrifugation (11,000 rpm, 15 min). The cycle of isolation and re-dispersion was repeated for a total of three times. The same etching procedure was carried out on another batch of the original silicon nanopowder (0.557 g). Then the combined HF/HNO₃ etched SiNPs (yield: 0.549 g, 50.0 %) were added in absolute ethanol (10 mL) in a 100 mL three-necked flask and the mixture were ultrasonicated for 10 min until the particles were well dispersed in the solvent. H₂O₂ (30 wt %, 30 mL) was then added into the resulting dispersion dropwise and the reaction mixture was refluxed under N₂ for 48 h. After the reaction, the NPs were isolated by centrifugation (11,000 rpm, 15 min). This washing process was repeated for a total of three times. The surface-oxidized SiNPs were dried in a vial under high vacuum at room temperature overnight. Yield: 0.480 g, 87.5 %. Surface-oxidized SiNPs (0.450 g) were added into absolute ethanol (20 mL), and the mixture was ultrasonicated until a homogeneous, stable dispersion was formed. A solution of ammonia (25% in water, 0.065 g) in ethanol (5 mL) was added dropwise into the particle dispersion. Then triethoxysilane-terminated long-chain ATRP initiator freshly synthesized from long-chain ATRP initiator (0.200 g, 0.41 mmol) was added into the resulting dispersion. After the reaction mixture was stirred at 60 °C for 45 h, the NPs were isolated by centrifugation (11,000 rpm, 30 min) and redispersed in THF. This process was repeated for a total of four times. The obtained initiator-functionalized SiNPs (INP-I-1) (yield: 0.420 g, 93.3 %) were then dried in a vial under high vacuum at room temperature overnight. INP-I-2 was prepared using the same method.

5.2.3.2 Synthesis of Polystyrene Brush-Grafted SiNPs from the Surface of INP-I-1 by Surface-Initiated ATRP (SI-ATRP)

The following description is a procedure for the synthesis of polymer brush-grafted SiNPs with free PS $M_{n,SEC}$ of 58.0 kDa . (PS-I-1-58.0k) from INP-I-1. INP-I-1 (0.230 g) were dispersed in anisole (3.000 g) with an NP concentration of 7.12 wt % in a 50-mL two-necked round bottom flask equipped with a stir bar. Then styrene (8.112 g, 78.70 mmol), free initiator EBiB (19.7 mg, 0.10 mmol), CuBr (15.4 mg, 0.11 mmol), PMDETA (20.3 mg, 0.12 mmol), trioxane (20.1 mg, 0.22 mmol) and anisole (5.000 g) were added into flask. After degassed by three freeze–pump–thaw cycles, the flask was placed in an oil bath with a preset temperature of 90 °C. Small portions of reaction mixture were withdrawn by degassed syringe at intervals for the purpose of monitoring the progress of the polymerization. After the reaction proceeded for 24 h, the polymerization was quenched by removing the flask from the oil bath and being opened to air. The reaction mixture was diluted with THF. The NPs were isolated by centrifugation (11,000 rpm, 30 min). This washing process was repeated for a total of five times. A portion of the supernatant liquid from the first cycle was passed through a short column of silica gel (bottom)/activated basic aluminum oxide (top) (2/1, v/v). The $M_{n,SEC}$ of the free polymer was 58.0 k with a PDI of 1.19. Degree of polymerization (DP) is 558, which is calculated by dividing $M_{n,SEC}$ with the molecular weight (M_w) of styrene. The conversion of the monomer is 73.7 %, calculated from the ^1H NMR spectra of the samples taken from the reaction mixture at the beginning and at the end of the polymerization using the integrals of the peaks at 5.26 – 5.32 ppm (-CH=CHH from styrene) and 5.18 – 5.19 ppm (-O-CH₂ from trioxane). PnBA-I-1-58.0k was synthesized using the same method from INP-I-1 with a polymerization temperature of 95 °C. Polystyrene brush-grafted SiNPs were prepared from INP-I-2 following similar procedure and was designated as PS-I-2-31.7k.

5.2.4 Synthesis of Polymer Brush-Grafted SiNPs from the Surface of ATRP Initiator-Functionalized SiNPs Made by Surface Hydrosilylation

5.2.4.1 Preparation of ATRP Initiator-Functionalized SiNPs via Surface Hydrosilylation

The following procedure is the preparation of ATRP initiator-functionalized SiNPs by surface hydrosilylation method. The original silicon nanopowder (0.485 g) was etched by a mixture acid of HF and HNO₃ using the same procedure described previously for the synthesis of INP-I-1. The freshly etched Si-H NPs were used directly in the next step without further drying. Si-H NPs (0.200 g) were dispersed directly in allyl 2-bromo-2-methylpropanoate (short-chain ATRP initiator, 1.965 g, 9.49 mmol) by ultrasonication to form a homogeneous, stable dispersion. The platinum–divinyltetramethyldisiloxane complex in xylenes (2.1–2.4% platinum concentration, 50 μL) was then added into the resulting dispersion by a microsyringe. After degassed by three freeze–pump–thaw cycles, the reaction mixture was placed in an oil bath with a preset temperature of 60 °C. After the reaction mixture was stirred for 70 h, the NPs were isolated by ultracentrifugation (11,000 rpm, 45 min) and redispersed in THF. After repeating this isolation–redispersion process for a total of three times, the obtained initiator functionalized NPs (yield: 0.189 g, 94.5 %) were dried in a vial under high vacuum at room temperature for over 5 h. Another batch of initiator NPs, INP-II-2, was synthesized using the same method.

5.2.4.2 Synthesis of Polymer Brush-Grafted SiNPs from the surface of INP-II-1 by SI-ATRP

Different polymers were grown from the surface of ATRP-initiator-functionalized silicon nanoparticles. What is shown here is the synthesis of PS brush-grafted SiNPs with free PS (formed from free initiator added) $M_{n,SEC}$ of 41.1 KDa (PS-III-41.1k) from INP-II-1. INP-II-1 (0.077 g, pre-dispersed in 3.600 g anisole with a NP concentration of 2.09 wt %) was added into a 25 mL two-necked round bottom flask, followed by the addition of styrene (5.825 g, 56.00 mmol), free

initiator EBiB (19.8 mg, 0.10 mmol), CuBr (15.9 mg, 0.11 mmol), PMDETA (19.0 mg, 0.11 mmol), trioxane (36.8 mg, 0.41 mmol) and anisole (2.500 g). After degassed by three cycles of freeze–pump–thaw, the flask was placed in an oil bath of which the temperature was set at 90 °C. ¹H NMR was employed to monitor the progress of polymerization. After the reaction proceeded for 6 h, the flask was removed from the oil bath and opened to air. The reaction mixture was diluted with THF. The particles were isolated by centrifugation (11,000 rpm, 30 min). After 5 times of washing cycle, a portion of the supernatant liquid from the first cycle of centrifuge was passed through a short column with silica gel at bottom and activated basic aluminum oxide on top (2/1, v/v). The molecular weight ($M_{n,SEC}$) of the free polymer was 41.1k and the PDI is 1.16. The conversion of monomer was 70.8 %, calculated from the ¹H NMR spectra of the samples taken from the reaction mixture at the beginning and at the end of the polymerization using the integrals of the peaks at 5.26 – 5.32 ppm (-CH=CHH from styrene) and 5.18 – 5.19 ppm (-O-CH₂ from trioxane), and the DP was 384. The same method was used to synthesize PnBA brush-grafted SiNPs PnBA-II-1-41.3 k from INP-II-1 and PnBA-II-2-50.5k from INP-II-2 with the temperature of polymerization setting at 95 °C.

5.2.4.3 Synthesis of Poly(methyl acrylate) Brush-Grafted SiNPs by Surface-Initiated Single Electron transfer “Living”/Controlled Radical Polymerization (SET-LRP)

In a typical experiment, initiator NPs (INP-II-2, 0.0588 g, pre-dispersed in 3.500 g of dimethyl sulfoxide (DMSO) with a NP concentration of 1.68 wt %), methyl acrylate monomer (4.853 g, 56.43 mmol), free initiator EBiB (21.2 mg, 0.11 mmol), Cu(0) powder (6.6 mg, 0.10 mmol) and DMSO (6.631 g) were added to a 50 mL two-neck round bottom flask in the following order: Cu(0), EBiB, MA, initiator NPs dispersion and DMSO. Freeze–pump–thaw was used to degass the reaction mixture and this process was repeated for another 2 times. Before the last cycle

of freeze-pump-thaw, Me₆-TREN (21.7 mg, 0.10 mmol) was added into the mixture through a degassed microsyring. After that, the temperature of the mixture was raised to room temperature in a water bath and stirred for 70 min. Then the polymerization was quenched by opening the flask to air and diluting the reaction mixture with THF; The NPs were isolated by centrifugation (11000 rpm, 30 min) and redispersed in THF, this isolation-dispersion process was repeated for another four times. The free polymer was purified by passing a portion of the supernatant liquid from the first cycle through a short column of silica gel (bottom)/activated basic aluminum oxide (top) (2/1, v/v). SEC results: $M_{n,sec} = 43.7$ k, PDI = 1.14. Calculated from the ¹H NMR spectrum taken right after the polymerization was stopped using the integrals of the peaks at the peaks at 3.58 – 3.65 ppm (-O-CH₃ from PMA) and 3.71 – 3.72 ppm (-O-CH₃ from MA), the conversion was 99.8 %, and the DP was 517. This hairy NP sample was designated as PMA-II-2-43.7k.

5.3 Results and Discussion

5.3.1 Solution Etching of SiNPs

The known etching process of SiNPs with HF is employed here to decrease the aggregation of the original SiNPs.⁴⁷ Furthermore, this etching process can introduce Si-H bonds onto the surface of SiNPs and create a platform for surface hydrosilylation. After solution etching, the particles show better dispersion in ethanol compared with the original SiNPs as indicated by the TEM pictures (Figure 5.1).

5.3.2 Synthesis of Hairy SiNPs from Initiator-Functionalized SiNPs Made by Surface Silanization

Surface silane chemistry in which polymers or small molecules end-functionalized with a silane are grafted onto the surface of a variety of inorganic NPs has been well established. In the

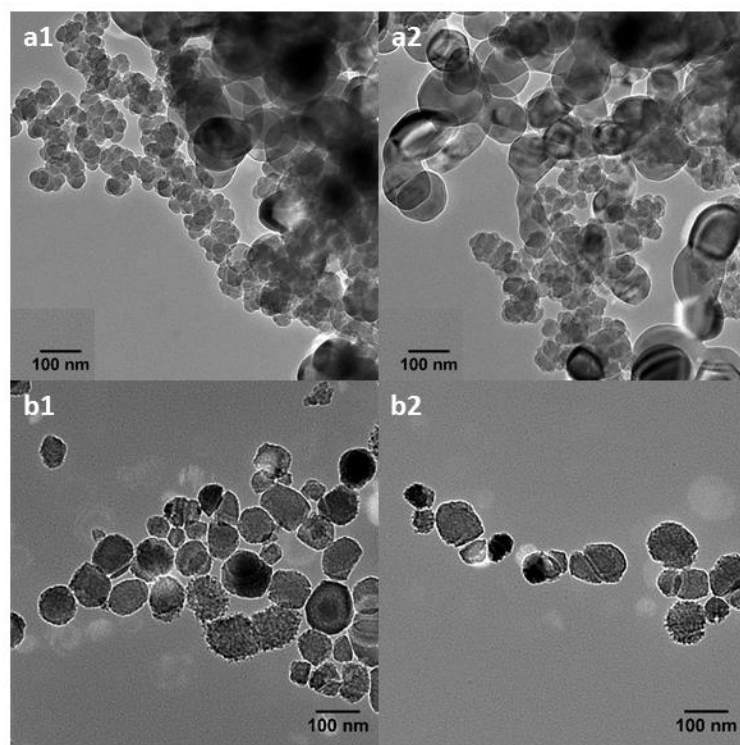


Figure 5.1 Bright field TEM micrographs of original silicon nanopowder (a1 and a2) and (b) SiNPs after HF/HNO₃ etching. The SiNPs were cast onto carbon-coated, copper TEM grids from the ethanol dispersions with a NP concentration of 1 mgmL⁻¹.

surface silanization route, the etched SiNPs, with an average size of 92 nm, determined from TEM micrographs, were surface oxidized by H₂O₂ to introduce hydroxyl groups onto the particle surface. An ATRP initiator was then immobilized onto the particle surface by ammonia-mediated hydrolysis/condensation of a triethoxysilane-terminated ATRP initiator. Si/Si_xO_y NPs were first homogeneously dispersed in absolute ethanol by ultrasonication, to which ammonia and the triethoxysilane-terminated ATRP initiator were added. Ammonia promoted the hydrolysis of silane. The mass ratio of the silane initiator to the oxidized SiNPs used here was 2:1, and the immobilization reaction was carried out at 45 °C for a total of 45 h. The initiator NPs were purified by centrifugation/dispersion process and were dried under high vacuum overnight. Then the dry particles were dispersed in anisole to form a homogeneous dispersion. Different polymer brushes including PS and PnBA were grown from the initiator NPs by surface-initiated ATRP of the corresponding monomer using CuBr/PMDETA as catalyst in the presence of free initiator EBiB. The purpose of the addition of free initiator is to have a better control of the surface polymerization as well as to provide a convenient way to monitor the progress of the reaction. Initiator NPs, INP-I-1 and INP-I-2, were synthesized using this route. PS-I-1-58.0k and PnBA-I-1-58.0k were made from INP-I-1, and PS-I-2-31.7k was made from INP-I-2. Take PS-I-1-58.0k as an example, after a desired monomer conversion was reached, the polymerization was quenched and the obtained hairy NPs were purified by repetitive dispersion in THF and centrifugation. SEC analysis showed that the $M_{n,SEC}$ and PDI of the free copolymer formed from EBiB were 58.0 kDa and 1.19, respectively. Hence, the DP of the polymer, calculated by dividing $M_{n,SEC}$ with the MW of styrene, was 558. Figure 5.2b shows the TGA curves of the initiator NPs and hairy particles. It is worth mentioning that the TGA analysis of the hairy nanoparticles was performed under argon purge instead of N₂ purge because silicon core might react with N₂, which will result in the increase in

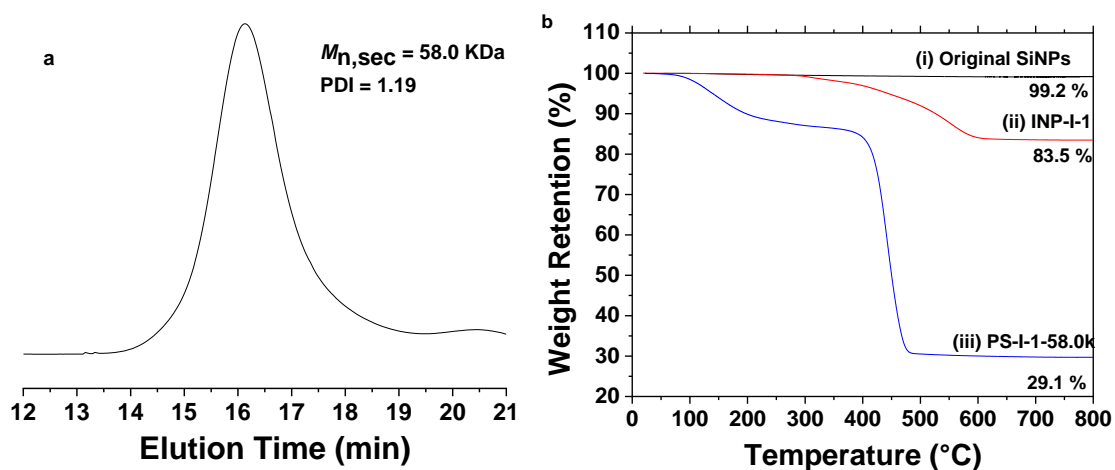


Figure 5.2 SEC trace of the dried free polymer polystyrene formed from the free initiator ethyl 2-bromoisobutyrate in the synthesis of PS-I-1-58.0k (a) and TGA of (i) original SiNPs, (ii) INP-I-1 and (iii) PS-I-1-58.0k (b)

weight retention on TGA curve. The weight retention of the PS-I-1-58.0k was 29.1 % at 800 °C, in contrast to 83.5 % for the initiator NPs, indicating that the polymer brushes were successfully grown from the surface of the SiNPs. The morphology of the hairy NPs was investigated by TEM (Figure 5.3). The nanoparticles were self-assembled into a pattern. Using the average size of SiNPs (92 nm), TGA data (Figure 5.2b), and the DP of the free polymer, and the density of SiNPs (2.33 g/cm^3), the grafting density of PS brushes was found to be 0.83 chains/nm². The molecular weights and grafting densities of PnBA-I-1-58.0k and PS-I-2-31.7k were summarized in table 5.1.

5.3.3 Synthesis of Hairy SiNPs from Initiator-Functionalized SiNPs made by Surface Hydrosilylation

Silane chemistry is a robust way to functionalize SiNPs with organic moieties. However, the nature of the silanization requires the surface of silicon to be oxidized first, where the composition of the resulting silicon-oxide surface is difficult to be precisely controlled. Therefore, it is of great significance to develop an immobilization method with which an ATRP initiator can be directly linked to the surface of SiNPs without introduction of a silanol group. Herein, transition-metal catalyzed hydrosilylation was used to directly immobilize ATRP initiator onto the surface of silicon nanoparticles by surface hydrosilylation of Si-H bond functionalized SiNPs. HF/HNO₃ etching was used here as the first step to introduce Si-H bond onto the surface of the bare SiNPs. It is worth mentioning that the obtained hydrogen-terminated SiNPs are usually not very stable toward slow oxidization by air. Therefore, the freshly etched Si-H NPs was used immediately in the next step in a semi-wet state. After homogeneously dispersed by ultrasonication in excessive amount short-chain ATRP initiator (the mass ratio of the initiator to Si-H NPs used was 15:1). To the dispersion, platinum–divinyltetramethyldisiloxane complex in xylenes (2.1–2.4% platinum concentration, 50 μL) was added as a catalyst. After degassed by three cycle of freeze-pump-thaw,

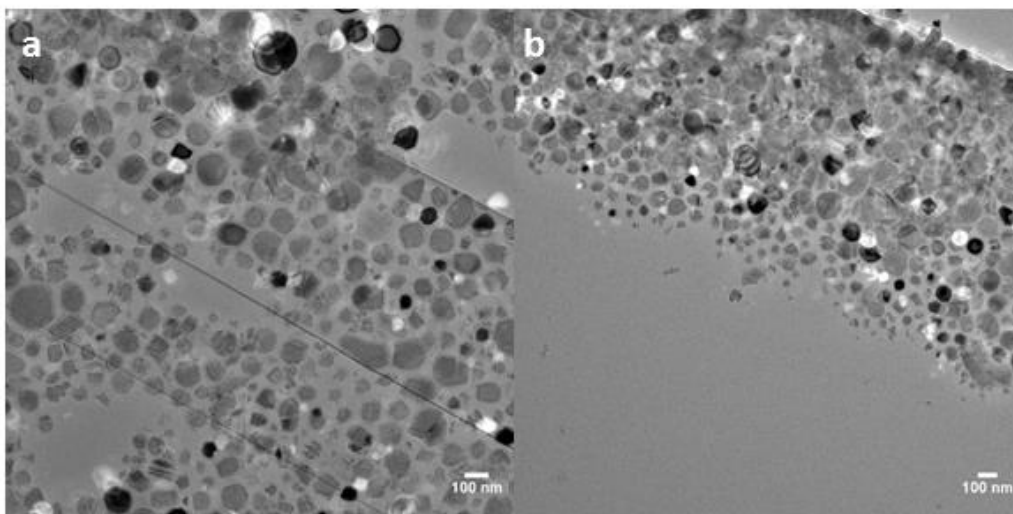


Figure 5.3. Bright field TEM micrographs of PS-I-1-58.0k. The hairy NPs were cast onto carbon-coated, copper TEM grids from the THF dispersion with a hairy NP concentration of 1 mgmL^{-1} .

Table 5.1. Summary of hairy SiNPs using initiator NPs made by surface silanization

Initiator NPs	Hairy NPs	Ratio ^a (M:I), Monomer Conversion (%)	$M_{n,SEC}$ (KDa), PDI ^b	DP ^c	σ (Chains/nm²) ^d
INP-I-1	PS-I-1-58.0k	780:1, 71.7	58.0, 1.19	558	0.83
	PnBA-I-1-58.0k	587:1, 70.3	58.0, 1.23	382	0.84
INP-I-2	PS-I-2-31.7k	422:1, 65.6	31.7, 1.26	305	0.77

^a [Monomer]/[free initiator]. ^b The values of $M_{n,SEC}$ and polydispersity indices (PDI) were obtained by size exclusion chromatography (SEC) calibrated with polystyrene standards. ^c The degree of polymerization (DP) was calculated using the monomer conversion and the molar feed ratio of monomer to the sum of free initiator and surface initiator. ^d Grafting density was calculated by using TGA data, DPs of polymers, and the core silicon nanoparticle size of 92 nm.

immobilization reaction was carried out at 60 °C for a total of 70 h. The initiator NPs were purified by precipitation and centrifugation and then dried under high vacuum overnight. For the preparation of surface-initiated SET-LRP or surface initiated ATRP, the dry particles were dispersed in DMSO or anisole, respectively, to form a homogeneous dispersion. Two batches of Initiator NPs, INP-II-1 and INP-II-2 were synthesized using this route. Using INP-II-1, hairy NPs PS-II-1-41.1k and PnBA-II-1-41.3k were synthesized. Hairy NPs (PMA-II-2-43.7k and PnBA II-2-50.5k) were synthesized using INP-II-2. Take PMA-II-2-43.7k as an example, PMA brushes were grown from the INP-II-2 by surface-initiated SET-LRP of methyl acrylate at ambient temperature using Cu(0)/Me₆-TREN as catalyst in the presence of free initiator EBiB. The monomer reached a nearly complete conversion (99.8 %). The hairy NPs were purified by repetitive dispersion in THF and ultracentrifugation. SEC analysis showed that the $M_{n,SEC}$ and PDI of the free copolymer formed from EBiB were 43.7 KDa and 1.14, respectively, indicating that the polymerization was controlled. TGA curves shows a 36.2 % difference between the initiator NPs and hairy particles at 800 °C (Figure 5.4b), which is a clear sign of successful surface-initiated polymerization. Using the final conversion of the monomer determined from the ¹H NMR spectrum and the molar ratio of the monomer to the sum of the free initiator and the surface initiator, the DP was calculated to be 517. The grafting density was 0.34 chains/nm². Table 5.2 gives a brief summary of the hairy SiNPs made by grafting polymers from the initiator NPs made by this oxide-free protocol. TEM pictures of PMA-II-2-43.7k were shown in Figure 5.5. The well-assembled SiNPs indicated the successful growth of PMA chains from the surface of SiNPs.

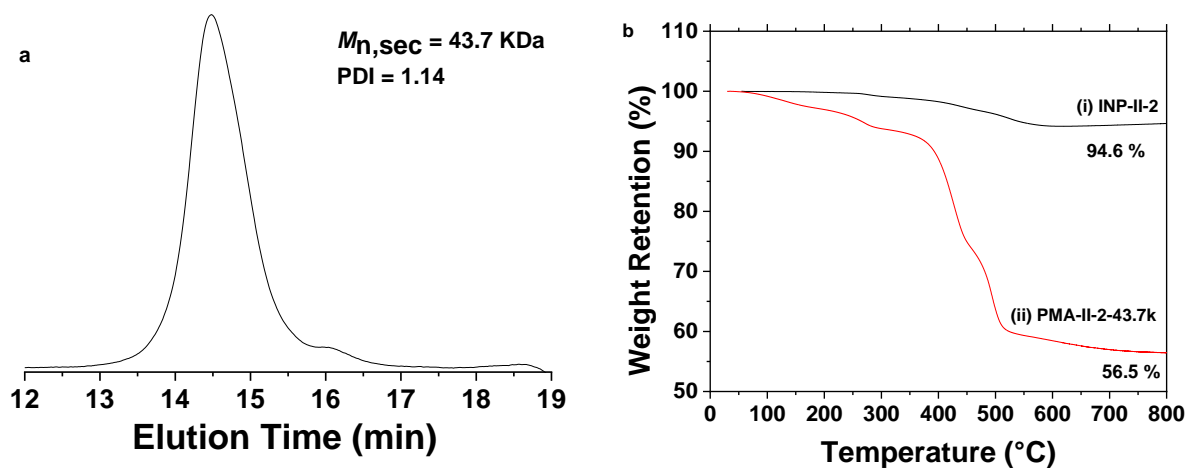


Figure 5.4. SEC trace of the dried free polymer PMA formed from the free initiator ethyl 2-bromoisobutyrate in the synthesis of PMA-II-2-43.7k (a) and TGA curves of (i) INP-II-2 and (ii) PMA-II-2-43.7k (b)

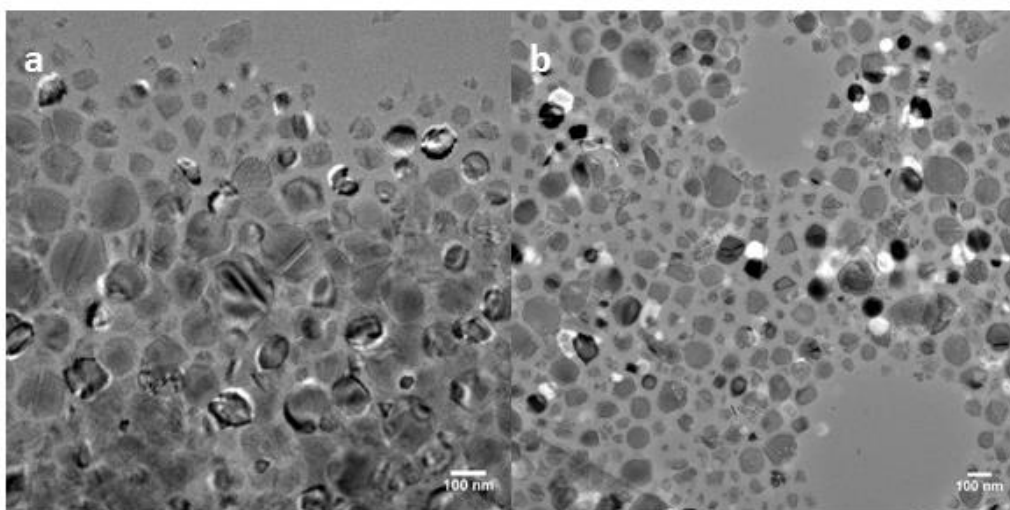


Figure 5.5 Bright field TEM micrographs of PMA-II-2-43.7k. The hairy NPs were cast onto carbon-coated, copper TEM grids from the THF dispersion with a hairy NP concentration of 1 mgmL⁻¹.

Table 5.2. Summary of hairy SiNPs using initiator NPs made by surface hydrosilylation

Initiator NPs	Hairy NPs	Ratio ^a (M:I), Monomer conversion	M_{n,SEC} (KDa), PDI ^b	DP ^c	σ (Chains/nm²) ^d
INP-II-1	PS-II-1-41.1k	560:1, 70.8 %	41.1, 1.16	384	0.38
	PnBA-II-1-41.3k	591:1 50.1 %	41.3, 1.25	299	0.56
INP-II-2	PMA-II-2-43.7	513:1 99.8 %	43.7, 1.14	517	0.34
	PnBA-II-2-50.5k	920:1 40.9 %	50.5, 1.24	373	0.30

^a [Monomer]/[free initiator]. ^b The values of $M_{n,SEC}$ and polydispersity indices (PDI) were obtained by size exclusion chromatography (SEC) calibrated with polystyrene standards. ^c The degree of polymerization (DP) was calculated using the monomer conversion and the molar feed ratio of monomer to the sum of free initiator and surface initiator. ^d Grafting density was calculated by using TGA data, DPs of polymers, and the core silicon nanoparticle size of 92 nm.

5.3.4 Comparison Between the Two Initiator Immobilization Methods

Two immobilization methods, (i) surface silanization and (ii) surface hydrosilylation are employed to functionalize SiNPs with ATRP initiator. The grafting densities (~ 0.8 chains/nm²) of the hairy NPs obtained by method (i) are generally higher than those of the hairy NPs made by method (ii), which are around 0.4 chains/nm². This is probably due to the fact that the hydrolysis/condensation reaction of triethoxysilane on the particle surface usually leads to the formation of a crosslinked layer of the initiator.⁴⁸ Surface hydrosilylation, by comparison, does not have that effect. Besides, oxidization of the unstable Si-H NPs in air is another possible reason that surface hydrosilylation is not effective as surface silanization. However, there is an advantage in surface hydrosilylation route in that it is an alternative way to attach initiator directly on the surface of original SiNPs without introduction of silanol group. This is especially important for the application of SiNPs in such industry as microelectronics or energy storage, where the introduction of silica could be an issue.

5.4 Conclusion

Polymer brush-grafted SiNPs were synthesized by surface-initiated “living”/controlled radical polymerization from the surface of initiator-functionalized SiNPs. The initiator SiNPs were made by two different immobilization methods, surface silanization and surface hydrosilylation. While the surface silanization approach gives hairy SiNPs with higher grafting densities, the surface hydrosilylation provides us with a non-oxide option to synthesize hairy SiNPs. Polymer brush-grafted SiNPs show good stability in common solvents as indicated by TEM pictures. Future works on this project include investigating other properties of hairy SiNPs such as compatibility with

polymer matrix, processability and mechanical strength and exploring the possibility of applying the particles in practical fields like high refractive index material and sustainable energy storage.⁴⁹

5.5 References

1. Brus, L., Luminescence of Silicon Materials: Chains, Sheets, Nanocrystals, Nanowires, Microcrystals, and Porous Silicon. *J. Phys. Chem.* **1994**, *98*, 3575–3581.
2. Heitmann, J.; Müller, F.; Zacharias, M.; Gösele, U., Silicon Nanocrystals: Size Matters. *Adv. Mater.* **2005**, *17*, 795–803.
3. Dasog, M.; De los Reyes, G. B.; Titova, L. V.; Hegmann, F. A.; Veinot, J. G. C., Size vs Surface: Tuning the Photoluminescence of Freestanding Silicon Nanocrystals Across the Visible Spectrum via Surface Groups. *ACS Nano* **2014**, *8*, 9636–9648.
4. Hessel, C. M.; Reid, D.; Panthani, M. G.; Rasch, M. R.; Goodfellow, B. W.; Wei, J.; Fujii, H.; Akhavan, V.; Korgel, B., A. Synthesis of Ligand-Stabilized Silicon Nanocrystals with Size-Dependent Photoluminescence Spanning Visible to Near-Infrared Wavelengths. *Chem. Mater.* **2012**, *24*, 393–401.
5. Papadimitrakopoulos, F.; Wisniecki, P.; Bhagwagar, D.E., Mechanically Attrited Silicon for High Refractive Index Nanocomposites. *Chem. Mater.* **1997**, *9*, 2928–2933.
6. Kim, H.; Seo, M.; Park, M. H.; Cho, J.A., Critical Size of Silicon Nano-Anodes for Lithium Rechargeable Batteries *Angew. Chem., Int. Ed.* **2010**, *49*, 2146–2149.
7. Graetz, J.; Ahn, C. C.; Yazami, R.; Fultz, B., Highly Reversible Lithium Storage in Nanostructured Silicon Electrochem. *Solid-State Lett.* **2003**, *6*, A194–A197.
8. Zhong, Y.; Peng, F.; Bao, F.; Wang, S.; Ji, X.; Yang, L.; Su, Y.; Lee, S.-T.; He, Y., Large-Scale Aqueous Synthesis of Fluorescent and Biocompatible Silicon Nanoparticles and Their Use as Highly Photostable Biological Probes. *J. Am. Chem. Soc.* **2013**, *135*, 8350–8356.

9. Borsella, E.; D'Amato, R.; Falconieri, M.; Trave, E.; Panarii, A.; Rivolta, I., An Outlook on the Potential of Si Nanocrystals as Luminescent Probes for Bioimaging. *J. Mater. Res.* **2013**, *28*, 193–204.
10. Choi, J.; Hui, C. M.; Pietrasik J.; Dong H. C.; Matyjaszewski K.; Bockstaller M. B., Toughening fragile matter: mechanical properties of particle solids assembled from polymer-grafted hybrid particles synthesized by ATRP. *Soft Matter*, **2012**, *8*, 4072.
11. Ngo, A. T.; Richardi J.; Pileni, M. P., Cracks in Magnetic Nanocrystal Films: Do Directional and Isotropic Crack Patterns Follow the Same Scaling Law? *Nano Lett.* **2008**, *8*, 2485–2489.
12. Pauchard, L.; Abou, B.; Sekimoto, K., Influence of Mechanical Properties of Nanoparticles on Macrocrack Formation. *Langmuir*, **2009**, *25*, 6672–6677.
13. Linford, M. R.; Chidsey, C. E. D., Alkyl monolayers covalently bonded to silicon surfaces. *J. Am. Chem. Soc.* **1993**, *115*, 12631-12632.
14. Linford, M. R.; Fenter, P.; Eisenberger, P. M.; Chidsey, C. E. D., Alkyl Monolayers on Silicon Prepared from 1-Alkenes and Hydrogen-Terminated Silicon. *J. Am. Chem. Soc.* **1995**, *117*, 3145–3155.
15. Boukherroub, R.; Morin, S.; Bensebaa, F.; Wayner, D. D. M., New Synthetic Routes to Alkyl Monolayers on the Si(111) Surface. *Langmuir* **1999**, *15*, 3831–3835.
16. Bateman, J. E.; Eagling, R. D.; Worrall, D. R.; Horrocks, B. R.; Houlton, A., Alkylation of Porous Silicon by Direct Reaction with Alkenes and Alkynes. *Angew. Chem., Int. Ed.* **1998**, *37*, 2683–2685.
17. Yang, Z.; Dobbie, A. R.; Cui, K.; Veinot, J. G. C.A., Convenient Method for Preparing Alkyl-Functionalized Silicon Nanocubes. *J. Am. Chem. Soc.* **2012**, *134*, 13958–13961.

18. Kelly, J. A.; Shukaliak, A. M.; Fleischauer, M. D.; Veinot, J. G. C., Size-Dependent Reactivity in Hydrosilylation of Silicon Nanocrystals. *J. Am. Chem. Soc.* **2011**, *133*, 9564–9571.
19. Hua, F.; Swihart, M. T.; Ruckenstein, E., Efficient Surface Grafting of Luminescent Silicon Quantum Dots by Photoinitiated Hydrosilylation. *Langmuir* **2005**, *21*, 6054–6062.
20. Tilley, R. D.; Warner, J. H.; Yamamoto, K.; Matsui, I.; Fujimori, H., Micro-Emulsion Synthesis of Monodisperse Surface Stabilized Silicon Nanocrystals. *Chem. Commun.* **2005**, 1833–1835.
21. Holland, J. M.; Stewart, M. P.; Allen, M. J.; Buriak, J. M., Metal Mediated Reactions on Porous Silicon Surfaces. *J. Solid State Chem.* **1999**, *147*, 251–258
22. Yu, Y., Hessel, C.M., Bogart, T.D., Panthani, M.G., Rasch, M.R. and Korgel, B.A., Room Temperature Hydrosilylation of Silicon Nanocrystals with Bifunctional Terminal Alkenes. *Langmuir* **2013**, *29*, 1533–1540.
23. Yu, Y.; Korgel, B. A., Controlled Styrene Monolayer Capping of Silicon Nanocrystals by Room Temperature Hydrosilylation. *Langmuir* **2015**, *31*, 6532–6537.
24. Yang, Z.Y.; Gonzalez, C.M.; Purkait, T.K.; Iqbal, M.; Meldrum, A.; Veinot, J.G.C., Radical Initiated Hydrosilylation on Silicon Nanocrystal Surfaces: An Evaluation of Functional Group Tolerance and Mechanistic Study. *Langmuir*, **2015**, *31*, 10540–10548.
25. Li, Y.; Wang, L.; Natarajan, B.; Tao, P.; Benicewicz, B. C.; Ullal, C.; Schadler, L. S., Bimodal “Matrix-Free” Polymer Nanocomposites., *RSC Adv.* **2015**, *5*, 14788-14795.
26. Zimmermann, L. W., M.; Caseri, W.; Suter, U.W., High Refractive Index Films of Polymer Nanocomposites. *J. Mater. Res.* **1993**, *8*, 1742-1748.

27. Tao, P.; Li, Y.; Rungta, A.; Viswanath, A.; Gao, J.; Benicewicz, B. C.; Siegel, R. W.; Schadler, L. S., TiO₂ Nanocomposites with High Refractive Index and Transparency. *J. Mater. Chem.* **2011**, *21*, 18623-18629.
28. Lee, S.; Shin, H.-J.; Yoon, S.-M.; Yi, D. K.; Choi, J.-Y.; Paik, U., Refractive Index Engineering of Transparent ZrO₂-Polydimethylsiloxane Nanocomposites. *J. Mater. Chem.* **2008**, *18*, 1751-1755.
29. Zhao, B.; Zhu, L., Mixed Polymer Brush-Grafted Particles: A New Class of Environmentally Responsive Nanostructured Materials. *Macromolecules* **2009**, *42*, 9369-9383.
30. Li, Y.; Tao, P.; Viswanath, A.; Benicewicz, B. C.; Schadler, L. S., Bimodal Surface Ligand Engineering: The Key to Tunable Nanocomposites. *Langmuir* **2013**, *29*, 1211-1220.
31. Zhou, F.; Liu, W.; Xu, T.; Liu, S.; Chen, M.; Liu, J., Preparation of silane-terminated polystyrene and polymethylmethacrylate self-assembled films on silicon wafer. *J. Appl. Polym. Sci.* **2004**, *92*, 1695-1701.
32. Siqueira, D. F.; Koehler, K.; Stamm, M., Structures at the Surface of Dry Thin Films of Grafted Copolymers. *Langmuir* **1995**, *11*, 3092-3096.
33. Tsujii, Y.; Ohno, K.; Yamamoto, S.; Goto, A.; Fukuda, T., Structure and Properties of High-Density Polymer Brushes Prepared by Surface-Initiated Living Radical Polymerization. *Adv. Polym. Sci.* **2006**, *197*, 1-45.
34. Wright, R. A. E.; Wang, K. W.; Qu, J.; Zhao, B., Oil-Soluble Polymer Brush-Grafted Nanoparticles as Effective Lubricant Additives for Friction and Wear Reduction. *Angew. Chem. Int. Ed.* **2016**, *55*, 8656-8660.

35. Zhang, J.; Cui, C. Q.; Lim, T. B.; Kang, E. T.; Neoh, K. G.; Lim, S. L.; Tan, K. L., Chemical Modification of Silicon (100) Surface via UV-Induced Graft Polymerization. *Chem. Mater.* **1999**, *11*, 1061–1068.
36. Peng, Q.; Lai, D. M. Y.; Kang, E. T.; Neoh, K. G., Preparation of Polymer–Silicon(100) Hybrids via Interface-Initiated Reversible Addition-Fragmentation Chain-Transfer (RAFT) Polymerization. *Macromolecules* **2006**, *39*, 5577–5582.
37. Perring, M.; Dutta, S.; Arafat, S.; Mitchell, M.; Kenis, P. J. A.; Bowden, N.B., Simple Methods for the Direct Assembly, Functionalization, and Patterning of Acid-Terminated Monolayers on Si (111). *Langmuir* **2005**, *21*, 10537–10544.
38. Xu, F. J.; Cai, Q. J.; Kang, E. T.; Neoh, K. G., Surface-Initiated Atom Transfer Radical Polymerization from Halogen-Terminated Si (111) (Si–X, X = Cl, Br) Surfaces for the Preparation of Well-Defined Polymer–Si Hybrids. *Langmuir* **2005**, *21*, 3221–3225.
39. Xu, F. J.; Yuan, Z. L.; Kang, E. T.; Neoh, K. G., Branched Fluoropolymer–Si Hybrids via Surface-Initiated ATRP of Pentafluorostyrene on Hydrogen-Terminated Si (100) Surfaces. *Langmuir* **2004**, *20*, 8200–8208.
40. Xu, F. J.; Zhong, S. P.; Yung, L. Y. L.; Tong, Y. W.; Kang, E. T.; Neoh, K.G., Collagen-Coupled Poly(2-hydroxyethyl methacrylate)–Si(111) Hybrid Surfaces for Cell Immobilization. *Tissue Eng.* **2005**, *11*, 1736–1748.
41. Moran, I. W.; Carter, K. R., Direct Passivation of Hydride-Terminated Silicon (100) Surfaces by Free-Radically Tethered Polymer Brushes. *Langmuir* **2009**, *25*, 9232–9239.
42. Thissen, P.; Seitz, O.; Chabal, Y., Wet chemical surface functionalization of oxide-free silicon. *J. Prog. Surf. Sci.* **2012**, *87*, 272-290.

43. Kang, Z.H.; Liu, Y.; Tsang, C.H.A.; Ma, D.D.D.; Fan, X.; Wong, N.B.; Lee, S.T., Water-Soluble Silicon Quantum Dots with Wavelength-Tunable Photoluminescence. *Adv. Mater.* **2009**, *21*, 661-664.
44. Puniredd, S. R.; Jayaraman, S.; Yeong, S. H.; Troadec, C.; Srinivasan, M. P., Stable Organic Monolayers on Oxide-Free Silicon/Germanium in a Supercritical Medium: A New Route to Molecular Electronics. *J. Phys. Chem. Lett.* **2013**, *4*, 1397-1403.
45. Harada, Y.; Koitaya, T.; Mukai, K.; Yoshimoto, S.; Yoshinobu, J., Spectroscopic Characterization and Transport Properties of Aromatic Monolayers Covalently Attached to Si (111) Surfaces. *J. Phys. Chem. C.* **2013**, *117*, 7497-7505.
46. Ciampolini, M.; Nardi, N., Five-Coordinated High-Spin Complexes of Bivalent Cobalt, Nickel, and Copper with Tris(2-dimethylaminoethyl)amine. *Inorg. Chem.* **1966**, *5*, 41-44.
47. Sato, K.; Tsuji, H.; Hirakuri, K.; Fukata, N.; Yamauchi, Y., Controlled Chemical Etching for Silicon Nanocrystals with Wavelength-Tunable Photoluminescence. *Chem Commun (Camb)* **2009**, 3759-3761.
48. Alexander Y. Fadeev.; Thomas J. McCarthy., Self-Assembly Is Not the Only Reaction Possible between Alkyltrichlorosilanes and Surfaces: Monomolecular and Oligomeric Covalently Attached Layers of Dichloro- and Trichloroalkylsilanes on Silicon. *Langmuir* **2000**, *16*, 7268-7274.
49. Tu, Z.; Zachman, M. J.; Choudhury, S.; Wei, S.; Ma, L.; Yang, Y.; Kourkoutis, L. F.; Archer, L. A., Nanoporous Hybrid Electrolytes for High – Energy Batteries Based on Reactive Metal Anodes. *Adv. Energy Mater.* **2017**, *7*, 1602367

**Appendix D for Chapter 5. Polymer Brush-Grafted Silicon Nanoparticles by
Surface-Initiated Controlled Radical Polymerization: Synthesis and
Characterization**

D.1 Supplemental Figures

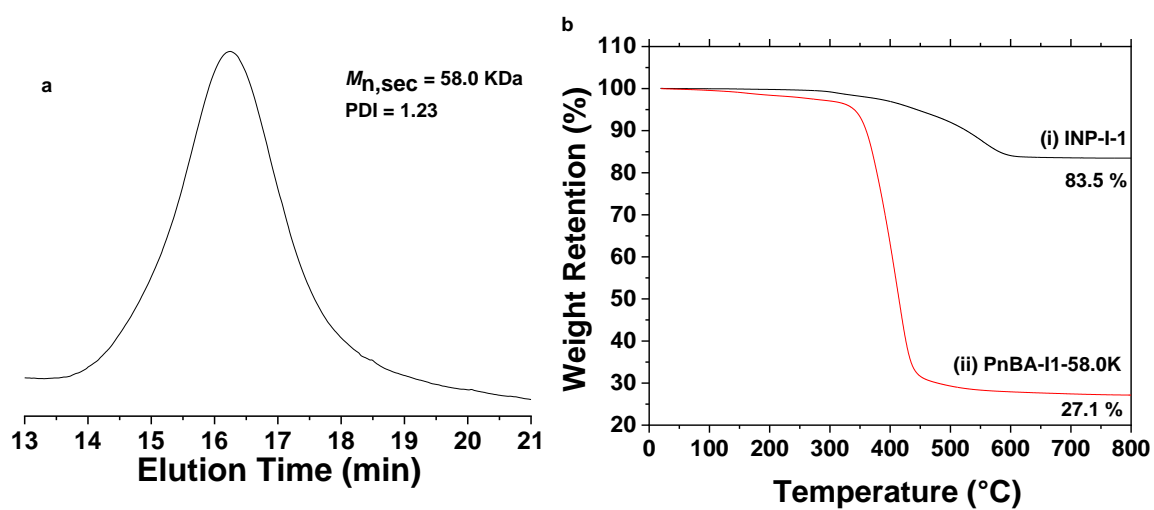


Figure D1. SEC trace of the dried free polymer PnBA formed from the free initiator ethyl 2-bromoisobutyrate in the synthesis of polymer brush-grafted silicon nanoparticles PnBA-I-1-58.0k (a) and TGA curves of (i) INP-I-1 and (ii) PnBA-I-1-58.0k (b).

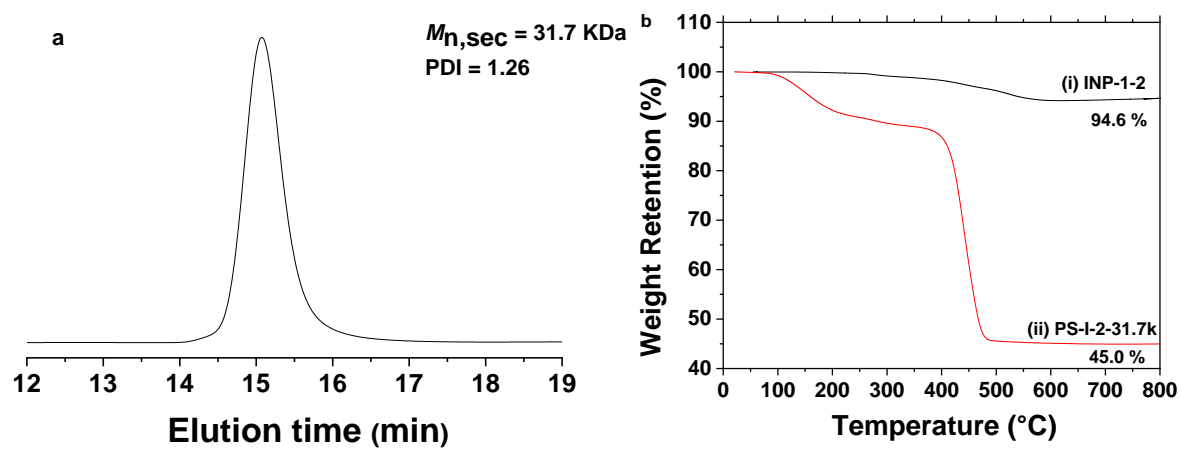


Figure D2. SEC trace of the dried free polymer polystyrene formed from the free initiator ethyl 2-bromoisobutyrate in the synthesis of polymer brush-grafted silicon nanoparticles PS-I-2-31.7k (a) and TGA curves of (i) INP-I-2 and (ii) PS-I-2-31.7k (b).

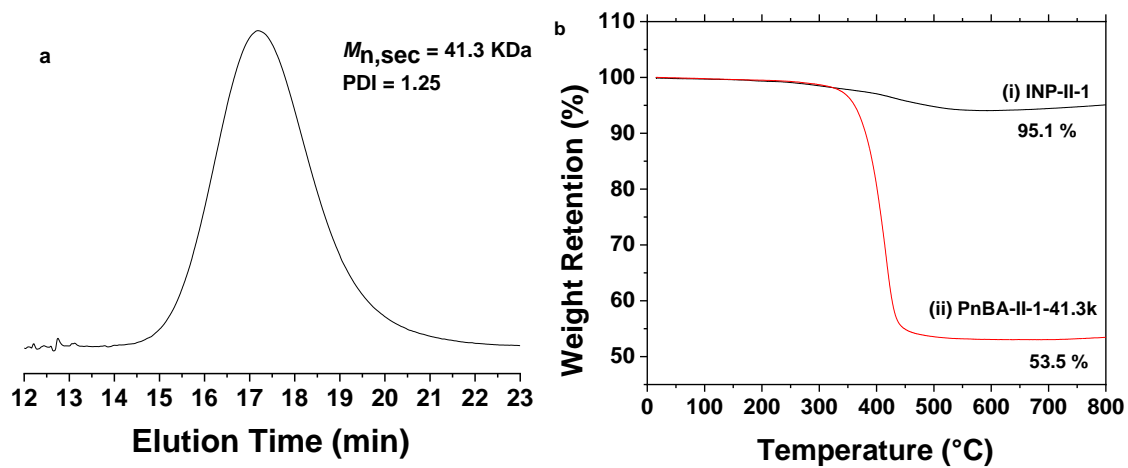


Figure D3. SEC trace of the dried free polymer PnBA formed from the free initiator ethyl 2-bromoisobutyrate in the synthesis of polymer brush-grafted silicon nanoparticles PnBA-II-1-41.3k (a) and TGA curves of (i) INP-II-1 and (ii) PnBA-II-1-41.3k (b).

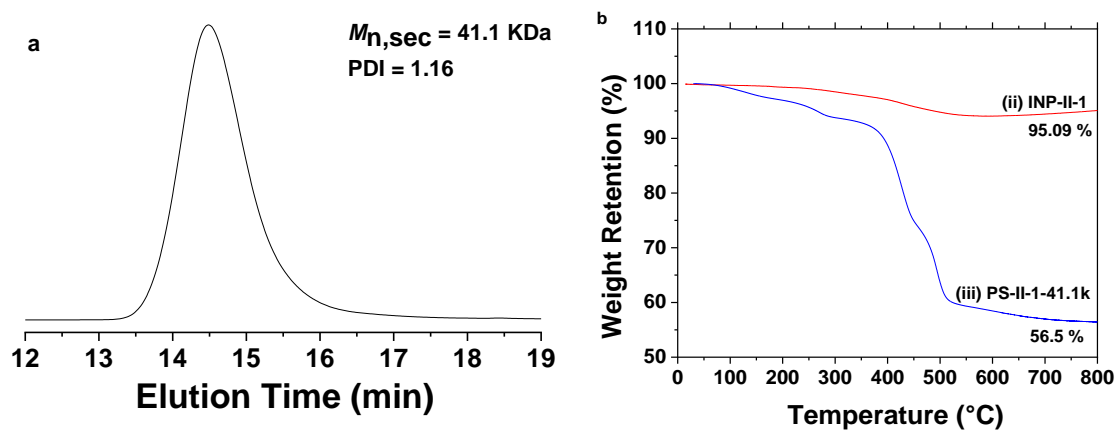


Figure D4. SEC trace of the dried free polymer polystyrene formed from the free initiator ethyl 2-bromoisobutyrate in the synthesis of polymer brush-grafted silicon nanoparticles PS-II-1-41.1k (a) and TGA curves of (i) INP-II-1 and (ii) PS-II-1-41.1k (b).

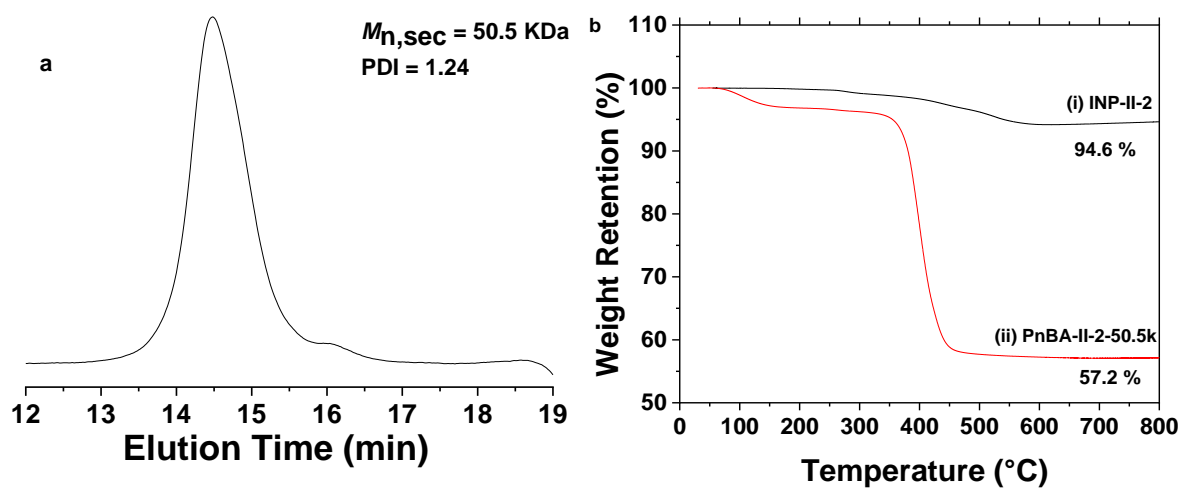


Figure D5. SEC trace of the dried free polymer PnBA formed from the free initiator ethyl 2-bromoisobutyrate in the synthesis of polymer brush-grafted silicon nanoparticles PnBA-II-2-50.5k (a) and TGA curves of (i) INP-II-2 and (ii) PnBA-II-2-50.5k (b).

D.2 Calculation of Grafting Density of polymer Brushes on 92 nm Silicon Nanoparticles

What is described here is the calculation of grafting density of polymer brushes on 92 nm silicon nanoparticles using PS-HNP-31.7k as an example. The data needed for the calculation include the size of the SiNPs determined by TEM, $M_{n,SEC}$ of polystyrene and TGA data of hairy NPs and initiator NPs. In order to correct the difference in the weight retentions at 100 °C of the TGA data between hairy NPs and initiator NPs, we choose the larger one of these two weight retentions as a reference and adjusted the weight retentions at 800 °C accordingly. The weight retentions at 100 °C of INP-II-1 and PS-HNP-31.7k were 99.96 % and 99.26 %, respectively, while the weight retentions at 800 °C were 94.64 % and 44.98 %, respectively. Thus, we set the weight retention at 100 °C as 99.96 %, and the weight retention of PS-HNP-31.7 k at 800 °C was adjusted to 45.68 %. Therefore, the ratio of the silicon residue to the volatile portion at 800 °C was 100:5.66 for INP-I-1 and 100:118.90 for PS-HNP-31.7k. The molecular weight of the polystyrene, determined by GPC, is 3.17×10^4 g/mol. Assuming that the SiNPs are spherical and the density is 2.33 g/cm^3 , the mass of a single silicon NP, of which the diameter is 92 nm, is 9.50×10^{-16} g. The mass of the grafted polymer on one single SiNPs is then calculated to be 1.08×10^{-15} g. Therefore the number of polystyrene chains grafted on one SiNPs is $1.08 \times 10^{-15} \text{ g} / (3.17 \times 10^4 \text{ g/mol}) \times 6.022 \times 10^{23} = 20516$ chains. Hence, the grafting density of PS brushes on SiNPs is $20516 \text{ chains} / (\pi \times 92^2) = 0.77 \text{ chains/nm}^2$. We use the molecular weight determined by GPC as the “actual” molecular weight of polystyrene here because polystyrene is used as the standard polymer for the calibration of the GPC. However, the molecular weight of PMA and PnBA should be calculated as the product of the DP of the polymer and the molecular weight of the monomer. Here, DP is the product of the monomer conversion and the molar ratio of the monomer to the sum of free initiator and surface initiator. Below is an example of calculation of DP based on sample PnBA-I-1-58.0k. First step is

to correct the difference in the weight retentions at 100 °C of the TGA data between hairy NPs and initiator NPs, we choose the larger one of these two weight retentions as a reference and adjusted the weight retentions at 800 °C accordingly. The weight retentions at 100 °C of INP-I-1 and PnBA-I-1-58.0k were 99.95 % and 99.56 %, respectively, while the weight retentions at 800 °C were 83.50 % and 27.10 %, respectively. Thus, we set the weight retention at 100 °C as 99.95 %, and the weight retention of PnBA-I-1-58.0k at 800 °C was adjusted to 27.20 %. Therefore, the ratio of the silicon residue to the volatile portion at 800 °C was 100:19.76 for INP-I-1 and 100:267.65 for PnBA-I-1-58.0k. Since the mass of the initiator NPs used is 230 mg, then the total mass of grafted PnBA is $[(267.65-19.76)/(100 + 19.76)] \times 230 \text{ mg} = 476 \text{ mg}$. Then using the monomer conversion 70.3 % and the mass of monomer 8.112 g (78 mmol), we can calculate the total amount of polymer (free polymer + grafted polymer), which is 5.703 g. Thus, the mass of free polymer is 5.225 g. The free initiator used on the polymerization is 19.7 mg (101 μmol), so the total moles of the initiator, including free initiator and surface initiator, is $101 \times (5.703/5.225) = 110 \mu\text{mol}$. Therefore, the ratio between monomer to total amount of initiator was 709 and the DP was 498. The molecular weight of PnBA is $6.37 \times 10^4 \text{ g/mol}$. Then using the same method as mentioned before, the grafting density of PnBA-I-1-58.0k was calculated as 0.84 chains/nm.

Chapter 6. Conclusions and Future Work

Successful implementation of application-specific surface functionalization of nanoparticles depends on a variety of factors, including the type of nanoparticles, the design of suitable functionalities and the selection of functionalization methods. This dissertation work provided two vivid cases demonstrating the development of effective nanoparticle surface functionalization methods confronting specific problems in different applications.

The first case is the application of silicon nanoparticles (SiNPs) as safe and high-capacity anode materials of next-generation lithium-ion battery. The biggest issue preventing massive commercialization of silicon anode is the drastic volume change during lithiation/delithiation process, which leads to many problems such as fracture of active materials, instability of electrode/electrolyte interface and isolation of active materials from conductive network, and eventually causes rapid capacity fade.¹ Chapter 2 presented a proof of concept that modification on particle level can help to improve the electrochemical performance of silicon electrode.² Surface silanization reaction was adopted to attach an epoxy group onto the surface of SiNPs. Silanization is a robust method to functionalize nanoparticle surface with organic moieties by the reaction between surface hydroxide group and silane compounds. For better functionalization effect, SiNPs was pretreated with boiling peroxide solution to introduce more hydroxy groups on the surface. Compared with the electrode made by pristine SiNPs, the electrode based on epoxy-functionalized SiNPs showed better capacity retention over extended electrochemical cycles and lower interfacial resistance. This improvement could be attributed to the reaction between surface epoxy group with poly(acrylic acid) binder as confirmed by both FTIR and TGA analysis. The reaction helped to promote integrity of conductive network as indicated by SEM analysis and peel tests. Furthermore, XPS analysis also revealed that surface functionalization helps to stabilize electrode/electrolyte interface and to mitigate parasitic reaction of electrolyte solvents and salts on

electrode surface. In Chapter 3, plasma-synthesized SiNPs covered with Si-H bonds provide a platform to anchor a series of specially designed functional groups featuring ethylene oxide of different chain lengths, which is also terminated with an epoxy group, onto the particle surface by surface hydrosilylation reaction. Surface hydrosilylation reaction is an alternative to surface silanization reaction to synthesize oxide-free SF-SiNPs.³ When applied as active materials in graphite-silicon composite electrode, SF-SiNPs had better stability in electrode lamination than bare particles as indicated by TEM and dispersion test. In addition, electrode based on SF-SiNPs showed improvements in both initial capacities and capacity retention than that of pristine SiNPs. SF-SiNPs with only ethylene oxide group were fabricated in a purpose to study the different roles of the two functional groups. Based on the results of this controlled experiment, it was derived that that surface ethylene oxide group mainly helped to mitigate irreversible capacity loss and increase capacity retention with its ability to facilitate transport of Li^+ , while surface epoxy group enhance utility efficiency of the capacity of active materials by promoting binder-particle interaction. Furthermore, it was found that the grafting density of surface functional groups is in positive relations with electrochemical performance of SiNPs. Significance of this work lies in that it demonstrated that surface properties of SiNPs can be tuned by manipulating the types and densities of surface functional groups and thus in turn influence the electrochemical performance. With this guideline, other surface functional groups can be designed to address specific problems related with silicon anode. For instance, a “sacrificial” SEI layer can be introduced onto the surface of SiNPs to stabilize the electrode/electrolyte interface or an electronic conductive functional group can be attached to enhance the electronic conductivity of anode surface.

The second case is the development of processable high RI materials. Many metal oxides nanoparticles have high RI but cannot be applied directly as optical materials due to poor

processability. Functionalization of metal oxide nanoparticles with polymers of excellent processability and mechanical properties is a feasible way towards the purpose.⁴ Chapter 4 described the synthesis of polymer brush-grafted titanium dioxide nanoparticles (hairy TiO₂ NPs) by SI-ATRP to make processable high RI hybrid materials. The incorporation of sulfur atom, which has high molar refraction and good compatibility with polymer matrix, into the side chain of styrenic- and methacrylate-type polymers increases the RIs of the polymers. SI-ATRP is an extensively used method to grow polymer chains with controlled structures and chain length from nanoparticles.^{5, 6} The hairy TiO₂ NPs can be made into thin films and have good potential to be used in high RI nanocomposites. Possible future work on this project includes introduction of other intrinsic high RI polymers such as organometallic polymers or different polymer architectures such as block polymers onto the nanoparticles to retain more functionalities.

The two cases in this dissertation work is just the tip of the iceberg. There are many other fields where surface functionalization can be employed to address the problems in the practical use of nanoparticles. In terms of SiNPs, apart from being a promising anode alternative for lithium-ion battery, SiNPs are also “star” materials in many other fields such as semiconductors, sensors, optics and so on. Successful application of SiNPs in these fields requires good compatibility and processability of the particles. Chapter 5 described a potential method to achieve this purpose. Polymer brush-grafted SiNPs (hairy SiNPs) were synthesized by SI-LRP. The LRP initiators are immobilized onto the particle surface with two different methods: surface silanization and surface hydrosilylation. Surface silanization method gives hairy SiNPs with higher grafting densities, while surface hydrosilylation provides an oxide-free functionalization option. TGA and TEM analysis confirms the success of the functionalization. The hairy SiNPs show good stability in common solvents. As for the future work, the processability and compatibility of the hairy SiNPs

needs to be further verified. The hairy SiNPs have many possible applications. For instance, the particles can be used as building block in polymer matrix to make high RI hybrid materials as SiNPs have very high RI values. Possible future work is to adopt this method in many other applications including nanocomposite electrolyte, biosensors and so on.

6.1 Reference

1. Chae, S.; Ko, M.; Kim, K.; Ahn, K.; Cho, J., Confronting issues of the practical implementation of Si anode in high-energy lithium-ion batteries. *Joule* **2017**, *1*, 47-60.
2. Jiang, S.; Hu, B.; Sahore, R.; Zhang, L.; Liu, H.; Zhang, L.; Lu, W.; Zhao, B.; Zhang, Z., Surface-Functionalized Silicon Nanoparticles as Anode Material for Lithium-Ion Battery. *ACS Appl. Mater. Interfaces* **2018**, *10*, 44924-44931.
3. Linford, M. R.; Chidsey, C. E. D., Alkyl monolayers covalently bonded to silicon surfaces. *J. Am. Chem. Soc.* **1993**, *115*, 12631-12632.
4. Lü, C.; Yang, B., High refractive index organic–inorganic nanocomposites: design, synthesis and application. *Journal of Materials Chemistry* **2009**, *19*, 2884-2901.
5. Hu, B.; Henn, D. M.; Wright, R. A. E.; Zhao, B., Hybrid Micellar Hydrogels of a Thermosensitive ABA Triblock Copolymer and Hairy Nanoparticles: Effect of Spatial Location of Hairy Nanoparticles on Gel Properties. *Langmuir* **2014**, *30*, 11212-11224.
6. Wright, R. A. E.; Hu, B.; Henn, D. M.; Zhao, B., Reversible sol–gel transitions of aqueous dispersions of silica nanoparticles grafted with diblock copolymer brushes composed of a thermosensitive inner block and a charged outer block. *Soft matter* **2015**, *11*, 6808-6820.

Vita

Sisi Jiang was born in Shanghai, China. She attended Fudan University from 2007 to 2011, where she received her B.S. degree in Macromolecular Materials and Engineering. After graduation, she worked as a quality inspector in Shanghai Tobacco Company from 2011 to 2013. Then she enrolled as a graduate student in the Department of Chemistry at Georgia State University in August 2013. She received her Master of Science degree at GSU in December 2014. After that she joined Professor Bin Zhao's research group in the Department of Chemistry at the University of Tennessee, Knoxville in January 2015 and worked on polymer brush-grafted nanoparticles. During her study at UTK, she worked as a visiting graduate student at Argonne National Lab, focusing on surface modification of silicon anode in lithium-ion battery. Sisi Jiang received her Doctor of Philosophy in Chemistry from the University of Tennessee, Knoxville in May, 2019.